CHAPTER 1: AN INTRODUCTION TO SECONDARY ION MASS SPECTROMETRY (SIMS) IN GEOLOGY

Richard A. Stern
Department of Earth and Atmospheric Sciences
University of Alberta
Edmonton, Alberta
Canada T6G 2E3
rstern@ualberta.ca

INTRODUCTION

The basis of the secondary ion mass spectrometry (SIMS) technique is the phenomenon where bombardment of a solid by a primary ion beam generates secondary ions. The secondary ions, analyzed for their mass-to-charge (m/z) ratios in a mass spectrometer, in turn reflect some compositional attribute of the solid (Fig. 1-1). In fact, as is the case for all mass spectrometric methods, it is the ratio of two secondary ion intensities (*e.g.*, $^{18}O^-/^{16}O^-$, $^{143}Nd^+/^{28}Si^+$) that is used for purposes of elemental or isotopic quantification. SIMS is an enormously widespread technique in the physical sciences and has many uses, including 'bulk' chemical or isotopic analysis from micro-volumes, imaging of element distributions, measuring compositional changes with depth, and surface molecular chemistry. The key advantages of SIMS are the ability to localize the analyses to the micro- and even nano-scale, the very low detection limits, and access to the entire periodic table. It is interesting to note that there exists a related technique called sputtered neutral mass spectrometry (SNMS), in which the large fraction of neutral sputtered species are ionized extrinsically (Benninghoven *et al.* 1987, Higashi 1999), but this has yet to be applied in geology.

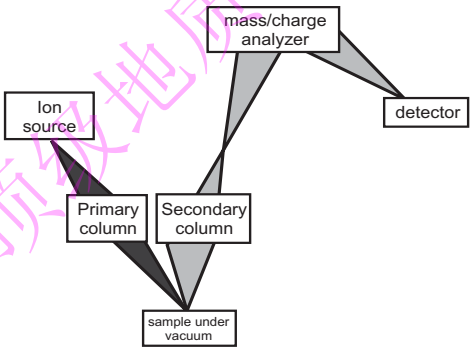


FIG. 1-1. Fundamental elements of a secondary ion mass spectrometer.

Although SIMS is a major technique employed in geochemistry and cosmochemistry, unfortunately no comprehensive treatments exist to guide geologists. A useful overview by Ireland (1995) remains relevant, and there are several texts and synopses for readers seeking details of the SIMS technique (Williams 1985, Benninghoven *et al.* 1987, Vickerman *et al.* 1989, Williams 1990). Readers seeking a broader understanding of mass spectrometry will find Becker's (2008) book useful. To understand SIMS applications in geology today, it is helpful to understand the basic analytical technique, and to become familiar with SIMS instrumentation, as they influence the approaches and capabilities to solve geochemical problems. Words in **bold** are defined in the glossary.

Brief Description of SIMS

The bombarding primary ions, typically of energies between 1 keV and 20 keV and either positively or negatively charged, become implanted within the uppermost atomic layers of the solid under **very high** to **ultra-high vacuum** (Fig. 1-2). The kinetic energy of the primary ions is transferred to target atoms by several generations of quasi-elastic collisions of the recoiling target atoms in a so-called '**collision cascade**' (Sigmund 1969). Recoil particles, both atoms and molecules (including molecular **fragments** or **clusters**), that have a component of motion toward the surface may escape (*i.e.*, are **sputtered**) if the kinetic energy of the recoiling atom exceeds the **surface binding energy** for the sputtered particle, typically <5 eV. Anywhere from one to tens of secondary particles may be sputtered for each incoming ion, termed the **total sputter yield**, and typical sputter rates are 1–5 nm/s. Most sputtered particles are neutral and simply fall back onto the sample, but the small fraction of particles that are ionized (typically <<10%, and highly variable) can be

Mineralogical Association of Canada Short Course 41, Toronto, May 2009, p. 1-18.

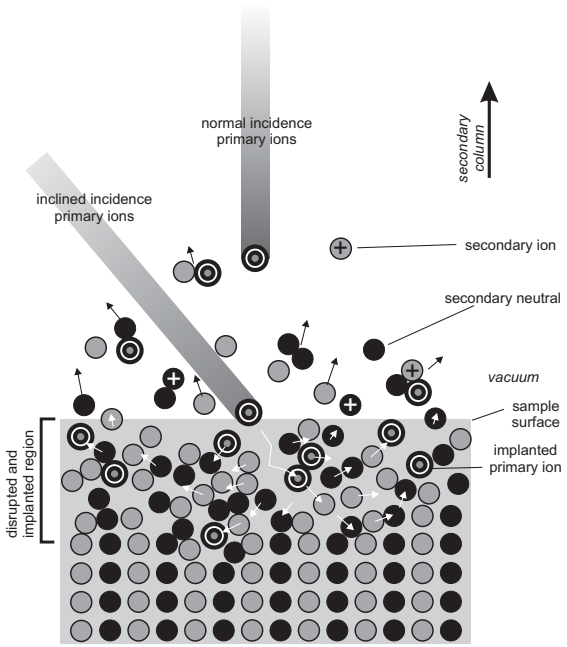


FIG. 1-2. Illustration of the sputtering process at the atomic scale. Shown are a normal incidence primary ion beam, utilized in some instruments, and the more common inclined incidence primary ions. The knock-on effects of the collision cascade are illustrated with the white arrows. Sputtered neutral and charged atoms and molecules are ejected from the implanted and structurally disrupted upper atomic layers. Ionization is generally considered to occur within the electrically and kinetically excited upper layers of the sample by processes still debated. Secondary ions are electrostatically drawn into the secondary column and then to the mass analyzer.

extracted into the secondary column and mass spectrometer (Figs. 1-1, 1-2). A figure of merit in SIMS is the **useful (ion) yield**, defined as the number of ions detected per atom of that species sputtered. Useful yields are highly variable, and depend on the element, the sample matrix, the instrument transmission (typically <0.5, but up to ~1.0 is possible) and the specific analytical conditions, but are generally 10^{-1} to 10^{-4} (*i.e.*, inefficient), which is typical of many other mass spectrometric techniques.

Although ion bombardment involves jostling of target atoms, the amounts of energy deposited are, compared with laser ablation, about five orders of magnitude lower, so *heating and vaporization are not the principal processes in SIMS*. Despite some success in describing the sputtering phenomenon in terms of the thermal behavior of the target, there is, in fact, no evidence that a plasma actually exists. The implantation of ions into the solid surface results in major changes to its electronic structure and bulk composition, as it momentarily becomes a mixture of the original target and the implanted ion species. Furthermore, the bombardment of the solid usually results in substantial damage to its crystalline structure, and the sputtered surface can be described as an 'amorphous selvedge' (Benninghoven *et al.* 1987). Sputtered particles are emitted mostly from the outer one or two atomic layers (<0.5 nm), whereas the primary ions penetrate several atomic layers, typically ~10 nm (Fig. 1-2). An ion that impacts a pristine surface will initially sputter some intact molecules from the uppermost atomic layer (**monolayer**), but subsequently the sputtered material will have been drastically altered by ion bombardment. The sputtered particles have a range of kinetic energies when they leave the surface, with most less than 10 eV and decreasing fractions up to 100s of eV. Atomic and molecular ions have distinct energy distributions, a fact that is often exploited in certain types of analyses.

A critical limitation of SIMS is relating secondary ion signal intensities to the actual (or relative, for isotopic analysis) abundances of the atoms of interest within the solid. In fact, the elemental specificity of ion yields is one of the defining characteristics of SIMS. Secondary ion signals are strongly dependent on the properties of the particular atom, such as its ionization potential, and its chemical and electronic environment, collectively termed **matrix effects**. We have seen, in fact, that bombardment itself changes the sample matrix, and therefore matrix effects are a combination of the nature of the undisturbed solid as well as the particular conditions employed during sputtering, including the type and energy of the primary ion. And despite the structural disruption induced by bombardment, secondary ion yields may also remain sensitive to the crystal structure of the original material. Secondary ions originate at or within the sample surface due to several interrelated factors, including the kinetic energy imparted by the implanted ions, and the chemical and electronic

http://bbs.3s001.com/

structure of the environment containing the **analyte** atom. Ion formation has, in fact, defied a theory of any practical significance in analytical chemistry of chemically complex targets (Williams 1985, Williams 1990). In general, matrix effects are less important for atomic ions of the same element (**isotopes**) compared with ions of different elements (*e.g.*, Hinton 1990).

Most types of quantitative analyses with SIMS, whether elemental or isotopic ratios, require empirical calibration of instrumental bias using **reference materials** that are assumed to be identical in composition to the unknown material, or bracket the unknown composition. Various types of analytical strategies have been adopted to reduce the matrix effects, such as measuring only high energy secondary ions (**energy filtering**). Additionally, secondary ion mass spectra are usually populated by numerous molecular ions, some of which may interfere with the ion of interest (*i.e.*, having nominally identical m/z (**isobars**)). The instrument type and conditions of analysis are important in reducing or resolving isobaric interferences and other potential analytical biases to an acceptable level. The efforts that practitioners take in calibration are directly related to the complexity of the target composition and the precision and accuracy desired, and most laboratories have developed unique reference materials and customized methods for their particular instruments and samples.

SIMS ORIGINS

SIMS has its roots in the development of mass spectrography (the recording of mass spectra on photographic film) and mass spectrometry (the electronic quantification of selected m/z signals) in the early part of the 20th century. Through to the middle part of the century, great improvements were made in the physics of designing better **mass analyzers**, and in the period 1945–1960 there was recognition of the potential for mass spectrometric techniques in analytical chemistry. New instruments were introduced and applications followed, particularly for the analysis of gases and liquids, which are relatively easy to ionize. However, producing ions directly from solids presented particular difficulties.

A significant advance in the analysis of solids was the development of an analytical platform that used (primary) ion bombardment and the resulting sputtering to generate (secondary) ions (Herzog & Viehböck 1949). The principle of secondary ion formation by sputtering had been recognized 40 years earlier by J.J. Thomson (1910), and received increasing attention just before and after WWII (for references, see Liebl 1974, Honig 1985). Instrumentation for SIMS comprises three distinct parts, the ion probe to generate the secondary ions, the secondary extraction column, and the mass analyzer (Fig. 1-1). We frequently refer to the 'ion (micro)probe' and imply that a mass analyzer is attached, although this is not necessarily the case. For example, ion microprobes nowadays can be used for micro-machining of solids in 'focused ion beam' (FIB) applications. In the case of SIMS instrument development, the concepts for mass analyzer design were generally well established, but the significant advance and foremost interest was in developing the ion probe as a source of secondary ions. It may come as a surprise that the initial motivation for SIMS development was not spatially controlled sampling, it was simply an improved method of generating ions from solids.

The first commercial SIMS instrument (IMS-101), initially called a 'solids mass spectrometer,' utilized Ar^+ primary ions to generate positive secondary ions (Liebl & Herzog 1963). The diameter of the probe was initially millimetres (*i.e.*, a 'macroprobe'). The development of the IMS-101, was, in fact, motivated by geology, as it was a NASA initiative related to the lunar program, and resulted in ground-breaking chemical and isotopic analyses of, amongst other things, meteorites (*e.g.*, Poschenrieder *et al.* 1965). The electronics industry quickly recognized SIMS as having low **detection limits** for many elements, and the unique ability to characterize the upper surface of solids, termed **in-depth** analysis. During the 1960s, the electronics industry developed their own SIMS instruments to analyze the chemical composition of semiconductors and thin-films (Honig 1985).

In parallel with the developments in SIMS to this point, another group had begun the journey towards using secondary ions from a slightly different angle. One of the pioneers in electron microscopy, R. Castaing, and his student, G. Slodzian, began exploring the possibility of using secondary ions to map the chemical composition of solid surfaces, *i.e.*, secondary ion *microscopy*. They sought a faster, more direct, and more sensitive method of producing chemical images than the existing approach of scanning an electron beam and quantifying secondary X-ray emission spectra. This work led to the design of the ion micro*scope* (Castaing & Slodzian 1962), an innovative concept

http://www.ssdm.com/

and a remarkable instrument made possible with a novel, if unusual, mass analyzer design. A millimetre diameter Ar^+ ion beam sputtered the sample, and an image (~10^2 μm diameter) of the intensity and distribution of selected secondary ions was projected onto a fluorescent screen with micrometre-scale spatial resolution. The commercial version of the direct imaging ion microscope was introduced as the Cameca IMS 300 'ion analyzer,' claimed to have numerous advantages over the electron microprobe, including better sensitivity and speed (Rouberol *et al.* 1972).

In the 1960s, researchers began developing and exploiting the high surface sensitivity of ion bombardment techniques to characterize the molecular chemistry of organic samples and polymers. It was recognized that a primary ion beam maintained at a sufficiently low beam density (*e.g.*, <1 nA cm^{-2}), would, over several minutes, sputter a high proportion of atoms and molecules originating from the outer monolayer. The term 'statical analysis' was coined for conditions where the surface remained largely intact and free of the damaging effects of bombardment (Benninghoven 1969). Once the undisturbed surface layer was gone, subsequent sputtered particles would originate from the chemically and structurally modified solid. "Dynamical analysis' (Benninghoven 1969) was introduced to refer to the use of high density primary beam currents in which the surface was continuously being destroyed and regenerated. We now refer to the two main branches of SIMS as '**static SIMS**' and '**dynamic SIMS**' (Benninghoven *et al.* 1987), which can be equated with low primary current density and high primary current density, respectively. Initially, static SIMS instrumentation utilized quadrupole mass analyzers, but over the last decade, time-of-flight (TOF) mass analyzers have become popular (Van Vaeck *et al.* 1999, Vickerman & Briggs 2001). Readers should note that TOF–SIMS instruments can be operated in either a dynamic or static SIMS mode. TOF–SIMS also allows the collection of complete mass spectra, so a large number and mass range of secondary ion signals are determined simultaneously.

In the geosciences, the majority of applications and instruments use dynamic SIMS, however the last decade has seen increasing interest in characterizing mineral surfaces through the use of static SIMS (Mogk & Mathez 2000, Sjövall *et al.* 2008). The important point is to note that although SIMS is inherently a surface-sensitive analytical technique, only in static SIMS, and using the specific instruments designed for this purpose, can the intact surface monolayers be measured. In all other cases the sputtered particles originate from an amorphous mixture of the primary particles and the solid, and therein lies much of the complexity in dynamic SIMS. Nevertheless, dynamic SIMS is required for most geological studies. The outer monolayer of a mineral is typically of no interest, as it almost certainly comprises numerous environmental contaminants, such as hydrocarbons, and may be oxidized. Furthermore, residual gas molecules in the (imperfect) vacuum stick to and contaminate the surface of the sample, and for this reason static SIMS requires ultra-high vacuum to reduce the contamination to an acceptable level. Secondly, quantification requires the strongest and most stable secondary ion signals possible, and this requires the use of a high density primary beam species, not only to sputter as many particles as possible, but to change the chemistry of the surface deliberately in order to enhance and stabilize secondary ion yields (see below).

Returning to the development of (dynamic) SIMS instrumentation, ion *microprobes* (*i.e.*, micrometre diameter probes) emerged from predecessor macroprobes in the late 1960s, and were combined with suitable mass analyzers, largely of the **double-focusing**, magnetic sector type. An important instrument of this type was the commercially produced (ARL Corporation) 'ion microprobe mass analyzer (IMMA)' (Liebl 1967, Andersen & Hinthorne 1972a). The IMMA set the standard for many years to come, and included novel features such as a normal incidence, **scanning ion** beam for imaging, whereby a finely focused primary beam is incrementally moved across the target, and the secondary intensities at each point are determined.

The developers of the IMMA made key discoveries on the importance of surface electrical and chemical properties in generating secondary ions. In particular, the use of a chemically reactive primary ion species, such O_2^+ or O^-, with its high electron affinity, produced significantly stronger positive secondary ion signals compared with using inert gases (*e.g.*, Ar^+) as the primary ions (Andersen 1969, Andersen & Hinthorne 1972a). Similar findings were made in the yields of negative secondary ions using Cs^+ primary ions, which are strongly electropositive (Andersen 1970), and decrease the work function of the solid. The **duoplasmatron** ion source used in generating oxygen primary ions (Coath & Long 1995 and

references therein), and the thermal ionization source for Cs^+ (Storms *et al.* 1977) eventually replaced the noble gas ion sources that were hitherto common, and remain the most important ion sources for geological SIMS applications. The IMMA instrument was used extensively for studying minerals, metals, and semiconductors, and became particularly well known for ground-breaking studies of lunar samples, including the first ion probe U–Pb geochronology (*e.g.*, Andersen & Hinthorne 1972b, Hinthorne *et al.* 1979).

Furthermore, the IMMA instrument inspired W. Compston at the Australian National University to embark on the design of the first ion microprobe designed especially for geology, the Sensitive High Resolution Ion MicroProbe, or 'SHRIMP.' The SHRIMP instruments were the first to incorporate very large magnetic and electrostatic sectors in the conventional double focusing design, allowing routine high mass **resolution**. During the 1980s, the prototype SHRIMP I and SHRIMP II (Fig. 1-3a) were introduced, and the SHRIMP II became commercially available in the early 1990s (De Laeter & Kennedy 1998, Ireland *et al.* 2008). There is little doubt that the SHRIMP instruments revolutionized the field of U–Pb geochronology of accessory minerals, by permitting spatially controlled dating (Williams 1998, Ireland & Williams 2003).

Meanwhile, Cameca continued on a parallel path to develop the ion microscope further, and introduced the IMS 3f in 1977. This newer instrument now used a conventional double focusing mass analyzer, and permitted both ion microscope and ion microprobe modes. Even though the Cameca 3f and successors (Fig. 1-3b) were not designed for geological applications *per se*, they nevertheless led the rapid expansion of SIMS applications in geochemistry and cosmochemistry in the 1980s, particularly trace element and stable isotope analyses of minerals (Shimizu *et al.* 1978, Zinner *et al.* 1983). The Cameca f-series remain the most commercially successful and widely used instruments in the geosciences, not to mention their dominance within materials sciences.

In the early 1990s, Cameca introduced a large geometry ion microprobe, the IMS 1270 (1280 currently), based upon the f-series (Fig. 1-3c), as a specialized instrument for geology and competitor to the SHRIMP II. It further added the capability of a multiple detector system, as well as maintaining Cameca's unique direct ion imaging optics (Conty *et al.* 1990, de Chambost *et al.* 1992, Harrison *et al.* 1995). Cameca also concurrently designed the NanoSIMS 50 (Fig. 1-3d) based upon a normal incidence, scanning ion probe with a working diameter for Cs^+ <0.1 μm (Slodzian *et al.* 1992, Hillion *et al.* 1994). The VG/Fisons Isolab 54 ion microprobe was also introduced during this period (England *et al.* 1992), although it was not commercially successful. The reverse geometry SHRIMP–RG is a prototype instrument designed for ultra-high (10,000–20,000 R) mass resolution (*e.g.*, Ireland & Bukovanska 2003), but it too has not been commercially successful. Currently, the SHRIMP II and Cameca magnetic sector type instruments dominate geoscience applications of dynamic SIMS. Recent applications of static SIMS in the geosciences have used time-of-flight mass analyzers, such as the German manufactured ION–TOF, employing primary beams of non-reactive species such as Ga^+ and Bi^+ (Fig. 1-3e). For various technical reasons, the TOF analyzers are not optimal for quantitative isotopic analysis, and therefore are not used in most dynamic SIMS applications in geology.

GEOLOGICAL (DYNAMIC) SIMS IN PRACTICE

Geological samples are usually chemically complex materials, and the elements and isotopes of interest may be at very low (*e.g.*, parts per million) concentrations. The compositional variability requires close attention to calibration, because to varying extents all SIMS element/element and isotopic ratios are biased from the true values in the solid, although generally less so for the latter. For element ratios, this fractionation is sometimes referred to as '**discrimination**,' and for isotopic ratios, **instrumental mass fractionation** (see below). Calibration in SIMS is done by analysis of matrix-matched reference materials, interspersed with the unknown samples. The more stringent the requirement for precision and accuracy, the more attention is placed upon the calibration scheme. Up to one third of analytical time may be spent in calibration. Most reference materials are natural minerals, with lesser use of natural or synthetic glasses (*e.g.*, SRM 610) or synthetic minerals. Use of ion-implanted reference materials is rare, although routine in materials science. It has been found that under conditions of extreme **energy filtering** (*i.e.*, selecting only very high energy ions), discrimination is less affected by matrix composition, which simplifies calibration in trace

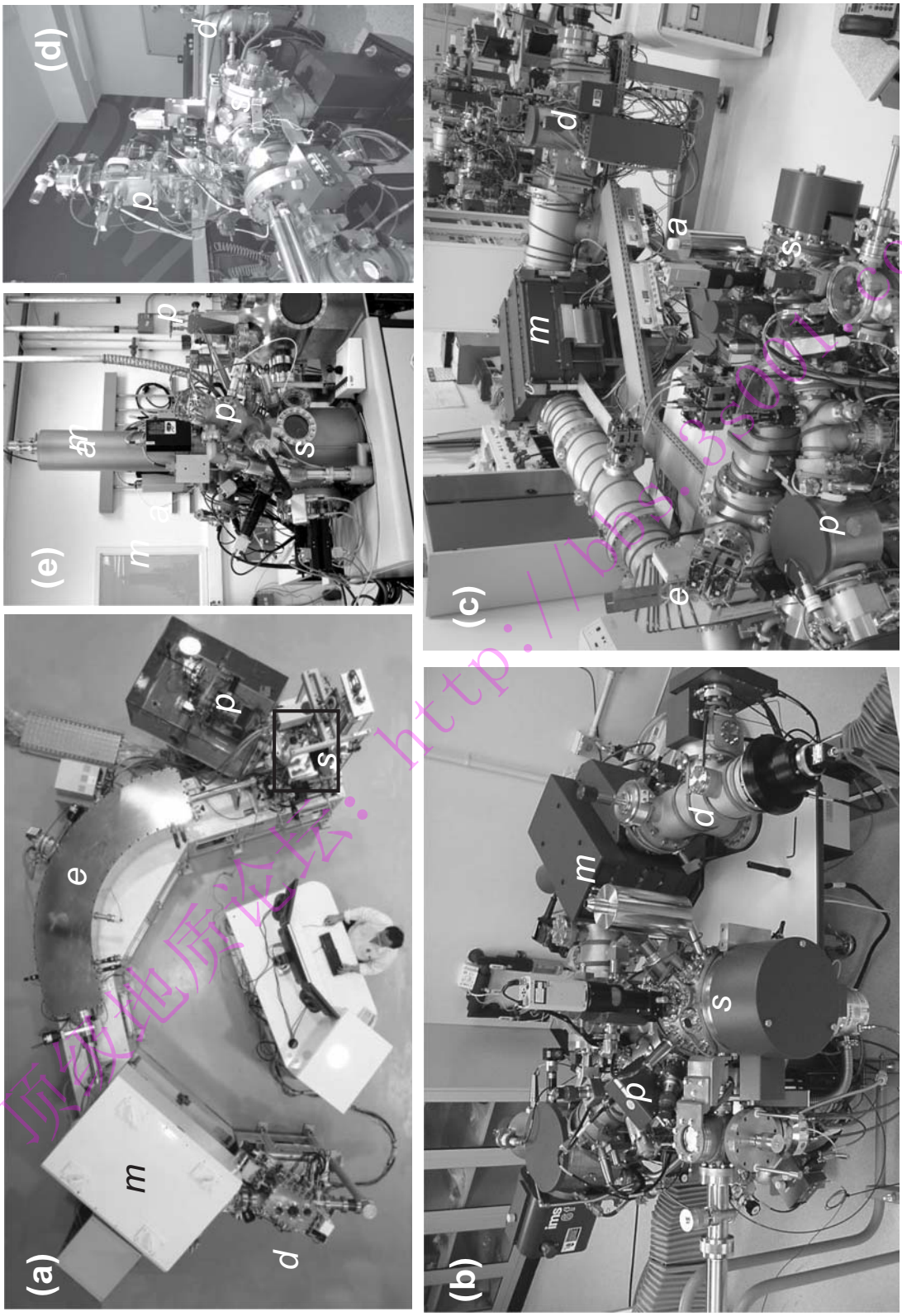


*FIG. 1-3. Photographs of various types of ion microprobes utilized in the analysis of geological samples: (**a**) SHRIMP II, ASI factory, Australia (image courtesy of ASI Pty Ltd); (**b**) Cameca IMS 6f, Arizona State University (image courtesy of L. Leshin); (**c**) Cameca IMS 1280, Paris; (**d**) Cameca NanoSIMS 50, The University of Western Australia (**e**) ION–TOF time-of-flight SIMS, University of Alberta. Symbols: a, analyzer; d, detector; e, electrostatic sector; m, magnetic sector; p, primary column; s, sample chamber *For color version of this figure, see http://www.mineralogicalassociation.ca/index.php?p=160

顶级地质论坛：http://bbs.3s001.com/

element analysis. For example, synthetic glasses may be used to calibrate trace elements in minerals (*e.g.*, Hinton 1990). Furthermore, secondary ion mass spectra of natural materials are complex, and atomic and molecular (*e.g.*, oxides) isobars are frequently present (Fig. 1-4a). Isobars present a problem in accurately measuring secondary ion intensities, and must be eliminated in most cases, through the use of either high mass resolution (Fig. 1-4b) or energy filtering, or a combination of both.

In typical dynamic SIMS applications in geology, a 10–25 keV primary beam of $^{16}O^-$, $^{32}(O_2)^-$, or $^{133}Cs^+$ ions is focused onto the surface of the sample at 0° to 45° relative to normal (Fig. 1-2). As discussed previously, chemically reactive primary ions enhance the formation of secondary ions. Targets bombarded with oxygen become saturated in oxygen, a strongly electronegative element, to depths of ~10 nm, enhancing the environment for forming positive secondary ions of most metallic elements (*e.g.*, Ca^+, REE^+, Pb^+). Cesium saturation reduces the work function of the solid, enhancing the number of free electrons available to combine with non-metallic elements (*e.g.*, C^-, O^-). For **scanning ion imaging**, the region of interest (ROI) must be rastered for several minutes prior to imaging in order to saturate the near-surface with the chemically reactive primary ions. The use of chemically reactive primary species is a double edged sword, as it increases and stabilizes secondary ion yields, but also magnifies matrix-related discrimination. Electron flood guns are available to neutralize positive charging of the sample when analyzing insulating minerals with a Cs^+ beam (Ireland 2005). Negative charging with O^- ion bombardment is less problematic in general, but all surfaces must be inherently conducting or coated with a conducting film of Au or C.

The secondary ions, usually of opposite polarity to the primary ions, are extracted normally from the sputtering site into the secondary column, and in the process are accelerated through typically 4.5–10 keV (Fig. 1-1). The secondary column imposes an electrostatic field upon the sample surface to guide and focus secondary ions towards the entrance slit of the mass analyzer. The secondary mass analyzers in dynamic SIMS differ greatly between various instruments, depending on their design specifications, but all are of the magnetic sector, double focusing design (Roboz

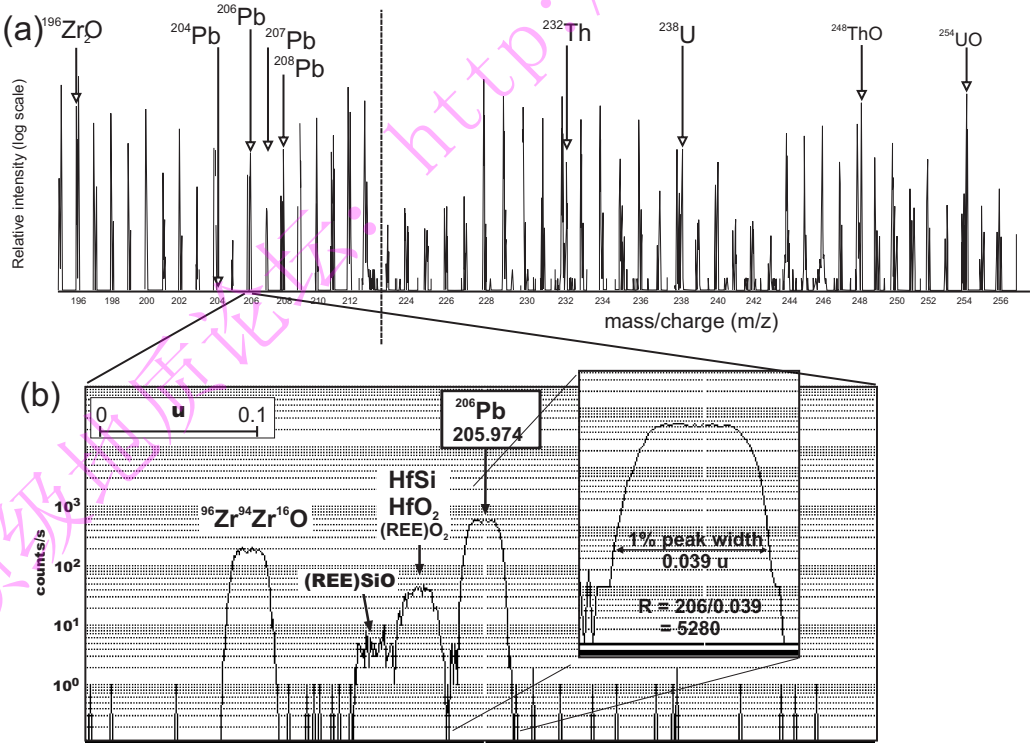


FIG. 1-4. Zircon ($ZrSiO_4$) positive secondary ion mass spectrum using primary $^{16}O^-$ (SHRIMP II ion microprobe). (**a**) 195–255 u, highlighting ions of interest in U–Pb geochronology; (**b**) detail of region near 206 u, adequately resolved from nearby isobars containing Zr, Si, REEs, and Hf.

顶级地质论坛 http://bbs.3510.com/

1968). This analyzer includes the magnetic and electrostatic sectors, various electrostatic lenses, stigmators and deflection surfaces, and beam limiting slits and apertures, all in various complex ion optical arrangements. The device which does the 'heavy lifting' is the magnet sector, and as a general rule, the larger its radius, the higher will be the routine working mass resolution and usually also the transmission and sensitivity of the instrument. For example, magnet radii are 0.5–1.3 m for high resolution instruments and 0.1–0.2 m for low resolution instruments. The electrostatic sector, which precedes the magnetic sector in conventional designs and is used for energy dispersion, has a variable radius (0.1–1.2 m), depending on the ion optical design.

Most types of quantitative analyses occur with the secondary ion focusing being astigmatic, meaning that the relative lateral positions of the ions generated immediately at the sample surface within the footprint of the probe are not preserved at the detector. Astigmatic focusing allows for maximum ion transmission, and usually optimal mass resolution. Note that for scanning ion imaging, astigmatic focusing is used, but additional measures are taken to reduce spatially related variations in ion yields. For IMS instruments, the option exists to use direct ion imaging (stigmatic focusing), using a large diameter primary beam, with the advantage of 'live' ion images at about 1 μm spatial resolution, but this is generally at the expense of sensitivity and mass resolution. The field of view for SIMS imaging, whether direct or scanning, is typically <300 μm, but lateral variations in secondary ion signals due to instrument artifacts are difficult to avoid beyond a ~100 μm field of view.

Detection systems comprise one or more (in a multi-collector apparatus) electron multipliers and Faraday cups, and may include a microchannel plate, a spatially sensitive type of electron multiplier used in ion microscopy. Due in part to the low rate of sample consumption during sputtering, secondary ion signals are typically weak (*e.g.*, $<10^6$ counts per second), and the electron multiplier detector is preferred due to its high signal to noise ratio and fast dynamic response. In some instances of analyzing major isotope species in geological materials, secondary ion signals are sufficiently intense to warrant the use of a Faraday detector. The detection limits for electron multipliers are governed by the background count rate, which is a combination of the electronic noise ('dark counts') of the detection system, scattered ions within the mass spectrum, and tailing from other species. As an example, assuming a background count rate of 0.1 $c.s^{-1}$ for $^{206}Pb^+$ for a 1 nA primary beam, and a sensitivity of 20 $c.s^{-1}ppm^{-1}nA^{-1}$, this would calculate to a detection limit of about 15 ppb for Pb in the sample. Detection limits are highly variable depending on the element, target, and analytical conditions.

For all instruments, the desire is usually to collect, transmit, and detect as many secondary ions as possible within the given sputtering time interval selected, typically seconds, but varying widely. The high 'sensitivity' of the high resolution ion microprobes essentially refers to the high fraction of ions transmitted at a specified mass resolution (*i.e.*, elemental **sensitivity**), but these instruments also have relatively high **abundance sensitivity**. Abundance sensitivity refers to the ability to measure a faint isotope adjacent to an abundant one, and is a reflection of peak 'tailing' (broadening) caused by scattering of secondary ions. Abundance sensitivity (10^{-8} to 10^{-9}) can be optimized by the use of additional energy filters, including retardation lenses (De Laeter & Kennedy 1998) and electrostatic sectors (Saxton *et al.* 1996). In practical terms, ratios up to 10^6 are possible to measure with SIMS, largely determined by abundance sensitivity, prohibiting analysis of rare isotope isotopes such as ^{14}C or ^{36}Cl.

Small geometry, double focusing, magnetic sector ion microprobes/microscopes such as the Cameca f-series (*e.g.*, Fig. 1-3b) are highly versatile, all-purpose instruments suitable for many types of elemental and isotopic analyses in geology that require low to moderate mass resolution, or in high resolution applications in which the precision requirements are relatively modest. For some light isotopes (*e.g.*, $^{18}O/^{16}O$), uncertainties of about ±0.5‰ are possible. Analysis of ions of higher mass and lower abundance with such instruments becomes less favorable, particularly for metallic elements that have intrinsically low secondary ion yields (*e.g.*, Ti^+, La^+, Pb^+). Spectral interferences also tend to become more problematic with increasing mass. With the small geometry instruments, there may be need to employ the energy-filtering technique to remove the interferences from complex molecular ions and reduce matrix effects, but always with a significant reduction of secondary ion transmission (Shimizu *et al.* 1978, Zinner & Crozaz 1986, Benninghoven *et al.* 1987). A significant disadvantage with the small instruments is that the small radius magnetic sector

severely limits the capabilities in parallel ion detection, despite newer instruments fitted with dual Faraday detectors. Despite these drawbacks, these instruments remain workhorses for geochemistry.

The limitations associated with small geometry ion microprobes are to a large extent removed with the SHRIMP and Cameca high resolution ion microprobes (Fig. 1-3a, c, d), which can routinely operate at a mass resolution up to 5000–8000 with flat-topped peaks, sufficient for a wide range of isotope ratio measurements in geology. As indicated, a significant advantage is the capability of multiple ion collection, with 5 or more detectors possible. The NanoSIMS instrument, for example is superbly suited to multicollection due to its Mattauch-Herzog ion optics, yielding a long focusing locus upon which the various detectors can be moved. In total there are about three dozen high resolution ion microprobes in various university and government laboratories around the globe, with two or three new ones sold annually. The disadvantages of such instruments are mainly their expense and complexity.

Samples

The one problematic aspect of SIMS compared with some other probe techniques is that there is usually more effort required to prepare the sample, as attention to detail can be quite important. Secondary ion yields are sensitive to local topographic and electrostatic features of the sample mount, and controlling these parameters is particularly important for high precision and high accuracy types of analysis and reducing imaging artifacts. Furthermore, for isotopic analyses, reference materials must be co-mounted with the unknowns in order to eliminate any potential differences between different mounts. This means that such reference materials are consumed in small amounts with each mount made, as they are seldom recovered.

An important consideration in conducting geological SIMS analysis is to determine whether it will occur *ex situ* or *in situ*. Most SIMS analyses are, in fact, *ex situ*, meaning that the mineral has been removed from the rock matrix. *In situ* analysis, although loosely used to refer to any type of probe analysis of a solid, is used here to refer to analysis of the mineral as it occurs in place within the rock matrix (*i.e.*, typically a polished thin section). Whether *ex situ* or *in situ* analysis, or both, is required principally depends on the nature of the scientific problem, but secondary factors such as cost effectiveness also play a role. Many people when first presented with the opportunity to conduct SIMS analysis assume that the easiest way to tackle the problem is *in situ*, as commonly done with the electron microprobe. Generally, *in situ* analysis is used only where context is critical or where the mineral cannot be easily removed from the rock matrix. The main disadvantage of *in situ* analysis is that one *in situ* mount may not provide a suitable number or type of the mineral being investigated. It is also more difficult to prepare *in situ* mounts with co-mounted reference materials, which is necessary for any work involving sub-percent level uncertainties.

Samples must be compatible with high to ultra-high vacuum and, if possible, be exposed as micrometre-flat surfaces. SIMS mounts are usually circular (1.0–2.5 cm diameter), and typically comprise either mineral separates embedded in epoxy, or grains pressed into a soft metal such as gold or indium (Fig. 1-5a). Thin sections may also be used, or cores from thin sections may be extracted from selected regions of thin sections and re-mounted in the more convenient circular forms. For some special samples, transmission electron microscope grids may be suitable, and even individual, ultra-small grains sprinkled onto a conducting surface are acceptable. As mentioned, samples are normally coated with conductive films, although for very weak primary beams it may not be necessary if the substrate is conductive.

The operator has a low resolution, magnified view of the sample surface in reflected light to permit accurate placement of the probe, aided in some of the Cameca instruments by secondary ion or (sputtering-induced) secondary electron imaging of the sample. In all circumstances, scanning electron microscope (SEM) characterization of the samples is essential, usually using backscattered or secondary electrons, and cathodoluminescence (Fig. 1-5b). The importance of thorough sample characterization prior to and after SIMS cannot be overstated.

Spatial Considerations

SIMS is currently the most powerful analytical tool for high spatial resolution geochemical and isotopic analyses. Examples of probe pits made in isotopic ratio analysis are shown in Figure 1-5 (b, c). Modern instrumentation is essentially reaching the theoretical limits of lateral spatial resolution during sputtering, which is about 10 nm, and depth resolution in dynamic SIMS is

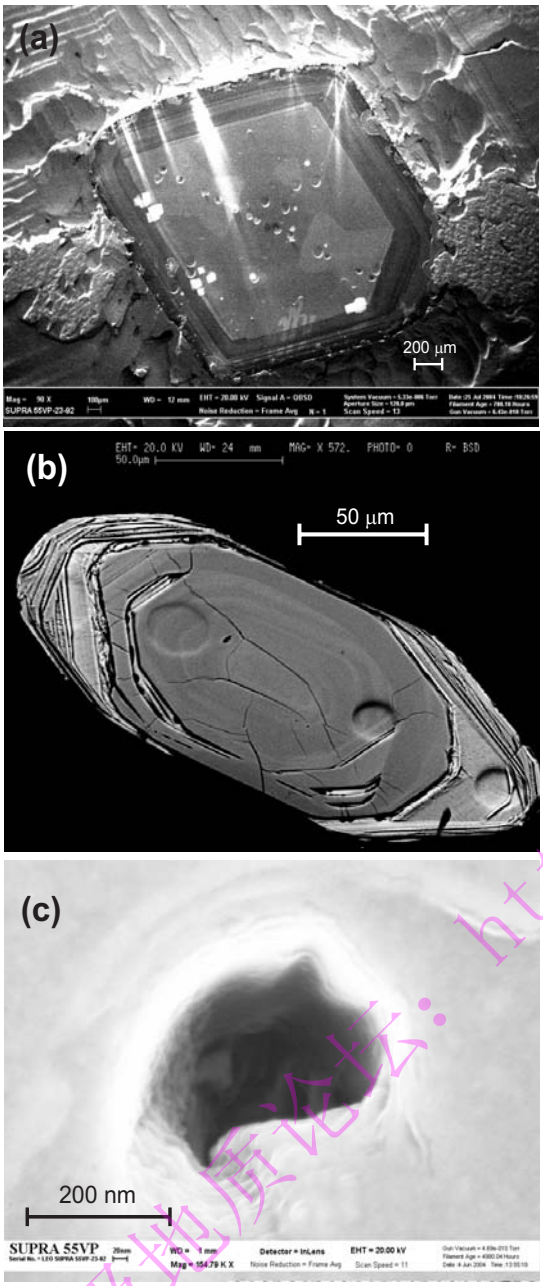


FIG. 1-5. Scanning electron microscope images of ion probe samples. (**a**) Backscattered electron image of a polished diamond embedded in indium and coated with gold for SIMS analysis. Circular ion probe analysis pits are visible. Bright areas are due to charging where Au has been removed. (**b**) Backscattered electron image of 15–25 µm x 1 µm pits in zircon sputtered with an $^{16}O^-$ probe; (**c**) ~200 nm diameter pit in diamond sputtered with a $^{133}Cs^+$ probe, secondary electrons.

similar but can literally be the thickness of an atomic layer under static SIMS conditions. However, higher spatial resolution comes at the price of analytical uncertainty, so in practice one selects the largest lateral and depth resolution that will suit the purpose, within the constraints of the instrumentation. For dynamic SIMS, typical working lateral spatial resolution would be 0.1–30 µm, and depth resolution <5 µm.

It is important to keep in mind the spatial dimensional options that may be available with the instrumentation:

a) Point source analysis, in which the primary beam is held on the target for seconds to minutes, sampling a disk-shaped volume of mineral (*e.g.*, Chapters 2–6, this volume). This is by far the most common type of analysis conducted in geology, and is used for determining elemental or isotopic compositions of minerals whose structural or compositional heterogeneity is exposed in cross-section. Because the total analysis depths are rarely more than a few micrometres, heterogeneity normal to the surface is usually undetectable. The analysis represents the average composition of the entire volume sputtered, which is typically 10^{-10} to 10^{-9} g (*i.e.* pg to ng).

b) Depth profiling (in depth) analysis, whereby the heterogeneity of the sample is parallel to the near-surface region (*e.g.*, Chapter 7, this volume). This type of analysis is a variation of the point source scheme whereby the data acquired during sputtering of a cylinder are subdivided during data processing into many small time (= depth) increments rather than integrating over the whole. Total depth may be greater than point source work, *e.g.*, 5–10 µm. This is the method employed when the highest spatial (depth) resolution is required for the analysis of grain outer surfaces that are too thin to be analyzed in section. The depth resolution is limited by the uniformity of the beam density of the probe and the amount of sample required to achieve the desired analytical precision.

c) Line scan analysis, in which the primary beam is moved in a straight line relative to the sample (or *vice versa*) for determining compositional variations across a suspected region of heterogeneity. For quantification, the line comprises closely spaced point source analyses. In fact, this type of analysis is not very common in geosciences applications.

矿物地质论坛：http://bbs.350.com/

d) Ion imaging, whereby compositional information is determined over a two dimensional region, either using a stationary and defocused primary beam (direct ion imaging) or a finely focused primary beam scanned across the region (scanning ion imaging). Scanning ion imaging is the technique of choice for quantitative analysis, and particularly isotopic ratio analysis.
e) 3-D imaging, is an extension of ion imaging, as a collection of discrete horizontal slices.

Data Essentials

The fundamental unit of data acquired during SIMS analysis is a measurement of the mean secondary ion count rate within a given sputtering time interval, essentially the point source analysis in the previous section. Raw count rates, or even simply counts, may be used for qualitative evaluations, such as in ion imaging of large compositional variations. But individual count rates are subject to many potential analytical artifacts, and so, for quantification, only pairs of isotope count rates are used. The secondary ions may be atomic or molecular species, and may belong to the same element ($^{i}S_x/^{j}S_x$, *e.g.*, $^{13}C^-/^{12}C^-$) or different elements ($^{i}S_x/^{j}S_y$, *e.g.*, $^{140}Ce^+/^{28}Si^+$, $^{140}Ce^+/^{172}YbO^+$). Data of the former are typically referred to as an 'isotope ratio' analysis, and the latter, an 'element ratio' analysis. Isotope ratios are considered the most powerful data for modeling and quantifying geological processes and reservoirs. Element ratio analyses, and derived absolute (*e.g.*, ppm Ce) or relative (*e.g.*, Ce/Yb) elemental abundances, typically provide complementary geochemical information.

For abundance determinations, quantification usually is based upon normalizing the element of interest (as an atomic or molecular secondary ion) to a matrix element, and comparing it to the same ratio in a reference material of known composition:

$$^{meas}(^{140}Ce^+/^{28}Si^+)_{unk} / {}^{meas}(^{140}Ce^+/^{28}Si^+)_{ref} = {}^{true}Ce_{unk} / {}^{true}Ce_{ref}.$$

In the above case, solving for $^{true}Ce_{unk}$ (*e.g.*, Ce $\mu g\ g^{-1}$) is straight forward, under the assumption that the matrix and analytical conditions for unknown and standard are the same, and the $^{140}Ce^+/^{28}Si^+$ is linearly related to Ce abundance. Similarly, for element ratios,

$$^{meas}(^{140}Ce^+/^{172}YbO^+)_{unk} / {}^{meas}(^{140}Ce^+/^{172}YbO^+)_{ref} = {}^{true}(Ce/Yb)_{unk} / {}^{true}(Ce/Yb)_{ref}.$$

In the above case, the equation is solved for $^{true}(Ce/Yb)_{unk}$.

Elemental and isotope ratio data are affected by random and systematic errors. Random errors are dominated by counting statistics, which are constrained by the total number of ions detected in pulse-counted electron multiplier detector (EM) systems, or the signal/noise ratio in Faraday (FAR) detection. Many potential sources of systematic error may cause the measured elemental and isotopic ratios to be different than within the sample, (*e.g.*, discrimination and instrumental mass fractionation (IMF), respectively). Element discrimination can be relatively large, in comparison to IMF. In both cases, there is complete reliance upon independently characterized reference materials, matrix-matched and analyzed along with the unknown. In SIMS isotope ratio analysis, it is common to determine IMF by measuring the ratio of interest within a reference material and then apply a fractional correction to the unknown ratio. For example, for the reference material,

$$\alpha = {}^{meas}(^{13}C^-/^{12}C^-)_{ref} / {}^{true}(^{13}C/^{12}C)_{ref},$$

where α is the fractionation factor. The IMF is commonly expressed as a % or ‰ deviation, as in:

$$IMF\ (‰) = 1000 * (1 - \alpha).$$

To correct the unknown for IMF,

$$^{true}(^{13}C/^{12}C)_{unk} = {}^{meas}(^{13}C^-/^{12}C^-)_{unk} / \alpha$$

Only in a minority of cases in ion microprobe isotopic analysis the ideal case exist of assessing IMF by simultaneous measurement of another ratio of the same element that has a fixed (known) composition (*i.e.*, 'internal fractionation correction,' Stern 1998). For external fractionation correction, as described above, it is not necessary to know the detailed behavior of fractionation, only the magnitude, and make the assumption that it is identical to the unknown. Of course, this approach is only valid if the identical ratios are measured in the reference material and unknown, as any extrapolation to other mass ranges would require an understanding of the fractionation systematics. The IMF may range from undetectable for isotopes of heavy elements, to several % u^{-1} for lighter elements.

Most high precision ion microprobe isotope ratio analyses are limited not by counting errors, but by systematic errors, mainly estimating and controlling IMF. The IMF may have spatial and temporal components. It is often found that the

顶级地质论坛 http://bbs.sinoni.com/

standard deviation of replicate isotope ratio analyses of the reference material greatly exceeds the uncertainties of the individual analyses. In other words, the reproducibility (often termed 'external error', but unambiguously, 'spot-to-spot' uncertainty) is often much worse than the calculated uncertainties would lead us to believe. For SIMS, the spot-to-spot uncertainty is, under ideal conditions, no less than about ±0.1‰ (95% confidence level), and more typically it could be 2–10x times this value. It is very common for a number of individual SIMS analyses to be pooled to increase analytical precision. To some extent this defeats the spatial resolution of the analysis, in that one now effectively has sampled a greater total mass of material. Also, it is implicit in aggregate results that the analyses are from isotopically homogeneous material. Although such an interpretation may be consistent with statistical tests, such as the **mean square of weighted deviates**, the precision of the individual analyses may conceal isotopic heterogeneity. Further detail on statistical approaches to SIMS can be found elsewhere (*e.g.*, Fitzsimons *et al.* 2000).

Isotope ratio analysis is usually done with a stationary small probe to optimize counting statistics on specific regions of complex targets. Scanning ion imaging normally requires the presence of % level or higher abundances in the solid, as the counting statistics otherwise become unacceptable. For isotopic analysis, there may be lateral variations in IMF. Nevertheless, the ability to perform two-dimensional isotopic mapping is a relatively new and powerful capability in geological sample characterization.

Applications and Limitations

Applications of SIMS in geochemistry and cosmochemistry are extremely diverse, and involve determinations of elemental abundance, and elemental and isotope ratios. Most applications in geology tend to be in one or more of the following categories:

1. Trace element analyses
2. Light **stable isotopes** (u < 50)
3. U–Th–Pb geochronology
4. Geochemistry and geochronology of extra-terrestrial samples

SIMS is the technique of choice for the ability to conduct mass spectrometry at the finest lateral and vertical resolution possible (Fig. 1-5 b, c). An abundance or isotopic measurement is possible from a cylinder ~50 nm in diameter and depth, which is as little as 10^{-15}–10^{-16}g (1–0.1 fg) of material consumed. In some cases, statistically significant results can be achieved with as few as 100 counts, and with a typical useful yield of 10^{-3}, can be achieved by sputtering only 10^5 atoms. Point source analyses are the most common, followed by ion imaging and depth profiling.

SIMS is not a universal analytical tool for geochemistry, particularly in the context of complementary technologies that are now available, such as laser ablation–inductively coupled plasma–mass spectrometry (LA–ICP–MS) and electron probe microanalysis (EMPA). For instance, although SIMS has particular strengths in trace element quantification due to its inherently low backgrounds and adequate sensitivity for many elements, it is seldom used for quantification of major and minor elements due to matrix effects. Nevertheless, major and minor elements are commonly analyzed in the course of ion imaging (*e.g.*, Fig. 1-6), where the spatial resolution of the ion probe can be superior to the X-ray based EPMA methods (Badro *et al.* 2007, Bland *et al.* 2007). The determination of rare earth elements (REE) and many others in minerals has historically been one of the strengths of SIMS, and remains an important technique using either the energy-filtering technique or high mass resolution (*e.g.*, Bebout *et al.* 2007, Grimes *et al.* 2007). Element abundances and ratios generally have uncertainties of the percent to tens of percent level, depending on many factors.

The greatest strength of SIMS is in isotope ratio measurements, and ion microprobes in various configurations can be utilized for applications covering a wide range of stable isotopes (*e.g.*, H, Li, B, C, N, O, Si, S, Cl, Ca, Cu) and others related to radioactive decay (parent–daughter) systems (*e.g.*, Al–Mg, Mn–Cr, Fe–Ni, U–Pb, Th–Pb, U–Th, Hf–W). The limitations of SIMS in isotopic analysis depend on a number of factors, including concentration in the sample, secondary ion yields, spatial resolution, presence of isobaric interferences, and analytical uncertainty desired. SIMS cannot be used to analyze materials where there exists a significant atomic isobar, such as ^{46}Ca at ^{46}Ti, ^{87}Rb at ^{87}Sr, ^{176}Lu at ^{176}Hf, ^{187}Re at ^{187}Os. Where there are minerals devoid of the parent isotope, then tracer isotopic measurements are possible (*e.g.*, Pb isotopes), as long as the application does not demand very high analytical precision (see Stern 1998).

The ability of SIMS to perform isotopic analyses on tiny quantities of matter introduces a major limitation, as it is not a method for applic-

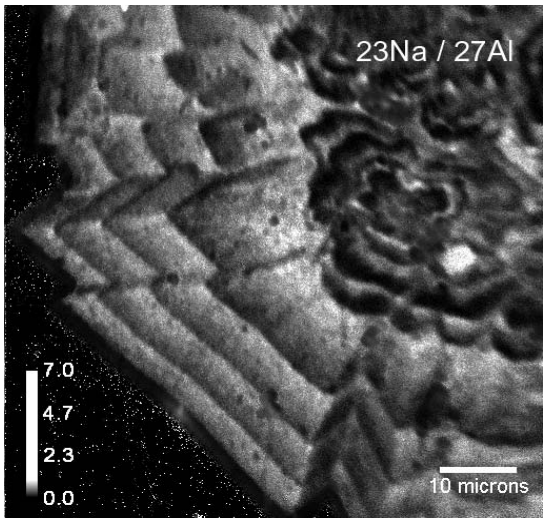


FIG. 1-6. Scanning ion image (NanoSIMS 50, with primary $^{16}O^-$) of an Al hydrate mineral (gibbsite), showing zoning in the minor element, Na, as represented using the raw $^{23}Na^+/^{27}Al^+$ ratio. The ratio has not been corrected for discrimination.

ations requiring the highest analytical precision and accuracy. Typically, SIMS secondary ion signals are relatively weak due to the small numbers of atoms actually sampled, requiring the use of electron multiplier detectors that introduce artifacts in the data that ultimately limit the achievable analytical uncertainties. Some high resolution ion microprobes with multiple Faraday detectors are capable of analytical uncertainties of ±0.1‰ (95% confidence) for individual measurements of some stable isotopes of major elements (*e.g.*, oxygen). Nevertheless, isotopic systems or applications routinely demanding uncertainties much less than 0.1‰ are impractical with SIMS, for example in measuring $^{143}Nd/^{144}Nd$, $^{176}Hf/^{177}Hf$, and "non-traditional" heavy stable isotopes (*e.g.*, Se, Fe, Cd, Zn). The limitation is related to the small ion currents typical of SIMS, difficulties resolving or peak-stripping isobaric interferences, and in controlling IMF.

SUMMARY

Geological applications were one of the motivations for the early development of the SIMS analytical technique, beginning more than 50 years ago, and now SIMS is routinely applied within a wide range of research areas. Over this period of time, numerous other probe technologies have emerged for the direct analysis of solids, especially electron- and photon-based methods, and in particular EPMA and LA–ICP–MS (*e.g.*, Sylvester 2008) have also become essential within the geochemical toolkit. Rather than the universal analytical instrument perhaps once envisioned, SIMS has a distinctly complementary role, as the technique of choice when the highest spatial resolution is demanded for trace element and isotopic analysis. Ion imaging, conceived very early on in SIMS development, is re-emerging as a powerful capability. Interest in mineral surface chemistry and the recognition of static (*e.g.*, TOF) SIMS as a molecular fingerprinting tool is also beginning to catch hold. In the chapters that follow, the analytical power of SIMS in geochemistry and cosmochemistry is amply demonstrated through a range of contemporary techniques and applications.

ACKNOWLEDGMENTS

The manuscript benefitted from a review by Mostafa Fayek.

REFERENCES

ANDERSEN C.A. (1969): Progress in analytic methods for the ion microprobe mass analyzer. International *J. Mass Spectrom. & Ion Physics* **2**, 61-74.

ANDERSEN C.A. (1970): Analytic methods for the ion microprobe mass analyzer. Part II. *Analytical Chem.* **3**, 413-428.

ANDERSEN C.A. & HINTHORNE J.R. (1972a): Ion microprobe mass analyzer. *Science* **175**, 853-860.

ANDERSEN C.A. & HINTHORNE J.R. (1972b): U, Th, Pb and REE abundances and $^{207}Pb/^{206}Pb$ ages of individual minerals in returned lunar material by ion microprobe mass analysis. *Earth & Planet. Sci. Lett.* **14**, 195-200.

BADRO J., RYERSON F.J., WEBER P.K., RICOLLEAU A., FALLON S.J. & HUTCHEON I.D. (2007): Chemical imaging with NanoSIMS: a window into deep-Earth geochemistry. *Earth & Planet. Sci. Lett.* **262**, 543-551.

BEBOUT G.E., BEBOUT A.E. & GRAHAM C.M. (2007): Cycling of B, Li, and LILE (K, Cs, Rb, Ba, Sr) into subduction zones: SIMS evidence from micas in high-P/T metasedimentary rocks. *Chem. Geol.* **239**, 284-304.

BECKER S. (2008): *Inorganic Mass Spectrometry: Principles and Applications*. Wiley-Interscience.

BENNINGHOVEN A. (1969): Analysis of submono-layers on silver by negative secondary ion emission. *Physica Status Solidi (B)* **34**, K169-K171.

BENNINGHOVEN A., RUDENAUER F.G. & WERNER H.W. (1987): *Secondary Ion Mass Spectrometry, Basic Concepts, Instrumental Aspects, Applications and Trends*. New York, John Wiley & Sons, 1227 pp.

BLAND P.A., STADERMANN F.J., FLOSS C., ROST D., VICENZI E.P., KEARSLEY A.T. & BENEDIX G.K. (2007): A cornucopia of presolar and early solar system materials at the micrometer size range in primitive chondrite matrix. *Meteoritics & Planet. Sci.* **42**, 1417-1427.

CASTAING R. & SLODZIAN G. (1962): Microanalyse par emission ionique secondaire. *J. Microscopy* **1**, 395-410.

COATH C.D. & LONG J.V.P. (1995): A high-brightness duoplasmatron ion source for microprobe secondary-ion mass spectrometry. *Rev. Scientific Instruments* **66**, 1018-1023.

CONTY C., RASSER B. & MIGEON H.N. (1990): The IMS1270–a new high transmission SIMS. *In*: Secondary Ion Mass Spectrometry SIMS VII. A. Benninghoven, C.A. Evans, K.D. McKeegan, H.A. Storms *and* H.W. Werner (*eds*.), Monterey, CA, J. Wiley & Sons, 831-834.

DE CHAMBOST E., HILLION F., RASSER B. & MIGEON H.N. (1992): The IMS 1270: A description of the secondary ion optical system. *In*: Secondary Ion Mass Spectrometry SIMS VIII. A. Benninghoven, K.T.F. Janssen, J. Tümpner & H.W. Werner (*eds*.), Amsterdam, J. Wiley & Sons, 207-210.

DE LAETER J.R. & KENNEDY A.K. (1998): A double focussing mass spectrometer for geochronology. *Internat. J. Mass Spectrom.* **178**, 43-50.

ENGLAND J.G., ZINDLER A., REISBERG L.C., RUBENSTONE J.L., SALTERS V., MARCANTONIO F., BOURDON B., BRUECKNER H., TURNERD P.J., WEAVER S. & READ P. (1992): The Lamont-Doherty Geological Observatory Isolab 54 isotope ratio mass spectrometer. *Internat. J. Mass Spectrom. & Ion Processes* **121**, 201-240.

FITZSIMONS I.C.W., HARTE B. & CLARK R.M. (2000): SIMS stable isotope measurement: counting statistics and analytical precision. *Mineral Mag.* **64**, 59-83.

GRIMES C.B., JOHN B.E., KELEMEN P.B., MAZDAB F.K., WOODEN J.L., CHEADLE M.J., HANGHØJ K. & SCHWARTZ J.J. (2007): Trace element chemistry of zircons from oceanic crust: a method for distinguishing detrital zircon provenance. *Geology* **35**, 643-646.

HARRISON T.M., MCKEEGAN K.D. & LE FORT P. (1995): Detection of inherited monazite in the Manaslu leucogranite by $^{208}Pb/^{232}Th$ ion microprobe dating: Crystallization age and tectonic significance. *Earth & Planet. Sci. Lett.* **133**, 271-282.

HERZOG R.F.K. & VIEHBÖCK (1949): Ion source for mass spectrography. *Physical Review* **76**, 855-856.

HIGASHI Y. (1999): Quantitative depth profiling by laser-ionization sputtered neutral mass spectrometry. *Spectrochimica Acta, Part B: Atomic Spectroscopy* **54**, 109-122.

HILLION F., DAIGNE B., GIRARD F. & SLODZIAN G. (1994): A new high performance instrument: the Cameca "NanoSIMS 50". *In*: Secondary Ion Mass Spectrometry SIMS IX. A. Benninghoven, Y. Nihei, N. Shimizu & H.W. Werner (*eds*.), John Wiley & Sons, 254-257.

HINTHORNE J.R., ANDERSEN C.A., CONRAD R.L. & LOVERING J.F. (1979): Single-grain $^{207}Pb/^{206}Pb$ and U/Pb age determinations with a 10 micron spatial resolution using the ion microprobe mass analyzer. *Chem. Geol.* **25**, 271-303.

HINTON R.W. (1990): Ion microprobe trace-element analysis of silicates: Measurement of multi-element glasses. *Chem. Geol.* **83**, 11-25.

HONIG R.E. (1985): The development of secondary ion mass spectrometry (SIMS): a retrospective. *Internat. J. Mass Spectrom. & Ion Processes* **66**, 31-54.

IRELAND T. (1995): Ion Microprobe Mass Spectrometry: Techniques and Applications in Cosmochemistry, Geochemistry and Geochronology. *In*: Advances in Analytical Geochemistry. M. Hyman & M. Rowe (*eds*.), Greenwich, Connecticut, JAI Press, **2**, 1-118.

IRELAND T. (2005): SIMS measurement of stable isotopes. *In*: Handbook of Stable Isotope Analytical Techniques. P.A. de Groot (*ed*.), Elsevier Science, 1.

IRELAND T. & BUKOVANSKA M. (2003): Initial $^{182}Hf/^{180}Hf$ in meteoric zircons. *Geochim. Cosmochim. Acta* **67**, 4849-4856.

IRELAND T., CLEMENT S., COMPSTON W., FOSTER J.J., HOLDEN P., JENKINS B., LANC P., SCHRAM N. & WILLIAMS I.S. (2008): Development of SHRIMP. *Austr. J. Earth Sci.* **55**, 937-954.

IRELAND T. & WILLIAMS I.S. (2003): Considerations

http://mbs.sso.com/

in zircon geochronology by SIMS. *In*: Zircon. J.M. Hanchar & P.W.O. Hoskin (*eds*.), Washington, D.C., Mineralogical Society of America, *Rev. Mineral. & Geochem.* **53**, 215-241.

ISO (1993): *International vocabulary of basic and general terms in metrology*. Geneva. [2 ed.].

LIEBL H. (1967): Ion microprobe mass analyzer. *J. Applied Physics* **38**, 5277-5283.

LIEBL H. (1974): Ion microprobe analysers: History and outlook. *Analyt. Chem.* **46**, 22A-30A.

LIEBL H.J. & HERZOG R.F.K. (1963): Sputtering ion source for solids. *J. Appl. Phys.* **34**, 2893-2896.

MCNAUGHT A.D. & WILKINSON A. (1997): *Compendium of Chemical Terminology, The Gold Book*, 2nd edition, Blackwell Science, 464 pp.

MOGK D.W. & MATHEZ E.A. (2000): Carbonaceous films in midcrustal rocks from the KTB borehole, Germany, as characterized by time-of-flight secondary ion mass spectrometry. *Geochemistry, Geophysics, Geosystems* **1**.

POSCHENRIEDER W.P., HERZOG R.F.K. & BARRINGTON A.E. (1965): The relative abundance of the lithium isotopes in the Holbrook meteorite. *Geochim. Cosmochim. Acta* **29** 1193-1195.

ROBOZ J. (1968): *Introduction to Mass Spectrometry Instrumentation and Techniques*. New York, John Wiley & Sons, 539 pp.

ROUBEROL J.M., BASSEVILLE P. & LENOIR J.-P. (1972): Recent improvements of the in analyzer and typical examples of applications. Journal of *Radioanalytical & Nuclear Chem.* **12**, 59-67.

SAXTON J.M., LYON I.C., CHATZITHEODORIDIS E., PERERA I.K., VAN LIERDE P., FREEDMAN P. & TURNER G. (1996): The Manchester Isolab 54 ion microprobe. *Internat. J. Mass Spectrom. & Ion Processes* **154**, 99-131.

SHIMIZU N., SEMET M.P. & ALLEGRE C.J. (1978): Geochemical applications of quantitative ion-microprobe analysis. *Geochim. Cosmochim. Acta* **42**, 1321-1334.

SIGMUND P. (1969): Theory of sputtering. I. Sputtering yield of amorphous and polycrystalline targets. *Physical Review* **184**.

SJÖVALL P., THIEL V., SILJESTRÖM S., HEIM C., HODE T. & LAUSMAA J. (2008): Organic geochemical microanalysis by time-of-flight secondary ion mass spectrometry (ToF-SIMS). *Geostandards & Geoanalytical Res.* **32**, 267-277.

SLODZIAN G., DAIGNE B., GIRARD F., BOUST F. & HILLION F. (1992): Scanning secondary ion analytical microscopy with parallel detection. *Biology of the Cell* **74**, 53-50.

STERN R.A. (1998): High-resolution SIMS determination of radiogenic tracer-isotope ratios in minerals. *In*: Modern Approaches to Ore and Environmental Mineralogy. L.J. Cabri & D.J. Vaughan (*eds*.), Mineral. Assoc. Can., *Short Course Series* **27**, 241-268.

STORMS H.A., BROWN K.F. & STEIN J.D. (1977): Evaluation of a cesium positive ion source for secondary ion mass spectrometry. *Analyt. Chem.* **49**, 2023-2030.

SYLVESTER P. (ED.) (2008): *Laser Ablation ICP-MS in the Earth Sciences: Current Practices and Outstanding Issues*. Mineral. Assoc. Can. *Short Course Series* **40**, 356 pp.

THOMSON J.J. (1910): Rays of positive electricity. *Philosophical Mag.* **20** (Series 6), 752-767.

VAN VAECK L., ADRIAENS A. & GIJBELS R. (1999): Static secondary ion mass spectrometry (S-SIMS) Part 1: Methodology and structural interpretation. *Mass Spectrom. Rev.* **18**, 1-47.

VICKERMAN J.C. & BRIGGS D. (EDS.) (2001): *ToF-SIMS: Surface Analysis Mass Spectrometry*. IM Publications and Surface Spectra, 789 pp.

VICKERMAN J.C., BROWN A. & REED N.M. (EDS.) (1989): *Secondary Ion Mass Spectrometry-Principles and Applications*. Oxford University Press, 340 pp.

WILLIAMS I.S. (1998): U-Th-Pb geochronology by ion microprobe. *In*: Applications of Microanalytical Techniques to Understanding Mineralizing Processes. M.A. McKibben, III Shanks, W.C.P. & W.I. Ridley (*eds*.), *Soc. Econ. Geol., Rev. Econ. Geol.* **7**, 1-35.

WILLIAMS P. (1985): Secondary ion mass spectrometry. *Ann. Rev. Materials Sci.* **15**, 517-548.

WILLIAMS P. (1990): Quantitative analysis using sputtering techniques: secondary ion and sputtered neutral mass spectrometry. *In*: Practical Surface Analysis. D. Briggs & M.P. Seah (*eds*.). J. Wiley & Sons **2**, 177-228.

ZINNER E. & CROZAZ G. (1986): A method for the quantitative measurement of rare earth elements in the ion microprobe. *Internat. J. Mass Spectrom. & Ion Processes* **69**, 17-38.

ZINNER E., MCKEEGAN K.D. & WALKER R.M. (1983): Laboratory measurements of D/H ratios in interplanetary dust. *Nature* **305**, 119-121.

http://ms.51001.com/

GLOSSARY

Definitions are the author's, and from various sources mentioned in the Introduction and elsewhere (ISO 1993, IUPAC, McNaught & Wilkinson 1997).

Abundance sensitivity: a measure of the ability of a **mass analyzer** to detect a small peak adjacent to a larger one.

Analyte: in the context of SIMS, the atom or molecule within the solid being analyzed.

Atomic mass unit: symbol, u, is equivalent to the mass of 1/12 the mass of the ^{12}C atom.

Cluster (ion): as used in SIMS, can also be referred to as a **molecular fragment**, generally implying molecular ions having an 'artificial' configuration, *i.e.*, not present originally in the target, as in $Zr_2Si_2^+$ in zircon ($ZrSiO_4$). The inference is often that the molecule has formed through some process of ion generation, either by combination or fragmentation. For **dynamic SIMS**, all molecular ions are presumably of this type, whereas for **static SIMS**, there may be intact molecules. On the whole, the term **molecular ion** is sufficient for most purposes without implying a genetic mechanism.

Collision cascade: the 'billiard ball' process of transferring kinetic energy from an impacting atomic or molecular ion to the atoms of a target via a succession of elastic atomic displacements. See Figure 1-2.

Depth profiling: also referred to as 'in-depth' analysis, in which the composition of a target is progressively measured with time, *i.e.*, normal to the sample surface.

Detection limit: the minimum level that can be distinguished from background, which is typically taken as 3 standard deviations of the background count rate; in physics and materials science applications of SIMS, detection limit units are atoms cm^{-3}, and the range is generally 10^{12} to 10^{16} atoms cm^{-3} (roughly ppb to ppm range).

Dimer: a molecule that includes only two of the same element, as in Si_2^+; monomer, trimer, and tetramer have also been used. As an adjective, has been used to describe more complex molecules, *e.g.*, dimeric niobium pentoxide $Nb_2O_5^+$.

Direct ion imaging: the technique of stigmatic focusing of secondary ions onto a spatially sensitive detector for live imaging of the distribution of secondary ions across a surface. Compare with **scanning ion imaging**.

Discrimination: often used to refer to the effect of SIMS analysis in biasing the element/element ratios from the true values in the sample, due to inherent differences in secondary ion yields and the specific analytical conditions employed.

Double focusing (mass analyzer): permits focusing of an ion beam of single mass/charge that has initially inhomogeneous angular (beam spread) and chromatic (= velocity) aberrations. Requires appropriately configured magnetic and electrostatic sectors to allow the directional and velocity loci of the mass analyzer to coincide.

Duoplasmatron: a device for generating primary ions, comprising a two-stage, magnetically confined plasma discharge.

Dynamic SIMS: a branch of SIMS conducted with a high density primary beam, whereby the upper layers of the target are continuously and thoroughly saturated with primary ions, and the sputtered material is a highly structurally and chemically modified version of the original.

Energy filtering: an analytical technique whereby ions are selected on the basis of kinetic energy; in many cases, high energy ions are preferentially selected to reduce matrix effects and isobaric interferences.

Fragment (ion): see **cluster**.

Instrumental Mass Fractionation (IMF): bias in an isotope ratio measurement (in ‰ or %), related to the isotope species, the sample, and the analytical method, determined from comparing a measured value to its independently determined ('true') value; often, it is assumed that IMF is systematically mass-dependent (*e.g.*, % u^{-1}), but this may not be correct in all cases.

In-depth analysis: equivalent to **depth profiling.**

Ion: an atom or molecule having a net positive or negative charge, as in atomic ion or **molecular ion.**

Ion Yield: number of ions of a particular type sputtered per primary ion impact; may also refer to the ratio of two secondary ions; may also refer qualitatively to the relative intensity of the ion signal.

Isobars: nuclides having nominally equivalent mass numbers (within the resolution of the instrument); strictly speaking isobars are atoms, although in SIMS it is also often used to refer to a molecule.

Isotopes: **nuclides** having the same number of protons (atomic number), but different number of neutrons, as in ^{12}C and ^{13}C.

Matrix effects: the combined influences of the sample and the sputtering conditions on secondary **ion yields**. Important factors relating to the atom(s) of interest include ionization potential, and chemical, electronic, and structural environment during sputtering.

Mean square of weighted deviates (MSWD): a statistic where the value quantifies the overall extent to which the individual values used to calculate a mean are actually likely to be measurements of that mean. Also termed the 'reduced chi-squared value.' A value near 1.0 is ideal. Values much less than unity usually indicate that individual uncertainties are too large, while values much greater usually indicate the sample is heterogeneous, or the individual uncertainties are underestimated.

Mass analyzer: an assembly that permits ions of uniform mass/charge (m/z) ratio to be separated from others of slightly different m/z.

Molecular ion: a molecule with one or more electrons lost or gained; see **cluster**, **fragment**.

Monolayer: a single layer of atoms or molecules, often referring to the topmost layer of a surface under vacuum.

Nuclide: a type of atom characterized by its mass number, atomic number, and nuclear energy state.

Primary (ion) beam: an electrostatically focused beam of **ions** that form the probe in SIMS.

(mass) Resolution: R, is *the inverse fractional mass separation of resolved peaks*, that is, the peaks are sufficiently separated such as not to influence a count rate determination. It is quantified from the observed mass spectra. There are several methods of calculating R. The mass-to-base-width ratio (*i.e.*, $M\,\Delta M^{-1}$ in atomic mass units, u) at a specified fraction of peak intensity is common, *e.g.*, at R = 5000, isotopes differing in mass by 1/5000 = 0.02% are considered resolved. Qualitatively, resolution can be described as low (<1000), medium (1000–3000), and high (>3000).

Radiogenic isotope: a nuclide derived from a **radionuclide**; it may be stable, or itself be a radionuclide.

Radionuclide: a radioactive nuclide (*i.e.*, undergoes nuclear decay).

(mass) Resolving power: equivalent to **mass resolution**, however some commercial SIMS software may use this term according to a different definition; check definitions when comparing performance.

Reference material (RM): in SIMS, a solid in which elemental or isotopic composition has been determined by independent analytical methods to specified limits, and is used for calibrating instrumental bias, assessing a measurement procedure, or assigning measurement uncertainties to the procedure. Ideally for SIMS, the RM is homogeneous at the micrometre scale, but many do not comply or have not been proven. The term 'standard' is commonly used in geology, but the term is imprecise, ambiguous, and is not equivalent to RM (ISO 1993), as a 'measurement standard' is for calibration only.

Scanning ion imaging: refers to the technique of incrementally moving a finely focused primary ion beam across the surface of the target in two dimensions, in order to determine spatially related secondary ion intensity variations; this is the imaging technique preferred for quantitative ion microscopy.

Secondary (ion) beam: the electrostatically and/or magnetically focused beam of ions derived from sputtering.

(elemental) Sensitivity: a figure of merit in SIMS relating the count rate of a particular secondary ion normalized to the abundance in the target and the primary beam current. See also **abundance sensitivity**.

SIMS: secondary ion mass spectrometry

Sputtering: ejection of atoms and molecules (often referred to as 'clusters' in dynamic SIMS) from a surface bombarded by a flux of ions. The particles may be neutral, positive, or negatively charged.

Stable isotope: a nuclide that is not radioactive, *i.e.*, not decaying to form another nuclide. Note that stable isotopes may also be **radiogenic isotopes**, but in isotope geochemistry, stable isotope normally refers to ones that are not part of any radioactive decay series.

Static SIMS: a branch of SIMS conducted with an extremely low density primary beam that permits sputtering of the undisturbed monolayer at the surface; the local environment of the sample is impacted by only one primary ion, and the total ion dose over a region is $< 10^{13}$ cm^{-2}.

Surface binding energy: the energy required to remove an atom from the top surface layer in vacuum during sputtering.

Total sputter yield: total number of all particles sputtered per primary ion impact (atoms/ion).

Useful Yield: the number of measured secondary ions of a particular atom per second, normalized

http://blog.sina.com/

to the total number of sputtered atoms (of the same type) per second (ions/atom); in some usages, it is defined as the number of detected atoms per atoms in target.

Ultra-high vacuum: an arbitrary range of gas pressure conditions, generally10^{-12} < pressure < 10^{-9} mbar (1 mbar = 100 Pa = 0.75 Torr).

Very high vacuum: an arbitrary range of gas pressure conditions, generally 10^{-9} < pressure < 10^{-6} mbar.

顶级地质论坛：http://bbs.3s001.com/

CHAPTER 2: *IN SITU* OXYGEN ISOTOPE GEOCHEMISTRY BY ION MICROPROBE

John W. Valley & Noriko T. Kita,
WiscSIMS Laboratory
Department of Geology and Geophysics
University of Wisconsin
Madison, WI 53706 U.S.A.
valley@geology.wisc.edu

INTRODUCTION

High precision and accuracy with *in situ* analysis has been a "holy grail" for generations of stable isotope geochemists who employed a range of strategies for separation of heterogeneous samples and for interpretation of data from mixed samples. However, *in situ* techniques have in the past suffered from relatively poor precision and accuracy. Recent advances by ion microprobe have improved precision and accuracy, and make these time-consuming, uncertain approaches unnecessary. *In situ* analyses can be correlated with textures and imaging, offering the promise of new and fundamental information about patterns of isotope distribution.

The importance of stable isotope geochemistry is well established in many disciplines (see Clark and Fritz 1997, Griffiths 1998, Kendall & McDonnell 1998, Criss 1999, Ambrose & Katzenberg 2000, Valley and Cole 2001, Unkovich *et al*. 2001, Hoefs 2004, De Groot 2004, Johnson *et al*. 2004, Sharp 2007). Many seminal studies are included in these reviews. However, the conventional analytical techniques employed in these studies require homogenization of bulk samples that are larger than the scale of zonation in a wide range of samples. Important information has been lost by analysis of powders.

The ion microprobe's ability to analyze isotope ratios with high precision and accuracy from micrometre-scale spots in natural samples (as well as experimental products) *in situ* from a microscope slide reduces sample size by factors of ten thousand to one billion, and allows isotopic data to be correlated with other geochemical information in spatial context with textures and imaging (Fig. 2-1). The accuracy of these data now approaches that of conventional techniques that require far larger samples. These advantages are revolutionizing stable isotope geochemistry, just as the electron microprobe revolutionized *in situ* chemical analysis and the SHRIMP (ion probe) revolutionized zircon geochronology (Ireland 1995, Hinton *et al*. 1995, Ireland & Williams 2003).

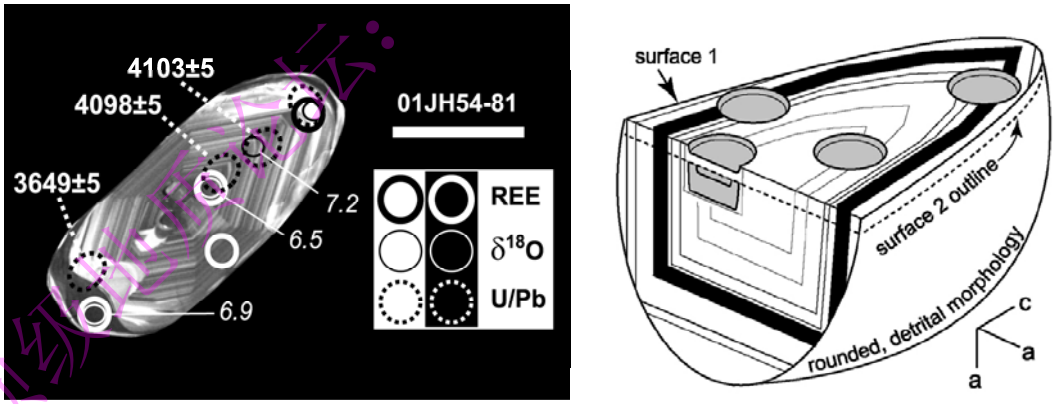


FIG. 2-1. Correlated ion microprobe analysis of $\delta^{18}O$, U-Pb, and trace elements in zircon. **Left:** CL image of a detrital zircon from the Jack Hills metaconglomerate, Australia, showing a concentrically zoned igneous core dated at 4.1 Ga and thin overgrowths that are younger than 3.7 Ga. Analysis pit locations are shown for $\delta^{18}O$, U-Pb, and REEs. Scale bar = 100 μm. **Right:** Cartoon of a zoned detrital zircon showing a strategy for three successive analyses from a domain <20 μm in diameter: U-Pb (surface 1), $\delta^{18}O$, and trace elements (surface 2, after repolishing). Note that zoning is finer than spot size; sub-μm analysis will be discussed below (from Cavosie *et al.* 2006).

Mineralogical Association of Canada Short Course 41, Toronto, May 2009, p. 19-63

This chapter discusses procedures for high precision and accuracy of ion microprobe analysis of oxygen isotope ratios, and reviews recent studies that have applied these techniques to Earth Science. It is beyond the scope of this chapter to discuss all of the earlier pioneering studies; additional references can be found in papers that are cited. Strategies for ion microprobe analysis vary according to trade-offs in instrument tuning, sample preparation, and analysis. Because of improved data quality at smaller spot sizes, applications discussed here emphasize results from the newest large-radius, multi-collector ion microprobe, IMS1280. These studies provide detailed records of zonation in samples including diagenetic cements, speleothems, foraminifera, otoliths, gems, zircon grains, and meteorites, which were previously inaccessible to analysis. In many cases, understanding the true scale and patterns of isotope variation provides new insight for processes as varied as diagenesis, paleoclimate, biomineralization, metamorphism, magma genesis, crustal evolution, and formation of the Solar System.

HIGH PRECISION *IN SITU* ANALYSIS OF OXYGEN ISOTOPE RATIOS

Analytical precision for analysis of $\delta^{18}O$ by ion microprobe has improved steadily over the past three decades due to development of new instrumentation and refinements in technique (Fig. 2-2): ±20‰ (2SD, IMS3f without electron-flood gun); ±2‰ (IMS4f, high mass resolution); ±1.0‰ (IMS4f, high energy offset); ± 0.6‰ (IMS1270, multi-collector); ± 0.3‰ (IMS1280) (Giletti *et al.* 1978, McKeegan 1987, Valley & Graham 1991, Hervig *et al.* 1992, Riciputi & Patterson 1994, Cavosie *et al.* 2005, Kelly *et al.* 2007, Kita *et al.* 2009). Precision is emphasized in this section before discussion of accuracy. Accuracy equal to precision can be attained in many samples by detailed monitoring of instrumental conditions, careful sample preparation, and use of appropriate standards. While ion microprobe precision for $\delta^{18}O$ has improved by an order of magnitude every 15 years since the first analyses were published (Giletti *et al.* 1978), and sample sizes have been reduced, this progress is reaching a plateau. Recent studies come close to the physical limit imposed by the number of atoms in spot sizes of 10 μm and below (Page *et al.* 2007a).

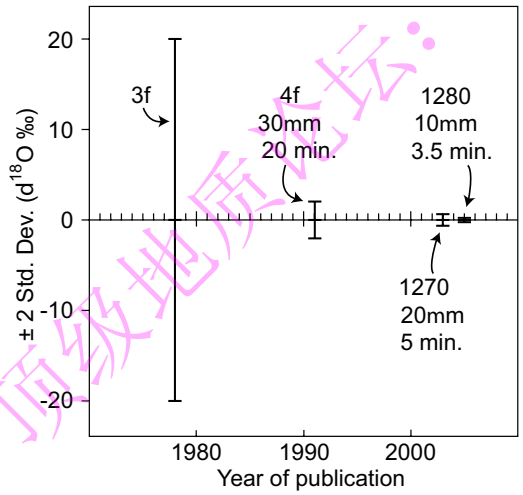


FIG. 2-2. The precision of ion microprobe analyses for $\delta^{18}O$ has improved from ±20‰ in 1978 to ±0.3‰ (2 SD) today due to the development of new instruments (IMS3f to IMS1280) and refinements in technique (see text). At the same time, accuracy, spot size, and speed of analysis have also improved.

The following figures present large data sets for $\delta^{18}O$ from 10, 3, and <1-μm diameter spots, and $\delta^{17}O$ from 15, 2, and 1 μm spots. A number of factors affect data quality. In general, there is a trade-off of precision, which may be limited by the number of ions counted, and spot size.

Figure 2-3 shows $\delta^{18}O$ values from 3.5-minute analyses of 10 μm diameter spots in quartz. Over 650 spot analyses were made in 48 hours from 12 different sample mounts. A quartz standard was analyzed four times every 10-20 sample spots. The sample data vary by over 40‰, revealing exciting trends in magmatic hydrothermal systems, but the standard data are constant with precision of ±0.3‰ (2 SD, standard deviation; ±0.02‰, 2 SE, standard error, N = 173). The repeated analysis of an appropriate standard and a well-prepared sample ensures that accuracy matches spot-to-spot precision.

Careful tuning of the instrument, sample preparation, and standardization are critical for obtaining results such as shown in Figure 2-3. Pertinent analytical details will be discussed in subsequent sections of this paper. Attention to detail pays off and it is important to note that not all ion microprobe data are of comparable quality. Procedures for reporting accuracy and precision vary, and the interested readers may want to evaluate precision and accuracy for themselves from the published tables of standard data. In general, this requires that standard analyses bracket samples and that data be published in chronological order of analysis.

顶级地质论坛: http://bbs.3sdz.com/

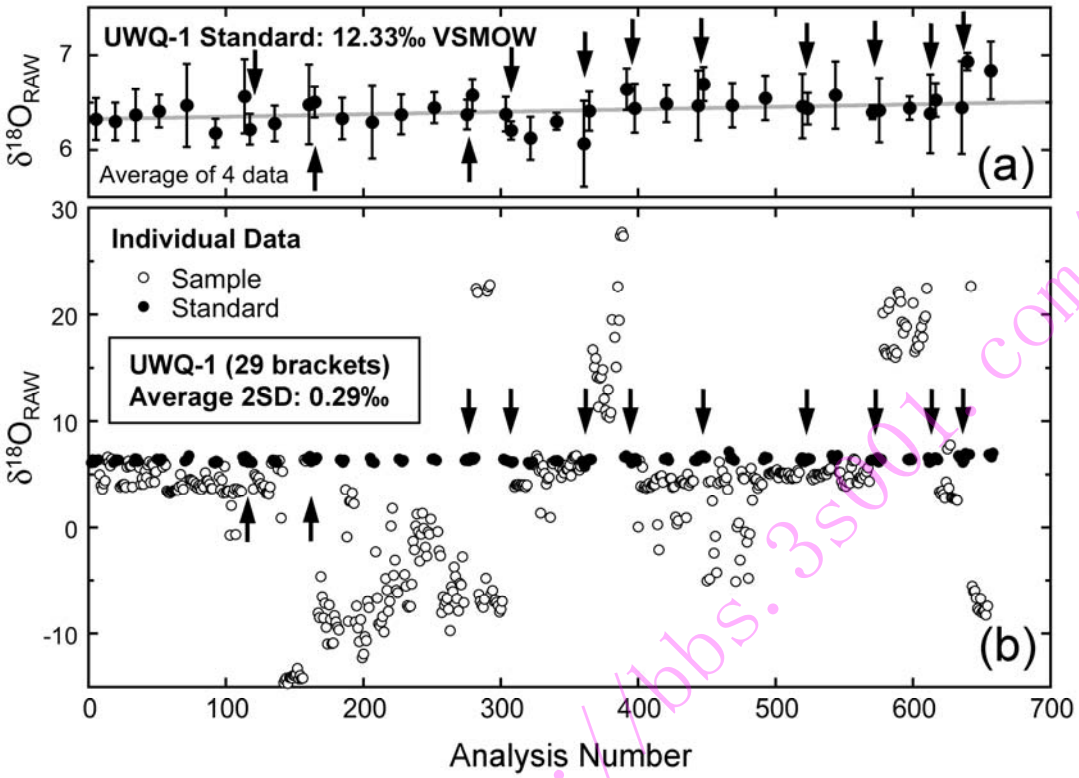


FIG. 2-3. Results from 48 hours of analysis of $\delta^{18}O$ in quartz from 12 sample mounts by IMS1280 at WiscSIMS. Data are from Rusk *et al.* (2007). The 658 spots analyzed include 173 from the quartz standard, UWQ-1 (solid dots). Grains of standard were cast in each mount. **(a)** Average value with 2 SD error bars for each group of 4 bracketing standard analyses. Arrows indicate sample changes. The spot-to-spot precision for each group of 8 standard analyses varies from 0.14 to 0.38 and averages 0.29‰ (2 SD; ±0.10‰ 2SE). **(b)** The 485 analyses of hydrothermal quartz samples (open circles) vary by 40‰ (from Kita *et al.* 2009).

Analysis of $\delta^{17}O$ in oxygen three-isotope studies is more challenging because of the ~5x lower natural abundance of ^{17}O than ^{18}O. Figure 2-4 shows $\delta^{18}O$ and $\delta^{17}O$ in an olivine standard, and samples of meteoritic olivine measured from 15 μm spots using an IMS1280 and three Faraday Cup detectors (Kita *et al.* 2008). Sample analyses are bracketed by analyses of standard in the same mount. The average values of precision for each group of eight bracketing standard analyses are 0.31‰ and 0.37‰ (2 SD) for $\delta^{18}O$ and $\delta^{17}O$, respectively (Kita *et al.* 2009).

Spot size is variable for ion microprobe analysis. The Cs beam, used for oxygen isotopes, can be focused to a diameter of 250 nm on the IMS1280 instrument, and 50 nm on the nanoSIMS. However, the primary beam current and the resulting signal varies with spot size, and the beam is generally defocused to a larger diameter in order to generate more secondary ions for analysis. At WiscSIMS, typical values for the 2 SD reproducibility of $\delta^{18}O$ for multiple analyses of a homogeneous material are ± 0.3‰ at 10 μm (Fig. 2-3), ± 0.7‰ at 3 μm (Fig. 2-5), and ± 2‰ at <1 μm (Fig. 2-6).

MULTI-COLLECTOR ION MICROPROBES

A number of ion microprobe instruments have been used for stable isotope analysis. Early workers used single-collector (detector) instruments such as the IMS4f. More recently, multicollector instruments have demonstrated key advantages. At present, the IMS1270/1280 series has proven best for the high precision needed for natural isotope abundances and sub-permil accuracy, but the multicollector nanoSIMS and SHRIMP II have also been employed, as have single channel instruments.

The first commercial ion microprobe multi-collector system was installed on an IMS1270 in 1998. This development led to major improvements in stable isotope performance, analogous to the

http://bbs.3s001.com/

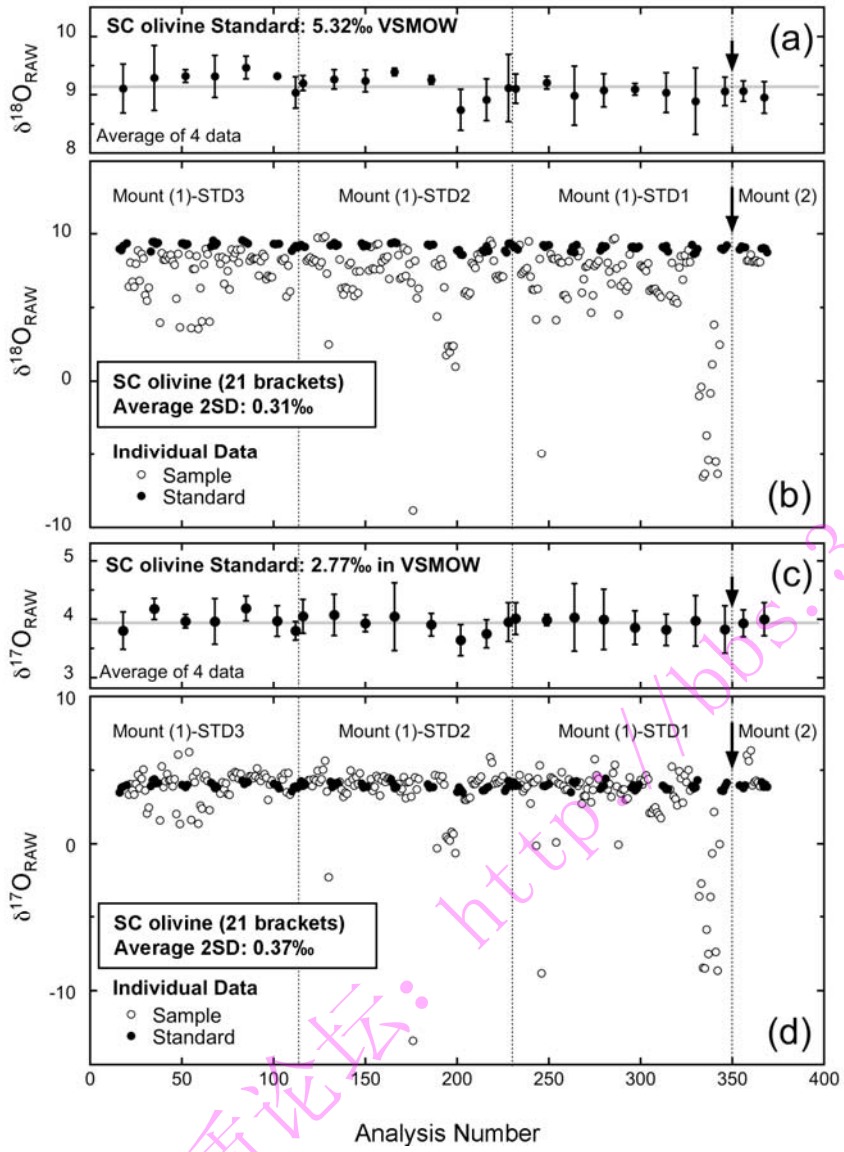


FIG. 2-4. Analyses of $\delta^{18}O$ and $\delta^{17}O$ in San Carlos olivine standard (SC, solid dots) and meteoritic olivine (open circles) using an IMS1280 at WiscSIMS (uncorrected data, Kita *et al.* 2008). 343 analyses were made in 56 hours including 103 standards. **(a)** Average $\delta^{18}O$ and 2 SD values of groups of four standard analyses. **(b)** Values of $\delta^{18}O$ for samples and standards. **(c)** Average $\delta^{17}O$ and 2 SD values of each group of four standard analyses. **(d)** Values of $\delta^{17}O$ for samples and standards. Arrows indicate sample change. The average values of 2 SD for each group of eight bracketing standard analyses are 0.31‰ and 0.37‰ for $\delta^{18}O$ and $\delta^{17}O$, respectively (error bars in (a) and (c) are 2 SD) (from Kita *et al.* 2009).

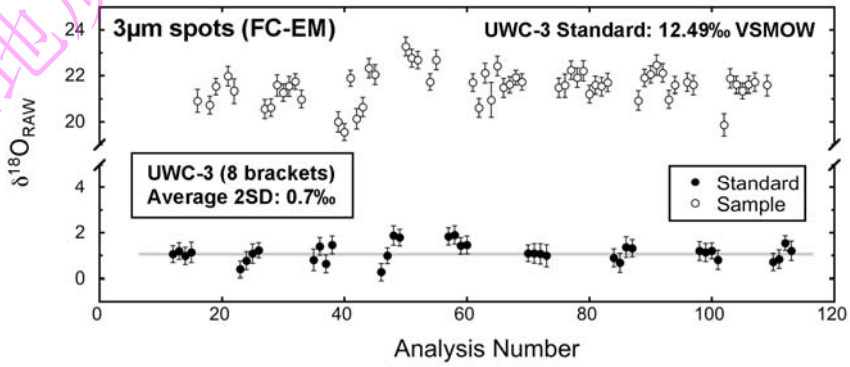


FIG. 2-5. Analyses of $\delta^{18}O$ in single foraminifera (open circles) and calcite standard, UWC-3 (solid dots), with a 3 μm diameter spot at WiscSIMS. Data are from Kozdon *et al.* (2009). A total of 94 analyses including 36 standard analyses were made in 48 hours. The average value of 2 SD for bracketing standard analyses is 0.7‰ (from Kita *et al.* 2009).

顶级地质论坛：http://bbs.3sgeo.com/

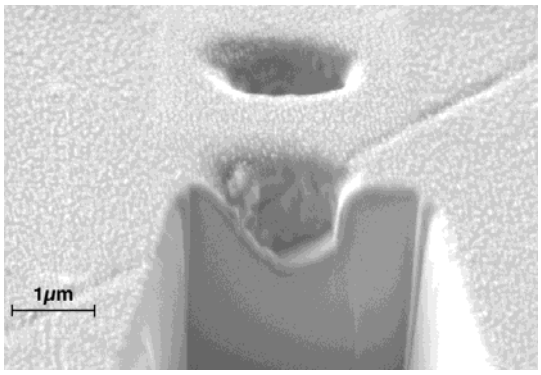


FIG. 2-6. SEM view of sub-micron pits from analysis of $\delta^{18}O$ in zircon (see Fig. 2-28). The pit in foreground was dissected by FIB (focused ion beam) revealing that dimensions are ~1 x 0.5 x 1 μm. Volume is ~ 0.5 μm^3 and weight is ~10^{-12} g per analysis (*vs.* 10^{-2}–10^{-3} g for conventional analyses). Spot-to-spot precision is degraded to ~2‰ (2 SD) for these analyses due to small sample size (from Page *et al.* 2007a).

advent of the double collector gas-source mass-spectrometer (Nier 1947). On an ion microprobe, simultaneous analysis of all isotopes of interest has many advantages including normalization of beam instability and drift, more rapid analysis, and efficient use of samples. The IMS1270/1280 multicollector system typically has a total of 11 detectors: 10 Electron Multipliers (EM) and Faraday Cups (FC), and a channel plate (Fig. 2-7). There is a trade-off in choice of EM *versus* FC detector. A FC is favored at high count rates where the relatively high background is not important. An EM has a much lower background signal, but is limited to lower count rates by deadtime, quasi-simultaneous arrivals (QSA), and aging. In practice, up to 5 detectors can be used simultaneously. The maximum dispersion is 17.3% in mass, sufficient for ^{6}Li and ^{7}Li. The minimum spacing of detectors permits adjacent isotopes of Pb to be analyzed. Significantly greater mass dispersion exists in nanoSIMS instruments offering the potential to analyze multiple isotope systems simultaneously (*i.e.*, C and O), but this requires compromises; such data are less accurate, but may be useful in certain studies.

For oxygen isotopes, the dynamic range problem (*i.e.*, $^{18}O/^{16}O$ ~1/500, $^{17}O/^{16}O$ ~1/2500) is solved by IMS1280 using either: 1) 3 FCs with high count rates (>10^6 cps) and 10 μm spots; or 2) for smaller spots with low count rates, sensitive, low background EMs for minor isotopes (^{17}O and ^{18}O) and a high count rate FC for the major isotope (^{16}O). Multiple collectors permit count rates of >10^9 cps for ^{16}O (by FC) such that counting precision of 0.1‰ for ^{18}O that takes many hours with a single EM (<2000 cps) is obtained in a few minutes (>10^6 cps). The use of 3 FCs avoids many difficulties associated with EMs (*e.g.*, deadtime, asymmetric pulse height distribution, focusing on the first dynode, aging of the detector, and QSA; Slodzian *et al*. 2001, Slodzian 2004, Schuhmacher *et al.* 2004), but the use of EMs is necessary for smaller spot size, or for analysis of minor or trace isotopes.

IMS1280

The IMS1280 features many improvements to the pioneering 1270 design that led to better precision and accuracy of isotope ratios, including: new primary beam ion optics; direct measurement of primary beam current to permit better correction of QSA (Slodzian *et al*. 2001, Slodzian 2004); automatic centering of the secondary beam to correct for small variability in sample geometry; NMR magnet control with long-term stability; control of stray magnetic fields; and a six-sample airlock chamber. Many of these features are available as upgrades and have been installed on earlier 1270 instruments.

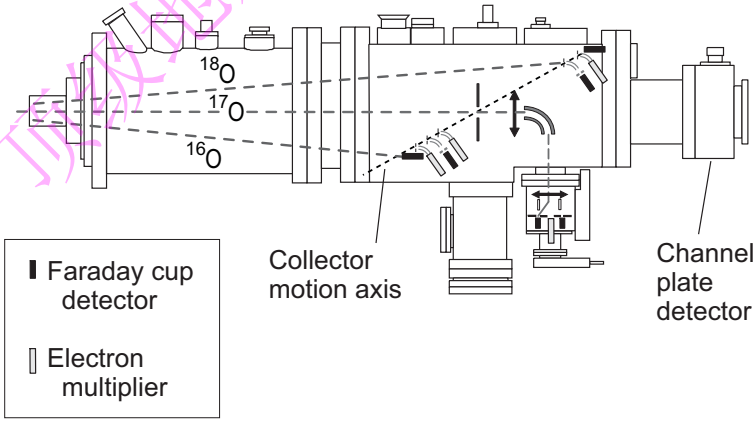


FIG. 2-7. The IMS1280 multicollector block at WiscSIMS has 11 detectors (4 electron multipliers, 6 Faraday cups, and a channel plate) including a fixed axial detector system and five independently movable trolleys. Alignment is shown for simultaneous analysis of three oxygen isotopes employing 3 FCs.

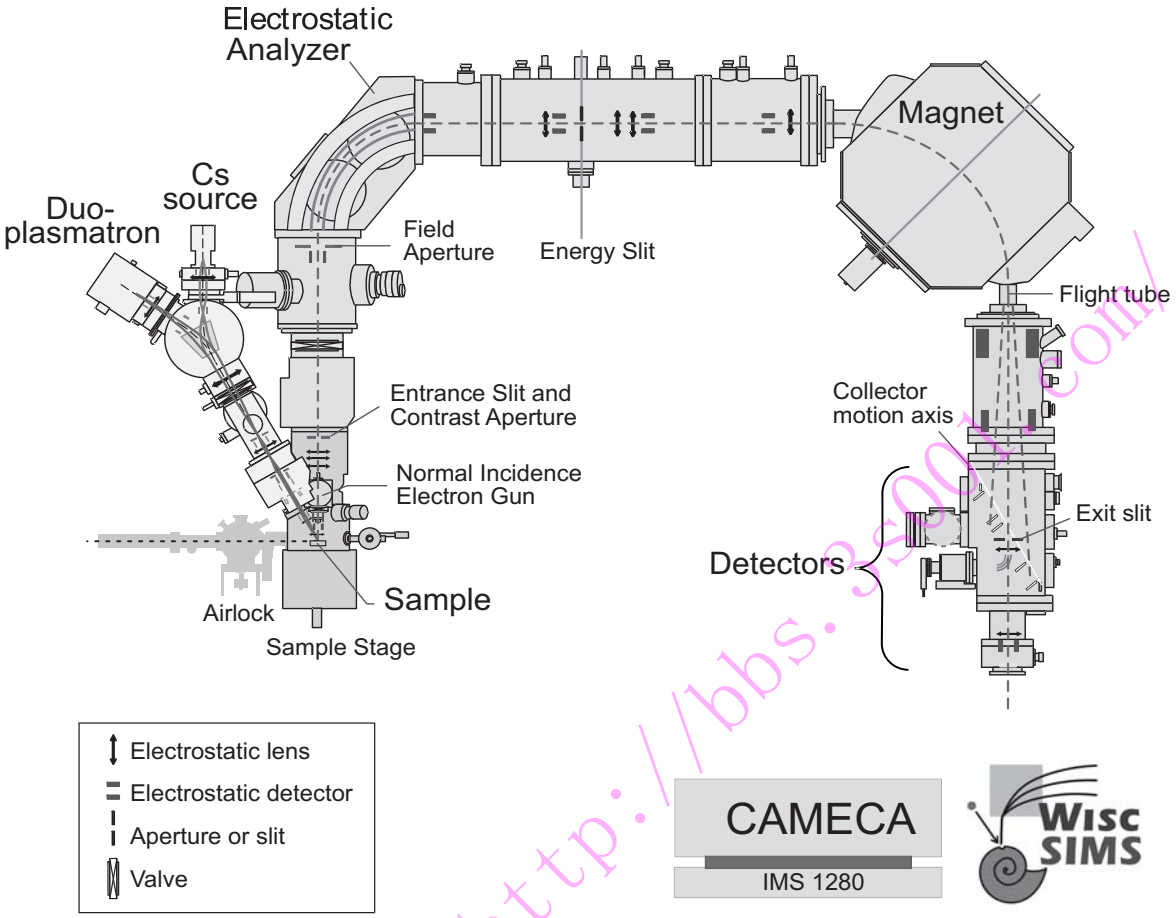


*FIG. 2-8. Schematic of the IMS1280, large radius, high resolution, multicollecting ion microprobe/ SIMS. For color version, see http://www.mineralogicalassociation.ca/index.php?p=160

Figure 2-8 shows a simplified diagram of the IMS1280. This instrument is variously referred to as an ion microprobe, a secondary-ion mass spectrometer (SIMS), or a double-focusing mass spectrometer. The name Ion Microprobe refers to the primary ion beam that is focused to a small spot on the sample surface. The primary beam is selected for efficient sputtering and ionization of the sample. For analysis of oxygen isotopes and many other elements, the Cs-source is used ($^{133}Cs^+$) necessitating charge compensation by conductive coatings and a normal incidence electron flood gun. Alternatively, the Duoplasmatron generates primary ions of $^{16}O^+$ or $^{16}O^-$, and other sources are available. The ion microprobe analyzes secondary ions that are sputtered from the sample surface and thus is one type of Secondary-Ion Mass Spectrometer. Some SIMS instruments have larger primary beam spots and hence are not ion microprobes. The secondary ions in a Double-Focusing Mass Spectrometer are sorted by the sector magnet according to mass and charge [turning radius is proportional to $(M/e)^{0.5}$], and at the same time focused in kinetic energy by the electrostatic analyzer such that high mass-resolving power can be obtained for secondary ions that are sputtered with a significant range of initial kinetic energy.

Instrument Bias and Use of Standards

Attaining high accuracy and precision by ion microprobe/SIMS requires the careful use of appropriate standards. SIMS analysis causes bias in isotope ratio and elemental composition. The bias (sometimes called instrumental mass fractionation or IMF) originates during the sputtering, transmission, and detection of secondary ions, but the details of this process are not well understood (Slodzian 1980, 1982, 2004, Lorin *et al.* 1981, Shimizu & Hart 1982, Gnaser & Hutcheon 1988, Zinner 1989, Ireland 1995). The magnitude of bias varies with the chemistry and crystal structure of the

矿物岩石论坛：http://bbs.sgcn.com/

target. It has been shown that bias also varies with crystal orientation for magnetite (Lyon *et al.* 1998, Huberty *et al.* 2009). This complication has been ruled out for many minerals by analysis of multiple grains of a homogeneous sample in known (or random) orientations. However, many minerals have not yet been tested (see below). To date, there is no theoretical basis upon which to make a correction for bias, as exists, for instance, for electron microprobe data. For some minerals, the magnitude of bias for $\delta^{18}O$ by IMS1270/1280 operated at higher mass resolution ($M/\Delta M = 2500$, Kita *et al.* 2009) is more than 10 times smaller than for IMS4f instruments operated at high energy offset (Hervig *et al.* 1992, Riciputi & Patterson 1994, Eiler *et al.* 1997, Valley *et al.* 1998, Riciputi *et al.* 1998). In all cases, accurate and precise analysis requires bracketing sample analyses with appropriate standards.

The best accuracy for stable isotope analysis is obtained for minerals showing limited solid solution where the standard is well calibrated, homogeneous, and has the same chemical composition and crystal structure as the sample. At WiscSIMS, this is routine for minerals such as quartz, calcite, and zircon. The recommended procedure is to place grains of standard in the center of each sample mount (Fig. 2-9, inset), and to repeatedly analyze the standard, bracketing sample data. This achieves two goals, calibration of instrument bias, and monitoring any drift or change in instrument parameters during the course of analysis. Typically, monitoring drift entails four analyses of standards before and after each group of 10–20 sample analyses. Standard data bracket all samples and comprise 25% or more of all analyses. This large effort is justified by the high precision that results. As seen in Figure 2-3 for 658 consecutive analyses of quartz, the standard data (solid dots) are homogeneous on the first 11 sample mounts (~600 analyses over 44 hours), but shift up by 0.47‰ for the last sample mount. This 0.47‰ difference is statistically significant at over 9 times the standard error for groups of 8 standard analyses (2 SD = 0.29; SE = SD/$N^{0.5}$; 2 SE = 0.29‰/$8^{0.5}$ = 0.1‰, N=8). Thus, repeated standardization can detect subtle changes that would otherwise go unnoticed. Such changes can occur, even after long periods of stable operation, due to a number of instrumental factors including variability of tuning, small changes in room or cooling water temperature (<1°C), baseline drift of the ^{18}O FC, or real differences among different mounts of the standard. Improvement of data can result from correcting to individual groups of 8 bracketing standard analyses rather than the global average for an entire analysis session, although the two procedures often lead to identical results.

Minerals that show a range of solid solution present special constraints as no single standard will be appropriate. For oxygen isotope ratios, a number of approximate empirical correlations have been demonstrated for large groups of minerals, but no master variable has been found to correlate closely to bias either by IMS4f with a single EM detector at high energy offset (Hervig *et al.* 1992, Riciputi & Patterson 1994, Eiler *et al.* 1997, Riciputi *et al.* 1998) or by IMS1280 with multiple FC detectors at low energy offset and high MRP (Fig. 2-10A). Thus, accurate analysis requires a suite of standards that spans the composition range of samples. The elemental composition and mineral identification of each ion microprobe spot should be known to determine the bias correction.

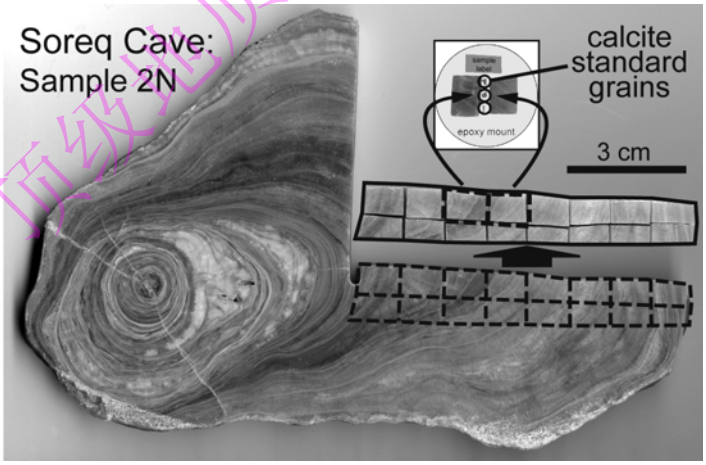


*FIG. 2-9. Annually banded speleothem from Soreq Cave, Israel dated by U-series geochronology to span 22.0–1.3 ka (Bar-Matthews *et al.* 2003). Long dimension = 168 mm. Inset: 10 mm-size chips cut from speleothem; two pieces were cast with calcite standard in 25 mm diameter epoxy mount for SIMS analysis. This mounting geometry allows efficient analysis of traverses along each sample piece with sample analyses regularly bracketed by standards. Note that all analysis spots are within 5 mm of the center of the mount (from Ian Orland).

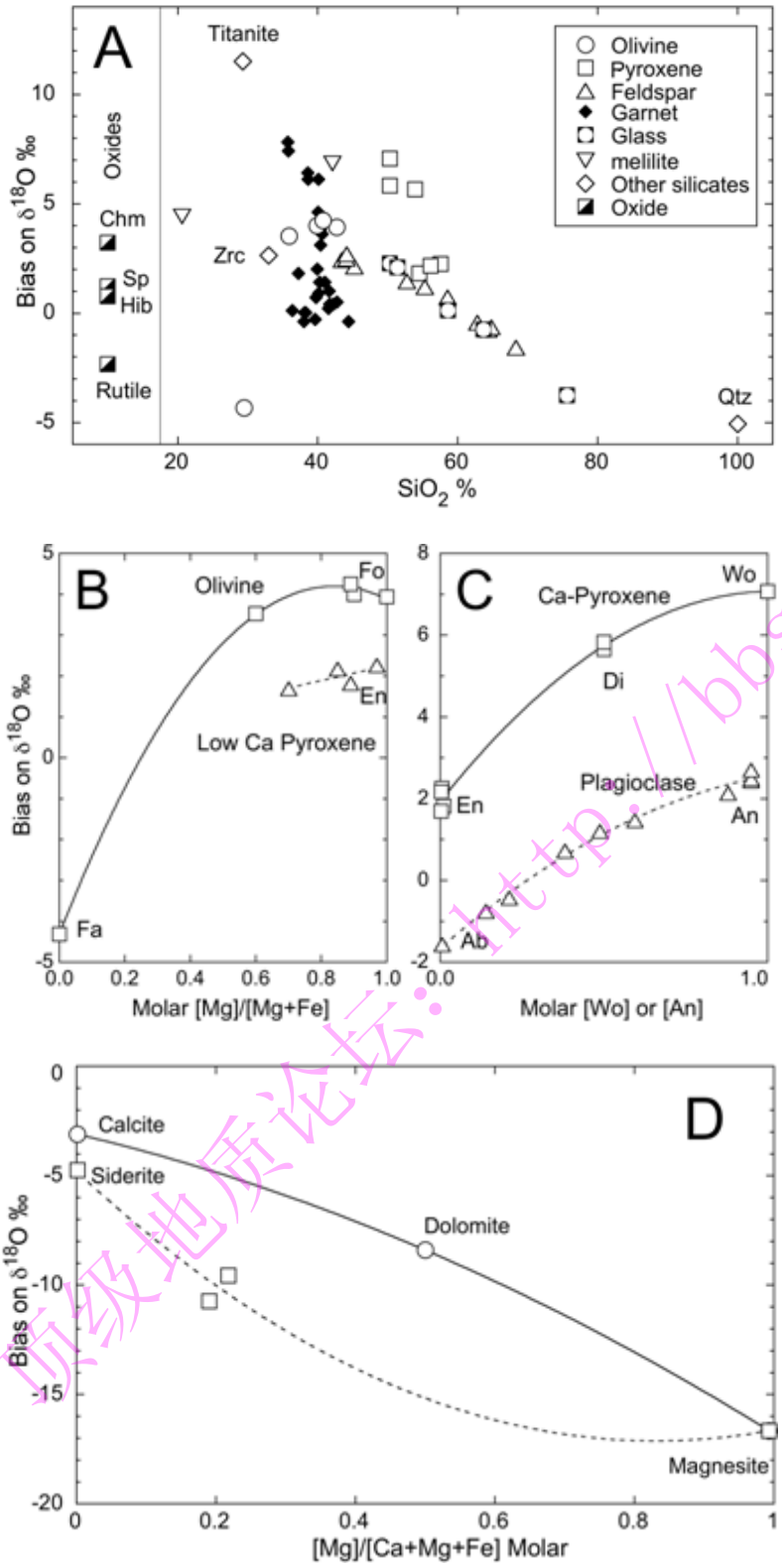


FIG. 2-10. Instrument bias for *in situ* analysis of oxygen isotope ratio by IMS1280 using dual FC detectors at WiscSIMS.
(A) Silicates and oxides plotted *vs.* wt.% SiO_2.
(B) Olivine and low Ca pyroxene *vs.* X_{Mg}.
(C) Pyroxene and plagioclase *vs.* X_{Ca}.
(D) Carbonates *vs.* X_{Mg} for Ca-Mg (solid line) and Fe-Mg (dashes).

Bias varies by up to 25‰ depending on chemical composition and crystal structure, and no master variable correlates well with bias. Accurate analysis is possible by construction of working curves for binary solid solutions within mineral groups such as plagioclase, carbonate minerals, olivine, or pyroxene. Sources of data: Kita *et al.* 2006, 2007b, 2009, Valley *et al.* 2007, Page *et al.* 2009.

质级地质论坛：http://bbs.cnqd.com/

The correlation of bias to mineral chemistry is considerably more accurate and precise if standards and samples all come from a binary solid solution within the same group of minerals such as the carbonate group (Fig. 2-10D; Valley *et al.* 1997, 2007, Eiler *et al.* 2002, Bowman *et al.* 2009); olivine or pyroxene (Fig. 2-10B,C; Kita *et al.* 2006, Downes *et al.* 2008); plagioclase (Fig. 2-10C; Kita *et al.* 2007b); garnet (Fig. 2-10A; Vielzeuf *et al.* 2005a, Lancaster *et al.* 2009, Page *et al.* 2009); or glasses (Fig. 2-10A; Eiler *et al.* 1998, 2007, Kita *et al.* 2007a,b). While Figure 2-10 shows nonlinear variations of bias up to 8‰ for $\delta^{18}O$ in silicates (olivine or garnet) and 14‰ for Ca-Mg carbonate, working curves fit the data well when multiple standards are available (*e.g.*, plagioclase, Fig. 2-10C). Thus, precise and accurate corrections of raw SIMS data can be achieved if sufficiently different standards are calibrated.

Page *et al.* (2009) expanded the sample set of Vielzeuf *et al.* (2005a) from 12 to 27 garnet compositions (Ca, Mg, Mn, Fe^{2+}, Al, Fe^{3+}) using an IMS1280 and standard operating procedures at WiscSIMS (see also Lancaster *et al.* 2009). They found that bias varies systematically by about 2‰ among the Mg, Mn, Fe^{2+} garnet compositions, but that Ca solid solution (grossular-andradite) extends the range of bias to 8‰. Fig. 2-10 shows that many Ca minerals have higher bias within their group (anorthite, calcite, wollastonite, and titanite). For garnet, Page *et al.* (2009) recommend mounting of a single garnet standard such as UWG-2 in each sample mount and constructing a working curve based on calibration of a group of garnet standards with compositions bracketing the unknowns. If the appropriate garnet standards are analyzed along with UWG-2 in the same analytical session as samples to calibrate bias, then the accuracy of this approach is indicated to be better than ±0.4‰, which is comparable to analytical precision.

Accuracy vs. Precision

It is important to distinguish accuracy from precision (Fig. 2-11). Confusion arises because of different definitions of "precision" and "accuracy". A critical observer may want to examine the data. In oxygen isotope geochemistry, isotope ratios are expressed on the $\delta^{18}O$-scale, normalized to V-SMOW, Vienna Standard Mean Ocean Water, or V-PDB, Peedee Belemnite (see O'Neil 1986). Accuracy is thus not expressed in absolute terms, but is actually the precision of comparisons to a standard. While the absolute abundances of oxygen

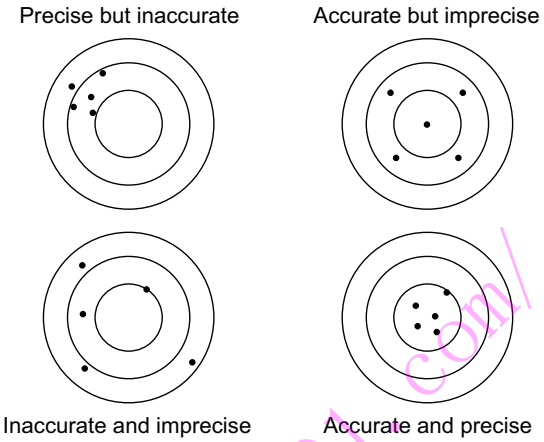


FIG. 2-11. Accuracy *vs*. precision.

isotopes in V-SMOW (water) are well known, they do not necessarily factor into the determination of $\delta^{18}O$. For ion microprobe analysis, the comparison becomes less direct as secondary standards must be calibrated by "conventional" techniques, typically fluorination or acid reaction combined with gas-source mass-spectrometry. The statistics of stable isotope analysis by SIMS are treated in detail by Fitzsimons *et al.* (2000).

The precision of SIMS analysis is generally limited by Poisson counting statistics (at low count rates, detector background may be a limitation). Thus, one standard deviation for a single analysis will not be better than $\pm N^{0.5}$ for N total counts; precision of ± 1‰ requires counting 10^6 atoms of ^{18}O and ± 0.1‰ requires 10^8 atoms. For $\delta^{18}O$, the number of ^{16}O atoms is also a factor, but with simultaneous analysis the total counts for ^{16}O are ~500x greater than for ^{18}O, and the uncertainty is much smaller and commonly ignored. Of course, a number of other factors can affect precision. Analytical error is more reliably evaluated from actual measurements than by theory.

Precision can be expressed as either the standard deviation of the mean (SD) or the standard error of the mean (SE). Each statistic has its appropriate use. The standard deviation describes the distribution of data about the mean. This is a reasonable proxy for the quality of a single spot-analysis by SIMS. The standard error is calculated as $SE = (SD/N^{0.5})$ where N is the number of observations. Thus, values of SE, in contrast to SD, typically get smaller as one analyzes more spots on a standard. SE is an indication of how well the mean for a population of data points is known and the likelihood that an additional analysis will change the mean. However, the SE of a group of

standard analyses is not a good measure of the quality of a single analysis.

As a further complication, both "internal" and "external" precision may be reported. For SIMS $\delta^{18}O$ measurements, the data for both ^{16}O and ^{18}O in a single spot are subdivided into a series of *n* cycles, and internal precision is based on the SE of the *n* comparisons. If a series of spots is analyzed, the external precision is the SD for those numbers. It is commonly thought that the external precision of multiple spot analyses should approach, but not be better than the internal precision. However, systematic errors can change this. For instance, the measured $^{18}O/^{16}O$ ratio in carbonate can vary significantly with depth during a single spot analysis, leading to a high internal error. However, this depth effect is reproducible from spot to spot and it is common to obtain external precision that is significantly better than would be predicted from internal precision. For this reason, internal precision may not be a useful measure of data quality. The mean square of weighted deviations (MSWD) is another measure, often used in geochronology that compares the measured SD of a data set to that predicted from the size of the population. A value of 1 indicates that the measured values match the statistics for Gaussian distribution, however this also ignores correlated effects.

The simplest and most direct measure of analytical precision is based on the spot-to-spot reproducibility of multiple analyses of different spots on a homogeneous standard. Since sample analyses need to be bracketed by standards, this provides a repeated measure of data quality during the analysis session. Values can be reported at 1, 2, or 3 SD depending on the desired confidence level. The SE is appropriate only for comparison of average values of multiple analyses.

Crystal Orientation Effects

Crystal orientation effects on the sputtered ion yields of single crystals have been an active field of study for the last 50 years (Robinson & Oen 1963). Channeling takes place when the incident ion beam is parallel to low index directions in the crystal lattice resulting in a reduced probability of ion–atom collisions and thus a lower sputtered yield. Channeling effects have also been found to influence the angular distribution of sputtered particles along low index directions (Wehner 1956). Further, preferential ejection of the sputtered species along low index directions has been attributed to focusing collision sequences where the ejection of surface atoms is due to momentum transport to the surface along closest packed rows of atoms (Silsbee 1957).

Channeling of the primary ion beam along specific planes in the crystal lattice of a mineral has long been proposed as a possible influence on SIMS instrument bias for isotope ratios. Lyon *et al.* (1998) reported a correlation of measured oxygen isotope ratio and crystallographic orientation of magnetite during ion microprobe analysis by Isolab 54. Values of $\delta^{18}O$ varied up to 10‰ upon rotation of a single crystal about [111] through a range of 290°. Huberty *et al.* (2009) investigated the crystallographic effect on bias using an IMS1280 and a sample mount with individual fragments of magnetite in random orientations. Electron backscatter diffraction (EBSD) by SEM was employed to determine the orientation of each grain. By rotation of the mount in the sample holder, the full range of possible orientations could be analyzed. The maximum variation of bias is ~4‰ (*vs*. 10‰ for Isolab) showing that instrumental parameters are important to determine the magnitude of this effect. The smallest bias was obtained when the incident Cs beam was parallel to low index directions, especially along <*hk*0>. These results suggest that it may be possible to minimize the orientation effect further or to make a correction.

For many other minerals, analysis of standard grains in random orientation at WiscSIMS proves that the magnitude of the orientation effect is less than spot-to-spot precision. Minerals for which crystallographic effects on bias have been shown to be less than ±0.5‰ for $\delta^{18}O$ include quartz, K-Na-Ca-feldspar, Mg-Fe ortho- and clinopyroxene, wollastonite, Fe-Ca-Al-Mg-Mn garnet, Mg-Fe olivine, zircon, chromite, $MgAl_2O_4$ spinel, and Ca-Mg-Fe carbonate.

X–Y Effects

Standardization monitors precision and stability of the instrument, and can be the basis of a correction for bias, but there are additional effects and careful standardization alone does not necessarily guarantee accuracy. It has long been suspected that small differences in sample and standard geometry can be significant (*e.g.*, Valley *et al.* 1998, Treble *et al.* 2007, Whitehouse & Nemchin 2009, Kita *et al.* 2009). These differences, herein referred to as X–Y effects, cause minor deflections of the secondary beam and can change the bias in isotope ratio. The IMS1280 compensates

for such differences with a manual Z-focus and by automatically adjusting secondary beam deflectors (DTFA) at the beginning of each analysis. Formerly, this correction was made crudely by hand, but even the improved computer controlled correction is imperfect. X–Y effects degrade precision for samples that are too far from the focusing axis, that have an inclined surface, or that have differences in height such as commonly result from polishing relief. For this reason, standards are mounted at WiscSIMS in the center of each sample and high precision analyses are attempted only within 5 mm of the center of the 25 mm round sample mount. This minimizes X–Y effects to sub 0.3‰-levels for $\delta^{18}O$ (2 SD, Kita *et al.* 2009). Topographic effects are more problematic, especially in samples that vary in hardness.

Figure 2-12 shows zircon grain fragments with relief of ~30 μm that commonly results when hard minerals are cast in softer epoxy and polished. Relief is also common on polished surfaces of rocks containing soft or easily plucked minerals such as carbonates or phyllosilicates. Relief can be monitored by use of a white light profilometer, which rapidly measures the elevation of the sample surface at sub-μm scale. Kita *et al.* (2009) analyzed $\delta^{18}O$ in chips of the homogeneous zircon standard, KIM-5, after a series of polishing steps that systematically reduced the polishing relief. A well polished mount with relief less than one micron yielded spot-to-spot precision of 0.3‰ (2 SD). However, the same zircon grains with more relief yielded less precise and less accurate results. The sample shown in Figure 3-12 produced analytical uncertainties of up to ±3‰ and average values are shifted in $\delta^{18}O$ (Fig. 2-13). These effects may also impact depth profiles for $\delta^{18}O$ and such studies should be evaluated by profiles into homogeneous materials.

Analysis near grain boundaries

Grain boundaries are of special interest in geological studies of growth zoning, alteration, and diffusion (Valley 2001, Desbois *et al.* 2007, Kelly

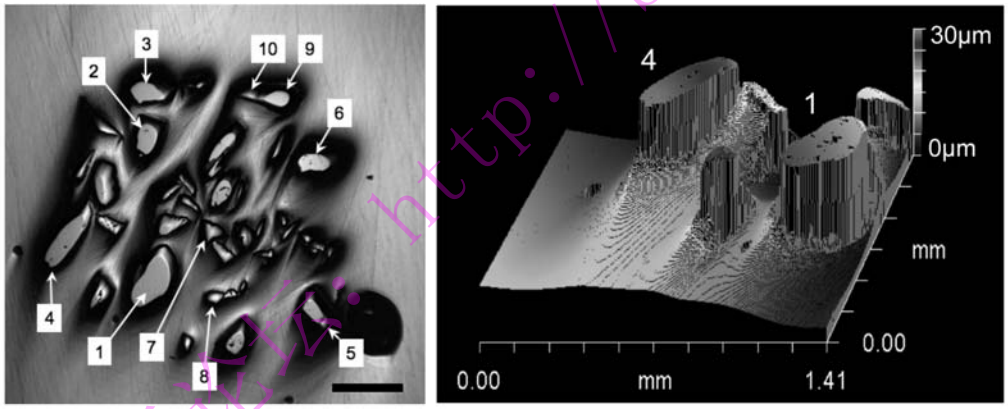


*FIG. 2-12. Zircon grains cast in epoxy showing smooth flat tops and ~30 micrometres of relief due to polishing. **Left:** Zircon grains in reflected light. (Scale = 500 μm). **Right:** Polishing relief measured by white light profilometer. Grains 1 and 4 are the same in both images (from Kita *et al.* 2009).

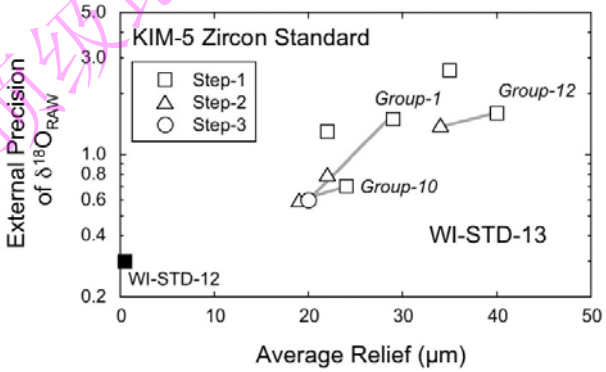


FIG. 2-13. Spot-to-spot reproducibility (2 SD) of SIMS measurements of $\delta^{18}O$ with 10 μm diameter spots in KIM-5 zircon standard grains. The amounts of polishing relief were reduced in three repolishing steps of the same grain mount, which has 13 groups of 100-500 μm chips of the KIM-5. Note that the reproducibility of analyses is shown on the Y-axis as a logarithmic scale. The filled square is from a second mount of KIM-5 with minimized relief (≤1 μm) analyzed during the same session (from Kita *et al.* 2009).

http://bbs.3s001.com/

et al. 2007, Page *et al.* 2007a). However, the impact of relief on instrument bias is greatest for surfaces that are not normal to the secondary beam and especially near the edge of a grain. For many samples, reproducibility is improved by restricting analysis to the cores of grains. For studies of grain boundaries or objects that are too small to avoid regions close to the edge (Eiler *et al.* 2007, Bindeman *et al.* 2008, Kozdon *et al.* 2009) extra care should be taken to minimize relief. Figure 2-14 shows a grain of homogeneous diopside standard cast in epoxy and polished with a minimum of relief (< ~1 μm, Kita *et al.* 2009). Analyses of $\delta^{18}O$(raw) from within 20 μm of the grain boundary (average = 30.53 ± 0.09‰, 2 SE) are identical to analyses ~100 μm from the boundary (average = 30.58 ± 0.08‰) showing that there is no measurable effect for a smooth flat sample with low relief.

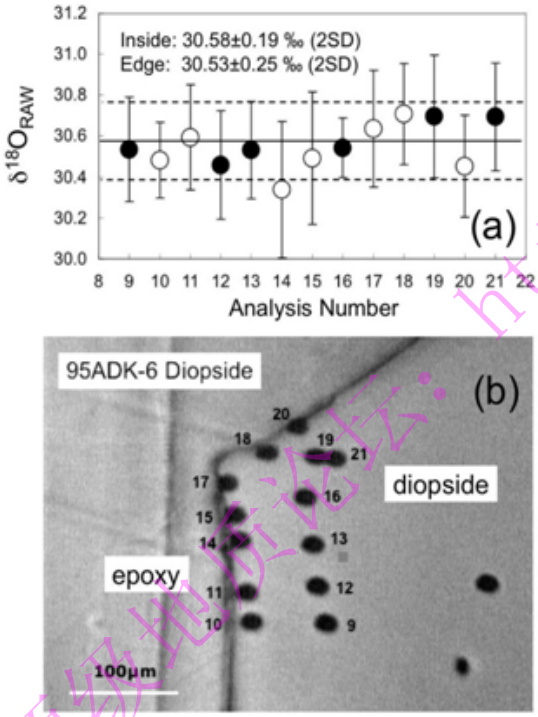


FIG. 2-14. Analyses of $\delta^{18}O$(raw) from the rim of homogeneous diopside, 95ADK-6, showing minimal polishing relief (< ~1 μm). **(a)** Analyses from within 20 μm of the nearest the grain boundary (open circles) and ~100 μm away (solid dots) are indistinguishable with spot-to-spot reproducibility of ±0.22‰ (2 SD) and 2 SE <0.09‰. **(b)** Reflected light image of the grain boundary between diopside and epoxy resin. The positions of the SIMS pits are shown with analysis number (from Kita *et al.* 2009).

QUARTZ OVERGROWTHS AND CEMENTS

Quartz and carbonate cements are ubiquitous in sedimentary rocks, control permeability in water and fossil fuel reservoirs, and record evidence of diagenetic history. Determining the timing, genesis, and geometry of cements is critical for extraction of natural resources, and for long-term sequestration of CO_2 and other industrial waste. There are several approaches to disaggregate quartz-cemented sandstone so that its constituent parts can be analyzed conventionally, however *in situ* analysis has shown such bulk samples to be mixtures not accurately reflecting the actual compositions (Graham *et al.* 1996). Ion microprobe analysis provides the means to resolve detrital grains *vs*. thin quartz overgrowth cements and to measure zoning among different generations of cement (Hervig *et al.* 1995, Graham *et al.* 1996, Williams *et al.* 1997a,b, Schieber *et al.* 2000, Lyon *et al.* 2000, Girard *et al.* 2001, Chen *et al.* 2001, Marchand *et al.* 2002, Alexandre *et al.* 2006, Kelly *et al.* 2007). Robert & Chaussidon (2006) correlated *in situ* analyses of $\delta^{18}O$ and $\delta^{30}Si$ in Precambrian chert to estimate Precambrian seawater temperatures. Carbonate cements are also well suited to *in situ* analysis (Riciputi *et al.* 1994, Mahon *et al.* 1998, Fayek *et al.* 2001); instrument bias can be corrected if chemical composition is determined for each spot by EMPA (Valley *et al.* 1997).

Mudstone

Mudstone is the most voluminous sedimentary rock type and the largest reservoir of high $\delta^{18}O$ material in the crust. The primary components are clay-size particles, including quartz that is generally thought to be detrital. Schieber *et al.* (2000) examined quartz silt grains from late Devonian shale of the eastern U.S. by CL imaging (Fig. 2-15) and ion microprobe analysis of $\delta^{18}O$. Grains texturally identified as detrital have $\delta^{18}O$ values averaging 9.4 ±3.0‰ (2 SD), consistent with igneous or metamorphic quartz (see also Aleon *et al.* 2002 for windblown aerosol quartz). Grains suggested to be quartz cement have much higher $\delta^{18}O$ values of 28.4 ± 2.0, confirming a low temperature diagenetic origin. Failure to recognize that up to 100% of the quartz in a mudstone formed *in situ* could lead to significant errors in interpretation of sedimentology, paleoproductivity, and biogeochemical cycling of silica (Schieber *et al.* 2000). Large amounts of high $\delta^{18}O$ diagenetic quartz would also suggest that variability of the $\delta^{18}O$ values of mudstones results in part from

http://bbs.3s001.com/

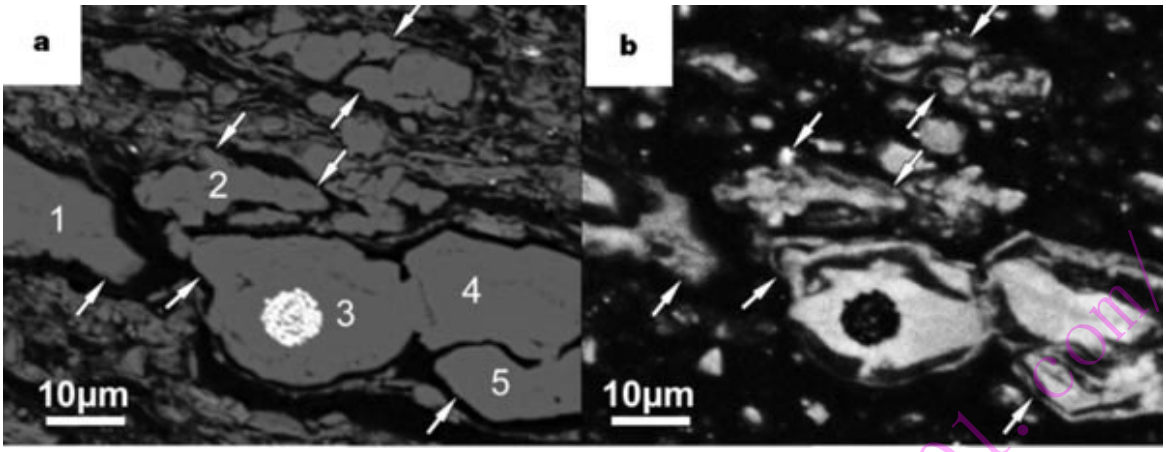


FIG. 2-15. Quartz grains in mudstone. **(a)** BSE image of quartz grains that are grey with uniform surfaces. **(b)** Cathodoluminescence (CL) image of the same area. Arrows show embayments and projections that suggest these quartz grains formed *in situ* as diagenetic cyst fills. Both larger and smaller grains show zoning in CL, further suggesting an *in situ* origin. Ion microprobe analysis shows that quartz silt has high $\delta^{18}O$ values, confirming the *in situ* diagenetic origin, and demonstrating almost complete absence of detrital quartz in this sample. Grain 3 contains a pyrite framboid (from Schieber *et al.* 2000).

differences in diagenesis and is not solely due to weathering.

St. Peter Sandstone

In the Ordovician St. Peter Sandstone of SW Wisconsin (Fig. 2-16), syntaxial quartz overgrowths are a minor component of poorly lithified rocks (Fig. 2-17). Because the lower Paleozoic sedimentary rocks of the Wisconsin Dome were never buried deeper than 1 km, the genesis of these optically continuous overgrowths has been uncertain (Graham *et al.* 1996, Chen *et al.* 2001). While pressure solution is extensive and causes thick overgrowths in samples that are deeply buried in the adjacent Michigan or Illinois basins, the shallow samples from SW Wisconsin show only trace evidence of pressure solution (arrow in Fig. 2-17) and other processes of overgrowth formation must be sought. It is widely thought that temperatures above 80°C are required to form

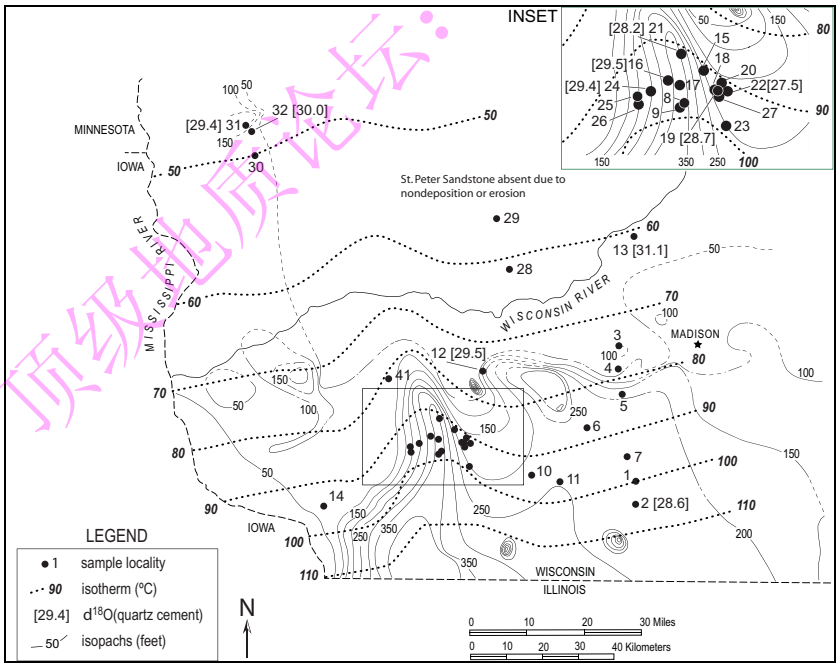


*FIG. 2-16. Isopachs of Ordovician St. Peter sandstone in SW Wisconsin. Deposits of the Upper Mississippi Valley Pb-Zn district are concentrated in dolomite above thicker sandstone domains, which are marked by the cluster of sample localities (filled dots) for which quartz overgrowths were studied by ion microprobe. Isotherms were modeled by Arnold *et al.* (1996) for heating of shallow sandstone by northward migrating Illinois Basin brines believed responsible for deposition of MVT base metals (from Kelly *et al.* 2007).

顶级地质论坛 http://bbs.geo1.com/

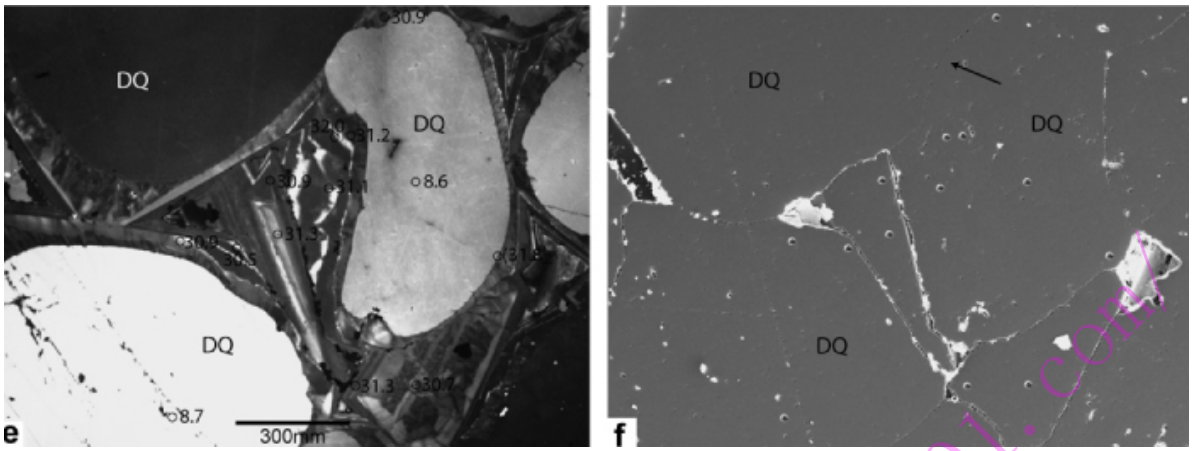


FIG. 2-17. Cathodoluminescence image (CL, left) showing complex quartz overgrowth textures and matching secondary electron images (SE, right). Ion microprobe pits are shown as circles in CL and as depressions in SE. DQ = cores of detrital quartz grains. Values of $\delta^{18}O$ are shown on CL image. Pore space is largely occluded by quartz cement as seen on right. An arrow points to minor pressure solution (compare SE and CL) that is not sufficient to generate cements. Scale bar = 300 μm (from Kelly *et al.* 2007).

quartz cement rather than opaline or fibrous silica, and burial depths in SW Wisconsin were never great enough to reach such temperatures at a normal geotherm. However, temperatures reached 100°C locally due to northward expulsion of ore-forming brines from the Illinois Basin into the Upper Mississippi Valley MVT–Pb–Zn District (Fig. 2-16). The St. Peter sandstone and underlying Cambrian sandstone units were aquifers for these brines and the ambient temperatures are estimated to have varied systematically from 110°C in the south to 50°C further north (Fig. 2-16, Arnold *et al.* 1996).

Did quartz overgrowths form during the MVT hydrothermal event and thus provide a record of regional fluid flow? Oxygen isotope ratios of the overgrowths provide a clear test of this hydrothermal model; variable temperatures of 110 to 50°C would cause $\delta^{18}O$(quartz) to change systematically by 9‰. Fig. 2-18 shows that $\delta^{18}O$ of detrital quartz cores (10.0 ±1.4‰, 1 SD) are distinct from quartz overgrowths (29.3±1.0‰, 1 SD) for 10 samples from SW Wisconsin. A small number of analysis pits with intermediate values were seen by post-analysis SEM imaging to have hit the boundaries of core and overgrowth. The constant value of $\delta^{18}O$(overgrowth) for samples distributed over a wide area indicates uniform conditions of

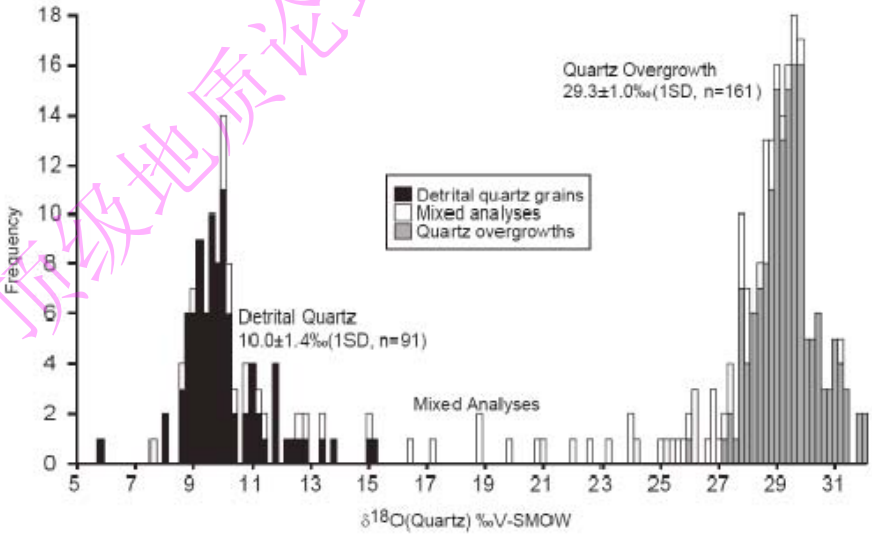


FIG. 2-18. Histogram showing the frequency of $\delta^{18}O$ for detrital quartz grains and quartz overgrowths in St. Peter sandstone measured from 10 μm spots at WiscSIMS. Mixed analyses hit overgrowth boundaries. All samples are from SW Wisconsin and SE Minnesota (from Kelly *et al.* 2007).

顶级地质论坛：http://bbs.3s001.com/

precipitation for all overgrowths and is not consistent with formation at variable temperatures during northward migration of Illinois Basin brines. Instead, the ion microprobe data suggest low temperature formation of overgrowths as silcrete. Apparently, syntaxial quartz can form at low temperatures (<40°C) in clean quartz arenite like the St. Peter Sandstone. In rocks containing clay minerals and glass, high degrees of supersaturation cause rapid precipitation of fibrous or hydrous silica. In contrast, clean quartz arenite is a nearly monomineralic rock, and slow equilibrium growth of quartz is possible at lower temperatures (Kelly *et al.* 2007).

FISH OTOLITHS

Fish otoliths are $CaCO_3$ ear stones, which record water conditions in daily growth bands (Fig. 2-19). Values of $\delta^{18}O$ respond to changes in temperature and indirectly to water chemistry (Campana 1999). Values of $\delta^{13}C$ are affected by temperature, diet, and dissolved inorganic carbonate, DIC. Weidel *et al.* (2007) studied 3 mm long otoliths from bluegill in Crampton Lake, Wisconsin, that underwent a 56-day experiment when $NaH^{13}CO_3$ was added to the lake to raise $\delta^{13}C$(DIC) in order to estimate the ratio of allochthonous to autochthonous nutrients (Pace *et al.* 2007). A rapid response of $\delta^{13}C$(otolith) to addition of this label shows that DIC is the dominant source of carbon in the otolith and not diet as previously thought (Weidel *et al.* 2007). In another study of nine larger otoliths from Pacific cod in the Gulf of Alaska, consistent 4‰ trends in $\delta^{18}O$ record a ~10-year migration history from shallow, warmer, possibly fresher (low $\delta^{18}O$), water to cold deeper water and back (Fig. 2-20). Thus, these otoliths are "flight recorders" of temperature and water composition through the life of the fish. Older otoliths at the same site have systematically higher "shallow water" $\delta^{18}O$ values consistent with lower temperatures during the Little Ice Age (A. Crowell & J. Valley, unpublished). The capability to measure such detailed stable isotope records presents as yet unexploited opportunities to decipher the provenance, migration history, diet, and age of fish, as well as paleoclimate.

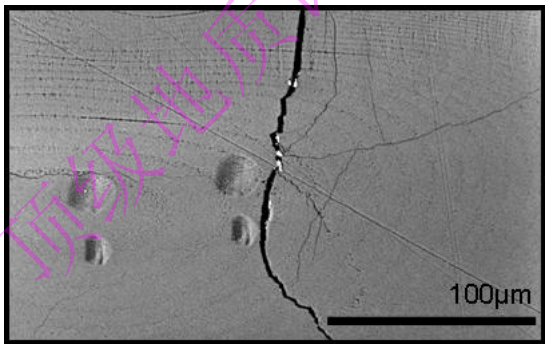


FIG. 2-19. SEM image of SIMS analysis pits for $\delta^{18}O$ (upper) and $\delta^{13}C$ (lower) in a Bluegill otolith from Crampton Lake, Wisconsin. Daily growth bands are resolved by single analyses (from Weidel *et al.* 2007).

FORAMINIFERA

Foraminifera are important calcifiers in the ocean, and their oxygen isotope ratios provide the most important and widely applied marine proxy of paleoclimate. However, because of small size and complexity, foraminifera present an analytical challenge. They do not necessarily precipitate their tests in equilibrium with seawater and the interpretation of paleoclimate requires a correction to data for vital effects. Fig. 2-21(left) shows the range of vital effects for $\delta^{18}O$ estimated for *N. pachyderma* (sin.) from conventional bulk analyses, expressed as [$\delta^{18}O$(foram) – $\delta^{18}O$(equilibrated calcite)] for the $\delta^{18}O$ and temperature of ambient seawater. Most of the paleoclimate record is based on analysis of pooled samples of many hand-picked organisms; some studies report data for single tests. It is implicitly assumed that these are homogeneous samples. However, foraminifera precipitate micrometre-scale layers during growth (Fig. 2-21, right) and some species precipitate calcite by more than one mechanism (Erez 2003). While it is common practice to apply a constant species-dependent vital effect to correct oxygen isotope ratios in foraminifera for paleoclimate and other applications, the range of values (Fig. 2-21, left) and complex internal structure (Fig. 2-21, right) suggest that foraminifera might be more complex. Only a handful of studies have investigated biogenic zoning of $\delta^{18}O$ by SIMS analysis of foraminifera (Rollion-Bard *et al.* 2008, Kozdon *et al.* 2009), corals (Rollion-Bard *et al.* 2004, 2008, Blamart *et al.* 2006), or conodonts (Trotter *et al.* 2008). The potential for new discoveries is high.

Kozdon *et al.* (2009) studied vital effects in *N. pachyderma* (sin.) collected live from the North Atlantic in net catches and shallowly buried in mud

http://vbook.ssdl.com/

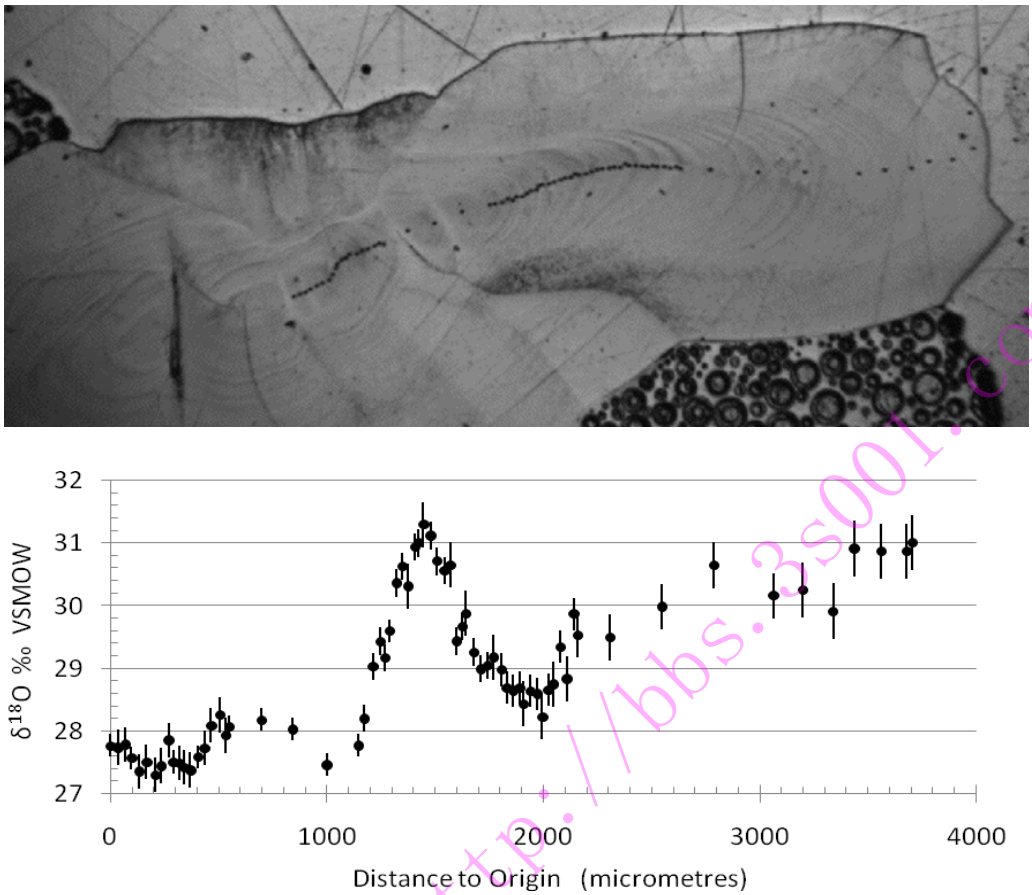


FIG. 2-20. **Upper:** SEM view of a Pacific cod otolith from Aialik Bay, Gulf of Alaska with 69 analyses spanning the ~10 year life of the fish. Field of view = 5 mm. **Lower:** Values of $\delta^{18}O$ vary by 4‰ due to movement from shallow, possibly freshened, waters (lower $\delta^{18}O$) to deeper colder water (high $\delta^{18}O$). Data are from A. Crowell and J. Valley (unpublished).

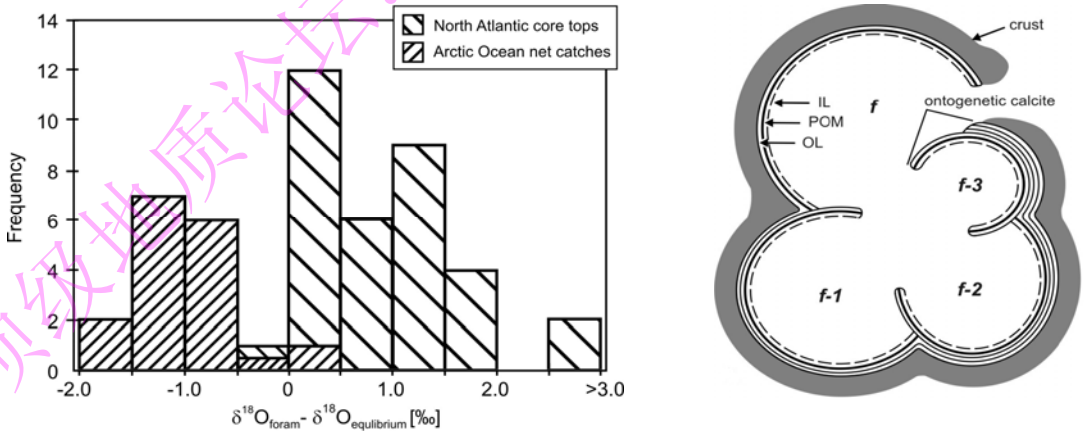


FIG. 2-21. **Left:** Histogram showing the range of vital effects in *N. pachyderma* (sin.) based on conventional bulk analyses. Values of $\delta^{18}O$(equilibrium) are calculated using the temperature and $\delta^{18}O$ of ambient seawater. **Right:** Schematic view of the *N. pachyderma* test (ca. 300μm dia.). Every time a new chamber is formed, the test is covered with a layer of calcite. The inner (IL) and outer (OL) calcareous layers are precipitated during the organism's ontogenetic development whereas the outer crust, which can contribute over 70% of the total test weight, is secreted near the end of life (from Kozdon *et al.* 2009).

质级地质论坛 http://bbs.3s001.com/

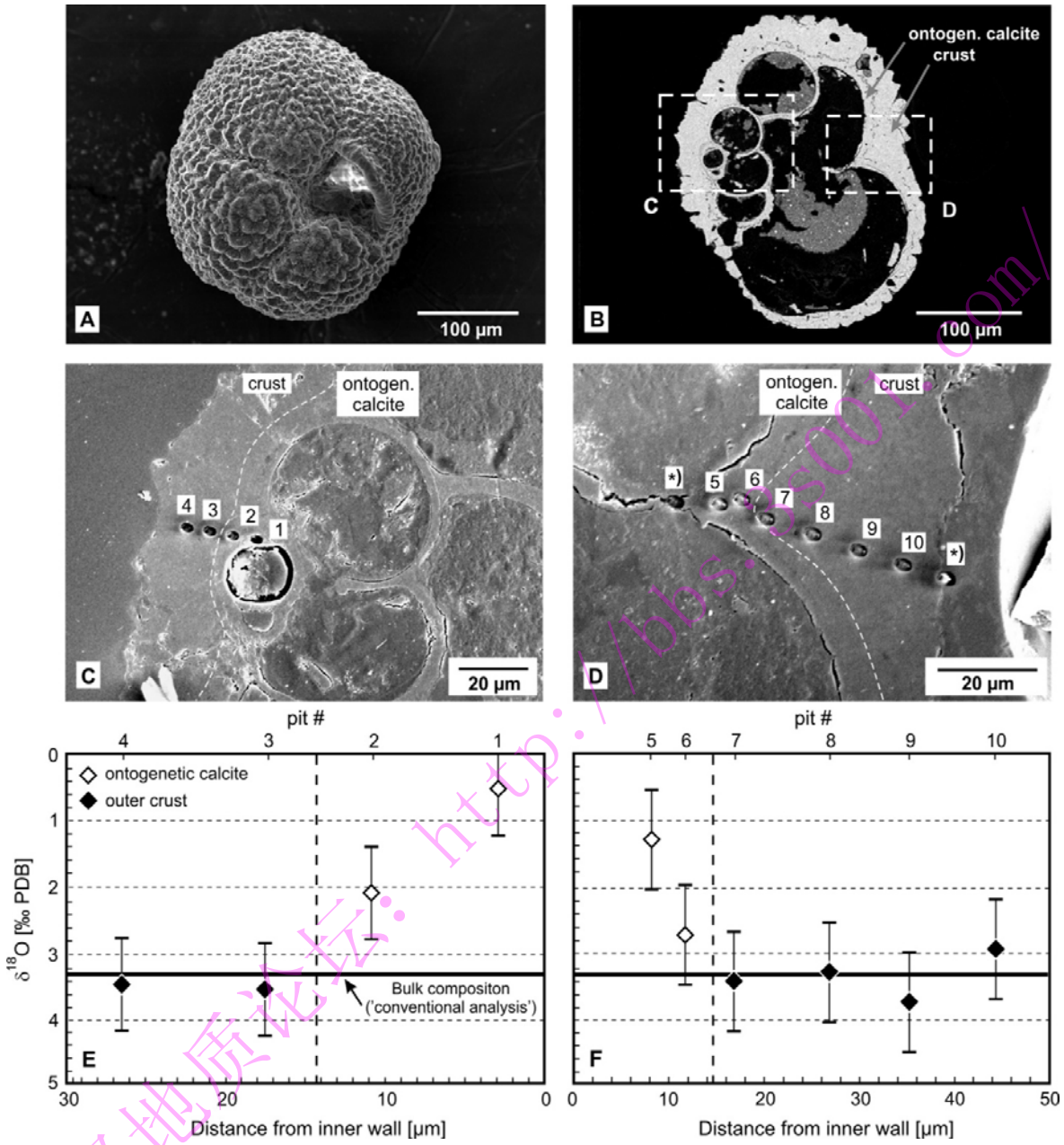


FIG. 2-22. **(A, B)** SEM images of an encrusted *N. pachyderma* test and a polished cross-section. Areas filled by epoxy are black in B, and dark grey in C and D. **(C, D)** SEM images of the gold-coated sample showing ion microprobe pits from traverses of early chambers and crust. Pits measure 2 x 3 µm. **(E, F)** Corresponding $\delta^{18}O$ values are arranged by distance from the inner chamber wall. Error bars are ±2 SD. Conventional bulk data (Simstich *et al.* 2003) represent analyses of multiple tests mixed together from the same size fraction (125-250 µm) as this sample (from Kozdon *et al.* 2009).

from the top of a piston core. Water chemistry and temperature of growth is known for these samples and diagenesis can be ruled out. Single tests ("shells") were cast in epoxy, polished to midsection, imaged by SEM, and analyzed for $\delta^{18}O$ by IMS1280 at WiscSIMS. Using a ~3 µm diameter beam, it was possible to make traverses of the walls of foraminifer tests with precision of ±0.7‰ (2 SD), which is sufficient to prove consistent zonation of 2–3‰ in $\delta^{18}O$ (Fig. 2-22). Significantly, these data show that *N. pachyderma* precipitates calcite by two different mechanisms and neither is in isotopic

http://bbs.3500.com/

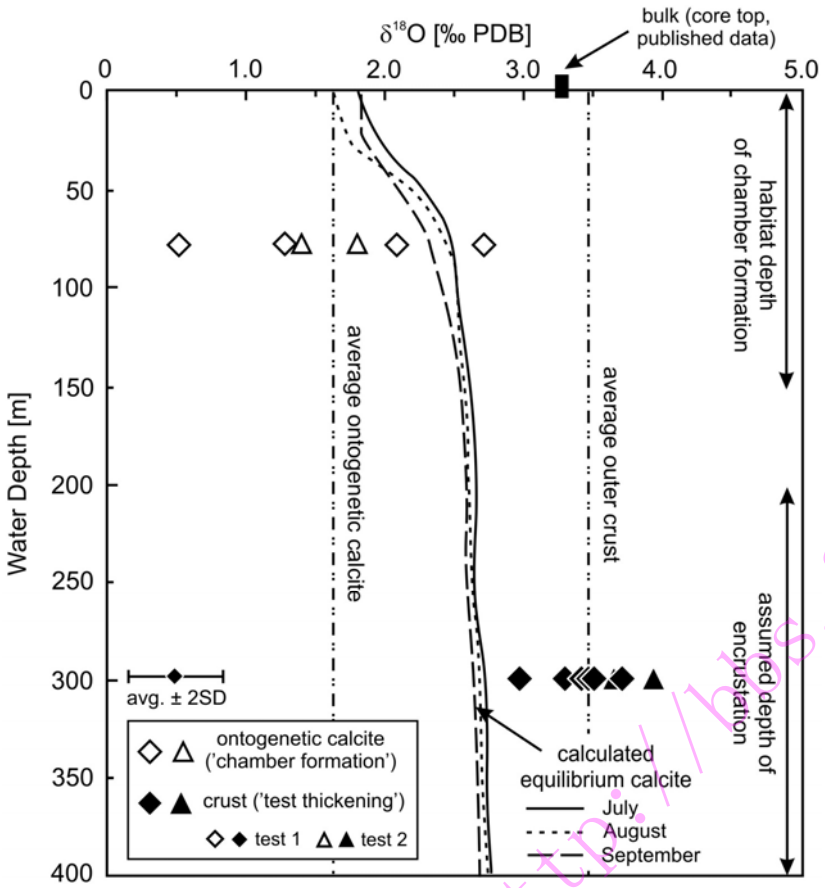


FIG. 2-23. Values of $\delta^{18}O$ from 2–6 μm spots in the ontogenetic calcite and outer crust from two individual tests of *N. pachyderma* (sin.) from the top of piston cores in North Atlantic sediments plotted against water depth and the calculated equilibrium $\delta^{18}O$(calcite) during the main planktonic bloom. Depth intervals for chamber formation and encrustation are based on plankton tow studies. Values of $\delta^{18}O$(crust) are similar to published 'whole test' data from bulk foraminiferal analysis, indicating a high degree of encrustation at this location (from Kozdon *et al.* 2009).

equilibrium with ambient seawater (Fig. 2-23). The inner ontogenetic calcite layers, precipitated during the growth of each new chamber, show a negative vital effect, while the crust, formed at the end of life, has a positive vital effect. Thus, there are two different vital effects with opposite signs that tend to cancel each other. The value of $\delta^{18}O$ obtained by a bulk analysis of one test is the average and could vary by up to 2‰ depending on the percentages of inner ontogenetic layers *vs.* crust. Failure to recognize this zonation could lead to incorrect conclusions. For instance, events that stress or alter the life cycle could be misinterpreted as temperature change.

SPELEOTHEMS

Speleothems are widely studied as a proxy of paleoclimate. Such carbonates are typically sampled by dental drilling at mm-scale, dated by U-series, and analyzed for $\delta^{18}O$ and $\delta^{13}C$ with the phosphoric acid technique. Recently, studies by ion microprobe have increased spatial resolution for oxygen isotope ratio to 20 μm (Kolodny *et al.* 2003, Treble *et al.* 2005, 2007, Fairchild *et al.* 2006) and to 10 μm (Orland *et al.* 2009).

Speleothems from Soreq Cave, Israel preserve a continuous isotopic record of the past 185,000 years (Bar-Matthews *et al.* 2003). Orland *et al.* (2009) imaged a stalagmite from Soreq Cave dated at 2.2 to 0.8 ka and analyzed $\delta^{18}O$ with a 10 μm spot at WiscSIMS. While previous 0.5 mm drill studies resolved decade to century scale climate variation, the ion microprobe analyses resolve seasonality with multiple spots within single years of speleothem growth. Figure 2-24 shows a section of the traverse dated at ~1.65 ka. This high-resolution record was measured in 10 mm cubes of sample cast in epoxy with calcite standard (Fig. 2-9). Before ion microprobe analysis, the polished sample was imaged by confocal laser fluorescent microscopy, which revealed concentric growth bands with gradational bright to dark fluorescence (Fig. 2-24). Oxygen isotope analysis demonstrates that these bands are annual and shows a consistent asymmetric pattern with lowest $\delta^{18}O$ at the beginning of each band (light-colored fluorescence, interpreted to be the annual wet season) grading upwards to higher values in dark calcite (interpreted

to be the annual dry season, Fig. 2-24). The difference in $\delta^{18}O$(calcite) between the lightest and darkest portion of each couplet, $\Delta^{18}O$(dark-light), is interpreted to reflect seasonality, with small $\Delta^{18}O$ values corresponding to dry years (Orland *et al.* 2009). This measure of seasonality correlates with estimates of annual rainfall based on $\delta^{18}O$(calcite) and with lake levels in the Dead Sea (Fig. 2-25). Taken together, these results indicate a long term drying of the climate, punctuated by droughts, from ca. 100 to 600 AD, which correlates with the period of decline and eventual defeat of the Roman and Byzantine empires in the Levant.

METAMORPHIC AND HYDROTHERMAL SYSTEMS

A number of classic questions in metamorphic petrology and mineral reaction kinetics can be studied by *in situ* analysis of stable isotope ratios. Oxygen isotope thermometry was one of the earliest applications of stable isotope geochemistry, however in metamorphic rocks thermometry has been plagued by difficulties and erroneous results (*e.g.*, Valley 2001). Just as petrologic thermometry only became viable once the electron microprobe was developed, isotope thermometry has been handicapped by the inability to make *in situ* measurements at the appropriate scale. Sub-millimetre scale heterogeneity of $\delta^{18}O$ can represent growth zoning preserved in minerals with slow oxygen diffusion, retrograde exchange in minerals with faster diffusion, or a variety of non-diffusive processes. The competing rates of diffusion and surface reaction are different for each mineral in a rock (Cole & Chakraborty 2001). In a purely diffusive system, minerals metamorphosed below their closure temperature for oxygen diffusion, such as garnet (Kohn *et al.* 1993, Kohn & Valley 1994, Jamtveit & Hervig 1994, Crowe *et al.* 2001, Vielzeuf *et al.* 2005b, Page *et al.* 2009), zircon (Peck *et al.* 2003, Page *et al.* 2007a, Lancaster *et al.* 2009), and monazite (Breecker & Sharp 2007), will preserve compositions from the time of crystallization and may preserve growth zoning of $\delta^{18}O$. Conversely, at temperatures above closure, minerals exchange with other "open" minerals and

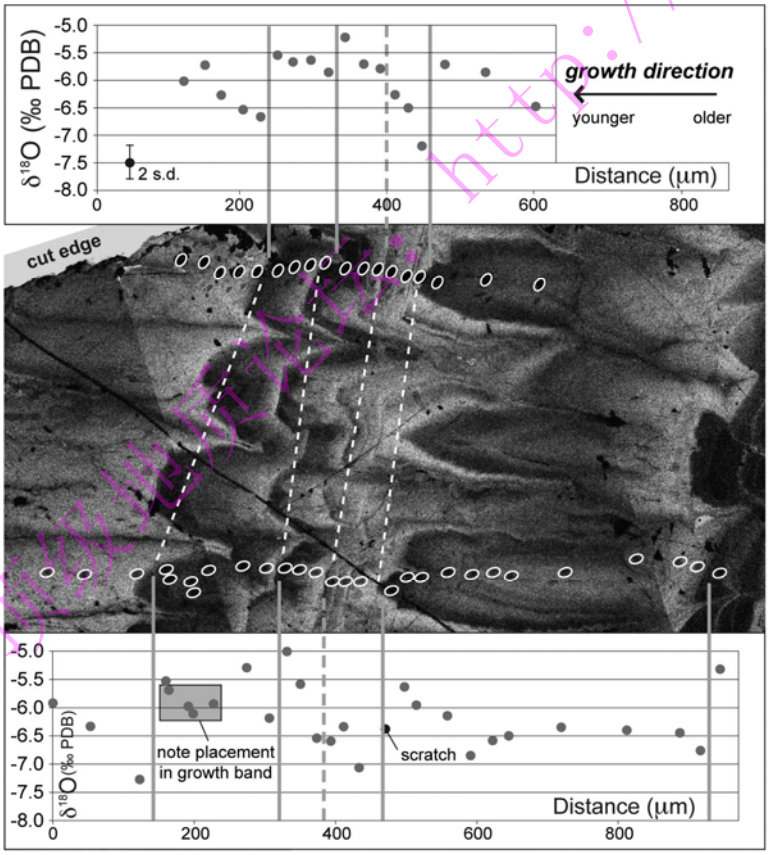


*FIG. 2-24. Fluorescent image of a 1 mm section of speleothem from Soreq Cave, Israel produced by laser confocal microscopy for several annual light-dark couplets dated *ca*. 1.65 ka. Ion microprobe analysis pits (IMS1280), 10 µm in diameter, are highlighted with ovals. Plots of two parallel 500-800 µm-long ion microprobe traverses show a good correlation of $\delta^{18}O$ (PDB) variation and growth bands. Growth is from right to left. Values of $\delta^{18}O$ show a consistent, saw-tooth asymmetry; they are lowest during the winter rainy season (bright fluorescence) and gradually increase during the dry season as fluorescence darkens (from Orland *et al.* 2009). Color version available at http://www.mineralogicalassociation.ca/index.php?p=160

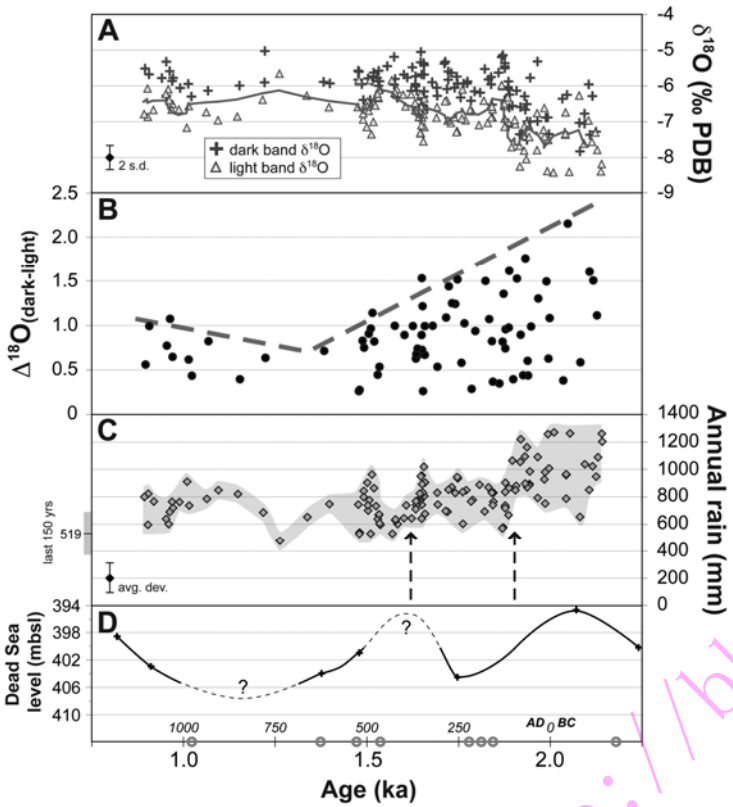


*FIG. 2-25. **(A)** Values $\delta^{18}O$(calcite) measured by ion microprobe for wet (light fluorescent band) and dry (dark band) season growth across a speleothem from Soreq Cave, Israel. Higher $\delta^{18}O$ values represent drier years and lower $\delta^{18}O$ values are wetter years. The line shows the general variability of $\delta^{18}O$ from 2.2–0.9 ka. **(B)** Values of $\Delta^{18}O_{dark\text{-}light}$ ($= \delta^{18}O_{dark\ cc} - \delta^{18}O_{light\ cc}$) for single annual bands show a decrease in maximum values of $\Delta^{18}O$ from 2.0–1.3 ka. **(C)** Estimates of annual precipitation (mm/y) calculated from the measured $\delta^{18}O$ of wet season calcite. Sharp decreases occur at ~1.9 and 1.6 ka (arrows). **(D)** Changes in lake level of the Dead Sea. Circles along the age-axis represent U-series dates for this sample (from Orland *et al.* 2009). Color version available at http://www.mineralogicalassociation.ca/index.php?p=160

any fluids. During cooling, such minerals are predicted to preserve diffusion profiles as a function of cooling rate (Eiler *et al.* 1993). However, a number of complexities are possible, including multiple heating events, localized recrystallization, micro-veining, and fast pathways for diffusion (Valley 2001, Watson & Baxter 2007). Microanalysis offers the possibility to distinguish such complex situations so that they may either be studied in detail, or avoided, according to the goals of a study (Fig. 2-26). Such studies will aid in the refinement of models of reactive metamorphic fluid flow that are based on stable isotope data and idealized assumptions about mineral exchange (Baumgartner & Valley 2001, Lüttge *et al.* 2004, Ague 2007, Watson & Baxter 2007, Bowman *et al.* 2009).

Bowman *et al.* (2009) studied layered marble near the contact of the Alta Stock in Little Cottonwood Canyon, Utah. Previous studies show that crystallization of periclase was driven by infiltration of water-rich fluids from the stock and that flow was concentrated in specific layers that are low in $\delta^{18}O$ (Cook & Bowman 2000). Sharp gradients in $\delta^{18}O$ (>6‰/10 cm, Fig. 2-27) are seen between these layers, but it was previously uncertain whether these gradients represent a metasomatic "front" or the "side" of a flow system, and if isotopic exchange was via volume diffusion in calcite or recrystallization. The ion microprobe data shown in Figure 2-27 test these questions. Individual crystals of calcite are not zoned in $\delta^{18}O$ indicating that marble was recrystallized during fluid flow parallel to layering. These Alta rocks show fundamentally different processes and scales of exchange than marble studied by Graham *et al.* (1998) from a polymetamorphosed contact aureole in the Hida Belt, Japan. The sample of Hida marble shows calcite with purple cathodoluminescence (CL) overprinted locally by yellow CL along grain boundaries, fractures, deformation lamellae, and replacement patches. The yellow CL domains are systematically lower in $\delta^{18}O$ by up to 15‰, with 200-300 μm wide gradients, which apparently formed by diffusion during infiltration of magmatic fluids. These differing conclusions illustrate important differences in process and support the use of reactive transport models that assume local equilibrium of fluids and calcite at Alta, but not at Hida.

A number of ion microprobe studies have documented sharp gradients in $\delta^{18}O$ due to hydro-

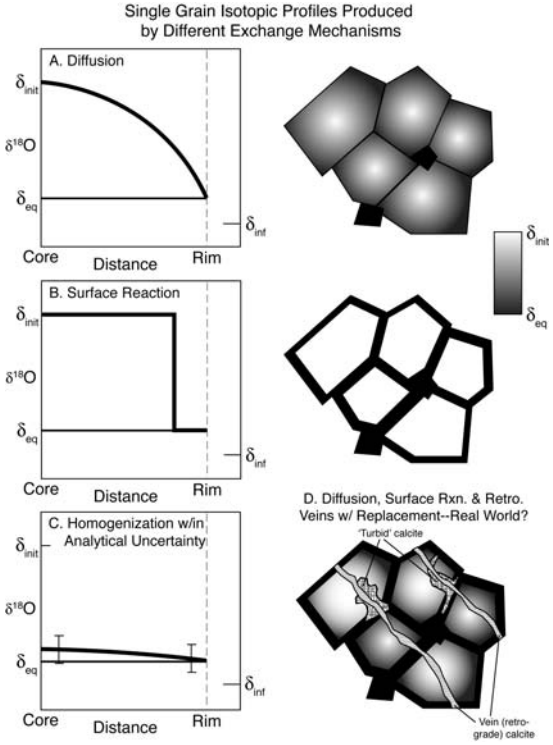


FIG. 2-26. Schematic profiles of $\delta^{18}O$ across a mineral grain that would result from exchange between the grain (δ_{init}) and an isotopically distinct grain-boundary fluid (δ_{inf}). **(A)** Diffusion only. **(B)** Surface Reaction (dissolution-reprecipitation) only. **(C)** Attainment of equilibrium (thin line, δ_{eq}) and equilibration to within analytical uncertainty (heavy line). Note that profiles could be composite, exhibiting effects of both diffusion and surface reaction, and that later events can be locally superimposed on the rock. *In situ* analysis is required to test these possibilities (from Bowman *et al.* 2009).

thermal alteration. Thin millimetre-scale amphibole veins in gabbro from a fast-spreading ocean ridge (Hess Deep) are bounded by sub-millimetre gradients of $\delta^{18}O$ in plagioclase and diffusion modeling suggests that they formed in less than 100 years (Coogan *et al.* 2007). Allan & Yardley (2007) compared cathodoluminescence imaging with analysis of fluid inclusions, trace elements and $\delta^{18}O$ in hydrothermal quartz from Mt. Leyshon, Australia. Oscillatory-zoned quartz grains vary systematically by up to 14‰ in $\delta^{18}O$ due to temperature changes from 650 to 280°C. Valley & Graham (1996) studied quartz from sub-volcanic Maol na Gainmhich granite, Isle of Skye, including one phenocryst that varies from magmatic values of $\delta^{18}O = +10$ to altered values of –3‰ over a distance of 400 μm due to crack-controlled infiltration of high temperature meteoric water. Mora *et al.* (1999) measured gradients up to 14‰ over 600 μm with $\delta^{18}O$ as low as –16‰ in feldspars of the Boehls Butte anorthosite also due to heated meteoric water. They inferred a chemical quench to oxygen diffusion due to rapid drying of retrograde fluids. Cole *et al.* (2004) also found gradients up to 15‰ within single crystals of plagioclase that were hydrothermally altered at Rico, Colorado. A coupled reaction–diffusion model suggests that high temperature fluids were active for 100–300 ka, while magma was present, and that circulation of 150–200°C waters continued for over a million years. These studies offer preliminary insight into a range of processes that regulate fluid flow, mineral exchange, and associated transfer of mass and heat preserved in the mineralogical record over very small length scales that without the ion microprobe would never have been observed.

GEM MINERALS

The genesis, mining locality, and trade routes of precious and semi-precious minerals is of interest for geological, historical and political reasons. Analysis by ion microprobe is preferred because of the small sample requirements (a 10 μm pit is invisible to the naked eye), and a number of studies have employed *in situ* oxygen isotope analysis to establish a "source fingerprint". Giuliani *et al.* (2000) studied $\delta^{18}O$ in emeralds from Roman to 18th century artifacts and found a 17‰ range in $\delta^{18}O$. They concluded that in antiquity emeralds from Pakistan and Egypt were traded by the Silk Route, and that after the 16th century, Colombian emeralds were traded across the Atlantic and Pacific. Likewise, *in situ* analysis of $\delta^{18}O$ combined with δD in turquoise differentiates among different mining districts and helped establish historical trade routes in pre-Columbian Mesoamerica (Fayek *et al.* 2002b).

A number of studies have shown that bulk values of $\delta^{18}O$ vary by up to 20‰ in rubies and sapphires, and thus $\delta^{18}O$ is an indicator of geological source (Giuliani *et al.* 2005, 2006, Zaw *et al.* 2006, Yui *et al.* 2005). While zoning of $\delta^{18}O$ is known from sapphire (Upton *et al.* 1999) and oxygen isotopes are readily analyzed by SIMS in corundum (Mariga *et al.* 2006), *in situ* analysis does not appear to have been applied yet to gem quality material.

Gem minerals are also studied for petrologic

http://bbs.ssoo.com

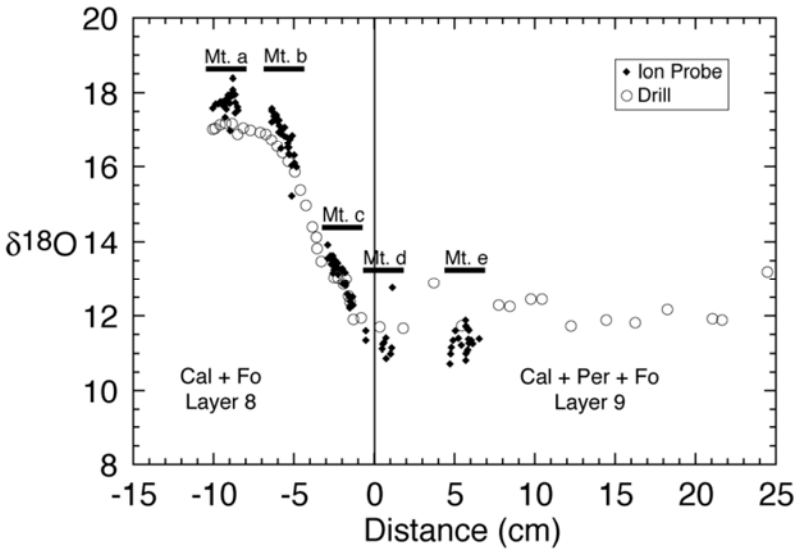


FIG. 2-27. Profile of $\delta^{18}O$(calcite) across the boundary of low $\delta^{18}O$ periclase-bearing marbles that were conduits for flow of magmatic fluids in the Alta Stock Aureole, Utah. Analyses by ion microprobe (solid diamonds, 10 μm spot) from 5 polished mounts (bars) show similar average values, but more variability, in comparison to larger samples obtained by dental drill (open circles, mm-scale) that inevitably mix larger domains, including late turbid calcite that is seen along grain boundaries (from Bowman *et al.* 2009).

reasons. Zoning of $\delta^{18}O$ varies with sequence of precipitation among different generations of jadeite that luminesce red, green, or blue by CL indicating multiple sources of jade-forming fluids during high pressure metamorphism (Sorenson *et al.* 2006). The composition of silicate inclusions within diamonds (DIs) varies by over 10‰ in $\delta^{18}O$. The highest $\delta^{18}O$ DIs are 50–100 μm coesite grains with $\delta^{18}O$ values up to 16.9‰, exceeding the highest value found in mantle xenoliths by up to 7‰ (Schulze *et al.* 2003). These high values are not in equilibrium with minerals of the host eclogite, yet the stability of coesite indicates that these unusual oxygen isotope compositions existed in the mantle and thus were armored by surrounding diamond. High $\delta^{18}O$ coesite DIs are found in highly zoned, low $\delta^{13}C$ eclogite diamonds, and a negative correlation of $\delta^{18}O$(coesite) and $\delta^{13}C$(diamond) indicates that subducted sediment is the ultimate source (Schulze *et al.* 2004).

ZIRCON

Zircon U-Pb geochronology provides the most robust and commonly applied ages in many Precambrian and younger terranes. *In situ* analysis of multiple geochemical systems in igneous and metamorphic zircon can directly link crystallization age to the compositions of coexisting minerals and melts, and provides constraints on the genesis and protoliths of host rocks. The ability to image growth zoning, inherited cores, and overgrowths (Figs. 2-28 and 2-35), as well as damaged domains and inclusions, facilitates the study of single zircon grains (Corfu *et al.* 2003, Valley 2003, Cavosie *et al.* 2006) and graphically demonstrates the importance of *in situ* analysis.

Because of the small volume of sample required for one ion microprobe analysis, multiple measurements can be made within single growth zones of a zircon to correlate age to other isotope systems ($\delta^{18}O$, $\delta^{7}Li$, εHf) or trace elements (REEs, Ti) (Cavosie *et al.* 2005, 2006, 2007, 2009, Booth *et al.* 2005, Martin *et al.* 2006, 2008, Kemp *et al.* 2006, 2007a, b, 2008, Hawkesworth & Kemp 2006a, b, Schmitt 2006, Schmitt *et al.* 2007, Bindeman *et al.* 2008, Page *et al.* 2007b, Trail *et al.* 2007, Schmitt & Hulen 2008, Fu *et al.* 2008, Moser *et al.* 2008, Appleby *et al.* 2008, Wilde *et al.* 2008, Ushikubo *et al.* 2008, Ickert *et al.* 2008, Cates & Mojzsis 2006, Pietranik *et al.* 2008, Harrison *et al.* 2008, Liu *et al.* 2009, Lancaster *et al.* 2009).

Other U-bearing minerals are more readily exchanged, allowing correlation of alteration events to *in situ* geochronology. Uraninite and coffinite are zoned at sub-millimetre scale with low values of $\delta^{18}O$ (to –33.9‰) due to low temperature interaction with meteoric water in the Cigar Lake deposit (Fayek *et al.* 2002a). Likewise, uraninite in shallow natural fission reactors at Oklo has lower $\delta^{18}O$ than the deeper reactor zones due to alteration by meteoric waters (Fayek *et al.* 2003). Monazite in hydrothermally altered sedimentary rocks of the Birch Creek contact aureole yields the same age and $\delta^{18}O$ as in the pluton, showing that they recrystallized, in contrast to unaltered detrital monazite in the same sedimentary rocks (Ayers *et al.* 2006).

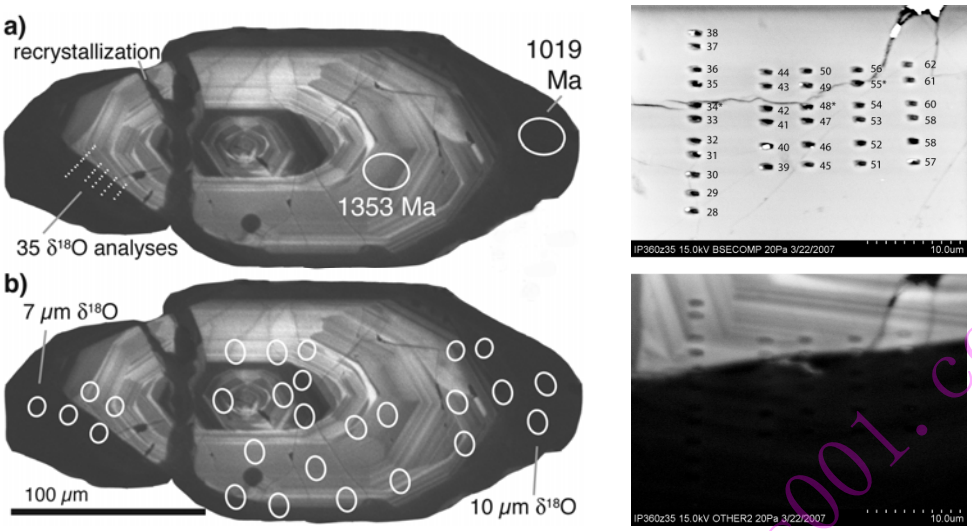


FIG. 2-28. Cathodoluminescence (CL) images of an Adirondack zircon showing bright oscillatory zoning in the core and darker CL in the rim. A dark recrystallized fracture cuts across the zircon. **(a)** Location of 30 μm U-Pb analysis pits by SHRIMP (Bickford *et al.* 2008) and sub-1 μm $\delta^{18}O$ pits by IMS1280. **(b)** Location and size of 10 μm and 7 μm oxygen isotope analyses by IMS1280. **(Right)** SEM and CL images of enlarged area of sub-1 μm pits from (A). See Fig. 2-6 for an enlarged view of two pits (from Page *et al.* 2007a).

$\delta^{18}O$ of Mantle-Derived Magmas

The $\delta^{18}O$ value of melts from the mantle is remarkably constant with only small outliers (Eiler 2001) and zircon in high temperature equilibrium with these compositions is likewise restricted in $\delta^{18}O$, averaging 5.3 ±0.6‰ (2 SD, Valley *et al.* 2005). Figure 2-29 shows the values of $\delta^{18}O$ for "mantle oxygen" in zircon from the Mid-Atlantic Ridge and kimberlite (Page *et al.* 2007b, Cavosie *et al.* 2009). The $\delta^{18}O$ values of zircon from the Moon have been measured (Whitehouse & Nemchin 2009) and are in good agreement with the compositions of Lunar basalt and gabbro (Wiechert *et al.* 2001, Spicuzza *et al.* 2007). The composition of mantle-derived olivine is nearly identical to this zircon, consistent with small fractionation at magmatic temperatures (Mattey *et al.* 1994, Eiler 2001). Zircon from evolved melts in the crust, if uncontaminated, is not greatly changed and commonly shares this same narrow range of "primitive" $\delta^{18}O$.

The fact that $\delta^{18}O$(zircon) values do not change appreciably during uncontaminated differentiation may seem surprising given that the $\delta^{18}O$ values of magmas can increase by 1 to 1.5‰ during fractional crystallization from mafic to felsic compositions. However, such increases in $\delta^{18}O$(magma) are caused by removal of mafic minerals that are lower in $\delta^{18}O$ than the melt, leaving the magma higher in $\delta^{18}O$ and enriched in quartzofeldspathic components. The changing chemistry of the melt causes $\Delta^{18}O$(magma–zircon) to increase at approximately the same rate as $\delta^{18}O$(magma), and thus $\delta^{18}O$(zircon) is unaffected. Valley (2003) discussed this process and summarized the equilibrium fractionation of oxygen isotopes between zircon and other minerals. Lackey *et al.* (2008) presented a relation for estimating the fractionation of zircon vs. melt:

$$\Delta^{18}O(\text{magma-zircon}) \approx 0.0612(\text{wt.\% } SiO_2, \text{ magma or WR}) - 2.50‰$$

There is a small temperature effect on fractionation at magmatic temperatures. However, the effect on values of $\Delta^{18}O$(magma-zircon) is especially small because zircon is intermediate in fractionating $\delta^{18}O$ among common rock-forming minerals; at equilibrium it is lower in $\delta^{18}O$ than quartz and feldspar and higher than magnetite and olivine (Valley 2003). Thus, values of $\delta^{18}O$(zircon) are closer to values of the melt than $\delta^{18}O$(quartz or feldspar) and are insensitive to changes in temperature. Bindeman & Valley (2002) demonstrated the small range of $\delta^{18}O$(zircon) values for temperature changes from ~700 to 800°C in the Bishop Tuff magma chamber (Fig. 2-30). At higher temperatures, this effect is even smaller.

http://bbs.gs001.com/

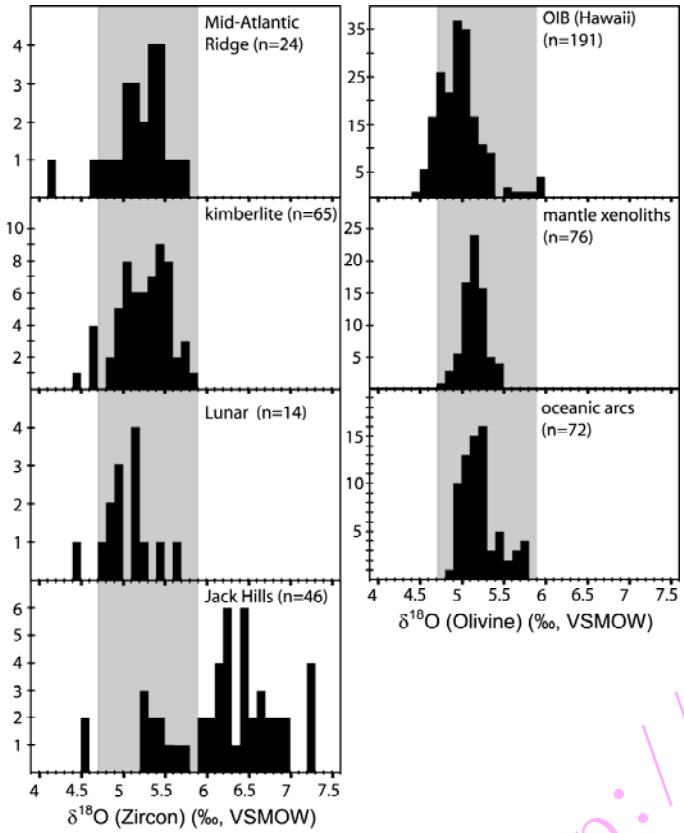


FIG. 2-29. Histogram of $\delta^{18}O$ values for igneous zircon and olivine from primitive sources on Earth and the Moon. The shaded field at $\delta^{18}O$ = 4.7 to 5.9‰ encompasses primitive or mantle values of $\delta^{18}O$(zircon) = 5.3 ±0.6‰ (from Cavosie *et al.* 2009 and references therein).

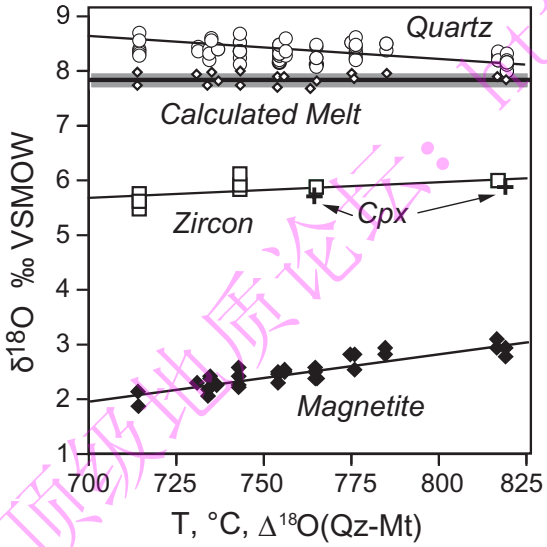


FIG. 2-30. Measured values of $\delta^{18}O$ (laser fluorination) for zircon, quartz, clinopyroxene, and magnetite in the Bishop Tuff plotted against magmatic temperature. Melt compositions are calculated. Values of $\delta^{18}O$(zircon) are relatively insensitive to changes in pre-eruptive temperature, even though quartz and magnetite vary by up to 1‰ (from Bindeman & Valley 2002).

Oxygen Diffusion and Exchange in Zircon

Zircon is highly retentive of chemical and isotopic composition due to its refractory character and extremely slow diffusion for most elements (Cherniak & Watson 2003, Peck *et al.* 2003, Page *et al.* 2007a). Both experiments and empirical studies indicate that closure temperature for oxygen isotope exchange is above 800°C for "dry" conditions. Sharp gradients in $\delta^{18}O$ within single zircon grains (Fig. 2-31) show that values are generally unaffected during amphibolite, granulite, and eclogite facies metamorphism, and at least some anatexis (Page *et al.* 2007a). In contrast, zircons that are discordant in age may be unaffected in $\delta^{18}O$, but in many instances have been shown not to be reliable in preserving magmatic values of $\delta^{18}O$ (Valley *et al.* 1994, Valley 2003, Booth *et al.* 2005, Nemchin *et al.* 2006, Cavosie *et al.* 2005, 2007). It has also been proposed that crystal-plastic deformation of zircon, which can be seen optically in thin section or by electron backscatter diffraction (EBSD), creates fast pathways for diffusion and facilitates Pb, REE, and oxygen isotope exchange (Reddy *et al.* 2006, Timms *et al.* 2008). However, detailed analysis of many

顶级地质论坛：http://bbs.geoc.com/

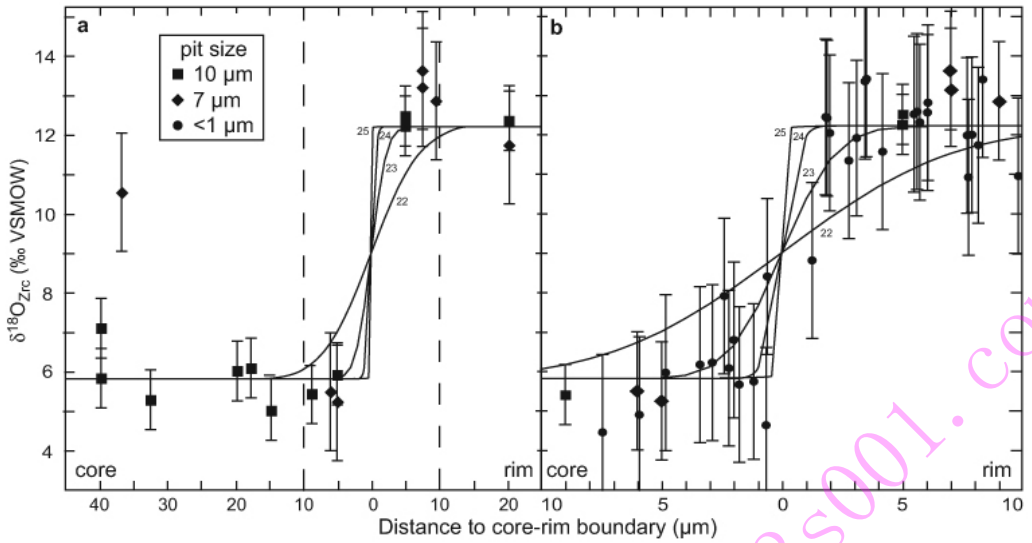


*FIG. 2-31. Oxygen isotope profile measured at WiscSIMS in the zoned zircon from Fig. 2-28. Error bars are 2 SD for the zircon standard. Data from 10, 7, and sub-1µm pits show a sharp increase in $\delta^{18}O$ from the core to the rim. Two spots with elevated $\delta^{18}O$ from the core may represent an earlier generation of zircon. Calculated diffusion profiles are for an isothermal period of 50 Myr and diffusion coefficients of 10^{-22} to 10^{-25} cm^2s^{-1}. The sub-1µm spot data are best fit by $D = 10^{-23.5}$ cm^2s^{-1} at 750°C (from Page *et al.* 2007a). Color at http://www.mineralogicalassociation.ca/index.php?p=160

crystals, including some that are clearly deformed, has thus far failed to identify an otherwise unaltered zircon that is zoned due to this process. Other internal checks against alteration include: imaging, age concordance, trace element pattern, internal zoning, and fractionation relative to coexisting phases (Valley 2003). Thus, values of $\delta^{18}O$ are preserved and (with care) reliably interpreted in many zircon grains even when coexisting minerals have been reset by high-grade metamorphism and deformation, intense hydrothermal alteration, or melting. Zircon offers a means to distinguish magmatic compositions from reequilibration or post-magmatic alteration, a common problem for igneous rocks.

Hydrothermal and Metamorphic Zircon

Direct precipitation of zircon from a hydrothermal fluid has been proposed in many studies. If correct, such zircon is important for providing age information of events that are typically difficult to date such as ore deposition and metamorphism. Likewise, if unrecognized, hydrothermal zircon could lead to errors of interpretation. Fu *et al.* (2009) analyzed zircon that had previously been interpreted as hydrothermal from the Gidginbung Au-Ag deposit, Lachlan Orogen, Australia and found that values of $\delta^{18}O$ were constant and mantle-like at 5.4 ±0.9‰ (2 SD), and that Ti, REEs, Hf isotopes, and CL zoning were all best explained by crystallization of zircon from a magma. Likewise, Cavosie *et al.* (2009) examined zircon from young oxide gabbro bodies and highly altered "veins" in serpentinite from the Mid-Atlantic Ridge, and found that the zircon is homogeneous with mantle-like values of $\delta^{18}O$ (5.3 ± 0.8‰ 2 SD), and magmatic CL zoning and REE profiles. Hydrothermal zircon in this environment is predicted to have $\delta^{18}O$ more than 5‰ lower than the measured values. Thus all analyzed zircon is interpreted as igneous and the "veins" appear to be very thin, altered dikes. While there is no reason to doubt the existence of hydrothermal zircon and convincing reports exist, these results suggest that zircon should be tested by detailed geochemistry and imaging before it is assumed to be hydrothermal.

Zircon commonly forms in high-grade metamorphic rocks as new crystals, overgrowths, or replacement. It is common to date zircon in order to establish the timing of metamorphism and to correlate age with estimates of pressure and temperature. However, the zircon-forming reaction can be driven by metasomatism, crystallization of anatectic melts, unmixing of Zr from igneous minerals like ilmenite, or breakdown reactions of metamorphic minerals such as garnet. Thus the timing of zircon growth cannot be assumed to

矿物地质论坛 http://blog.3s001.com/

coincide with the thermal peak of metamorphism. *In situ* analysis of the oxygen isotope ratio is a useful adjunct for interpretation of *in situ* geochronology of metamorphic zircon. Combined with CL imaging, it is possible to test equilibration between zircon and other petrologically significant minerals such as garnet. This is necessary in order to use zircon ages to calibrate the chronology or P–T–t path of a rock (Harley & Kelly 2007, Moser *et al.* 2008, Lancaster *et al.* 2009).

Crustal Recycling

The oxygen isotope ratio of igneous zircon is sensitive to differences in the source and contamination of magmas (Valley 2003). Crustal recycling can be recognized from magmatic values of $\delta^{18}O$(zircon), especially if crustal components were weathered or hydrothermally altered before they became incorporated into magmas. In many plutonic environments, this process is basically one of cannibalism, new magmas remelt earlier co-magmatic rocks of similar chemistry, and the only geochemical evidence will come from isotopes and elements that are altered. Hydrothermal alteration can change the $\delta^{18}O$ of a rock on a time scale of tens to thousands of years, while heavy isotope systems such as Sr, Nd, and Hf require many millions of years to become distinctive by radiogenic in-growth. Thus, if country rocks are igneous and young at the time of remelting, $\delta^{18}O$ may be the only geochemical signature of that interaction. While this distinction might seem moot to a geochemist, the implications are significant for other processes such as heat transport.

Shallow hydrothermal alteration affects vast amounts of crust and is especially prevalent in sub-volcanic environments. Exchange with heated meteoric waters commonly results in low $\delta^{18}O$ values for felsic extrusive and intrusive rocks, but whether this interaction creates low $\delta^{18}O$ magmas has been controversial (see Taylor 1986). The best evidence to resolve this question comes from analysis of zircon that, once crystallized, is unaffected by hydrothermal alteration.

The Yellowstone volcanic field exposes voluminous rhyolite tuff and flows, erupted over the past 2 m.y., including three major caldera-forming eruptions (100–2000 km^3) and many that are smaller. Bindeman & Valley (2001) showed that quartz and zircon are in oxygen isotopic equilibrium for many of the rhyolite units at Yellowstone, but that profound disequilibrium exists for low $\delta^{18}O$ intra-caldera flows that erupted shortly after large caldera-forming eruptions. The conclusions of the 2001 study were based on bulk analysis of $\delta^{18}O$ in zircon concentrates and have been reinvestigated with *in situ* analysis. Bindeman *et al.* (2008) found that individual zircon grains have inherited cores with diverse values of $\delta^{18}O$, that rims can be either higher or lower in $\delta^{18}O$, and that zoning in $\delta^{18}O$ resulted largely from dissolution and crystallization of zircon, rather than diffusion. These results suggest that isolated domains and unexposed intrusive units existed within what had been inferred to be a single magma body. This conclusion contrasts with earlier models where a long-lived magma chamber is periodically tapped. Instead, Bindeman *et al.* (2008) concluded that silicic magmatism proceeded via rapid, shallow-level remelting of earlier erupted and hydrothermally altered Yellowstone crust, driven by on-going intrusion of basaltic magma. Similar complex zoning and low $\delta^{18}O$ values are seen by ion microprobe analysis of zircon from the Cougar Point Tuff, an earlier rhyolite (12.4-10.5 Ma) from the Snake River Plain, showing that mafic intrusions from the Yellowstone hot spot have created voluminous low $\delta^{18}O$ rhyolite magmas (Cathey *et al.* 2007). Apparently, continuous mafic magmas ponding in focused areas of continental crust provide ideal conditions for the successive cycles of intrusion, melting, hydrothermal alteration, and remelting, necessary to form low $\delta^{18}O$ felsic magmas.

Deep penetration of seawater and associated hydrothermal alteration have been documented for oceanic crust at spreading centers. Oxygen isotope ratios record the intensity of alteration and temperature. At high temperatures, values of $\delta^{18}O$(rock) can drop from 6 to below 4‰, while at low temperatures, values exceed 10‰ in highly altered rocks (see Eiler 2001). In this environment, it might be expected that both high and low $\delta^{18}O$ magmas would be produced by remelting of altered basaltic wallrocks. Zircon is found in a number of lithologies from modern spreading centers, however values of $\delta^{18}O$(zircon) show the same narrow range of values found in other primitive reservoirs. Igneous zircon from gabbro and serpentinite from the Mid-Atlantic Ridge averages 5.3 ±0.8‰ (2 SD, Cavosie *et al.* 2009). One large, 10 mm long, zircon grain from an oxide gabbro on the Indian Ridge was analyzed 44 times at WiscSIMS because its ductile deformation was proposed to facilitate chemical alteration (see Fig. 2 in Reddy *et al.* 2006), however

版权所有 http://bbs.sinoss.com/

$\delta^{18}O$ values are homogeneous and identical to unaltered zircon (average = 5.28 ± 0.34‰ 2 SD; 2 SE = 0.05‰, Wilde & Valley, unpublished). Likewise, igneous zircon from 24 samples of plagiogranite, Fe-Ti oxide gabbro and veins in serpentinite show mantle-like values of 5.17 ± 0.50‰ (n = 140, 2 SD, Grimes & Valley, unpublished). Why are the effects of hydrothermal alteration and remelting, that are prominent at Yellowstone, not seen in $\delta^{18}O$(zircon) values of magmas from mid-ocean ridges? Possible answers to this question include: 1) zircon-bearing magmas at spreading centers may be direct differentiates from the mantle and remelting is not important, 2) alteration drives $\delta^{18}O$ of wallrocks to both higher and lower values and the average effect is small, or 3) only a relatively small sample set has been analyzed. Correlated *in situ* analysis of age, $\delta^{18}O$, and trace elements in such zircon will provide critical new evidence to resolve this question.

Magmatism in convergent margins is generally believed to be dominated by partial melting of metasomatized peridotite in the overlying mantle wedge, but arc magmas can also result from melting of the slab itself and the importance of slab melting is controversial. Oxygen isotopes are useful to recognize slab melts because of the involvement of high $\delta^{18}O$ sediment, but magmatic $\delta^{18}O$ must be distinguished from subsolidus alteration. Samples of trapped melt inclusions (now glass) within phenocrysts can be armored from subsolidus exchange (Eiler *et al.* 1998, 2007, Gurenko *et al.* 2001, Hauri 2002, Gurenko & Chaussidon 2002, Bouvier *et al*. 2008). For instance, hydrous melt inclusions within olivine from peridotite xenoliths in basaltic andesite of Batan Island were analyzed and found to preserve magmatic values of $\delta^{18}O$, and trace, minor, and major element composition. The glass inclusions are broadly dacitic with $\delta^{18}O = 6.45 \pm 0.51$‰ indicating that they resulted from low-degree melting of metasomatized peridotite rather than subducted ocean crust, and suggesting that some adakite-like magmas may have a similar origin (Eiler *et al.* 2007).

Maturation of the Crust Through Time

Valley *et al.* (2005) reported $\delta^{18}O$ and U–Pb ages for magmatic zircon from 1200 rocks that vary in age from 4.4 Ga to Recent (Fig. 2-32). Taken as a whole, there are no systematic differences observed for ion microprobe data from individual zircon grains *vs*. laser fluorination analyses of bulk samples comprising hundreds of zircon grains. These results show a remarkable consistency throughout the Archean; values for terranes on five continents range from the mantle value to mildly elevated in $\delta^{18}O$, *ca*. 4.7 to 7.5‰. Soon after the end of the Archean, higher $\delta^{18}O$ zircon becomes increasingly common; by 1.5 Ga, many zircon grains yield values in the range of 8 to 10‰, which would be in equilibrium with whole rock $\delta^{18}O$ values of 9 to 12‰. Such elevated oxygen isotope ratios indicate recycling of sedimentary rocks into magma by assimilation or wholesale melting. Clearly, conditions were different in the Archean, both in the rates and style of tectonic processes responsible for melting of crust, and in the availability of high $\delta^{18}O$ supracrustal materials, especially clay-rich mud rocks (Valley *et al.* 2005). During the Proterozoic, the average $\delta^{18}O$ of magmatic zircon increased as the crust matured and high $\delta^{18}O$ material was recycled into magmas.

Archean Magmas and Early Earth

The uniformly primitive to mildly elevated Archean values of $\delta^{18}O$(zircon), 4.7 to 7.5‰, extend to the oldest terrestrial zircon known. This ~3‰ range of $\delta^{18}O$ values is relatively small when viewed in the context of all magmas in Figure 2-32, however it is still significantly expanded relative to the ~1‰ range of zircon from mantle-derived magmas and other primitive sources, 4.7 to 5.9‰ (5.3 ±0.6‰) (Fig. 2-29). The values above 6.3‰ (*i.e*., distinctly higher than 5.9‰, considering analytical uncertainty conservatively at 0.4‰) are best explained by low temperature aqueous alteration of rock and sediment on the surface of Earth followed by burial and melting to form high $\delta^{18}O$ magmas from which zircon crystallized. The exact details of burial and melting are controversial. Some researchers favor modern-style tectonics, subduction, and mantle melting, while others envision processes such as plumes, calderas, and impacts, with melting in the crust. Regardless of process, such mildly elevated values of $\delta^{18}O$ indicate a supracrustal input and cannot form at high mantle temperatures where oxygen isotope fractionations are very small. Figure 2-32 shows $\delta^{18}O$ values measured on five different ion microprobes for detrital zircon older than 3.9 Ga from the Jack Hills, Australia in comparison to values measured in bulk samples by laser fluorination (Peck *et al.* 2001, Wilde *et al.* 2001,

矿物岩石地球化学通报 http://hbs.bsgpt.com

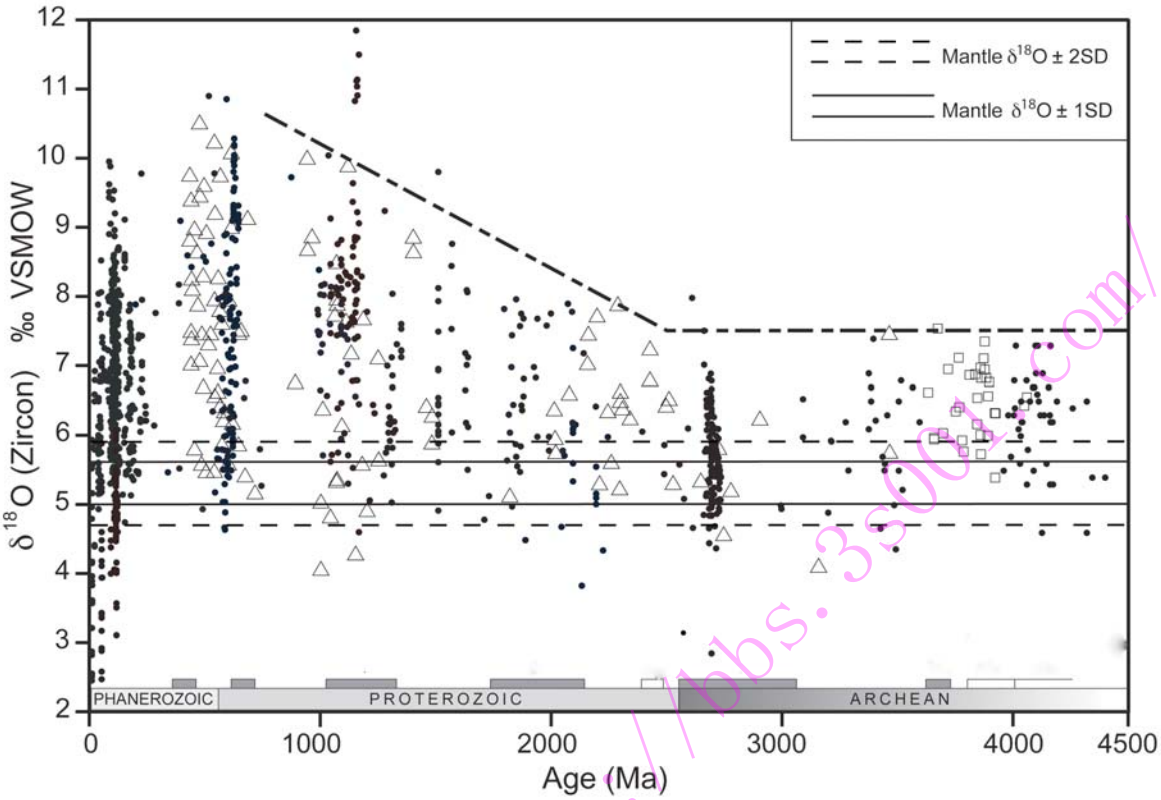


FIG. 2-32. Values of $\delta^{18}O$ for igneous zircon from 4.4 Ga to recent. The composition of zircon in high-temperature equilibrium with mantle $\delta^{18}O$ averages 5.3 ±0.6 (2 SD). Sources of data: dots, Valley *et al.* 2005; triangles and squares, Kemp *et al.* 2006, Wilde *et al.* 2008. Values of $\delta^{18}O$(zircon) range from mantle-like to mildly elevated in the Archean. Values of $\delta^{18}O$ above 7.5‰ reflect increased recycling of high $\delta^{18}O$ crustal material on the post-Archean Earth.

Mojzsis *et al.* 2001, Cavosie *et al.* 2005, Nemchin *et al.* 2006, Trail *et al.* 2007). In addition, oxygen 3-isotope analysis at WiscSIMS shows values of $\Delta^{17}O = 0‰$ confirming the terrestrial origin of this ancient (4.4 to 4 Ga) zircon (see Fig. 2-39). The few values of $\delta^{18}O$ above 7.5‰ in Figure 2-33 were originally interpreted as coming from S-type granite magmas (Mojzsis *et al.* 2001), but are no longer interpreted as igneous (Valley *et al.* 2006, Trail *et al.* 2007). All studies have found a significantnumber of zircon grains with $\delta^{18}O$ above the mantle-equilibrated range of 5.3 ±0.6‰. While several studies have emphasized the complex nature of such zircon and the possibility that some $\delta^{18}O$ values reflect post-magmatic processes (Cavosie *et al.* 2005, Nemchin *et al.* 2006, Valley *et al.* 2006), a large number of samples show concentric CL zoning, concordant ages, and normal trace element compositions (Fig. 2-1). It is difficult to imagine a process whereby the oxygen of a zircon, which is tetrahedrally coordinated and strongly bonded to silicon, could be completely exchanged by diffusion while the Pb, which resides in non-ionic sites caused by radiation damage, is preserved. Thus concordant U-Pb ages provide a good criterion that specific domains of a zircon are unaltered. However, U and Th content and radiation damage can be zoned in zircon, and this test requires correlation of the analysis spots. There is no evidence that the mildly elevated values of $\delta^{18}O$ in the pre-4 Ga zircon samples result solely from younger subsolidus exchange, weathering or alteration of the zircon grains themselves, and thus the compositions of these zircon "time-capsules" are robust evidence of conditions on the Early Earth.

Values of $\delta^{18}O$ above the mantle composition extend as early as 4.325 Ga (Fig. 2-34), suggesting that the surface of Earth was cool enough to condense liquid water at this time and that hotter "Hadean" conditions ended before 4.3 Ga. The existence of liquid water and thus oceans at this time is also suggested by high [Li] of 10–70 ppm

http://bbs.3500.com/

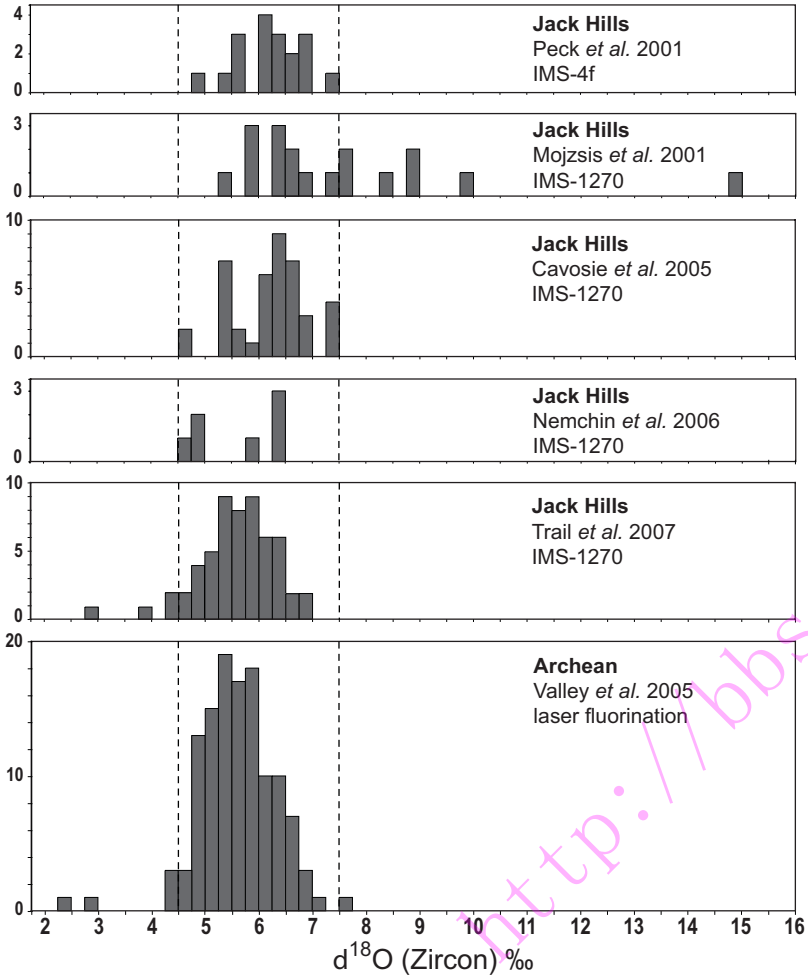


FIG. 2-33. Comparison of values of $\delta^{18}O$ measured by SIMS for detrital > 3.9 Ga zircon from the Jack Hills, Australia, and by laser fluorination for other Archean igneous zircon.

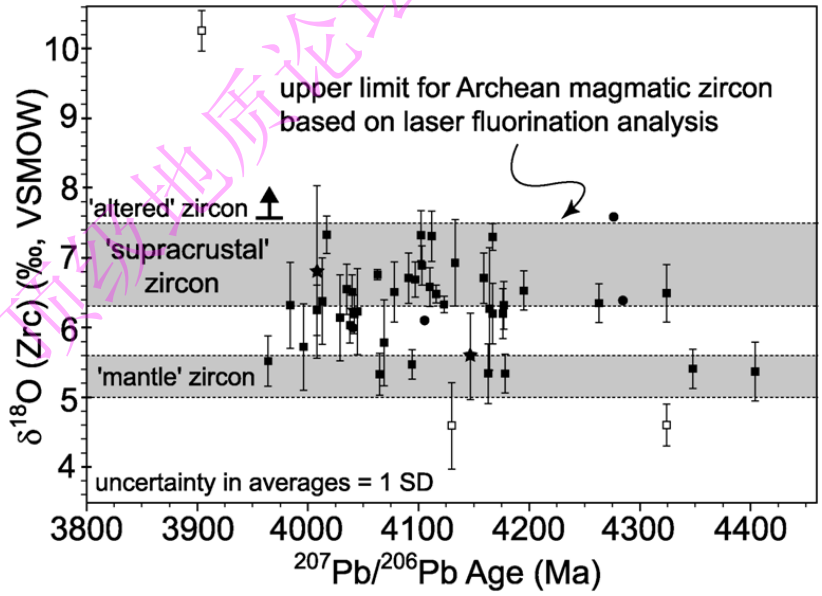


FIG. 2-34. Average $\delta^{18}O$ *vs.* age for Early Archean zircon. Solid squares are zircon analyses preserving magmatic $\delta^{18}O$ (Cavosie *et al.* 2005). Open squares are altered zircon grains. The 'mantle' zircon field is plotted with 1 SD limits, 5.3 ±0.3‰ (Valley *et al.* 1998). The 'supracrustal' field indicates a range in magmatic $\delta^{18}O$(zircon) that is elevated relative to equilibrium with mantle melts (from Cavosie *et al.* 2007).

质谱地质论坛：http://bbs.3s001.com/

and low δ^7Li values of 0 to –10‰ in zircon grains as old as 4.3 Ga (Ushikubo *et al.* 2008). Heavy weathering on early Earth is consistent with sauna-like temperatures and a CO_2-rich atmosphere that would have created thick saprolite horizons and destroyed igneous rocks exposed on the surface, possibly explaining the absence of known rocks older than 4 Ga. Alternatively, in the absence of greenhouse gases, Snowball Earth conditions may have prevailed under a fainter young Sun (Zahnle 2006). Either way, liquid water existed in geothermal regions and weathering and low temperature alteration was common. Possibly, secluded pools evolved, confined by ice or land that provided unusual habitats for the first life.

Zircon as the Record of the Kapuskasing Orogen

Moser *et al.* (2008) described the genesis of neo-Archean lithosphere recorded in zircon from the Kapuskasing Uplift of the Superior Province. Ion microprobe analysis was used to correlate U-Pb age and δ^{18}O (Fig. 2-35). Four periods are recognized between 2.9 and 2.5 Ga: creation of primitive to evolved crust (2870–2670 Ma); rapid uplift, arc unroofing, erosion of detrital zircon, and burial of sediments to the lower crust (2670–2660 Ma); prolonged high temperature metamorphism (2660–2580 Ma); and Huronian continental rifting and magma intra-plating (< 2510 Ma). Thus single zircon grains can preserve evidence of multiple prolonged tectonic events.

Hafnium, U-Pb, and Oxygen

In combination with laser-ablation ICP-MS, other geochemical systems such as Lu-Hf can be correlated to SIMS data for δ^{18}O and age (Kemp *et al.* 2006, 2007a, 2008, Hawkesworth & Kemp 2006a, 2006b, Hawkesworth *et al.* 2006, Valley *et al.* 2006, Bolhar *et al.* 2008, Harrison *et al.* 2008, Pietranik *et al.* 2008).

Kemp *et al.* (2007) studied zircon from three suites of hornblende-bearing "I-type" granite from the Lachlan Fold Belt, eastern Australia. The common interpretation of the Lachlan I-type and S-type granite plutons, based in part on whole rock δ^{18}O, is that protoliths were igneous and sedimentary rocks, respectively (O'Neil & Chappell 1977, Chappell & White 2004). However, the new data show that I-type granite zircon has elevated δ^{18}O and that protoliths contained from 25 to 60% metasedimentary material (Fig. 2-36). The combination of *in situ* data for δ^{18}O, U-Pb, and Hf suggests a revised view of the genesis of these rocks, starting with a low δ^{18}O (5–6‰), probably mantle-derived, parent magma, and proceeding through anatexis of the deep crust, emplacement of magmas in the mid-crust, and then zircon growth synchronous with assimilation and fractional crystallization (AFC). Zoning of δ^{18}O in some zircon records magmatic evolution during AFC. Thus the I-type granite bodies are reinterpreted as largely sedimentary in origin, but representing a component of evolved primitive magmas and growth of the crust (Kemp *et al.* 2007a).

METEORITES: OXYGEN THREE-ISOTOPES

The fractionation of oxygen isotopes follows mass-dependent processes in most planetary environments. Thus, on Earth, there is generally no need to analyze ^{17}O, the "forgotten isotope" (but see Bao *et al.* 2000). This arises because both equilibrium and kinetic isotope fractionations are linearly proportional to $\Delta M/M$, and any chemical process that fractionates $^{18}O/^{16}O$ by a given amount will fractionate $^{17}O/^{16}O$ by one-half of that amount. Thus, data fall along a Terrestrial Fractionation Line (TFL) that has a slope of approximately 0.52 in plots of δ^{18}O *vs*. δ^{17}O (McKeegan & Leshin 2001, Miller 2002).

In contrast to Earth and the Moon, oxygen three-isotope analysis of meteorites has been common since Clayton *et al.* (1973) discovered compositions of carbonaceous meteorites that proved the importance of Mass-Independent Fractionations (MIF). Apparently, material was mixed during formation of the Earth-Moon system, homogenizing any pre-existing MIFs, but these differences are preserved in other bodies. The most precise oxygen three-isotope data are made by conventional laser-fluorination techniques, but ion microprobe analysis is increasingly important for meteoritic samples that may contain fine-scale zoning or heterogeneity (McKeegan & Leshin 2001, Kita *et al.* 2004, Krot *et al.* 2006, Nakamura *et al.* 2008).

Oxygen three-isotopes in various primitive meteorites record the variety of materials formed in the earliest solar system and constrain the processes that fractionated oxygen isotopes (Clayton & Mayeda 1996; see also McKeegan & Leshin 2001, Clayton 2007). Improved precision of ±0.3‰ for δ^{17}O and Δ^{17}O for 15μm spots (Kita *et al.* 2007a, 2009), *vs*. ~2‰ in earlier ion microprobe studies, resolves mass-dependent fractionation processes, superimposed on mass-independent trends (Fig. 2-37). High precision, *in situ* analysis with spot

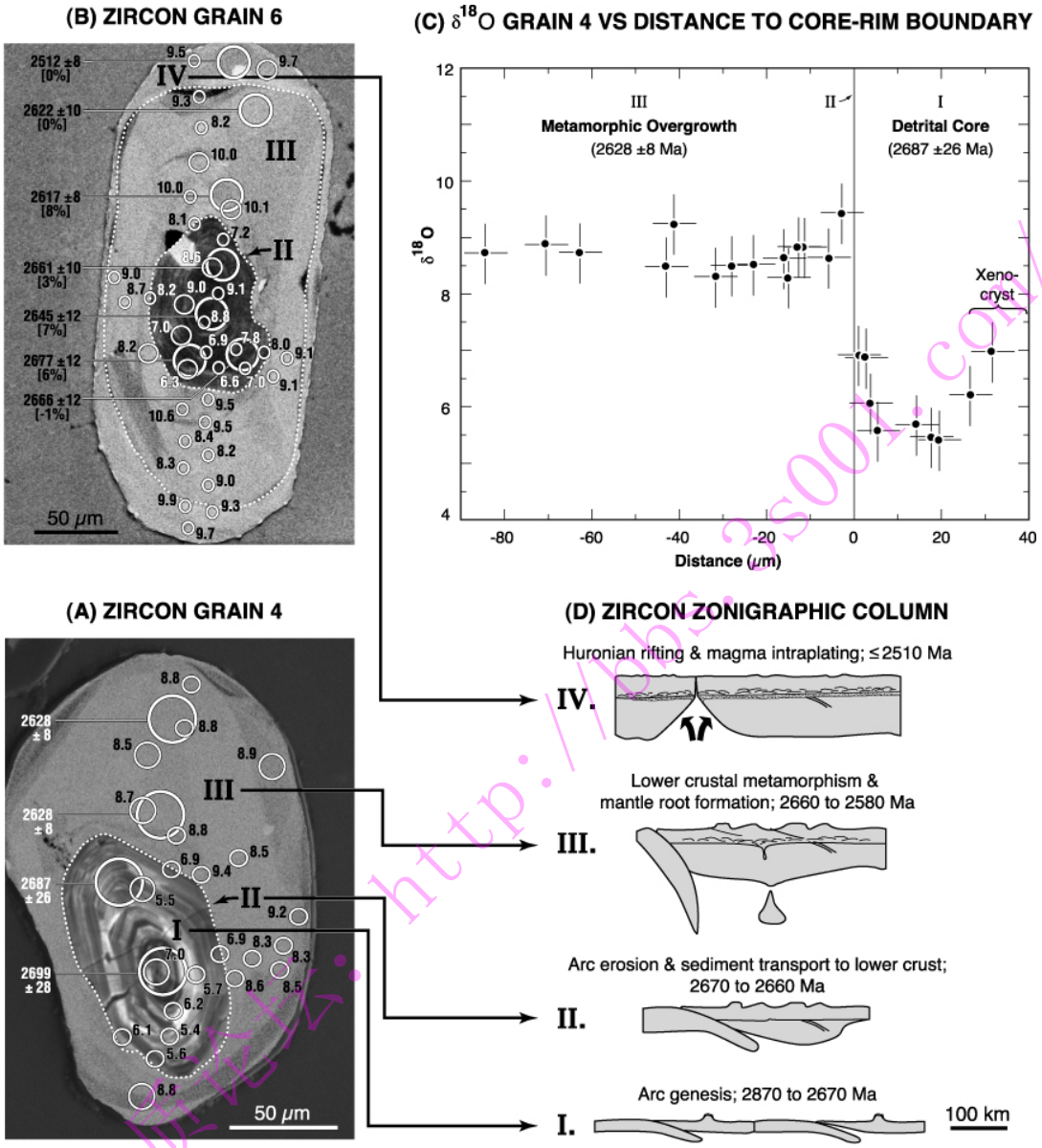


FIG. 2-35. **(A, B)** CL images of Archean zircon from the Kapuskasing Uplift showing ion microprobe spots and values of U-Pb age and $\delta^{18}O$. Zircon 6 shows patchy re-setting of age to metamorphic values and domain enrichment of $\delta^{18}O$ associated with darkening/disruption of CL. **(C)** Primary $\delta^{18}O$ values from magmatic core and metamorphic rim of zircon 4. **(D)** Stages of continental plate creation and local destruction as recorded in zircon zoning (from Moser *et al.* 2008).

sizes as small as 1 μm can resolve composite samples and zoning that was previously unknown. A more complete discussion of this topic is in chapter 1 of this volume. Therefore, examples are presented here that illustrate the new capabilities.

Stardust

The NASA Stardust mission returned sub-micrometre to 10 micrometre-scale particles from comet Wild 2, which contain high temperature minerals similar to those in primitive meteorites (McKeegan *et al.* 2006). The possibility of chondritic material in a comet is surprising because they are thought to form in the inner Solar Nebula, while comets contain material formed in cold interstellar regions of the Kuiper Belt.

Nakamura *et al.* (2008) sectioned four 10 to 40 μm chondrule-like particles from comet Wild 2 containing olivine, pyroxene and metal by microtome, and analyzed for oxygen three-isotopes

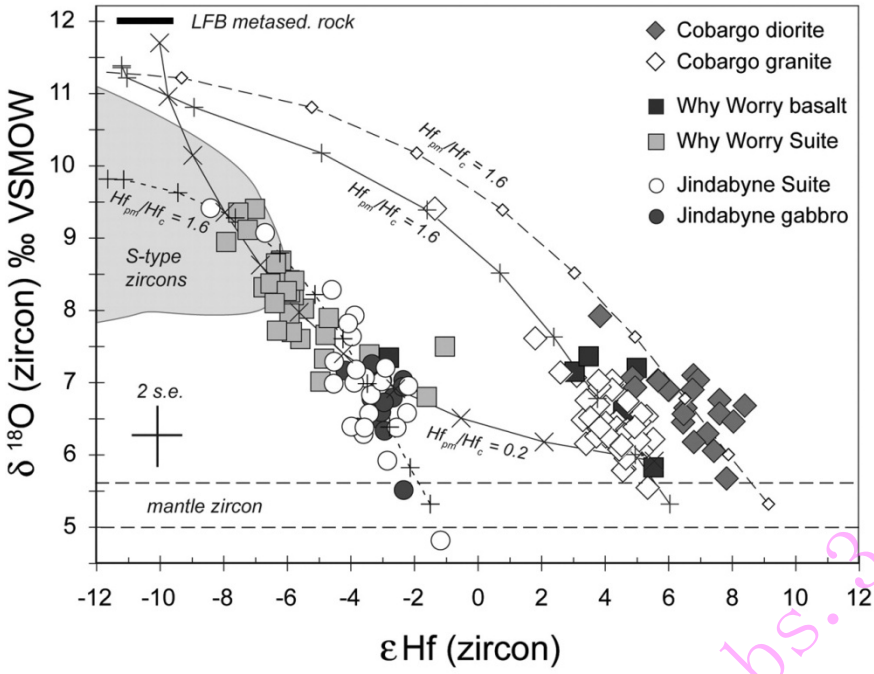


FIG. 2-36. Values of $\delta^{18}O$ *vs.* εHf for zircon from hornblende granite (I-type) in comparison to zircon in S-type granitic and metasedimentary rocks from the Lachlan Fold Belt (LFB). Curves model AFC, assimilation and fractional crystallization, of the magma for different ratios of Hf in the parent magma and in the crust (from Kemp *et al.* 2007a).

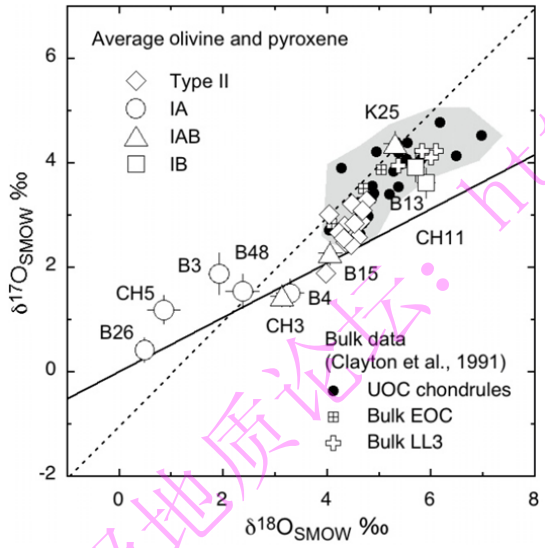


FIG. 2-37. Oxygen three-isotope plot of olivine and pyroxene measured by SIMS (from Kita *et al.* 2006).

in 2 μm and in 1 μm diameter spots at WiscSIMS (Fig. 2-38C). In the largest particle, two 5–10 μm grains of olivine were resolved by X-ray imaging (Fig. 2-38B), and analyzed 4 to 10 times each for oxygen three-isotopes. The oxygen isotope ratios of these samples are chondrule-like and fall along the CCAM line with the lowest values approaching the composition of the Sun (Fig. 2-38D). Furthermore, the compositions of these two adjacent olivine grains (Fig. 2-38B) are distinctly different. These results suggest formation in the inner Solar Nebula and transport to the outer Solar System by X-wind or outward flow in the mid-plane (Nakamura *et al.* 2008).

Martian Meteorites

The only solid samples of Mars available for analysis on Earth are 57 samples from 34 meteorites classified as the SNC group (shergottite, nakhlite, Chassigny) with a cumulative mass of 91 kg. All SNCs are thought to come from the same planet and individual meteorites within this group have ages and rare gas compositions that suggest they formed on Mars. The most important unifying characteristic of the SNC group of meteorites is that they all plot along a mass-dependent fractionation line with a slope of 0.52 in $\delta^{18}O$ *vs.* $\delta^{17}O$ that parallels the terrestrial fractionation line, but is offset by 0.3‰ (*i.e.*, $\Delta^{17}O = +0.3$, Clayton & Mayeda 1996, Franchi *et al.* 1999, Spicuzza *et al.* 2007).

The ALH84001 meteorite is the most famous of the Martian clan because of thin 50–100 μm diameter rosettes of late, radial fibrous, concentrically zoned carbonate that were proposed to harbor evidence for microbial life on Mars (McKay *et al.* 1996). Every aspect of this proposal has been disputed, some would say refuted. For instance, the origin of the carbonates themselves has been proposed to be terrestrial contamination (Kopp

顶级地质论坛：http://bbs.3s001.com/

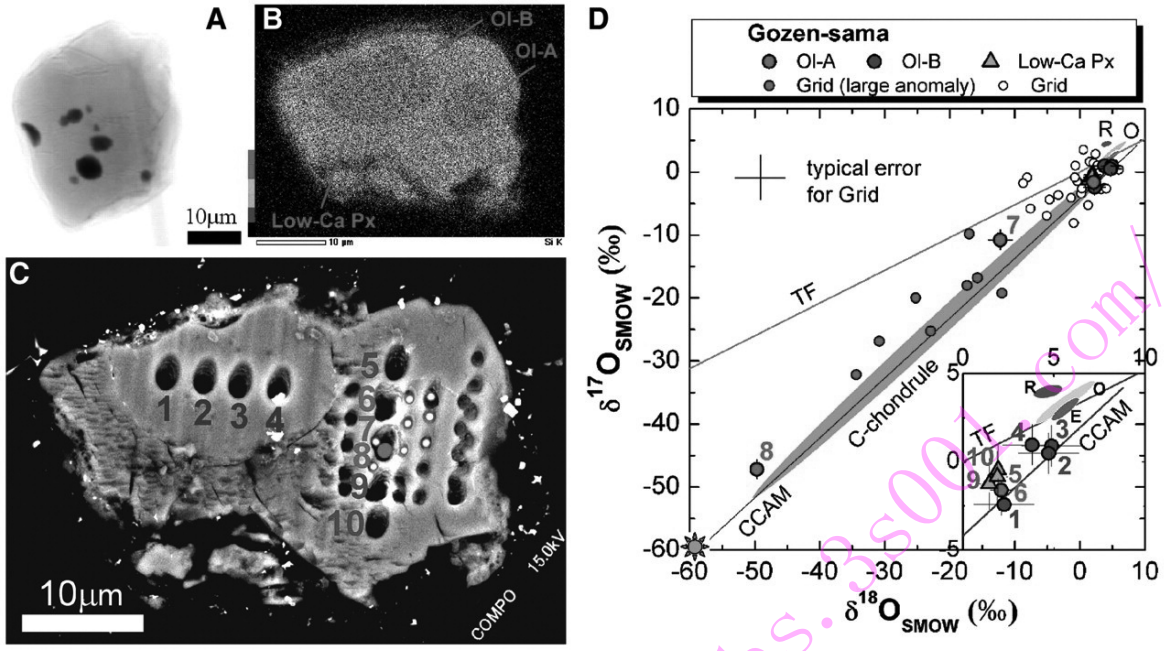


FIG. 2-38. Cross-section of a particle from comet Wild 2. **(A)** Transmitted X-ray image showing inclusions of Fe-Ni metal. **(B)** X-ray map of Si showing two olivine grains within low Ca pyroxene (rotated 90° from A). **(C)** BSE image of (B) showing ten 2-μm diameter analysis pits and 36 1-μm pits. **(D)** Values of $\delta^{18}O$ vs. $\delta^{17}O$ for 2 μm pits (large dots) and 1 μm pits (small dots) measured at WiscSIMS. Values of $\delta^{18}O$ and $\delta^{17}O$ from 2 μm pits are precise at ±1.3‰ (2 SD) and smaller pits are ±4.1‰. The star at lower left shows the composition of the Sun (McKeegan *et al.* 2008) (from Nakamura *et al.* 2008).

& Humayun 2003). This conclusion is consistent with evidence from other meteorites, found in Antarctic ice (CM Chondrites), that have been demonstrated to contain terrestrial carbonates (Tyra *et al.* 2007) and measurements showing that much of the organic matter in ALH84001 is of terrestrial origin (Jull *et al.* 1998). If the carbonates in ALH84001 are terrestrial, this would disprove any link to extraterrestrial life and this possibility has been tested by SIMS analysis.

Several ion microprobe studies of carbonates in ALH84001 have shown that the rosettes are zoned by *ca*. 25‰ in $\delta^{18}O$, and that $\delta^{18}O$ correlates to X(Mg) of the carbonate (Valley *et al.* 1997, Leshin *et al.* 1998, Eiler *et al.* 2002, Saxton *et al.* 1998, Holland *et al.* 2005). In contrast, phosphates in this meteorite are relatively constant with $\delta^{18}O$ = 3 to 6‰ (Greenwood *et al.* 2003). Eiler *et al.* (2002) showed that a second type of carbonate (clots) can be distinguished from the rosettes in this meteorite based on textures, chemical composition and $\delta^{18}O$. They proposed that rosettes formed at low temperatures (<180°C) and that the clots are shock-melted rosettes.

Analysis of $\delta^{18}O$ alone cannot rule out terrestrial contamination for some component of the carbonates in ALH84001, which are complexly zoned, fractured, and formed at different times. However, analysis of oxygen three-isotopes in the different generations of carbonate can resolve this issue because of the distinctive difference in $\Delta^{17}O$ of Earth *vs*. Mars. Ion microprobe analysis shows that both the carbonate rosettes and clots have $\Delta^{17}O$ ~0.8‰ (Fig. 2-39, Valley *et al.* 2007), confirming analysis of bulk carbonate powder that shows $\Delta^{17}O$ = 0.8 (Farquhar *et al.* 1998) *vs*. 0.32‰ for host orthopyroxene (Clayton & Mayeda 1996, Franchi *et al.* 1999, Spicuzza *et al.* 2007). Taken together, these results prove that all of the major generations of carbonate in ALH84001 are extraterrestrial in genesis and come from the same planet. Furthermore, the difference in $\Delta^{17}O$ (0.8 for carbonate *vs*. 0.3‰ for bulk silicate Mars) shows that the carbonates were not in oxygen isotope equilibrium with the silicate crust of Mars (Farquhar *et al.* 1998). On Earth, the atmosphere and crust actively exchange oxygen (and have similar $\Delta^{17}O$) via the oceans and ocean ridge hydrothermal processes, but in the absence of tectonics and an ocean, such exchange does not happen on Mars.

http://vbs.3s001.com/

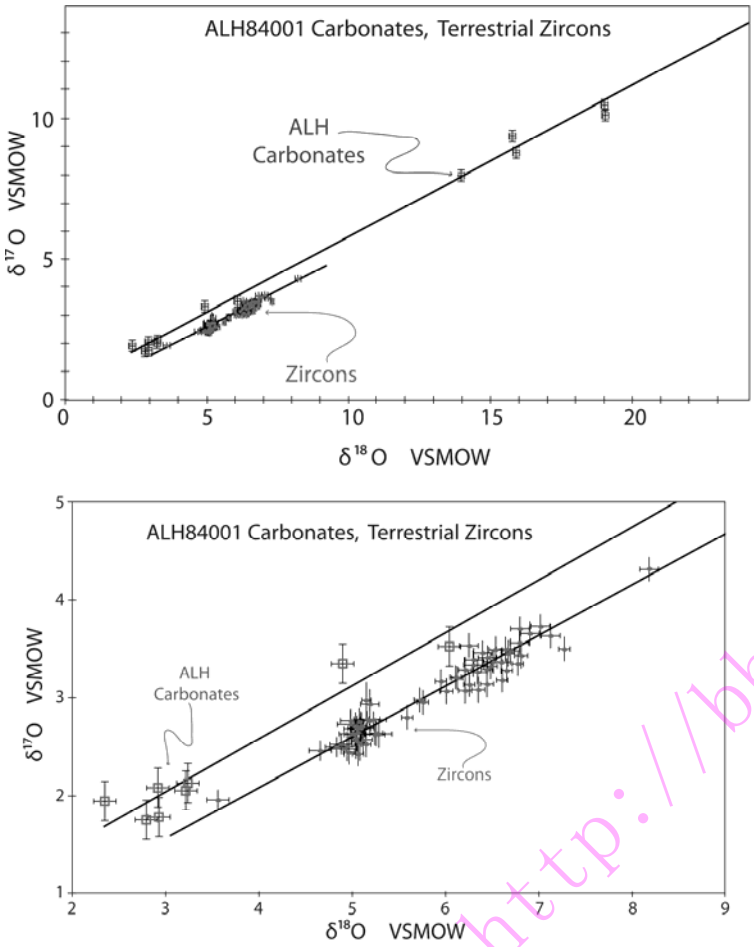


*FIG. 2-39. *In situ* oxygen three-isotope analyses of carbonates from the Martian meteorite, ALH84001, and terrestrial zircon by ion microprobe. Both data sets plot on mass-dependent fractionation lines, but all components of the ALH carbonates are offset at $\Delta^{17}O \approx 0.8‰$ (Valley *et al.* 2007), relative to Earth ($\Delta^{17}O = 0‰$) proving a non-terrestrial origin and suggesting exchange with an atmosphere on Mars that was not equilibrated with the Martian silicate crust (Farquhar *et al.* 1998). The terrestrial zircon analyses show no resolvable difference in $\Delta^{17}O$ between ~0.1 Ga mantle megacrysts from kimberlite and 4.4 to 4 Ga detrital zircon. Color available at http://www.mineralogicalassociation.ca/index.php?p=160

WHAT NEXT?

The past decade has seen dramatic improvements in instrumentation for *in situ* isotope analysis and new studies are just starting to appear that employ these tools. This paper reviews progress for just one element, oxygen, the most common element in the crust and the most heavily studied stable isotope system. We think that some of the lessons learned in oxygen isotope studies will be useful in development of other isotope systems. The quality of analytical results can depend on attention to detail. Experimental and theoretical calibrations of equilibrium fractionation factors and of the kinetics of isotope exchange are critical to interpretation of natural data. *In situ* analysis can aid in interpreting experimental products and also creates greater need for new experiments, especially of diffusion rates and reaction kinetics. *In situ* analysis also creates new demand for homogeneous standards of minerals, glasses, and compounds.

In coming years, the ion microprobe will be applied in many new areas and to reevaluate classic studies. Already, some conventional wisdom has been changed; but will the ion microprobe become the analytical tool of choice? We think the answer is: sometimes. The "conventional" and "*in situ*" techniques are complimentary. The better accuracy and precision of conventional gas source mass spectrometers will always be important for large homogeneous materials. In some situations, even with a heterogeneous sample, a single average composition is most useful. Likewise, the cost and complexity of operating an ion microprobe is a factor. Some *in situ* studies will show that materials are homogeneous and nothing new is to be learned at high magnification. Such materials will likely continue to be analyzed at the millimetre scale. However for other studies, including many reviewed here, the ion microprobe reveals new information leading to fundamental insights that could not be obtained in any other way. There is no end in sight for the fun and excitement of these studies.

http://bbs.ssdn.com/

ACKNOWLEDGEMENTS

The authors thank J. Bowman, A. Cavosie, A. Crowell, B. Fu, C. Grimes, P. Heck, J. Huberty, R. Kozdon, P. Lancaster, D. Moser, I. Orland, F. Z. Page, W. Peck, B. Rusk, M. Spicuzza, S. Wilde, and T. Ushikubo for helpful conversations, and use of unpublished or in press data and figures. M. Diman and A. Valley assisted in drafting, and M. Spicuzza aided in preparation of this manuscript. We also thank A. Cavosie, D. Cole, R. Kozdon, D. Miller, K. Muehlenbachs, I. Orland, F. Z. Page for helpful reviews of this paper, and M. Fayek for editing this volume. WiscSIMS is partly supported by NSF-EAR (0319230, 0744079), DOE (93ER14389), and the NASA Astrobiology Institute.

REFERENCES

AGUE, J.J. (2007): Models of permeability contrasts in subduction zone mélange: Implications for gradients in fluid fluxes, Syros and Tinos Islands, Greece. *Chem. Geol*. **239**, 217-227.

ALÉON, J., CHAUSSIDON, M., MARTY, B., SCHUTZ, L. & JAENICKE, R. (2002): Oxygen isotopes in single micrometer-sized quartz grains: Tracing the source of Saharan dust over long-distance atmospheric transport. *Geochim. Cosmochim. Acta* **66**, 3351-3365.

ALEXANDRE, A., BASILE-DOELSCH, I., SONZOGNI, C., SYLVESTRE, F., PARRON, C., MEUNIER, J.-D. & COLIN, F. (2006): Oxygen isotope analyses of fine silica grains using laser-extraction technique: Comparison with oxygen isotope data obtained from ion microprobe analyses and application to quartzite and silcrete cement investigation. *Geochim. Cosmochim. Acta* **70**, 2827-2835.

ALLAN, M.M. & YARDLEY, B.W.D. (2007): Tracking meteoric infiltration into a magmatic-hydrothermal system: A cathodoluminescence, oxygen isotope and trace element study of quartz from Mt. Leyshon, Australia. *Chem. Geol*. **240**, 343-360.

AMBROSE, S. & KATZENBERG, M.A. (*eds*.) (2000): Biogeochemical Approaches to Paleodietary Analysis. Adv in Archaeol. and Mus. Sci. **5**, Kluwer Academic, New York.

APPLEBY, S.K., GRAHAM, C.M., GILLESPIE, M.R., HINTON, R.W. & OLIVER, G.J.H. (2008): A cryptic record of magma mixing in diorites revealed by high-precision SIMS oxygen isotope analysis of zircons. *Earth Planet. Sci. Lett*. **269**, 105-117.

ARNOLD, B.W., BAHR, J.M. & FANTUCCI, R. (1996): Paleohydrogeology of the Upper Mississippi Valley zinc-lead district. *In* Carbonate-hosted Lead-zinc Deposits (D. Sangster, *ed*.). Soc. Econ. Geol. **4**, pp. 378-389.

AYERS, J.C., LOFLIN, M., MILLER, C.F., BARTON, M.D. & COATH, C.D. (2006): In situ oxygen isotope analysis of monazite as a monitor of fluid infiltration during contact metamorphism: Birch Creek Pluton aureole, White Mountains, eastern California. *Geology*, **34**, 653-656.

BAO, H., THIEMENS, M.H., FARQUHAR, J., CAMPBELL, D.A., LEE, C.C., HEINE, K. & LOOPE, D.B. (2000): Anomalous ^{17}O compositions in massive sulphate deposits on the Earth. *Nature* **406**, 176-178.

BAR-MATTHEWS, M., AYALON, A., GILMOUR, M., MATTHEWS, A. & HAWKESWORTH, C.J. (2003): Sea-land oxygen isotopic relationships from planktonic foraminifera and speleothems in the Eastern Mediterranean region and their implication for paleorainfall during interglacial intervals. *Geochim. Cosmochim. Acta* **67,** 3181-3199.

BAUMGARTNER, L.P. & VALLEY, J.W. (2001): Stable Isotope Transport and Contact Metamorphic Fluid Flow: *In* Stable Isotope Geochemistry, *Rev. Min. & Geochem*. (J.W. Valley & D.R. Cole, *eds*.) **43**, 415-468.

BICKFORD, M.E., MCLELLAND, J.M., SELLECK, B.W., HILL, B.M. & HEUMANN, M.J. (2008): Timing of anatexis in the eastern Adirondack Highlands: Implications for tectonic evolution during *ca*. 1050 Ma Ottawan orogenesis. *Geol. Soc. Am. Bull.* **120**, 950-961.

BINDEMAN, I.N. & VALLEY, J.W. (2001): Low $\delta^{18}O$ rhyolites from Yellowstone: magmatic evolution based on analysis of zircons and individual phenocrysts. *J. Petrol*. **42**,1491-1517.

BINDEMAN, I.N. & VALLEY, J.W. (2002): Oxygen isotope study of the Long Valley magma system, California: isotope thermometry and convection in large silicic magma bodies. *Contr. Min. Petrol*. **144**, 185-205.

BINDEMAN, I.N., FU, B., KITA, N.T. & VALLEY, J.W. (2008): Origin and evolution of silicic magmatism at Yellowstone based on ion microprobe analysis of isotopically zoned zircons. *J. Petrol*. **49**, 163-193.

BLAMART, D., ROLLION-BARD, C., CUIF, J.-P. & JUILLET-LECLERC, A., LUTRINGER, A., VAN WEERING, T.C.E. & HENRIET, J.-P. (2006): C and O isotopes in a deep-sea coral (*Lophelia pertusa*) related to skeletal microstructure. *In* Cold-water corals and ecosystems (A. Freiwald & J.M. Roberts, *eds*.) Springer, 1005-1020.

BOLHAR, R., WEAVER, S.D., WHITEHOUSE, M.J., PALIN, J.M., WOODHEAD, J.D. & COLE, J.W. (2008): Sources and evolution of arc magmas inferred from coupled O and Hf isotope systematics of plutonic zircons from the Cretaceous Separation Point Suite (New Zealand). *Earth Planet. Sci. Lett*. **268**, 312-324.

BOOTH, A.L., KOLODNY, Y., CHAMBERLAIN, C.P., MCWILLIAMS, M., SCHMITT, A.K. & WOODEN, J. (2005): Oxygen isotopic composition and U-Pb discordance in zircon. *Geochim. Cosmochim. Acta* **69**, 4895-4905.

BOUVIER, A.-S., MÉTRICH, N., DELOULE, E. (2008) Slab-derived Fluids in Magma Sources of St-Vincent (Lesser Antilles Arc): Volatile and Light Element Imprints, *J. Petrol*. **49**, 8, 1427-1448.

BOWMAN J.R., VALLEY J.W. & KITA N.T. (2009): Mechanisms of oxygen isotopic exchange and isotopic evolution of $^{18}O/^{16}O$-depleted periclase zone marbles in the Alta aureole, Utah: Insights from ion microprobe analysis of calcite. *Contr. Min. Petrol.* **157**, 77-93.

BREECKER, D.O. & SHARP, D.Z. (2007): A monazite oxygen isotope thermometer. *Am. Mineral*. **92**, 1561-1572.

CAMPANA, S.E. (1999): Chemistry and composition of fish otoliths: pathways, mechanisms, and applications. *Mar. Ecol. Prog. Ser*. **188**, 263–297.

CATES, N.L. & MOJZSIS, S.J. (2006): Chemical and isotopic evidence for widespread Eoarchean metasedimentary enclaves in southern West Greenland. *Geochim. Cosmochim. Acta* **70**, 4229-4257.

CATHEY, H.E., NASH, B.P., VALLEY, J.W., KITA, N.T., USHIKUBO, T. & SPICUZZA, M.J. (2007): Pervasive and persistent large-volume, low $\delta^{18}O$ silicic magma generation at the Yellowstone hotspot: 12.7- 10.5 Ma: Ion microprobe analysis of zircons in the Cougar Point tuff. *Eos Trans. AGU*, **88**(52) Fall Meet. Suppl., Abstract V51C-0708.

CAVOSIE, A.J., KITA, N.T. & VALLEY, J.W. (2009): Magmatic zircons from the Mid-Atlantic Ridge: Primitive oxygen isotope signature. *Am. Mineral*. (in press).

CAVOSIE, A.J., VALLEY, J.W. & WILDE, S.A. (2005): Magmatic $\delta^{18}O$ in 4400-3900 Ma detrital zircons: A record of the alteration and recycling of crust in the Early Archean. *Earth Plan. Sci. Lett*. **235**, 663-681.

CAVOSIE, A.J., VALLEY, J.W. & WILDE, S.A. (2007): The oldest terrestrial mineral record: A review of 4400 to 4000 Ma detrital zircons from the Jack Hills, Western Australia. *In* Earth's Oldest Rocks. (M.J. van Kranendonk, R.H. Smithies & V.C. Bennett, eds.) *Devel. Precam. Geol*. **15**, 91-111.

CAVOSIE, A.J., VALLEY, J.W. & WILDE, S.A. (2006): Correlated microanalysis of zircon: Trace element, $\delta^{18}O$, and U-Th-Pb isotopic constraints on the igneous origin of complex >3900 Ma detrital grains. *Geochim. Cosmochim. Acta* **70**, 5601-5616.

CHAPPELL, B.W. & WHITE, J.R. (2004): Two contrasting granite types: 25 years later. *Austral. Jour. Earth Sci.* **48**, 489-499.

CHEN, Z., RICIPUTI, L.R., MORA, C.I. & FISHMAN, N.S. (2001): Regional fluid migration in the Illinois basin: Evidence from in situ oxygen isotope analysis of authigenic K-feldspar and quartz from the Mount Simon Sandstone. *Geology*. **29**, 1067-1070.

CHERNIAK, D.J. & WATSON, E.B. (2003): Diffusion in zircon. *In* Zircon. Reviews in Mineralogy & Geochemistry (J.H. Hanchar & P.W.O Hoskin, eds.) **53**, 113-144.

CLARK, I.D. & FRITZ, P. (1997): Environmental isotopes in hydrogeology. Lewis Publ., New York: 328 p.

CLAYTON, R.N. (2007): Isotopes: From Earth to the Solar System. *Annual Rev. Earth Planet. Sci*. **35**, 1-19.

CLAYTON, R.N. & MAYEDA, T.K. (1996): Oxygen isotope studies of achondrites. *Geochim. Cosmochim. Acta* **60**, 1999-2017.

CLAYTON, R.N., GROSSMAN, L. & MAYEDA, T.K. (1973): A component of primitive nuclear composition in carbonaceous meteorites. *Science* **182**, 485-488.

COLE, D.R., & CHAKRABORTY, S. (2001): Rates and mechanisms of kinetics of isotopic exchange in homogeneous and heterogeneous systems. *In* Stable Isotope Geochemistry, Rev. in Min. and Geochem. (J.W. Valley & D.R. Cole, *eds*.) **43**, 83–223.

COLE, D.R., LARSON, P.B., RICIPUTI, L.R. & MORA, C.I. (2004): Oxygen isotope zoning profiles in hydrothermally altered feldspars: Estimating the duration of water-rock interaction. *Geology* **32**, 29-32.

COOGAN, L.A., MANNING, C.E. & WILSON, R.N. (2007): Oxygen isotope evidence for short-lived high-temperature fluid flow in the lower oceanic crust at fast-spreading ridges. *Earth Planet. Sci.* **260**, 524-536.

COOK, S.J. & BOWMAN, J.R. (2000): Mineralogical evidence for fluid-rock interaction accompanying prograde contact metamorphism of siliceous dolomites: Alta Stock Aureole, Utah, USA. *Jour. of Petrology*, **41**, 739-757.

CORFU, F., HANCHAR, J.M., HOSKIN, P.W.O. & KINNY, P. (2003): Atlas of zircon textures. *In* Zircon. Reviews in Mineralogy & Geochemistry (J.H. Hanchar & P.W.O Hoskin, eds.) **53**, 469-500.

CRISS, R.R. (1999): Principles of stable isotope distribution. Oxford Press, 254p.

CROWE, D.E., RICIPUTI, L.R., BEZENEK, S. & IGNATIEV, A. (2001): Oxygen isotope and trace element zoning in hydrothermal garnets: windows into large-scale fluid-flow behavior. *Geology* **29**, 479-482.

DE GROOT, P.A., *ed*. (2004): *Handbook of stable isotope analytical techniques*. Vol. 1, Elsevier.

DESBOIS, G., INGRIN, J., KITA, N.T., VALLEY, J.W. & DELOULE, E. (2007): New constraints on metamorphic history of Adirondack diopsides (NY, USA): Al and $\delta^{18}O$ profiles. *Am. Mineral.* **93**, 453-459.

DOWNES, H., MITTLEFEHLDT, D.W., KITA, N.T. & VALLEY, J.W. (2008) Evidence from polymict ureilite meteorites for a disrupted and re-accreted single ureilite parent asteroid gardened by several distinct impactors. *Geochim. Cosmochim. Acta* **72**, 4825-4844.

EILER, J.M. (2001): Oxygen isotope variations of basaltic lavas and upper mantle rocks. *In* Stable Isotope Geochemistry, Rev. in Min. and Geochem. (J.W. Valley & D.R. Cole, eds.) **43**, 319-364.

EILER, J.M., GRAHAM, C. & VALLEY, J.W. (1997): SIMS analysis of oxygen isotopes: matrix effects in complex minerals and glasses. *Chem. Geol.* **138**, 221-244.

EILER, J.M., MCINNES, B., VALLEY, J.W., GRAHAM, C.M. & STOLPER, E.M. (1998): Oxygen isotope evidence for slab-derived fluids in the sub-arc mantle. *Nature* **393**, 777-781.

EILER, J.M., SCHIANO, P., VALLEY, J.W., KITA, N.T. & STOLPER, E.M. (2007): Oxygen-isotope and trace element constraints on the origins of silica-rich melts in the sub-arc mantle. G^3: *Geochem. Geophys. Geosyst*. **8**, #9, 21p, DOI:10.1029/2006GC001503.

EILER, J.M., VALLEY, J.W. & BAUMGARTNER, L.P. (1993): A new look at stable isotope thermometry. *Geochim. Cosmochim. Acta* **57**, 2571-2583.

EILER, J.M., VALLEY, J.W., GRAHAM, C.M. & FOURNELLE, J. (2002): Two populations of carbonate in ALH84001: Geochemical evidence for discrimination and genesis. *Geochim. Cosmochim. Acta* **66**,1285-1303.

EREZ, J. (2003); The source of ions for biomineralization in foraminifera and their implications for paleoceanographic proxies. *In* Biomineralization, Rev. in Min. and Geochem. (P.M. Dove, J.J. De Yoreo & S. Weiner, *eds*.) **54**, 115-149.

FAIRCHILD, I.J., SMITH, C.L., BAKER, A., FULLER, L., SPOTL, C., MATTEY, D. & MCDERMOTT, F. (2006): Modification and preservation of environmental signals in speleothems. *Earth Sci. Rev*. **75**, 105-153.

FARQUHAR, J., THIEMENS, M.H. & JACKSON, T. (1998): Atmosphere-surface interactions on Mars:

矿床地质论坛 http://bbs.gs001.com/

$D^{17}O$ measurements of carbonate from ALH 84001. *Science* **280**, 1580-1582.

FAYEK, M., HARRISON, T.M., GROVE, M., MCKEEGAN, K.D., COATH, C.D. & BOLES, J.R. (2001): *In situ* stable isotopic evidence for protracted and complex carbonate cementation in a petroleum reservoir, North Coles Levee, San Joaquin Basin, California, U.S.A. *J. Sed. Res*. **71**, 444-458.

FAYAK, M., HARRISON, T.M., EWING, R.C., GROVE, M. & COATH, C.D. (2002a): O and Pb isotopic analyses of uranium minerals by ion microprobe and U-Pb ages from the Cigar Lake deposit. *Chem. Geol*., **185**, 205-225.

FAYEK, M., RICIPUTI, L.R., MILFORD, H.E. & MATHIEN, F.J. (2002b): Sourcing turquoise using O and H isotopes. *Geol. Soc. Amer. Abstr with Prog.* **39** (6), p. 396.

FAYEK, M., UTSUNOMIYA, S., EWING, R.C., RICIPUTI, L.R. & JENSEN, K.A. (2003): Oxygen isotopic composition of nano-scale uraninite at the Oklo-Okélobondo natural fission reactors, Gabon. *Amer. Mineral*. **88**, 1583-1590.

FITZSIMONS, I.C.W., HARTE, B. & CLARK, R.M. (2000): SIMS stable isotope measurement: counting statistics and analytical precision. *Mineral. Mag*. **64**, 59-83.

FRANCHI, I.A., WRIGHT, I.P., SEXTON, A.S. & PILLINGER, C.T. (1999): The oxygen-isotopic composition of Earth and Mars. *Meterorit. Planet. Sci.* **34**, 657-661.

FU, B., PAGE F.Z., CAVOSIE, A.J., FOURNELLE, J., KITA, N.T., LACKEY, J.S., WILDE, S.A. & VALLEY, J.W. (2008): Ti-in-zircon thermometry: applications and limitations. *Contr. Min. Petrol*. **156**, 197-215.

FU B., MERNAGH T.P., KITA N.T., KEMP A.I.S., VALLEY J.W. (2009): Distinguishing magmatic zircon from hydrothermal zircon: a case study from the Gidginbung high-sulphidation Au-Ag-(Cu) deposit, SE Australia. *Chem. Geol.* **259**, 131-142. doi:10.1016/j.chemgeo.2008.10.035

GILETTI, B.J., SEMET, M.P. & YUND, R.A. (1978): Studies in diffusion: III, Oxygen and feldspars, an ion microprobe determination. *Geochim. Cosmochim. Acta* **42**, 45-57.

GIRARD, J.-P., MUNZ, I.A., JOHANSEN, J., HILL, S. & CANHAM, A. (2001): Conditions and timing of quartz cementation in Brent reservoirs, Hild Field, North Sea: constraints from fluid inclusions and SIMS oxygen isotope analysis. *Chem Geol*. **176**, 73-92.

GIULIANI, G., CHAUSSIDON, M., SCHUBNEL, H.J., PIAT, D.H., ROLLION, B.C., FRANCE-LANORD, C., GIARD, D. & RONDEAU, B. (2000): Oxygen isotopes and emerald trade routes since antiquity. *Science* **287**, 631-633.

GIULIANI, G., FALLICK, A.E., GARNIER, V., FRANCE-LANORD, C., OHNENSTETTER, D. & SCHWARZ, D. (2005): Oxygen isotope composition as a tracer for the origins of rubies and sapphires. *Geology* **33**, 249-252.

GIULIANI, G., FALLICK, A., RAKOTONDRAZAFY, M. OHNENSTETTER, D., ANDRIAMAMONJU, A., RALANTOARISON, T., RAKOTOSAMIZANANY, S., RAZANATSEHENO, M., OFFANT, Y., GARNIER, V., DUNAIGRE, C., SCHWARZ, D., MERCIER, A., RATRIMO, V. & RALISON, B. (2006): Oxygen isotope systematics of gem corundum deposits in Madagascar: relevance for their geological origin. *Mineral. Deposita* **42**, 251-270.

GNASER, H. & HUTCHEON, I.D. (1988): Preferential Emission of Lighter Isotopes in the Initial-Stage of Sputtering. *Surf. Sci.* **195**, 499-512.

GRAHAM, C.M., VALLEY, J.W., EILER, J.M. & WADA, H. (1998): Timescales and mechanisms of fluid infiltration in a marble: an ion microprobe study. *Contrib. Mineral Petrol.* **132**, 371-389.

GRAHAM, C.M., VALLEY, J.W. & WINTER, B.L. (1996): Ion microprobe analysis of $^{18}O/^{16}O$ in authigenic and detrital quartz in St. Peter sandstone, Michigan Basin and Wisconsin Arch, USA: Contrasting diagenetic histories. *Geochim. Cosmochim. Acta* **24**. 5101-5116.

GREENWOOD, J.P., BLAKE, R.E. & COATH, C.D. (2003): Ion microprobe measurements of $^{18}O/^{16}O$ ratios of phosphate minerals in the Martian meteorites ALH84001 and Los Angeles. *Geochim. Cosmochim. Acta* **67**, 2289-2298.

GRIFFITHS, H. (1998): Stable isotopes: Integration of biological ecological and geochemical processes. Bios Scientific Publishers, Oxford, UK: 438 p.

GURENKO, A.A. & CHAUSSIDON, M. (2002): Oxygen isotope variations in primitive tholeiites of Iceland: evidence from a SIMS study of glass inclusions, olivine phenocrysts and pillow rim glasses. *Earth Planet. Sci. Lett*. **205**, 63-79.

GURENKO, A.A., CHAUSSIDON, M. & SCHMINCKE, H.U. (2001): Magma ascent and contamination beneath one intraplate volcano; evidence from S and O isotopes in glass inclusions and their host clinopyroxenes from Miocene basaltic hyaloclastites southwest of Gran Canaria (Canary Islands). *Geochim. Cosmochim. Acta* **65**, 4359-4374.

HARLEY, S.L. & KELLY, N.M. (2007): The impact of zircon-garnet REE distribution on the interpretation of zircon U-Pb ages in complex high-grade terrains: an example from the Rauer Islands, East Antarctica. *Chem. Geol*., **241**, 62-87.

HARRISON, T.M., SCHMITT, A.K., MCCULLOCH, M.T. & LOVERA, O.M. (2008): Early (≥4.5 Ga) formation of terrestrial crust: Lu-Hf, $\delta^{18}O$, and Ti thermometry results for Hadean zircons. *Earth Plan. Sci. Lett*. **268**, 476-486.

HAURI, E. (2002): SIMS analysis of volatiles in silicate glasses, 2: isotopes and abundances in Hawaiian melt inclusions. *Chem. Geol*. **183**, 115-141.

HAWKESWORTH, C.J. & KEMP, A.I.S. (2006a): Evolution of the continental crust. *Nature* **443**, 811-817.

HAWKESWORTH, C.J. & KEMP, A.I.S. (2006b): Using hafnium and oxygen isotopes in zircons to unravel the record of crustal evolution. *Chem. Geol*. **226**, 144–162, doi:10.1016/j.chemgeo.2005.09.018.

HERVIG, R.L., WILLIAMS, L.B., KIRKLAND, I.K. & LONGSTAFFE, F.J. (1995): Oxygen isotope microanalyses of diagenetic quartz: possible low temperature occlusion of pores. *Geochim. Cosmochim. Acta* **59**, 2537-2543.

HERVIG, R.L., WILLIAMS, P., THOMAS, R.M., SCHAUER, S.N. & STEELE, I.M., (1992): Microanalysis of oxygen isotopes in insulators by secondary ion mass spectrometry. *Intern. J. of Mass Spectrom. and Ion Proc*. **120**, 45-63.

HINTON, R.W. (1995): Ion microprobe analysis in geology. *In* Microprobe techniques in Earth sciences. (P.J. Potts, J.J. Bowles, & S.J.B. Reed, eds.) Chapman and Hall, 235-289.

HOEFS, J. (2004): Stable Isotope Geochemistry, 5th ed. Springer, Berlin. 201pp.

HOLLAND, G., SAXTON, J.M., LYON, I.C. & TURNER, G. (2005): Negative $\delta^{18}O$ values in Allan Hills 84001 carbonate: Possible evidence for water precipitation on Mars. *Geochim. Cosmochim. Acta* **69**, 1359-1369.

HUBERTY, J.M., KITA, N.T., HECK, P.R., KOZDON, R., FOURNELLE, J.H., XU, H., VALLEY, J.W. (2009) Crystal orientation effects on bias of $\delta^{18}O$ in magnetite by SIMS. Goldsch. Conf., in press.

ICKERT, R.B., HEISS, J., WILLIAMS, I.S., IRELAND, T.R., LANC, P., SCHRAM, N., FOSTER, J.J. & CLEMENT, S.W. (2008): Determining high precision, in situ, oxygen isotope ratios with a *SHRIMP II*: Analyses of MPI-DING silicate glass reference materials and zircon from contrasting granites. *Chem. Geol*. **257**, 461-474.

IRELAND, T. (1995): Ion microprobe mass spectrometry: techniques and applications in cosmochemistry, geochemistry, and geochronology. *In* Advances in analytical geochemistry, (M. Hyman & M.W. Rowe, *eds*.). JAI Press 2, 1-118.

IRELAND, T. & WILLIAMS, I.S. (2003): Considerations in zircon geochronology by SIMS. *Rev. in Min. Geochem*. **53**, 215-242.

JAMTVEIT, B. & HERVIG, R.L. (1994): Constraints on transport and kinetics in hydrothermal systems from zoned garnet crystals. *Science* **263**, 505-508.

JOHNSON, C.M., BEARD, B.L. & ALBAREDE, F. (2004): Geochemistry of Non-traditional Stable Isotopes. *Rev. in Min. Geochem.* **55**. 454 p.

JULL, A.J.T., COURTNEY, C., JEFFREY, D.A. & BECK J.W. (1998): Isotopic evidence for a terrestrial source of organic compounds found in Martian meteorites Allan Hills 84001 and Elephant Moraine 79001. *Science* **279**, 366-369.

KELLY, J.L., FU, B., KITA, N.T. & VALLEY, J.W. (2007): Optically continuous silcrete cements of the St. Peter Sandstone: Oxygen isotope analysis by ion microprobe and laser fluorination. *Geochim. Cosmochim. Acta*. **71**, 3812-3832.

矿物地质论坛 http://blog.sina.com.cn/

KEMP, A.I.S., HAWKESWORTH, C.J., PATERSON, B.A. & KINNY, P.D. (2006): Episodic growth and the Gondwana Supercontinent from hafnium and oxygen isotopes in zircon. *Nature*, **439**, 580–583, doi: 10.1038/nature04505.

KEMP, A.I.S., HAWKESWORTH, C.J., FOSTER, G.L., PATERSON, B.A., WOODHEAD, J.D., HERGT, J.M., GRAY, C.M. & WHITEHOUSE, M.J. (2007a): Magmatic and crustal differentiation history of granitic rocks from Hf-O isotopes in zircon. *Science,* **315**, 980-983.

KEMP, A.I.S., SHIMURA, E. & HAWKESWORTH C.J. (2007b): Linking granulites, silicic magmatism, and crustal growth in arcs: Ion microprobe (zircon) U-Pb ages from the Hidaka metamorphic belt, Japan. *Geology* **35**, 807-810.

KEMP, A.I.S., HAWKESWORTH, C.J., PATERSON, B.A., FOSTER, G.L., KINNY, P.D. & WHITEHOUSE, M.J. (2008): Exploring the plutonic-volcanic link: a zircon U-Pb, Lu-Hf, and oxygen isotope study of paired volcanic and granitic units from southeastern Australia. *Trans. Royal. Soc. Edinburgh: Earth Sci*. **97**, 337-355.

KENDALL, C. & MCDONNELL, J.J. (1998): *Isotope tracers in catchment hydrology*. Elsevier Science BV, Amsterdam: 839 p.

KITA, N.T., IKEDA, Y., TOGASHI, S., LIU, Y.Z., MORISHITA, Y. & WEISBERG, M.K., (2004): Origin of ureilites inferred from a SIMS oxygen isotopic and trace element study of clasts in the Dar al Gani 319 polymict ureilite. *Geochim. Cosmochim. Acta*, **68**, 4213-4235.

KITA, N.T., NAGAHARA, H., TACHIBANA, S. & VALLEY, J.W. (2006): The systematic oxygen isotopic variations among chondrules from the least equilibrated ordinary chondrites: New ion microprobe study. *Lun. Plan. Sci. Conf.*, **37**, abstr. #1496.

KITA, N.T., NAGAHARA, H., TACHIBANA, S., FOURNELLE, J.H. & VALLEY, J.W. (2007a): Oxygen isotopic compositions of chondrule classes in Semarkona (LL3.0): Search for ^{16}O-depleted components in chondrules. *Lunar Planet. Sci. Conf. 38*, abstr. #1791.

KITA, N.T., USHIKUBO, T., FU, B., SPICUZZA, M.J. & VALLEY, J.W. (2007b): Analytical developments on oxygen three isotope analyses using a new generation ion microprobe IMS-1280. *Lunar Planet. Sci. Conf. 38,* abstr. #1981.

KITA, N.T., KIMURA, M., USHIKUBO, T. & VALLEY, J.W. (2008): Oxygen isotope systematics of chondrules from the least equilibrated H chondrite. *Lunar Planet. Sci. Conf. 39*, Abstr. #2059.

KITA, N.T., USHIKUBO, T., FU, B. & VALLEY J.W. (2009): High precision SIMS oxygen isotope analyses and the effect of sample topography, *Chem. Geol*., doi:10.1016/j.chemgeo.2009.02.012

KOHN, M.J. & VALLEY, J.W. (1994): Oxygen Isotope Constraints on Metamorphic Fluid Flow, Townshend Dam, Vermont, USA. *Geochim. Cosmochim. Acta* **58**, 5551-5566.

KOHN, M.J., VALLEY, J.W., ELSENHEIMER, D., & SPICUZZA, M. (1993) Oxygen Isotope Zoning in Garnet and Staurolite: Evidence for Closed System Mineral Growth During Regional Metamorphism. *Amer. Mineral*. 78, 988-1001.

KOLODNY, Y., BAR-MATTHEWS, M., AYALON, A. & MCKEEGAN, K.D. (2003): A high spatial resolution δ^{18}O profile of a speleothem using an ion microprobe. *Chem. Geol*. **197,** 21–28.

KOPP, R.E. & HUMAYUN, M. (2003): Kinetic model of carbonate dissolution in Martian meteorite ALH84001. *Geochim. Cosmochim. Acta* **67**, 3247-3256.

KOZDON, R., USHIKUBO, T., KITA, N.T. & VALLEY, J.W. (2009): Intratest oxygen isotope variability in planktonic foraminifera: New insights from in situ measurements by ion microprobe. *Chem. Geol*., **258**, 327-337.

KROT, A.N., YURIMOTO, H., MCKEEGAN, K.D., LESHIN, L., CHAUSSIDON, M., LIBOUREL, G., YOSHITAKE, M., HUSS, G.R., GUAN, Y. & ZANDA, B. (2006): Oxygen isotopic compositions of chondrules: Implications for evolution of oxygen isotopic reservoirs in the inner solar nebula. *Chemie der Erde - Geochemistry* **66**, 249-276.

LACKEY, J.S., VALLEY, J.W., CHEN, J.H. & STOCKLI, D.F. (2008): Dynamic Magma Systems, Crustal Recycling, and Alteration in the Central Sierra Nevada Batholith: The Oxygen Isotope Record. *J Petrol*. Doi:10.1093/petrology/egn030, **49**,1397-1426.

LANCASTER, P.J., FU, B., PAGE, F.Z., KITA, N.T., BICKFORD, M.E., HILL, B.M., MCLELLAND, J.M.

& VALLEY, J.W. (2009): Genesis of metapelitic migmatites in the Adirondack Mts., New York, *J. Meta. Geol*. **27**, 41-54.

LESHIN, L.A., MCKEEGAN, K.D., CARPENTER, P.K. & HARVEY, R.P. (1998): Oxygen isotopic constraints on the genesis of carbonates from Martian meteorite ALH 84001. *Geochim. Cosmochim*. *Acta* **62**, 3-13.

LIU, D., WILDE, S.A, WAN, Y., WANG, S., VALLEY, J.W., KITA, N.T., DONG, C., XIE, H., YANG, C., ZHANG, Y. & GAO, L. (2009): Combined U-Pb, hafnium and oxygen isotope analysis of zircons from metaigneous rocks in the southern North China Craton reveal multiple events in the Late Mesoarchean-Early Neoarchean. *Chem. Geol*. doi:10.1016/j.chemgeo.2008.10.041

LORIN, J.C., HAVETTE, A. & SLODZIAN, G. (1981): Isotope effect in secondary ion emission. *In* SIMS III, (A. Benninghoven, J. Giber, J. László, M. Riedel, & H.W. Werner, eds). 115-123.

LÜTTGE, A., BOLTON, E.W. & RYE, D.M. (2004): A kinetic model of metamorphism: An application to siliceous dolomites, *Contr. Min. Pet*., DOI: 10.1007 / s00410-003-0520-8, **146**, 546 - 565.

LYON, I.C., SAXTON, J.M. & CORNAH, S.J. (1998): Isotopic fractionation in secondary ionization mass spectrometry: crystallographic orientation effects in magnetite. *Intl. J. Mass Spectrom. Ion Proc.* **172**, 115-122.

LYON, I.C., BURLEY, S.D., MCKEEVER, P.J., SAXTON, J.M. & MACAULAY, C. (2000): Oxygen isotope analysis of authigenic quartz in sandstones; a comparison of ion microprobe and conventional analytical techniques. *In* Quartz cementation in sandstones (R.H. Worden & S. Morad, eds.) Spec. Pub. Internatl. Assoc. Sediment. **29**, 299-316.

MAHON, K.I., HARRISON, T.M. & MCKEEGAN, K.D. (1998): The thermal and cementation histories of a sandstone petroleum reservoir, Elk Hills, California: Part 2, *In situ* oxygen and carbon isotopic results. *Chem. Geol*. **152**, 257-271.

MARCHAND, A.M.E., MACAULAY, C.I., HASZELDINE, R.S. & FALLICK, A.E. (2002): Pore water evolution in oilfield sandstones: constraints from oxygen isotope microanalyses of quartz cement. *Chem Geol*. **191**, 285-304.

MARIGA, J., RIPLEY, E.M., LI, C., MCKEEGAN, K.D., SCHMIDT, A. & GROOVE, M. (2006): Oxygen isotopic disequilibrium in plagioclase-corundum-hercynite xenoliths from the Voisey's Bay Intrusion, Labrador, Canada. *Earth Planet. Sci.* **248**, 263-275.

MARTIN, L., DUCHENE, S., DELOULE, E. & VANDER HAEGHE, O. (2006): The isotopic composition of zircon and garnet: A record of the metamorphic history of Naxos, Greece. *Lithos* **87**, 174-192.

MARTIN, L.A.J., DUCHENE, S., DELOULE, E. & VANDERHAEGHE, O. (2008): Mobility of trace elements and oxygen in zircon during metamorphism: Consequences for geochemical tracing. *Earth Planet. Sci. Lett*. **267**, 161-174.

MATTEY, D., LOWRY, D. & MACPHERSON, C. (1994): Oxygen isotope composition of mantle peridotite. *Earth and Plan. Sci. Lett.* **128**, 231-241.

MCKAY, D.S., GIBSON, E.K., THOMAS-KEPRTA, K.L., VALI, H., ROMANEK, C.S., CLEMETT, S.J., CHILLIER, X.D.F., MAECHLING, C.R. & ZARE, R.N. (1996): Search for past life on Mars: Possible relict biogenic activity in martian meteorite ALH84001. *Science* **273**, 924-930.

MCKEEGAN, K.D. (1987): Oxygen isotopes in refractory stratospheric dust particles: proof of extraterrestrial origin. *Science* **237**, 1468-1471.

MCKEEGAN, K.D. & LESHIN, L.A. (2001): Stable isotope variations in extraterrestrial materials, *In* Stable Isotope Geochemistry, Rev. in Min. and Geochem. (J.W. Valley & D.R. Cole, eds.) **43**, 279–311.

MCKEEGAN, K.D. & 46 OTHERS (2006): Isotopic compositions of cometary matter returned by Stardust. *Science* **314**, 1724-1728.

MCKEEGAN K.D., JARZEBINSKI, G., MAO, P.H., COATH, C.D., KUNIHIRO, T., WIENS, R., ALLTON, J., CALLAWAY, M., RODRIGUEZ, M. & BURNETT, D.S. (2008): A first look at oxygen in a genesis concentrator sample. *Lunar Planet. Sci. Conf*. ***39***, abstr. #2020.

MILLER, M.F. (2002): Isotopic fractionation and the quantification of ^{17}O anomalies in the oxygen three-isotope system: an appraisal and geochemical significance. *Geochim. Cosmochim. Acta* **66**, 1881-1889.

http://bbs.sscnet.com/

MOJZSIS, S.J., HARRISON, T.M. & PIDGEON, R.T. (2001): Oxygen-isotope evidence from ancient zircons for liquid water at the Earth's surface 4,300 Myr ago. *Nature* **409**, 178-181.

MORA, C.I., RICIPUTI, L.R. & COLE, D.R. (1999): Short-lived oxygen diffusion during hot, deep-seated meteoric alteration of anorthosite. *Science* **286**, 2323-2325.

MOSER, D.E., BOWMAN, J.R., WOODEN, J., VALLEY, J.W., MAZDAB, F. & KITA, N. (2008): Creation of a Continent recorded in zircon zoning. *Geology* **36**, 239-242.

NAKAMURA, T., NOGUCHI, T., TSUCHIYAMA, A., USHIKUBO, T., KITA, N.T., VALLEY, J.W., ZOLENSKY, M.E., KAKAZU, Y., SAKAMOTO, K., MASHIO, E, UESUGI, K. & NAKANO, T. (2008): Chondrule-like objects in short-period comet 81P/Wild 2. *Science* **321**, 1664-1667.

NEMCHIN, A.A., PIDGEON, R.T. & WHITEHOUSE, M.J. (2006): Re-evaluation of the origin and evolution of >4.2Ga zircons from the Jack Hills metasedimentary rocks. *Earth Planet. Sci. Lett.* **244**, 218-233.

NIER, A.O. (1947): A mass spectrometer for isotope and gas analysis. *Review of Sci. Instr.* **18**, 398-411.

O'NEIL, J.R. (1986) Terminology and Standards. *In* "Stable Isotope in High Temperature Geological Processes", J.W. Valley, J.R. O'Neil, & H.P. Taylor, *eds*.) *Mineral. Soc. Am. Rev. in Mineralogy* **16**, 561-570.

O'NEIL, J.R. & CHAPPELL, B.W. (1977): Oxygen and hydrogen isotope relations in the Berridale batholith. *Jour. Geochem. Soc. London* **133**, 559-571.

ORLAND, I.J., BAR-MATTHEWS, M., KITA, N.T., AYALON, A., MATTHEWS, A. & VALLEY, J.W. (2009): Climate deterioration in the Eastern Mediterranean as revealed by ion microprobe analysis of a speleothem that grew from 2.2 to 0.9 ka in Soreq Cave, Israel. . *Quat. Res*. **71**, 27-35.

PACE, M.L, CARPENTER, S.R. COLE, J.J., COLOSO, J.J., KITCHELL, J.R., HODGSON, J.R., MIDDELBURG, J.J., PRESTON, N.D., SOLOMON, C.T. & WEIDEL, B.C. (2007): Does terrestrial organic carbon subsidize the food web in a clear-water lake? *Limnol. Oceanogr.* **52**, 2177-2189.

PAGE, F.Z., USHIKUBO, T., KITA, N.T., RICIPUTI, L.R. & VALLEY, J.W. (2007a): High precision oxygen isotope analysis of picogram samples reveals 2-μm gradients and slow diffusion in zircon. *Am. Mineral*. **92**, 1772-1775.

PAGE, F.Z., FU, B., KITA MARTIN, L., DUCHENE, S., DELOULE, E. & VANDERHAEGHE, N.T., FOURNELLE, J., SPICUZZA, M.J., SCHULZE, D.J., VILJOEN, V., BASEI, M.A.S. & VALLEY, J.W. (2007b): Zircons from kimberlites: New insights from oxygen isotopes, trace elements, and Ti in zircon thermometry. *Geochim. Cosmochim. Acta* **71**, 3887-3903.

PAGE, F.Z., KITA, N.T. & VALLEY, J.W. (2009): Ion microprobe analysis of oxygen isotopes in garnets of complex chemistry. *Chem. Geol*. (in review).

PECK, W.H., VALLEY, J.W., WILDE, S.A. & GRAHAM, C.M. (2001): Oxygen isotope ratios and rare earth elements in 3.3 to 4.4 Ga zircons: Ion microprobe evidence for high $\delta^{18}O$ continental crust and oceans in the Early Archean. *Geochim. Cosmochim. Acta* **65**, 4215-4229.

PECK, W.H., VALLEY, J.W. & GRAHAM, C.M. (2003): Slow oxygen diffusion rates in igneous zircons from metamorphic rocks. *Am. Mineral*. **88**, 1003-1014.

PIETRANIK, A.B., HAWKESWORTH, C.J., STOREY, C.D., KEMP, T.I., SIRCOMBE, K.N., WHITEHOUSE, M.J. & BLEEKER, W. (2008): Episodic, mafic crust formation from 4.5 to 2.8 Ga: New evidence from detrital zircons, Slave craton, Canada. *Geology*, **36**, 875–878, doi: 10.1130/G24861A.1.

REDDY, S.M., TIMMS, N.E., TRIMBY, P., KINNY, P.D., BUCHAN, C., BLAKE, K. (2006): Crystal plastic deformation of zircon: A defect in the assumption of chemical robustness. *Geology* **34**, 257-260.

RICIPUTI, L.R. & PATERSON, B.A. (1994): High spatial-resolution measurement of O isotope ratios in silicates and carbonates by ion microprobe. *Am. Mineral*. **79**, 1227-1230.

RICIPUTI, L.R., MACHEL, H.G. & COLE, D.R. (1994): An ion microprobe study of diagenetic carbonates in the Devonian Nisku Formation of Alberta, Canada. *Jour. Sed. Res*. **A64**, 115-127.

http://bbs.3s001.com/

RICIPUTI, L.R., PATERSON, B.A. & RIPPERDAN, R.L. (1998): Measurement of light stable isotope ratios by SIMS: Matrix effects for oxygen, carbon, and sulfur isotopes in minerals. *Internl. J. Mass. Spec*. **178**, 81-112.

ROBERT, F. & CHAUSSIDON, M. (2006) A paleotemperature curve for the Precambrian oceans based on silicon isotopes in cherts. *Nature* **443**, 969- 972.

ROBINSON, M.T. & OEN, O.S. (1963): Computer Studies of the Slowing Down of Energetic Atoms in Crystals, *Phys. Rev*. **132**, 6, 2385-2398.

ROLLION-BARD, C., BLAMART, D., CUIF, J.P. & JUILLET-LECLERC, A. (2004): Microanalysis of C and O isotopes of azooxanthellate and zooxanthellate corals by ion microprobe. *Coral Reefs*, **22**, 405-415.

ROLLION-BARD, C., EREZ, J. & ZILBERMAN, T. (2008): Intra-shell oxygen isotope ratios in the benthic foraminifera genus *Amphistegina* and the influence of seawater carbonate chemistry and temperature on this ratio. *Geochim. Cosmochim. Acta* **72**, 6006-6014.

RUSK, B., HOFSTRA, A., LEACH, D., LOWERS, H., KOENIG, A., VALLEY, J.W. & KITA, N.T. (2007): Combined cathodoluminescence, oxygen isotopes, and trace element study of vein quartz from several hydrothermal ore deposits. *Geol. Soc. Amer. Abstr w prog*. **39** (6) p. 396.

SAXTON, J.M., LYON, I.C. & TURNER, G. (1998): Correlated chemical and isotopic zoning in carbonates in Martian meteorite ALH84001. *Earth Planet. Sci.* **160**, 811-822.

SCHIEBER, J., KRINSLEY, D. & RICIPUTI, L. (2000): Diagenetic origin of quartz silt in mudstones and implications for silica cycling: *Nature* **406**, 981-985.

SCHMITT, A.K. (2006): Laacher See revisited: High-spatial-resolution zircon dating indicates rapid formation of a zoned magma chamber. *Geology* **34**, 597-600.

SCHMITT, A.K. & HULEN, J.B. (2008): Buried rhyolites within the active, high-temperature Salton Sea geothermal system. *Jour. Volc. Geotherm. Res*. **178**, 708-718.

SCHMITT, A.K., MARKS, M.A.W., NESBOR, H.D. & MARKEL, G. (2007): The onset and origin of differentiated Rhine Graben volcanism based on U-Pb ages and oxygen isotopic composition of zircon. *Eur J. Mineral*. **19**, 849-857.

SCHULZE, D.J., HARTE, B., VALLEY, J.W., BRENAN, J.M. & CHANNER, D.M.R. (2003): Extreme crustal oxygen isotope signatures preserved in coesite in diamond. *Nature* **423**, 68-70.

SCHULZE, D.J., HARTE, B., VALLEY, J.W. & CHANNER, D.M.D. (2004): Evidence of subduction and crust-mantle mixing from a single diamond. *Lithos*. **77**, 349-358

SCHUHMACHER, M., FERNANDES, F. & DE CHAMBOST, E. (2004): Achieving high reproducibility isotope ratios with the Cameca IMS 1270 in the multicollection mode. *Applied Sur. Sci.* **231-232**, 878-882.

SHARP, Z. (2007): Principles of Stable Isotope Geochemistry. Prentice Hall. 344 p.

SHIMIZU, N. & HART, S.R. (1982): Applications of the ion microprobe to geochemistry and cosmochemistry. *Ann. Rev. Earth Planet. Sci*. **10**, 483-526.

SILSBEE, R.H. (1957): Focusing in Collision Problems in Solids, *J. Applied Phys*. **28**, 1246-1250.

SLODZIAN, G. (1980): Microanalyzers using secondary ion emission: advances in electronics and electron physics. *In* Advances in Electronics and Electron Physics (A. Septier ed.), *Academic Press* ***138***, 1-44.

SLODZIAN, G. (1982): Dependence of ionization yields upon elemental composition: isotopic variations. *In* Secondary ion mass spectrometry, (A. Benninghoven, J. Giber, J. László, M. Riedel & H.W. Werner, eds.). *SIMS III*, 115-123.

SLODZIAN, G. (2004): Challenges in localized high precision isotope analysis by SIMS. *Applied Surf. Sci***. 231-232**, 2-12.

SLODZIAN, G., CHAINTREAU, M., DENNEBOUY, R. & ROUSSE, G. (2001): Precise in situ measurements of isotopic abundances with pulse counting of sputtered ions, *Eur. J. Applied Physics* **14**, 19 – 232.

SORENSEN, S., HARLOW, G.E. & RUMBLE, D.R., III (2006): The origin of jadeitite-forming subduction-zone fluids: CL-guided SIMS

地质学报 http://bbs.geojournals.cn/

oxygen-isotope and trace-element evidence. *Am. Mineral*. **91**, 979-996.

SPICUZZA, M.J., DAY, J.M.D., TAYLOR, L.A., VALLEY, J.W. (2007): Oxygen Isotope constraints on the origin and differentiation of the Moon. *Ear. Plan. Sci. Lett.* **253**, 254-265.

TIMMS, N.E., REDDY, S.M, KINNY, P.D., MOSER, D.E., NEMCHIN, A., EVANS, K., CLARK, C., HAMILTON, P.J. (2008): The effects of crystal plastic deformation on zircon geochemical systems. *Trans. Am. Geophys. Un. Abst.* MR21C-02.

TRAIL, D., MOJZSIS, S.J., HARRISON, T.M., SCHMITT, A.K., WATSON, E.B. & YOUNG, E.D. (2007): Constraints on Hadean zircon protoliths from oxygen isotopes, Ti-thermometry, and rare earth elements. *Geochem. Geophys. Geosystems* 8:6. Doi:10.1029/2006GC001449.

TREBLE, P.C., CHAPPELL, J., GAGAN, M.K., MCKEEGAN, K.D. & HARRISON, T.M. (2005): *In situ* measurement of seasonal $\delta^{18}O$ variations and analysis of isotopic trends in a modern speleothems from Australia. *Earth Plan. Sci. Lett.* **233**, 17-32.

TREBLE, P.C., SCHMITT, A.K., EDWARDS, R.L., MCKEEGAN, K.D., HARRISON, T.M., GROVE, M., CHEN, H. & WANG, Y.J. (2007): High resolution SIMS $\delta^{18}O$ analyses of Hulu Cave speleothem at the time of Heinrich event 1. *Chem. Geol.* **238,** 197-212.

TROTTER, J.A., WILLIAMS, I.S., BARNES, C.R., LECUYER, C. & NICOLL, R.S. (2008): Did cooling oceans trigger Ordovician biodiversification? Evidence from conodont thermometry. *Science* **321**, 550-554.

TYRA, M.A., FARQUHAR, J., WING, B.A., BENEDIX, G.K., JULL, A.J.T., JACKSON, T. & THIEMENS, M.H. (2007): Terrestrial alteration of carbonate in a suite of Antarctic CM chondrites: Evidence from oxygen and carbon isotopes. *Geochim. Cosmochim. Acta* **71**, 782-795.

UNKOVICH, M.J., PATE, J., MCNEILL, A. & GIBBS, J. (2001): Stable isotope techniques in the study of biological processes and functioning of ecosystems. Kluwer, Dordrecht: 289 p.

UPTON, B.G.J., HINTON, R.W., ASPEN, P., FINCH, A. & VALLEY, J.W. (1999): Megacrysts and associated xenoliths: Evidence for migration of geochemically enriched melts in the upper mantle beneath Scotland. *J. Petrol.*, **40**, 6, 935-956.

USHIKUBO, T., KITA, N.T., CAVOSIE, A.J., WILDE, S.A., RUDNICK, R.L. & VALLEY, J.W. (2008): Lithium in Jack Hills zircons: Evidence for extensive weathering of Earth's earliest crust. *Ear. Plan. Sci. Lett*. **272**, 666-676.

VALLEY, J.W. (2001): Stable isotope thermometry at high temperatures. *In* Stable Isotope Geochemistry, Rev. in Min. and Geochem. (J.W. Valley & D.R. Cole, eds.) **43**, 365-414.

VALLEY, J.W. (2003): Oxygen isotopes in zircon. *In* Zircon, Rev. in Min. and Geochem. (J.M. Hanchar & P.W.O Hoskin, eds.). **53**, 343-385.

VALLEY, J.W. & COLE, D.R. (2001): Stable isotope geochemistry. Rev. in Mineral., Vol. 43: 662 p.

VALLEY, J.W. & GRAHAM, C.M. (1991): Ion microprobe analysis of oxygen isotope ratios in metamorphic magnetite-diffusion reequilibration and implications for thermal history. *Contr. Mineral. Petrol.* **109**, 38-52.

VALLEY, J.W. & GRAHAM, C.M. (1996): Ion microprobe analysis of oxygen isotope ratios in quartz from Skye granite: healed micro-cracks, fluid flow, and hydrothermal exchange. *Contr. Mineral. Petrol.* **124**, 225-234.

VALLEY, J.W., CHIARENZELLI, J., & MCLELLAND, J.M. (1994): Oxygen Isotope Geochemistry of Zircon. *Earth. Planet. Sci. Letts.* **126**, 187-206.

VALLEY, J.W., EILER, J.M., GRAHAM, C.M., GIBSON, E.K., ROMANEK, C.S. & STOLPER, E.M. (1997): Low temperature carbonates in the Martian meteorite, ALH84001. *Science* **275**, 1633-1638.

VALLEY, J.W., GRAHAM, C.M., HARTE, B., KINNY, P. & EILER, J.M. (1998): Ion microprobe analysis of oxygen, carbon, and hydrogen isotope ratios. In: McKibben, M.A., *et al.* (eds), Soc. Econ. Geol. Rev. in Econ. Geol. 7, 73-98.

VALLEY, J.W., LACKEY, J.S., CAVOSIE, A.J., CLECHENKO, C.C., SPICUZZA, M.J., BASEI, M.A.S., BINDEMAN, I.N., FERREIRA, V.P., SIAL, A.N., KING, E.M., PECK, W.H., SINHA, A.K. & WEI, C.S. (2005): 4.4 billion years of crustal maturation: Oxygen isotopes in magmatic zircon. *Contr. Mineral. Petrol*. **150**, 561–580, doi: 10.1007/s00410-005-0025-8.

VALLEY, J.W., CAVOSIE, A.J., FU, B., PECK, W.H. & WILDE, S.A. (2006): Comment on "Heterogeneous Hadean Hafnium: Evidence of Continental Growth at 4.4 to 4.5 Ga". *Science* **312**, 1139a.

VALLEY, J.W., USHIKUBO, T. & KITA, N.T. (2007): *In situ* Analysis of Three Oxygen Isotopes and OH in ALH 84001: Further Evidence of Two Generations of Carbonates. *Lunar Planet. Sci. Conf*. **38**, abstr. #1147.

VIELZEUF, D., CHAMPENOIS M., VALLEY J.W., BRUNET F. & DEVIDAL J.L. (2005a): SIMS analysis of oxygen isotopes: Matrix effects in Fe-Mg-Ca garnets. *Chem. Geol*. **223**, 208-226.

VIELZEUF, D., VESCHAMBRE, M. & BRUNET, F. (2005b): Oxygen isotope heterogeneities and diffusion profile in composite metamorphic-magmatic garnets from the Pyrenees. *Am. Mineral.* **90**, 463-472.

WEHNER, G.K. (1956): Controlled Sputtering of Metals by Low-Energy Hg Ions, Phys. Rev. **102**, 3, 690-704.

WATSON, E.B. & BAXTER, E.F. (2007): Diffusion in solid-earth systems. *Ear. Plan. Sci. Lett.* **253**: 307-327.

WEIDEL, B.C., USHIKUBO, T., CARPENTER, S.R., KITA, N.T., COLE, J.J., KITCHELL, J.F., PACE, M.L. & VALLEY, J.W. (2007): Diary of a bluegill (*Lempomis macrochirus*): daily $\delta^{13}C$ and $\delta^{18}O$ records in otoliths by ion microprobe. *Can. J. Fish. Aquat. Sci*. **64**, 1641-1645.

WHITEHOUSE, M.J. & NEMCHIN, A.A. (2009): High precision, high accuracy measurement of oxygen isotopes in a large lunar zircon by SIMS. *Chem. Geol*. **261**: 31-41.

WIECHERT, U., HALLIDAY, A.N., LEE, D.-C., SNYDER, G.A., TAYLOR, L.A. & RUMBLE, D. (2001): Oxygen isotopes and the Moon forming giant impact. *Science* **284**, 345-348.

WILDE, S.A., VALLEY, J.W., PECK, W.H. & GRAHAM, C.M. (2001): Evidence from detrital zircons for the Existence of continental crust and oceans on the Earth 4.4 Gyr ago. *Nature* **409**, 175-178.

WILDE, S.A., VALLEY, J.W., KITA, N.T., CAVOSIE, A.J. & LIU, D. (2008): SHRIMP U-Pb and CAMECA 1280 oxygen isotope results from ancient detrital zircons in the Caozhuang quartzite, Eastern Hebei, N. China Craton: Evidence for crustal reworking 3.8 Ga ago. *Am. J. Sci*. **308**, 185–199, doi: 10.2475/03.2008.01.

WILLIAMS, L.B., HERVIG, R.L. & BJORLYKKE, K.. (1997a): New evidence for the origin of quartz cements in hydrocarbon reservoirs revealed by oxygen isotope microanalyses. *Geochim. Cosmochim. Acta* **61**, 2529-2538.

WILLIAMS, L.B., HERVIG, R.L. & DUTTON, S.P. (1997b): Constraints on paleofluid compositions in the Travis Peak Formation, East Texas: evidence from microanalyses of oxygen isotopes in diagenetic quartz. *In* Basin-wide diagenetic patterns: integrated petrologic, geochemical, and hydrologic considerations. (I.P. Montanez, J.M. Gregg & K. Shelton, eds.), *SEPM* **57**, 269-279.

YUI, T.-F., WU, C.-M., LIMTRAKUN, P., SRICHARN, W. & BOONSOONG, A. (2005): Oxygen isotope studies on placer sapphire and ruby in the Chanthaburi-Trat alkali basaltic gemfield, Thailand. *Lithos* **86**, 197-211.

ZAHNLE, K.J. (2006): Earth's earliest atmosphere. *Elements* **2**, 217-222.

ZAW, K., SUTHERLAND, F.L., DELLAPASQUA, F., RYAN, C.G., YUI, T.-F., MERNAGH, T.P. & DUNCAN, D. (2006): Contrasts in gem corundum characteristics, eastern Australian basaltic fields: trace elements, fluid/melt inclusions and oxygen isotopes. *Mineral. Mag*. **70**, 669-687.

ZINNER, E. (1989): Isotopic measurements with the ion microprobe. *In* New frontiers in stable isotopic research: laser probes, ion probes, and small-sample analysis (W.C. Shanks, III & R.E. Criss, eds.), U.S. Geol. Survey. Bull. 1890, 145–162.

矿床地质杂志 http://kcdz.ijournals.cn/

顶级地质论坛：http://bbs.3s001.com/

CHAPTER 3: HYDROGEN, CARBON, NITROGEN, AND SULFUR ISOTOPE MICROANALYSES BY SECONDARY ION MASS SPECTROMETRY

Mostafa Fayek
Department of Geological Sciences
University of Manitoba
Winnipeg, MB Canada, R3T 2N2
fayek@cc.umanitoba.ca

INTRODUCTION

In situ measurements are important in many geoscience applications because much of the information relating to the origin and evolution of rock and fluid systems is retained at scales smaller than individual mineral grains (*e.g.*, Reed 1989 1990). The stable isotopic ratios of hydrogen (H), carbon (C), nitrogen (N), and sulfur (S) undergo significant mass fractionation during many geochemical processes, and can be used to determine the temperatures of fluids, trace fluid–rock interactions, and identify biological processes. Therefore, the development of *in situ* micro-analytical measurement techniques for isotopic ratios of these elements has remained important.

Secondary ionization mass spectrometry (SIMS) or the ion microprobe is a technique that was developed to provide *in situ* measurement of isotopic ratios with a spatial resolution on the scale of a few μm. SIMS analysis uses a focused beam of primary ions (a few μm in diameter) to bombard a solid sample surface in order to obtain a small-scale localized analysis. The bombardment or "sputtering" removes atoms from the polished surface of the specimen (Fig. 3-1). Some of these atoms are ionized during the process and can be focused and accelerated as a "secondary" beam through a slit and into a mass spectrometer (Reed 1989). The relatively high ionization probability for many elements during sputtering, allows measurement of isotope ratios for major and trace elements as well as determining elemental abundances in thin sections and individual grains (Neal *et al*. 1995). A typical analysis consumes a few nanograms of material and therefore SIMS is considered a relatively non-destructive technique (Ireland 2004). Consequently, SIMS is ideal for many studies, and over the past ~30 years considerable effort has been made to develop precise and accurate methods for the analysis of the isotopic ratios of many elements by SIMS (*e.g.*, McKeegan 1987, Nutman & Collerson 1991, Valley & Graham 1991 1996, Liu *et al*. 1992, Hervig *et al*. 1992, Anders & Zinner 1993, Riciputi & Paterson 1994, Eiler *et al*. 1997a, b, Leshin *et al*. 1998, Valley *et al*. 1998).

Secondary ion mass spectrometers typically used for stable isotope analysis are complicated instruments that consist of a multitude of deflectors, lenses, and apertures to guide the trajectory of the ion beams, as well as slits and mass and energy filters to separate or reduce the effects of molecular interferences. Therefore, numerous methods have been developed over the years to obtain precise stable isotopic ratios from a variety of minerals. This chapter discusses the methodology used for collecting high precision *in situ* hydrogen, carbon,

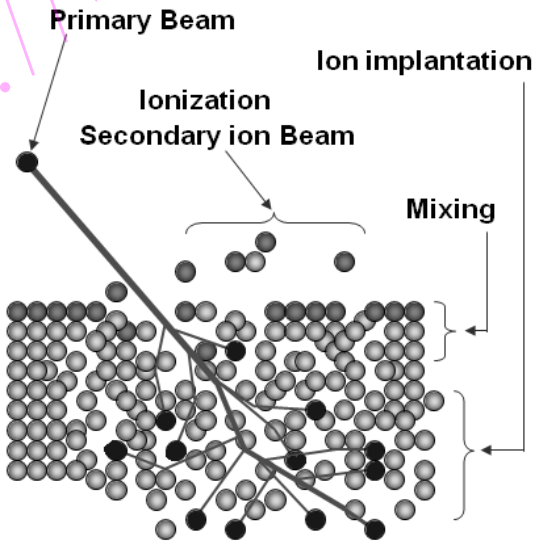


*FIG. 3-1. Schematic cross section of a collision cascade showing the implantation of the primary beam ions into the matrix, the generation of the secondary beam of ions, and mixing between layers (in the third dimension) in complex stratified samples. Geological samples are generally considered homogeneous in the third dimension; however, researchers should be aware that thin layers or inclusions can contribute to the secondary ion beam signal.

Mineralogical Association of Canada Short Course 41, Toronto, May 2009, p. 65-88

nitrogen and sulfur isotopic analyses from selected minerals. The second part of the chapter will show how these methods have been applied to study chemically complex mineral systems from a variety of geological environments. Oxygen isotope analysis by SIMS is discussed in a separate chapter in this volume. Although this chapter attempts to provide some general recipes for H, C, N, and S isotopic analysis by SIMS, the reader should keep in mind that recipes for analysis depend on the mineral of interest (*e.g.*, anhydrous *vs*. hydrous), the type of instrument used (*e.g.*, large or small radius instruments) as well as the age of instrumentation (*e.g.*, CAMECA 3f *vs*. CAMECA 7f) because each instrument may have a unique configuration and capabilities have changed significantly. A more detailed review of historical developments can be found in Shimizu & Hart (1982), Zinner (1989), Ireland (1995, 2004), Harmon & Hinton (1992), Hinton (1995), McKibben & Shanks (1998), and Valley *et al*. (1998). Benninghoven *et al*., (1987) gives a comprehensive review of instrument design and ion trajectory calculations.

GENERAL PRINCIPLES OF SECONDARY ION MASS SPECTROMETRY

In secondary ion mass spectrometry, a primary beam of ions with energies typically between 10 and 20 keV is generated, accelerated and focused onto a sample surface (*i.e.*, target). The impact of these primary ions erodes or sputters the surface, which causes a fraction of the atoms and molecules to become ionized (Fig. 3-1). These secondary ions are then electrostatically transferred from the sample surface into a mass spectrometer where they are separated according to mass and energy before they are introduced into a detector (Ireland 2004). Accelerating voltages of secondary ion beams are typically 5–10 keV.

The primary column is generally at an angle of 20–45° away from normal to the sample surface where it has been shown that there is optimal secondary ion emission. An exception is the CAMECA nanoSIMS, where both the primary and secondary ion beams are co-axial and normal to the sample surface (Ireland 2004). This is one of the features that enables extremely small spots (50 nm) on the nanoSIMS to be obtained.

The primary beam is typically composed of ^{16}O or ^{133}Cs (cesium) because these elements produce enhanced ionization of electropositive and electronegative species, respectively (Ireland 1995). Most lithophile metal elements are best analyzed with an oxygen primary beam, whereas the halogens and other electronegative species are preferentially ionized by a Cs primary beam. A Cs primary beam is in the form of Cs^+, whereas O primary beams can either be O^-, O_2^+, or O_2^-. The secondary column extraction voltage and secondary ion beam are generally opposite polarity to the primary column voltage and ion beam. The oxygen primary beam is usually generated in a duoplasmatron, which consists of a cold hollow cathode, an intermediate electrode, surrounding magnetic fields to shape the plasma, and the anode extraction aperture where the ion beam is formed (Coath & Long 1995). The O beam that is generated consists of an outer ring of O^- ions and a central portion that is dominated by O^+ ions (Coath & Long 1995). Movement of the intermediate electrode allows the operator to select O^- or O^+ beams. The Cs beam is generated in a thermal ion gun, where a reservoir consisting of a pellet of Cs-carbonate, Cs-chromate or Cs-silicate is heated to cause vaporization of the Cs pellet. The Cs vapor is passed through a heated frit that causes ionization of the Cs. The impact of the primary ion beam transfers energy and charge (– or +) to the sample. Therefore, the spot can charge up and the sample potential can change. This charge build-up can cause the deflection of the secondary ion beam such that it is no longer focused through the mass spectrometer, and can reduce and destabilize secondary ion emission such that secondary ion signals degrade over a period of time. Charge build-up is particularly severe for insulating minerals such as carbonates and silicates and less severe for conducting and semi-conducting materials such as some sulfides and oxides. Therefore, for SIMS of geological and biological materials a method to compensate for the charge build-up is necessary. For analysis with an O^- primary ion beam (and positive secondary ion extraction), the negative charge build-up can be dissipated by coating the samples with a thin conductive layer (*e.g.*, C, Au, Au–Pd). Analysis using a Cs^+ primary ion beam presents the greatest analytical challenge because a positive charge builds up on the surface, which cannot be handled by the thin conductive layer alone. It is for this reason that O_2^+ beams are generally not used for analysis of non-conductive geological or biological material. However, for O, C and S stable isotope analysis, a Cs^+ primary beam is required, therefore most instruments are equipped with an electron flood gun, which delivers electrons onto the surface of the sample to neutralize the

positive charge build-up (Slodzian *et al*. 1987, Lyon *et al*. 1994, Saxton *et al*. 1996, Ireland 2004). Regardless of the method used to compensate for charge build-up, of primary concern is that a stable secondary beam of ions can be generated and that the composition of the secondary ion beam reflects the composition of the target. Therefore, in addition to sufficient charge compensation, the extraction field geometry is also improved by the use of well polished samples. Under these conditions, stable secondary ion signals can be sustained for several hours.

Isobaric Interferences

Geological materials are not chemically simple compounds and secondary ion mass spectra of geological materials can be quite complicated. Isobaric interferences can be in the form of atomic or molecular (*i.e.*, hydrides, oxides, *etc.*). For most elements, atomic isobars can be avoided by selection of an alternative isotope. However, molecular interferences are a little more difficult to avoid. Therefore, to produce sufficient mass dispersion to eliminate or reduce all possible isobaric interferences from the isotopes of interest, and to produce stable ion beams suitable for high-precision isotope measurements, a mass analyzer is required. Consequently, most SIMS used for the isotopic analysis of geological material are of the magnetic sector variety rather than quadrupole or time-of-flight SIMS.

Sputtering produces secondary ions with a variety of energies (Fig. 3-2). Consequently, a double focusing mass spectrometer is required so that secondary ion beams with a range of energies can be focused. A double focusing SIMS consists of an electrostatic analyzer (ESA) and a magnet (see chapter 1, this volume). The ESA disperses the ions according to energy and the magnet refocuses these ions on the basis of energy and mass. Therefore, isobaric interferences can be separated or reduced using two methods: (1) mass resolution, also referred to as mass-resolving power or (2) energy-filtering.

Mass resolution is defined as M/ΔM where ΔM is the full width at 10% height of a peak (Fig. 3-3a). The mass resolving power is the peak to valley ratio between adjacent equal size peaks separated by one mass unit and is achieved by using a large magnet and adjusting the exit slit located after the magnet. If an interfering species is small, it may not contribute to the analysis even though a valley between the peaks is not defined (Fig. 3-3b). For example, there is a valley between M1 and M2, but there is no valley between M2 and M3 (Fig. 3-3b). However, interfering mass M3 is small compared to the desired mass M2. Therefore, at 10% peak height M3 contributes very little to the M2 signal. Although an interfering species may be fully resolved at the 10% level, higher mass resolution may be required, if the interfering species is large and contributes to the measurement. Therefore, it is often necessary to monitor or measure the potential interfering masses or to avoid possible interfering masses by selecting a different isotope of the element of interest.

Molecular interferences can also be excluded by energy filtering (Shimizu & Hart 1982, McIntyre

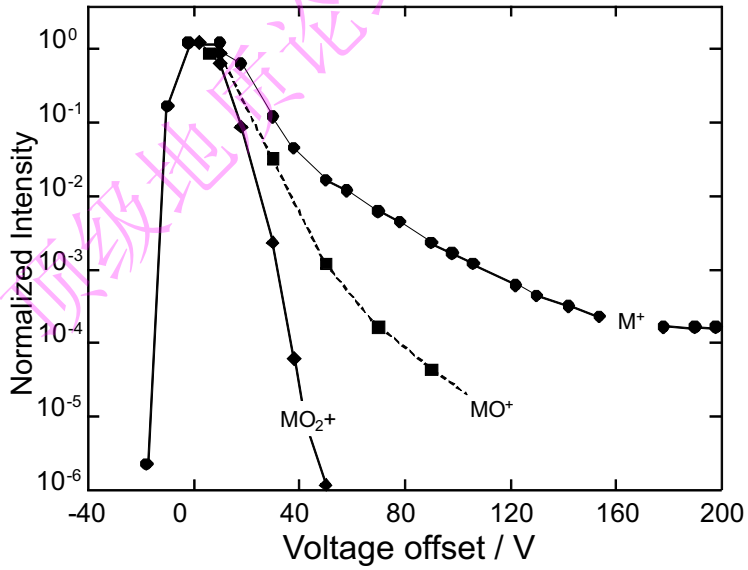


FIG. 3-2. A plot of normalized intensities for secondary ions of molecules of a hypothetical substrate M-oxide, where M represents any element (*e.g.*, Si), and M *vs*. voltage offset. Note the relative intensities of all three M species are the same at 0 volt offset. However, the intensities of the molecules drop off significantly as the voltage offset is increased, while the intensity of the M ion remains relatively high at 200 V offset. Therefore, using energy filtering (applying a voltage offset) removes potentially interfering molecular ions (modified from Ireland 1995).

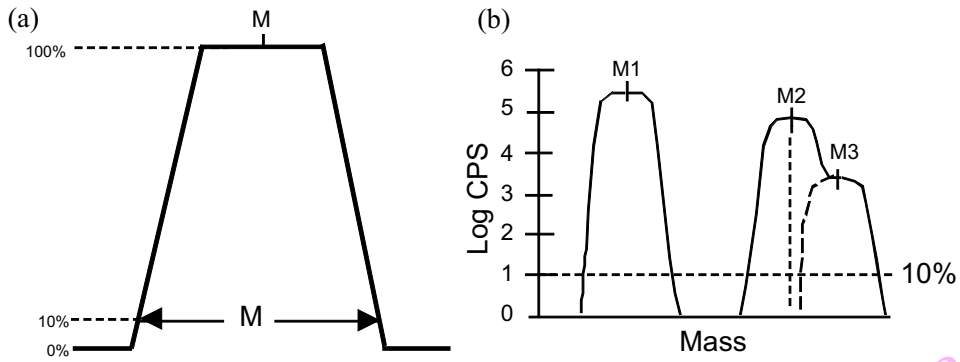


FIG. 3-3. Schematics of peaks showing mass resolution, mass resolving power, and estimation of the contribution to a peak from an interference. **(a)** A linear representation of peak shape illustration the flat top peak shape essential for producing high precision isotope ration analysis. Mass resolution, in this case defined at the 10% level is given by M/ΔM. **(b)** Peak M1 is clearly separated from peaks M2 and M3. However, peak M2 is not clearly resolved from peak M3 (modified from Ireland 2004). Abbreviations: CPS= counts per second, M= mass.

et al. 1985, Zinner & Crozaz 1986, Hervig *et al*. 1992). As mentioned above, secondary ions have a range of energy levels and polyatomic ions have a narrower energy distribution than the atomic ions (Fig. 3-2). For a hypothetical metal (M)-oxide substrate (Fig. 3-2), the relative intensities of all three M species are the same at 0 V offset. However, the intensities of the molecules drop off significantly as the voltage offset is increased, while the intensity of the M ion remains relatively high at 200 V offset. The energy filtering process is achieved by selecting a suitable energy window that will extract secondary ions with a specific kinetic energy, which the interfering molecular species do not possess, thus reducing or eliminating the molecular isobaric species. Energy filtering is generally used when magnets are not sufficiently large (*e.g.*, small radius instruments) to produce the desired mass dispersion to separate molecular interferences. However, when energy filtering is used up to 90% of the signal is eliminated. Therefore, in stable isotope analysis using the energy filtering method, where the minor isotope may be in very low abundance, longer analysis times may be required to obtain the desired precision. Fortunately, there are no atomic isobaric interferences for the light stable isotopes. The only interferences that must be considered are hydride interferences that require medium mass resolution (~1000–6000) or can be minimized (but not eliminated) using energy filtering.

Instrumental Mass Fractionation (IMF) and Mass Bias

A characteristic of SIMS is that the lighter isotope is generally ionized preferentially relative to the heavier isotope such that the observed isotope ratios of the secondary ion beam are typically enriched in the light isotopes relative to that of the target. The principles governing secondary ion mass spectrometry are not well understood. Therefore, it has not been possible to derive a quantitative or theoretical model with sufficient accuracy and precision (*e.g.*, ‰) necessary for stable isotope analysis that predicts the abundances of the secondary ion species relative to the actual concentration in the matrix.

While the development of the flood gun, energy filtering and multicollector detection system (see below) has improved precision, accuracy can remain poor if standards are not chemically or in some cases structurally similar to unknown materials because of the existence of compositionally dependent fractionations that are commonly referred to as “matrix effects” (*e.g.*, Ireland 1986, Valley *et al*. 1997). The intrinsic mass-dependent bias introduced during measurement of isotope ratios is referred to as instrumental mass fractionation (IMF). This effect is common to all forms of isotopic analysis and can limit measurement accuracy if appropriate corrections are not implemented. Therefore, IMF must be well characterized and stabilized. A variety of processes combine to produce the observed IMF. These include secondary atom extraction (sputtering) and ionization (Sigmund 1969, Shroeer *et al*. 1973, Williams 1979, Yu & Lang 1986), secondary ion transmission (Shimizu & Hart 1982), and detection (Valley & Graham 1991, Lyon *et al*. 1994). The contributors to the IMF that depend most strongly upon sample characteristics (*i.e.*, sputtering and ionization) are the sources of what are referred to as

matrix effects. Use of different analytical conditions, most notably energy filtering, can significantly influence the relationship between IMF and composition (*e.g.*, Hervig *et al*. 1992). While isotopic fractionation in a single element sample (Slodzian *et al*. 1980, Shimizu & Hart 1982, Weathers *et al*. 1993) is well documented and qualitatively explicable by secondary ion product-ion theory, the physics of matrix effects is relatively unknown and must be calibrated empirically.

In SIMS analysis, IMF is corrected for by comparing measurements of a chemically and isotopically homogeneous mineral standard that is compositionally similar to the unknown. SIMS results from the standard are compared to their accepted isotopic compositions in order to compute a correction factor that is applied to the unknown samples measured during the same analysis session (*e.g.*, Leshin *et al*. 1998). To the extent that the composition of the unknown sample differs from the standard, additional corrections must be performed for matrix effects. Variation of matrix effects with composition have been explored for oxygen isotope ratios in silicates (McKeegan 1987, Lorin *et al*. 1990, Hervig *et al*. 1992, Jamtveit & Hervig 1994, Riciputi & Paterson 1994, Yurimoto *et al*. 1994, Leshin *et al*. 1998, Eiler *et al*. 1997a, Valley *et al*. 1997), binary alloys (Slodzian *et al*. 1980, Shimizu & Hart 1982), and carbonates (Eiler *et al*. 1997b, Leshin *et al*. 1998, Saxton *et al*. 1998, Riciputi *et al*. 1998, Valley *et al*. 1998), whereas Riciputi *et al*. studied sulfur isotopes and matrix effects in sulfides. The combination of IMF and matrix effects is known as mass bias.

Material Selection for Standards and Sample Preparation

The majority of SIMS instruments only accept one inch (2.25 cm) round samples or smaller samples that can be placed in masked sample holders (Fig. 3-4, top left). Samples must fit within these round holders and make contact with the holders, be flat and flush with the top of the holders as well as well polished, and must be sufficiently conductive when coated with a thin layer of conductive material (*e.g.*, Au). Samples and standards can be either in the form of grain mounts embedded in vacuum-safe epoxy (*e.g.*, Buehler "*Epoxide*" or "*Epothin*" epoxy resin) or indium (In) metal, and round thick or thin sections (Fig. 3-4, lower right). The amount of epoxy used should be minimized because epoxy out-gasses, which can increase background hydrogen levels and increase the hydride ion yields. Unfortunately, at this time SIMS instruments cannot accept typical rectangular polished thin sections. It is also preferable that standards and samples are mounted in the same sample block to reduce errors associated with different sample holders. However, SIMS standards are typically rare. Therefore, researchers often have standards on one mount that is continually re-used and samples are mounted on a different block.

As mentioned above, the intrinsic mass-dependent bias introduced during measurement of isotope ratios is common to all forms of isotopic analysis and can limit measurement accuracy if appropriate corrections are not implemented. Therefore, mass bias must be well characterized and

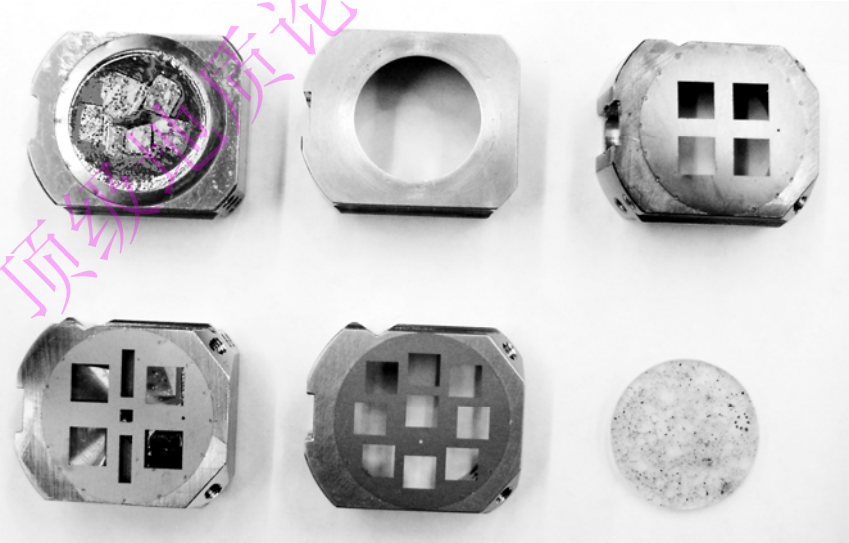


*FIG. 3-4. Image of a variety of sample holders used for SIMS analysis. The holder on the top left contains a gold-coated sample. Single hole sample holders (left top two) can hold grain mounts or round thin sections (lower right). Multiple hole sample holders can hold smaller samples. Color available at http://www.mineralogicalassociation.ca/index.php?p=160

顶级地质论坛 http://bbs.sinoss.com/

stabilized by comparing measurements of a chemically and isotopically homogeneous, well polished mineral standard that is compositionally similar to the unknown. Therefore, the ability to assess analytical precision and accuracy depends on the stability of the instrument during the analytical period, which includes extraction field geometry, the similarity in chemical composition of the standard relative to the unknown, and homogeneity of the standard at the micrometer scale. The homogeneity of the standard at the micrometer scale is difficult to establish because most traditional analytical methods (*e.g.*, conventional mass spectrometry) require bulk, powdered samples. Only when the level of homogeneity can be reliably determined at the micrometer scale, can the level of analytical reproducibility be established. For that reason, good SIMS standards are very valuable both in calibrating instrumental mass fractionation and to assess measurement statistics. A great deal of effort is expended in calibrating and assessing standards for SIMS analysis.

STABLE ISOTOPE ANALYSIS BY SIMS

Two types of isotope measurements can be made by SIMS; those where only two isotopes are measured and those where three or more isotopes are analyzed. Where only two isotopes are measured, mass bias is calibrated to an external standard of the same mineralogical composition and known isotopic composition. This is the most common method used for stable isotope analysis. Where three isotopes or more are analyzed, one of the ratios can be used for an internal calibration such that the deviations of third isotope ratio from a mass fractionation law can be used to derive a residual. This method can be used to determine mass-independent fraction effects. For a more detailed discussion of the mass fractionation laws and the multiple isotope ratio method see Esat (1984) and Ireland (2004).

A great deal of stable isotope technique development has been associated with analysis of extraterrestrial materials because stable isotope fractionation in these samples can be extreme (*e.g.*, percent fractionation) and therefore analytical precision at the sub-permil level is not necessary. In addition, mass-independent fractionation (*e.g.*, ^{16}O anomalies) is common (*e.g.*, McKeegan *et al*. 1998) and so limitations imposed from the determination of IMF are not as stringent. The quest for improved precision comes from the requirements for stable isotopic analysis of terrestrial samples.

For stable isotopic measurements by most current SIMS instruments, the selected area is sputtered with a 10 keV Cs^+ primary beam which generates a secondary negative ion beam of the desired element (*e.g.*, H, C, S). Initially, the SIMS technique for electrically insulating samples (*i.e.*, carbonates and silicates) was hampered by both imprecision (±3–5‰, for $^{18}O/^{16}O$, 1σ, point to point reproducibility) due to low count rates and charging of the sample during analyses and by variable IMF (McKeegan 1987, Giletti & Shimizu 1989, Lorin *et al*. 1990, Yurimoto *et al*. 1994). The development of the normal incident electron 'flood gun', which avoids the charging of insulating samples, has helped improve precision. Internal and point-to-point reproducibility are now routinely ±1.0‰ and sometimes as good as ±0.1‰, 1σ (Hervig *et al*. 1992, Riciputi & Paterson 1994, Valley & Graham 1996, Eiler *et al*. 1997a, Valley *et al*. 1997, Leshin *et al*. 1998, Mahon *et al*. 1998, Fayek *et al*. 2001, Valley & Kita 2009). Some studies analyzed secondary ions with initial kinetic energies greater than 300 eV (energy filtering) and used shorter dead times (~15 ns) for the electron multipliers and obtained ~1.0‰ precision (Eiler *et al*. 1997a 1997b, Valley *et al*. 1998). This precision may be sufficient for stable isotopic analyses of minerals from extraterrestrial samples because the isotopic variation between the distinct phases can be as large as ~20‰ (*e.g.*, $\delta^{18}O$ values of carbonates from ALH84001; Leshin *et al*. 1998). However, the isotopic composition of minerals from terrestrial rocks can span a much narrower range (*e.g.*, ~5‰ for $\delta^{18}O$ values of carbonates) and therefore require precision below ±1‰. Therefore, a great deal of effort to improve instrumentation and methodology has led to advances in stable isotope analysis using SIMS with precision that rivals conventional methods.

Instrumentation

For most stable isotope applications a dynamic magnetic sector SIMS is used rather than static SIMS (*i.e.*, TOF–SIMS; see Chapter 1 this volume). CAMECA ion microprobes are by far the most common instrument used for stable isotope analysis. These ion microprobes come in two sizes: small radius and large radius instruments. The large radius instruments (CAMECA 1270 and 1280) are high transmission instruments with large magnets, which can routinely operate at a mass-resolving power of 10,000. The CAMECA ims–nf (n = 3, 4, 5, 6, 7) are smaller instruments with smaller

magnets and thus require significant beam masking or energy filtering to eliminate isobaric interferences, which reduced transmission. Both CAMECA instruments generally have a duoplasmatron and Cs source permanently mounted on the primary column (see chapter 1, this volume) with primary column magnet that allows the selection of the primary ion beam from one of the two sources.

Until recently, SIMS measurements were made using a single detector (either a Faraday cup or electron multiplier) and by changing the magnetic field different masses were sequentially analyzed. Therefore, small changes in the primary ion beam or instrumental conditions that could occur between the analysis of different masses could introduce error in the measurements and thus reduce the precision of stable isotope analysis. The development of the multicollector detection system for the CAMECA IMS 1270 and 1280 secondary ion microscope has permitted routine high resolution (~10 μm scale) high precision (sub-per mil) *in situ* stable isotopic analyses of geological materials. The multicollector consists of several motorized, computer-controlled, movable collector units. Each unit can be configured to contain either an electron multiplier (EM) or Faraday cup (FC) with a slit assembly. The multicollector comes with a set of large and miniaturized Hammamatsu EMs. Recently, Lorincik *et al*. (2006) developed a multi-collector system for the small radius ims–nf series instruments and showed that ^{32}S and ^{34}S isotopes can be simultaneously measured on a CAMECA 3f.

A third type of instrument that is relatively new to stable isotope analysis is the CAMECA nanoSIMS. As mentioned above, the feature of this instrument is its ability to produce small primary beam spots (~50 nm) and still maintain high transmission due to its unique configuration. However, its ability to produce high precision routinely is not yet sufficiently explored.

SHRIMP ion microprobes produced some of the earliest reliable S isotopic results (Eldridge *et al*. 1987). Despite their initial success, SHRIMPs have been somewhat neglectful of stable isotope analysis (Ireland 2004). SHRIMP ion microprobes use Wien filter on the primary column, which allows only ions with a specific velocity to be transmitted down the primary column. Therefore, only one source (either Cs or duoplasmatron) can be placed on the instrument at a given time and seamless switching between different sources is more involved than for CAMECA instruments.

The ISOLAB 54 is the least common of all brands of ion microprobes and has design elements that are similar to both the SHRIMP (England *et al*. 1992, Saxton *et al*. 1996) and CAMECA instruments. For example, it is equipped with an electron gun for charge compensation when analyzing positively charged insulating samples and a multiple collector for simultaneous ion detection incorporating a Faraday cup for the major isotope and conversion dynode/channel plates for the detection of the low abundance isotope (Ireland 2004).

The main limitation of precision of a pulse-counting system (EM) is the total counts (N) on the minor isotope for which the Poisson counting statistic dictates a variance in N, and hence the limitation on precision is $1/\sqrt{N}$. Therefore, 10^6 counts of the minor isotope will give 1‰ precision (1σ), whereas 10^8 counts will give 0.1‰ precision. Unfortunately, to maintain the life of an electron multiplier stability count rates should be less than 2 x 10^6 cps. Therefore, by varying the time for analysis one can obtain the desired internal precision for a single analysis.

Data Presentation

All isotopic data are presented using standard δ-notation relative to the appropriate standards, Vienna Standard Mean Ocean Water (V–SMOW) for D/H ($^2H/^1H$), Vienna Peedee Belemnite (V–PDB) for $^{13}C/^{12}C$, atmosphere for $^{15}N/^{14}N$, and Canyon Diablo Troilite for $^{34}S/^{32}S$. The equation for calculating δ values in units of per mil (‰) is:

$$\delta_{sample}=\{(R_{sample}-R_{std})/R_{std}\}x10^3 \qquad [1]$$

where R_{sample} and R_{std} are the absolute ratios in sample and standard, respectively. Isotope ratios measured by SIMS are compared to the accepted ratios (calculated from δ values determined by conventional analyses and gas source mass spectrometry) for each mineral using equation [2]:

$$R_{sample}=\{(R_{sample}/10^3)+1\}R_{std} \qquad [2]$$

where R_{std} (D/H) for V–SMOW is defined as 1.557 $x10^{-4}$ (Hagemann *et al*. 1970), R_{std} ($^{13}C/^{12}C$) for V–PDB is defined as 1.12375 $x10^{-2}$ (Craig 1957), R_{std} ($^{15}N/^{14}N$) for atmosphere is defined as 3.613 $x10^{-3}$ (Sharp 2005), and R_{std} ($^{34}S/^{32}S$) for CDT is 4.450045 x 10^{-2} (Jenson & Nakai 1962). These data can be used to calculate isotope mass fractionation that occurs during SIMS analysis by using equation [3]:

$$\alpha SIMS=R_{SIMS}/R_{conv.} \qquad [3]$$

where $R_{SIMS.}$ is the ratio measured by SIMS and R_{conv} is the accepted ratio measured by conventional mass spectrometry. These ratios can be converted to ‰ notation by:

$$\delta_{bias} = (\alpha SIMS - 1) x 10^3 \quad [4]$$

RECENT APPLICATIONS

Hydrogen Isotopic Analysis

There are relatively few studies on hydrogen isotope analysis of terrestrial material using SIMS (*e.g.*, Deloule *et al*. 1991, Kingsley *et al*. 2002, Hauri *et al*. 2002, 2006, Koga *et al*. 2003, Hull *et al*. 2008) largely because obtaining high precision hydrogen isotope ratios using SIMS is difficult. Hydrogen isotopes can be measured either as negative or positive secondary ions using either a Cs^+ or an O^- primary ion beam, respectively. The H^- secondary ion yields are only marginally higher than H^+ secondary ion yields. There are advantages and disadvantages to using either method to analyze hydrogen isotopes by SIMS. The main advantage in using a Cs^+ primary ion beam to generate H^- secondary ions is the higher ion yields for H and D, which will either allow the operator to use smaller primary ion beam sizes (higher spatial resolution), reduce the analytical time required for a given level of precision or improve the overall precision given a specific time for analysis, and there are no hydride interferences associated with D. The lack of interferences associated with D allow for low mass resolution analysis (the exit slit is left wide open and the entrance slit is closed enough to form flat-top peaks) and higher secondary ion transmission. The main disadvantage in using a Cs^+ primary ion beam to analyze hydrogen isotopes from an insulating sample such as clay or silicate minerals is a negative electron flood gun must be used to neutralize the positive charge build-up on the sample surface. Small fluctuations in sample conductivity and in the electron flood gun can produce an additional source of error in the analysis because H and D are more sensitive to small variations in secondary ion extraction geometry (*e.g.*, edge effects from poorly shaped craters) due to the large mass difference between H and D and the low mass of both isotopes.

The main advantage in using an O^- beam for hydrogen isotope analysis is that an electron gun is not required because a conductive coating (*e.g.*, Au) is sufficient to dissipate charge build-up on the sample surface. The main disadvantage in using an O^- beam is hydride interference (H_2^+) associated with D must be resolved. The H_2^+ is generally much larger than the D peak and a mass-resolving power of ~1000–1500 is generally sufficient to resolve this mass interference, and largely depends on the quality of the vacuum in the instrument. However, background hydrogen contamination must be monitored closely when analyzing nominally anhydrous minerals with low hydrogen contents in older instruments with poor vacuums (Deloule *et al*. 1991, Valley *et al*. 1998).

Regardless of the method employed to analyze hydrogen isotopes, generally a vacuum better than 10^{-8} torr is preferred and therefore many researchers bake their instruments prior to an analytical session, limit the amount of epoxy in their sample mounts or mount their samples using In metal, and use a liquid N trap to improve the vacuum in the sample chamber.

Volcanic glasses: Hauri *et al*. (2002, 2006) used a Cameca 6f to develop methods and investigate matrix effects on H isotope analysis of volcanic glasses. The major improvements over previous SIMS techniques are the high quality vacuum of the Cameca 6f (<5 x 10^{-9} torr) and the use of Cs^+ primary beam with collection of negatively charged secondary ions. These conditions reduced the hydrogen background and allowed measurement of hydrogen isotopes to be obtained using low mass resolution (MRP = 300). A 5–10 nA primary beam was accelerated to 10 kV and slightly defocused to obtain 20–40 μm diameter spots with homogeneous intensity using Kohler illumination and 100 μm diameter primary beam aperture, resulting in flat bottom sputter craters. Kohler illumination (Liebl 1983) is achieved by defocusing and tuning the primary beam such that it has a uniform ion density. An aperture is then placed in front of the defocused beam to define the beam diameter. At the beginning of each analytical session, the sample potential and electron gun were held at –5 kV so that electrons arrive at the sample surface with near-zero energy. Tuning the intensity and density of the electrons was achieved by offsetting the sample voltage to +20 V, allowing electrons to impact the conductive sample surface (*e.g.*, Cu–Si grid) and viewing the H^- image, desorbed from the sample surface. This image defines the impact area of the electron beam and the electron gun was tuned to deliver 40 μA of electron current, which produced a homogeneous image over a 150 μm diameter area. The final tuning of the electron beam was made by returning the sample potential to –5 kV, sputtering a gold-

http://doc.3sum.com/

coated insulating sample, and examining the images of H, O and Si with a narrow energy slit (± 2–3 eV). Particular attention was paid to achieving a homogeneous spot image, which indicated even charge compensation, and precise spatial coincidence of H, O, and Si. Finally, the electron gun filament current is decreased to an electron emission current of ~200–300 nA, which provided adequate charge compensation while reducing the instrumental hydrogen background derived from electron beam sputtering. These conditions provided the best conditions for secondary ion extraction while maintaining effective charge compensation (Hauri *et al*. 2002 2006).

Hauri *et al*. (2002) used the conditions described above to measure the H isotopic composition of volcanic glasses with a range of composition (rhyolitic to basaltic) and with a range of water content (0.1 to 5.6 wt.% H_2O). In order to maximize the instrument sensitivity for H, a large field aperture (FA = 400 µm) and a smaller contrast or image aperture (CA = 100 µm) was used so that ions from the outer 10 µm of the sputter crater were eliminated from analysis to reduce crater edge effects. A typical SIMS analysis required 20–40 minutes to reach 2–3‰ precision (1σ) and was limited only by the counting statistics on D.

Hauri *et al*. (2002, 2006) found that precise SIMS analysis of H isotopes in silicate glasses requires well characterized standards with a range of compositions, because instrumental mass fractionation (IMF) correlates with several compositional indices. The IMF value is a complex function of sample composition, as found for amphibole (Deloule *et al*. 1991), but the most significant correlations are the abundance of H_2O and the Fe content of the glass. For example, IMF negatively correlates with H_2O content for basaltic, andesitic, and rhyolitic glass, and positively correlates with Fe content in glass with similar H_2O abundances. Basalt with <1 wt.% H_2O have similar IMF values whereas the IMF for rhyolite within this ranges correlates with H_2O content (Fig. 4-5).

Turquoise deposits: Hull *et al*. (2008) used a CAMECA 4f and CAMECA 7f SIMS to study the H isotope systematics of turquoise deposits from the U.S. Southwest. In their study, they used a ~20 µm, 5 nA primary beam of O^- ions. During analytical sessions, a mass resolving power of ~2000 was sufficient to limit hydride interferences with D to <0.1‰. The primary beam was focused through a 200 µm primary beam aperture to produce spot sizes on the sample surface between 30 and 50 µm. The magnet was sequentially switched to collect hydrogen and deuterium. They found that the greatest contributor to mass bias was the Fe content of the turquoise and therefore developed a series of standards and calibration curves to correct for mass bias. Therefore, IMF calibration curves using 2 to 3

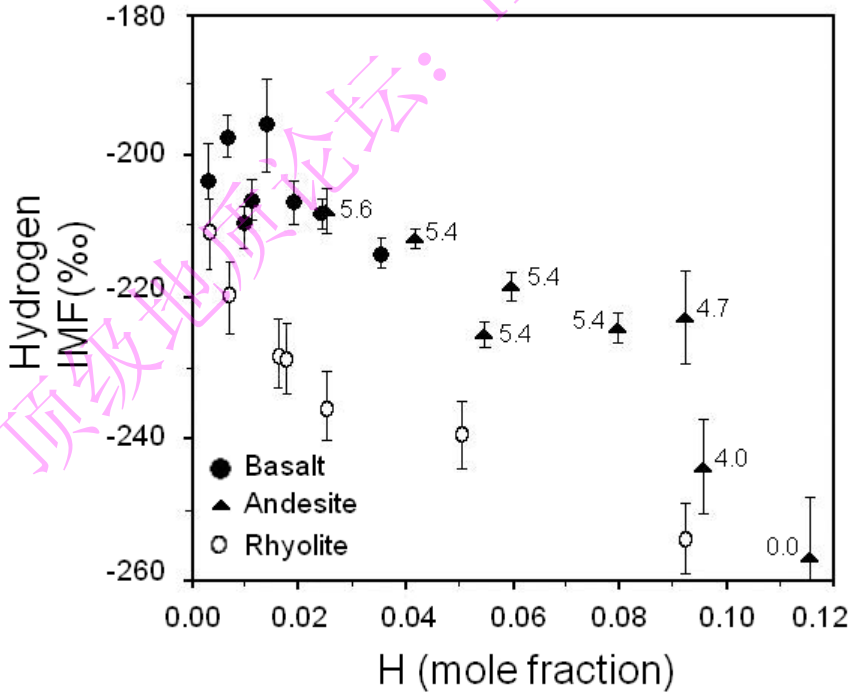


FIG. 3-5. Instrumental mass fractionation (IMF) factors for D/H measurements in silicate glasses (given as the ‰ deviation of the measured D/H ratio from the true D/H ratio) against mole fraction of water in the standards. IMF measurements on any single standard are usually reproducible to ±3‰ (1σ), but some glasses show subtle heterogeneity. Significant matrix effects are apparent, as IMF is strongly correlated with H_2O content within each group of glasses. Small numbers beside andesite points (triangles) give the total FeO content (from Huari *et al*. 2002).

顶级地质论坛：http://bbs.3501.com/

standards with a range in Fe contents from 0.5 wt.% to 25 wt.% FeO where derived for each analytical session to correct for mass bias. Typical analysis for each spot lasted 20–30 minutes, which resulted in precision of ± 3–4‰ (1σ).

Combining the H isotopic composition with Cu isotopes, they were able to show that turquoise deposits from different regions throughout the U.S. Southwest can have distinct H and Cu isotopic values. Turquoise is a supergene enrichment mineral that largely precipitates along fractures (Lueth 1998) from meteoric water at a specific redox zone in near surface environments similar to the process involved in the precipitation of malachite. They postulated the variation in H isotopic composition between turquoise deposits regions was due to differences in meteoric water composition for each region studied (Fig. 3-6). Hull *et al*. (2008) used these isotopic methods to analyze 12 turquoise deposits and link several turquoise artifacts found in prehistoric archaeological sites located several hundreds of kilometres from the deposits to a specific turquoise deposit or regions (Fig. 3-7); thus providing insight on how turquoise was procured and traded in pre-contact American Southwest.

Carbon and Nitrogen Isotopic Analyses

Several recent studies have examined C isotope systematics using SIMS in a variety of geological materials (*e.g.*, Harte & Otter 1992, Mathez *et al*. 1995, Eiler *et al*. 1997b, Riciputi *et al*. 1998, Fayek *et al*. 2001, Hauri *et al*. 2002, Sangély *et al*. 2005 2007). Carbon isotopes using SIMS are generally measured using Cs^+ primary beam and negative secondary ions. Although medium to high mass resolution (2000–4500) is typically the preferred method for analyzing C isotopes (Valley *et al*. 1998 for review), extreme energy filtering has also been used (Riciputi *et al*. 1998). Fayek *et al*. (2001) used a CAMECA ims 1270 SIMS in multi-collection mode to measure C isotopes in carbonates, by sputtering with a ~10 µm × 20 µm, 0.5 nA primary beam of Cs^+ ions with impact energy ~20 keV. A normal incidence electron flood gun was used to neutralize positive charge build-up in the analysis area (Slodzian *et al*. 1987) and low energy (0 to 30 eV) negative secondary ions were analyzed. A mass resolving power (M/ΔM) of ~2000 (full width at 10% full height) was sufficient to eliminate isobaric hydride interferences and generate flat peak tops ~0.020 amu wide for C isotopes. At this resolution, the contribution to the

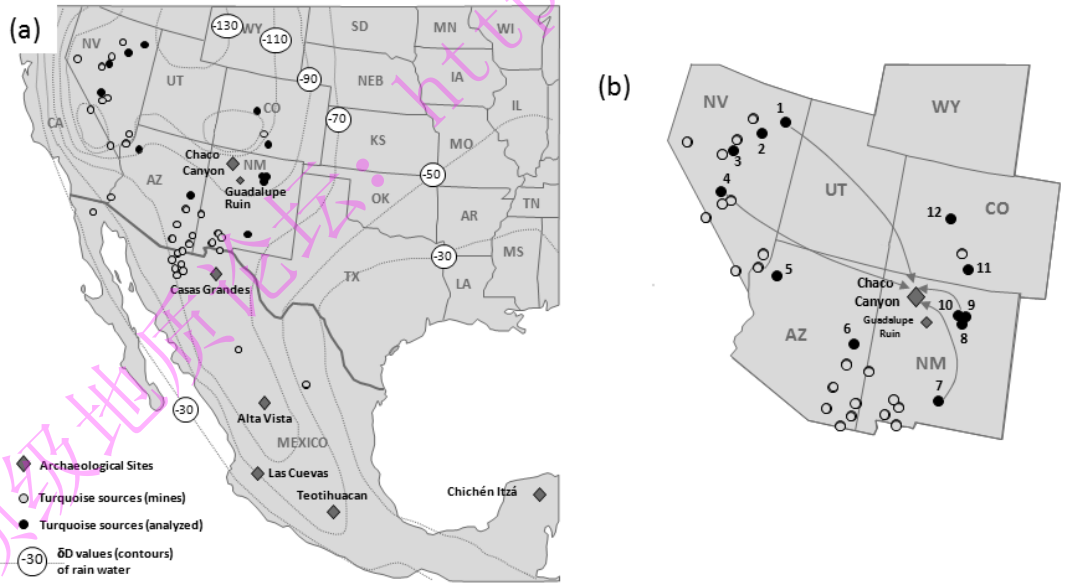


*FIG. 3-6. **(a)** Map of the southwestern United States and Mexico showing the δD contours for meteoric water, location of turquoise sources (mines), and archaeological sites where turquoise artifacts have been recovered (modified from Harbottle & Weigand 1992). **(b)** Detailed map of a portion of the southwestern United States showing the sources of the turquoise artifacts recovered from Chaco Canyon and the site in the Guadalupe Community. The turquoise sources (mines) analyzed are numbered as follows: 1. Number Eight Mine; 2. Fox Mine; 3. Carico Lake; 4. Montezuma; 5. Kingman; 6. Sleeping Beauty; 7. Orogrande, 8. Mt. Chalchihuitl; 9. Tiffany; 10. Castillian; 11. King's Manassa Mine; 12. Leadville (from Hull *et al*. 2008). Color available at http://www.mineralogicalassociation.ca/index.php?p=160

顶级地质论坛: http://bbs.sinomine.com

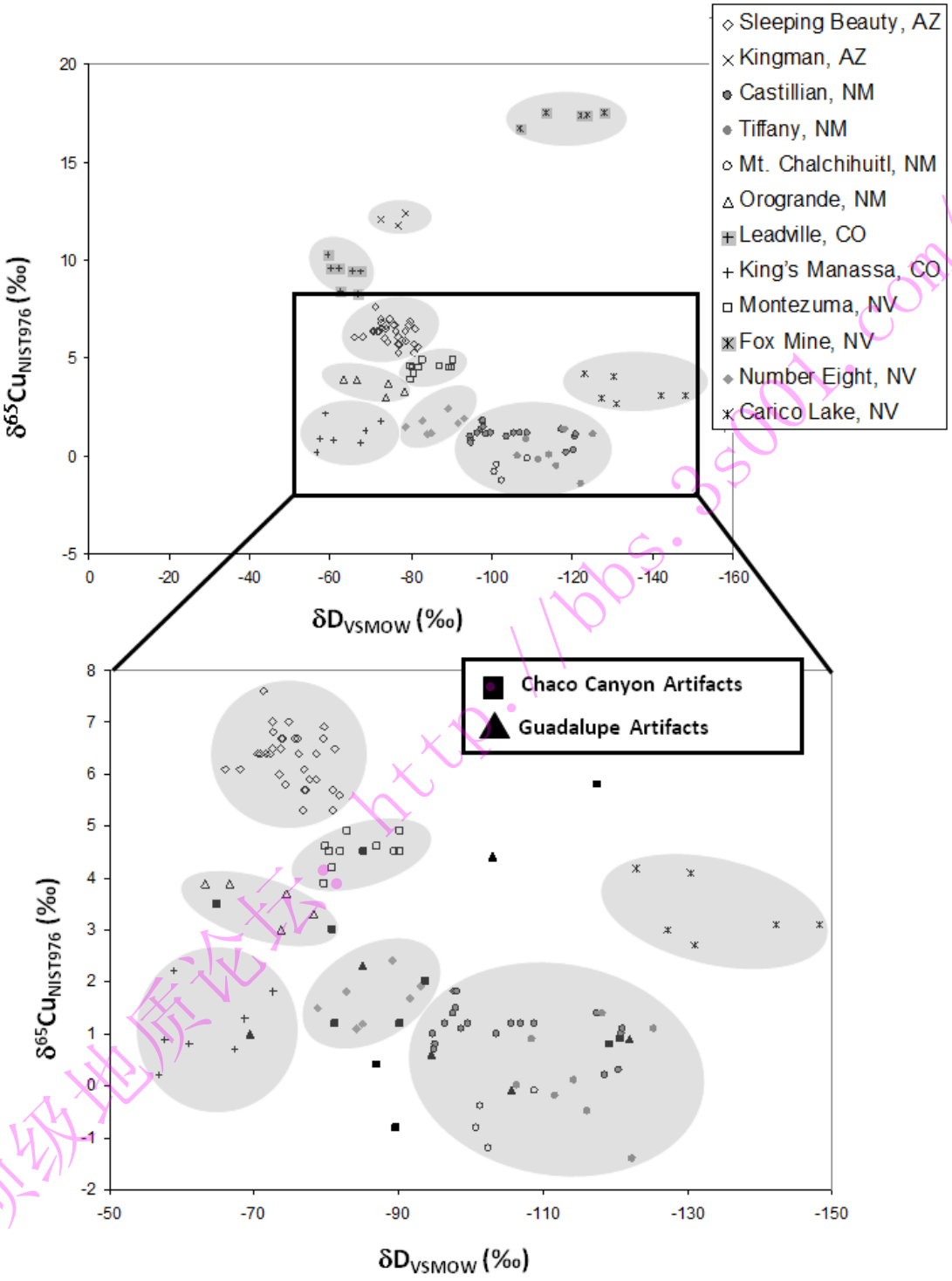


FIG. 3-7. A plot of δ^{65}Cu vs. δ D for all the turquoise mines. Note the variation of the turquoise regions and the grouping of the three mines from the Cerrillos Hills Mining District. Bottom of image is an enlarged plot of δ^{65}Cu vs. δ D values showing the distribution pattern for several mines and the results of the analyses of the artifacts from Chaco Canyon and site ENM848 of the Guadalupe Community. Note four artifacts do not fall within the distribution pattern of any of the mines analyzed (Hull *et al*. 2008).

顶级地质论坛 http://bbs.3s001.com/

minor isotope measurement from the tail of the interference is estimated to be <0.1 ‰.

Carbon isotopes were collected using a FC detector for $^{12}C^-$ and an EM for $^{13}C^-$. The primary beam current was ~2.0 nA. The entrance slit was adjusted to produce the best peak shapes and the widest exit slit (500 μm) was used. Typically, $^{12}C^-$ beam intensities were ~0.5 pA. Internal precision of ± 0.3‰ under these conditions was routinely obtained for analyses of <5 minutes duration.

The reproducibility between analyses on different spots of standards and unknowns (*i.e.*, external reproducibility) with this technique depends primarily, on a) for mixed detector (EM/FC) measurements, the stability of the EM counting efficiency, and b) the stability of the electric potential in the analysis area which is a function of the stability of the normal incidence electron flood gun.

Riciputi *et al*. (1998) analyzed C isotopes in carbonates using a CAMECA 4f. Carbon isotope analyses were obtained using extreme energy filtering of the negative secondary ions, where the sample potential was reduced by 320–350 V relative to the secondary column high voltage, and normal incident electron gun (tuned as describe above) for charge compensation. The extreme energy filtering reduced the effects of hydride interferences such as ^{12}CH on ^{13}C. In their study, 100–350 ratios were measured, with 1 s and 5 s count times for ^{12}C and ^{13}C, respectively. All ions were detected using an electron multiplier. Total analysis was ~15–60 minutes, which resulted in an internal precision between 1.5 and 3‰ (1σ).

Huari *et al*. (2002) measured C isotopes in volcanic glass using the same conditions described above for H, except they increased the mass resolution to 3200 rather than using extreme energy filtering to eliminate hydride interferences such as ^{12}CH on ^{13}C. Generally, mass resolution is used to reduce the effects of isobaric interferences when the abundance of the desired isotope is low because extreme energy filtering dramatically reduces the secondary ion signal.

There are very few N isotope studies of geological materials using SIMS largely because N is a difficult element to ionize by SIMS and produces very low secondary ion yields either as N^- or N^+ (Ireland 2004). However, Zinner *et al*. (1987) showed that in the presence of C, CN^- molecules form and produced a very intense and stable secondary ion beam. The high secondary ion yields of the CH^- molecule make this species attractive for biological SIMS where organic matter can be imaged (*e.g.*, Larras-Regard & Mony 1997). Isotopically labeled biological experiments can also be examined using SIMS where ^{15}N can be tracked throughout the cell structure. However, quantitative studies of N using SIMS have largely examined N contents in geological material such as diamond (Harte *et al*. 1999).

Carbonate cements. Carbonate cements are an important feature of hydrocarbon reservoirs because they restrict fluid flow, thereby enhancing hydrocarbon accumulation (Heald & Larese 1973, Hayes 1979, Boles 1987, Boles & Ramseyer 1987, Sharp *et al*. 1988, Boles 1998). Their O and C isotopic composition can potentially provide estimates of the temperature at the time of cement formation, and information regarding the source of the dissolved C in the evolving pore waters. However, the temperature of formation and source of C can be difficult to assess accurately (Craft & Hawkins 1991) because cement zones within a single reservoir often consist of microscale (20–100 μm) mineral phases with distinct isotopic compositions which may be obscured by bulk measurements. Thus high precision and high resolution *in situ* oxygen O and C isotopic analyses of carbonates by SIMS presents an attractive approach for documenting the fluid history of these zones.

Fayek *et al*. (2001) used SIMS to measure C and O isotopic composition of early dolomite, calcite, and paragenetically late Fe-dolomite cement from the North Coles Levee petroleum oil field, San Joaquin Basin, California. The mineral phases ranged in size (20–100 μm) and have variable chemistry. Isotopic measurements were corrected for IMF by calibration on appropriate standard carbonates measured during the same analysis session. The chemical composition was used to correct the isotopic data for dolomite and Fe-dolomite for matrix effects by linearly interpolating the appropriate IMF obtained on analyses of standards. The relatively small compositional range of the dolomite and Fe-dolomite (from ~5–17 wt.% FeO) means that this approximation results in an additional systematic uncertainty on the order of 1‰ or less. Calcite from the North Coles Levee samples and the calcite standards were similar in composition, therefore corrections for matrix effects were negligible in this case.

SIMS results show that early dolomite has a range of $\delta^{18}O_{PDB}$ values (+2.0 ‰ to +4.6 ‰) and

$\delta^{13}C_{PDB}$ values between +6.2‰ and +11.5‰, whereas Fe-dolomite has a range of $\delta^{18}O_{PDB}$ values from –6.1 to –7.4‰ and $\delta^{13}C_{PDB}$ values between –6.9‰ and +1.0‰ (Fig. 3-8). Calcite has a restricted range of $\delta^{18}O_{PDB}$ values (–9.9 ‰ to –7.2‰) and $\delta^{13}C_{PDB}$ values between –9.4‰ and –5.1‰ (Fig. 3-8; Fayek *et al*. 2001).

Oxygen and C isotopic analyses by SIMS of early dolomite are consistently heavier than bulk acid dissolution analysis ($\delta^{18}O_{PDB}$ = –3.5‰ to 0‰ and $\delta^{13}C_{PDB}$ = +4 ‰ to +10 ‰) reported by Boles & Ramseyer (1987) for the same samples (Fig. 3-9). The relatively light $\delta^{18}O_{PDB}$ values and $\delta^{13}C_{PDB}$ values obtained by bulk acid dissolution techniques are likely due to analyses of mixed dolomite phases (*i.e.*, early dolomite with heavy $\delta^{18}O_{PDB}$ values and $\delta^{13}C_{PDB}$ values and late Fe-dolomite with light $\delta^{18}O_{PDB}$ values and $\delta^{13}C_{PDB}$ values), because the bulk $\delta^{18}O_{PDB}$ values and $\delta^{13}C_{PDB}$ values are approximately the average of the *in situ* results (Fig. 3-9). Calcite cements have a restricted range of $\delta^{18}O_{PDB}$ values (–9.9 ‰ to –7.2 ‰) and $\delta^{13}C_{PDB}$ values between –9.4 ‰ and –5.1 ‰. These values are similar to the bulk acid dissolution results obtained by Wood & Boles (1991) (Fig. 3-9). All calcite samples have negative $\delta^{18}O_{PDB}$ and $\delta^{13}C_{PDB}$ values and therefore are distinctive from Fe-dolomite and early dolomite which have relatively heavier $\delta^{18}O_{PDB}$ and $\delta^{13}C_{PDB}$ values (Fayek *et al*. 2001).

The C isotopic composition of the carbonate cements was used to infer the source of C. SIMS results show that early dolomite cements have heavy $\delta^{13}C_{PDB}$ values between +6.2 ‰ and +11.5 ‰ (Fig. 3-9) suggesting that they formed in a reducing environment where methane preferentially fractionates light carbon, leaving the pore fluid enriched in ^{13}C (Coleman *et al*. 1986). In contrast, the calcite cements have light $\delta^{13}C_{PDB}$ values between –9.4‰ and –5.1‰ suggesting a mixture of C from two sources; detrital shell material with a $\delta^{13}C_{PDB}$ = 0‰ and organic carbon $\delta^{13}C_{PDB}$ = –20‰ (Fig. 3-9). Fe-dolomite has a wide range in $\delta^{13}C_{PDB}$ values between –6.9‰ and +1.0‰ (Fig. 3-9). These values represent a continuum between the heavy $\delta^{13}C_{PDB}$ values of early dolomite and the light $\delta^{13}C_{PDB}$ values of calcite, and likely represent a mixture of C from several sources, including detrital shell material, organic carbon, and early dolomite (Fayek *et al*. 2001).

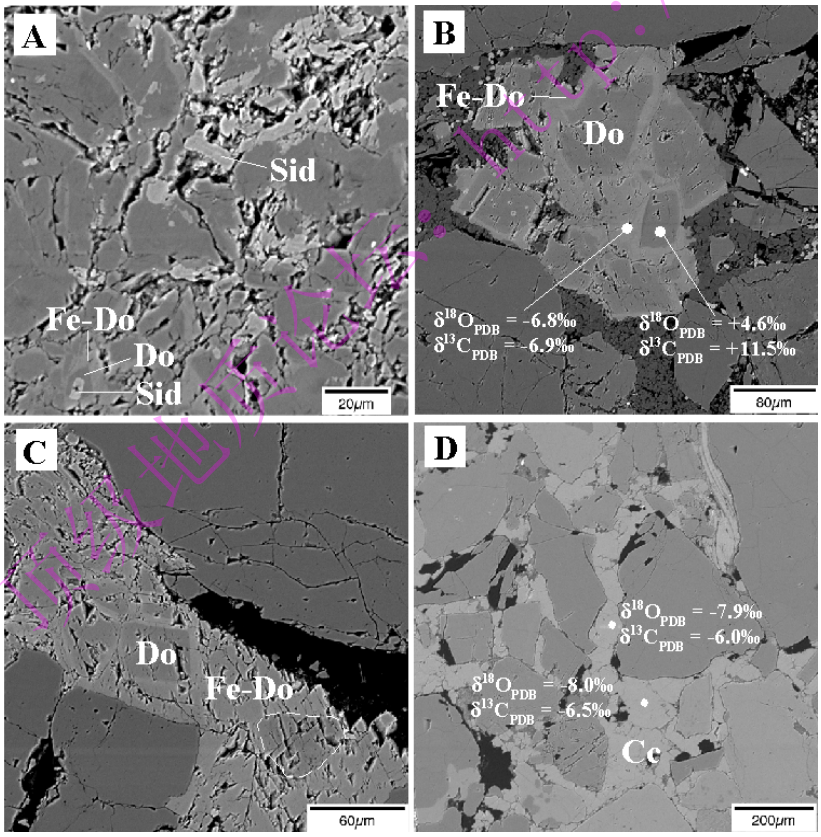


FIG. 3-8. Back-scattered electron photographs of carbonate cements from North Coles Levee oil field. **(A)** Sample (488-29; 2780 m) showing siderite (Sid), early dolomite (Do), and late Fe-dolomite (Fe–Do). **(B)** Sample (488-29; 2780 m) showing partially altered early euhedral dolomite (Do) in a matrix of late Fe-dolomite. **(C)** Sample (488-29; 2780 m) showing highly altered early euhedral dolomite (Do) in a matrix of late Fe-dolomite. Dashed line outlines a grain of early dolomite that is almost entirely altered to Fe-dolomite. White dots represent spots analyzed for their $\delta^{18}O$ values and $\delta^{13}C$ values (shown). **(D)** Sample (488-29; 2665 m) showing calcite cements (Cc). White dots represent spots analyzed for their $\delta^{18}O$ values and $\delta^{13}C$ values (shown) (from Fayek *et al*. 2001).

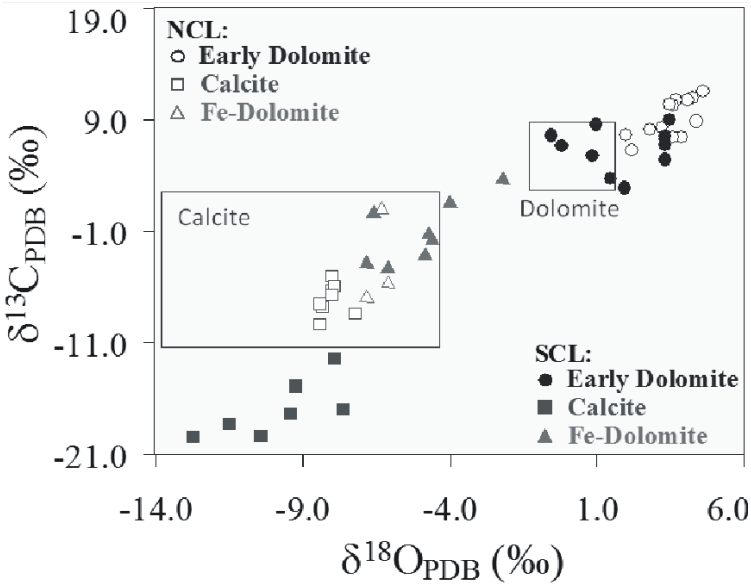


*FIG. 3-9. Relationship between $\delta^{18}O$ values and $\delta^{13}C$ values, for calcite, early dolomite, and Fe-dolomite. Symbol size is indicative of 1σ error (from Fayek *et al.* 2001). Color available at http://www.mineralogicalassociation.ca/index.php?p=160

Early life: Mojzsis *et al.* (1996) used a CAMECA ims 1270 to measure C isotopes in carbonaceous inclusions contained in apatite from early Archean sedimentary rocks (chert in banded iron formation from Western Australia (>3,250 Ma) and West Greenland (>3,700 Ma)). Instrumental conditions were similar to those used by Hauri *et al.* (2002). Carbonaceous fossils are typically characterized by $\delta^{13}C$ values of –20 to –35‰ for photoautotrophic bacteria, and can be as light as –50 to –60‰ for products for methane-recycling microbial communities. The data they obtained from the carbonaceous inclusions from the Akilia Island banded iron formation (BIF) ranged from –21(±2)‰ to –49(±7)‰, whereas inclusions from the Pilbara sedimentary rocks and Isua BIF gave weighted mean values of –26(±3)‰ and –30(±3)‰, respectively. Although controversial, their interpretation of the C isotopic values from these inclusions is that they represent the presence of life on Earth at 3800 Ma.

In a similar study of eukaryotic algal microfossils (acritarchs), extracted from shale of the Proterozoic (1400 Ma) Ruyang Group in North China, Kaufman & Xiao (2003) used a CAMECA 6f ion microprobe where a primary beam of Cs ions was focused on the minute carbonaceous microfossils to measure their $^{13}C/^{12}C$ ratio using a mass resolving power of ~3000. Their approach was to compare the C isotope compositions of eukaryotic algal microfossils (acritarchs) to carbonate produced from CO_2 by inorganic processes at 1400 Ma because isotopic effects associated with these reactions led to a fractionation of the $^{13}C/^{12}C$ ratio by about 25‰, between organic C and carbonate C that is in equilibrium with atmospheric CO_2, such that organic materials are depleted in ^{13}C relative to consanguineous carbonate. Marine photosynthesis is responsible for about 99% of primary productivity and is performed by single-celled eukaryotic algae using the Calvin cycle; a major pathway for oxygenic photosynthesis (Shively & Barton 1991).

Prior to analysis, Kaufman & Xiao (2003) used an acid extraction technique, which isolated and cleaned microfossil surfaces of the phosphate cement. Therefore, they suggest that these analyses of microfossil closely reflect the isotopic composition of primary photosynthate. The averaged C isotopic compositions of individual microfossils ranged narrowly between –33.4‰ and –36.4‰, with an overall species average of –34.9‰. The pooled data have a similar average (–34.8‰) but a larger range (–31.5‰ to –38.4‰). These microfossils are 3–6‰ more depleted in ^{13}C than kerogen isolated from the fossil-bearing shale, which has a $\delta^{13}C$ –31.9±3.1‰. They interpreted these low $\delta^{13}C$ values and the magnitude of fractionation to be consistent with organisms that use Calvin cycle metabolism, and therefore suggested that the Calvin Cycle was operating at least 1400 Ma. Kaufman & Xiao (2003) concluded that calculated magnitudes of the C isotope fractionation in these large, morphologically complex microfossils suggest elevated levels of CO_2 in the ancient atmosphere between 10 and 200

WWW.MINERALOGICALASSOCIATION.CA

times the present atmospheric level. They suggested that CO_2 was an important greenhouse gas during periods of lower solar luminosity, probably dominating over methane after the atmosphere and hydrosphere became pervasively oxygenated between 2 and 2.2 Ga.

Sulfur Isotopic Analysis

In comparison with the other light stable isotopes mentioned in this chapter (H, C, N) and elsewhere in this volume (*e.g.*, O), S isotopic analysis by SIMS is relatively easy and numerous studies have developed S isotopic SIMS techniques (*e.g.*, Primminger *et al*. 1984, Eldridge *et al*. 1987, Hervig 1992, Riciputi 1996, Paterson *et al*. 1997, McKibben & Riciputi 1998, Riciputi & Greenwood 1998, Lorincik *et al*. 2006). Sulfur isotopes can be measured using a variety of primary beams and secondary ion species (*e.g.*, Primminger *et al*. 1984 (O^+/S^-), Eldridge *et al*. 1987 (O^-/S^+), MacFarlane & Shimizu 1991 (O^-/S^-)). However, using Cs^+ primary ion produces very high S^- ion yields and therefore it is the preferred method.

The abundance of the minor isotope ^{34}S is high (~4.5%) relative to the major isotope ^{32}S. This allows favorable counting statistics for the minor isotopes, thus reducing the analytical time for each analysis, while maintaining good precision during analysis. Sub-per mil precision can be readily obtained in 10–15 minute analysis. Many sulfides are conducting; therefore, problems associated with surface charging are eliminated and the use of the complicated electron gun is generally not required. In many low temperature systems, the variations in $\delta^{34}S$ are large, so that meaningful results can be obtained even when the precision is limited to 1 or 2‰ (McKibben & Riciputi 1998).

Riciputi (1996) & Paterson *et al*. (1997) compared two SIMS S isotope analytical methods: extreme energy filtering and high mass resolution using a CAMECA 4f. As described above, extreme energy filtering is based on the fact that the energy distribution of molecular ions is much narrower than that of atomic ions (McIntyre *et al*. 1985, Hervig *et al*. 1992). In the studies by Riciputi (1996) and Paterson *et al*. (1997), a mass-filtered Cs^+ primary ion beam was used to sputter S^- ions. The primary beam was focused to a spot size of 15–20 μm and the ~12 minute analyses produced an internal precision of ± 0.2‰. For extreme energy filtering analysis, the sample potential was set at –4150 V resulting in a 350 V offset relative to the electrostatic analyzer, which was set to receive –4500 V. However, a 250 voltage offset is often sufficient to remove all interfering molecular ions from the secondary ion spectrum during the measurement of S isotopes under good vacuum conditions. Mass resolution measurements were made using the same conditions for extreme energy filtering except that there was no voltage offset and mass resolving power of 4500 was used to separate all possible isobaric interferences. Both studies concluded that both extreme energy filtering and high mass resolution analysis of S isotopes produce precise measurements within a single section. However, the accuracy of the high mass resolution results are significantly worse than those obtained using extreme energy filtering when a standard cannot be mounted with the unknown sample. For example, Paterson *et al*. (1997) reported a 7‰ range between pyrite standards mounted on different sample blocks when high mass resolution is used. Analysis of the same samples using extreme energy filtering showed no variation in instrumental mass bias within 0.5‰. Similar results were reported for troilite. One possible explanation for the difference between the techniques is poor magnet control associated with unlaminated magnets, which is typical of older CAMECA instrumentation such as the CAMECA 4f. Good magnet control and stability is crucial for high precision and accurate analysis using high mass resolution.

Riciputi *et al*. (1998) studied the matrix effects for S isotopes in several sulfides. They analyzed S isotopes using several primary beam types (Cs^+, O_2^+ and O^-) and both S^- and S^+ secondary ion species. They made the following general observations based on results from pyrrhotite, pentlandite, pyrite, and chalcopyrite:

1) The mass bias between all four sulfides is 3‰ when using a Cs^+ primary beam, 9‰ when using an O_2^+ beam and 15‰ when using an O^- beam.
2) When using a Cs^+ beam difference in mass bias for all four sulfides is 3‰ when using low energy ions (0 V offset) and high mass resolution and 5‰ when using 350 V offset and low mass resolution.

Mississippi Valley-Type Mineralization: Peevler *et al*. (2003) studied the S isotope composition of zoned sulfides from the Mascot-Jefferson City Zn district in East Tennessee. The deposits are of the Mississippi Valley-type (MVT), hosted by carbonate rocks and dominated by sphalerite mineralization in stratabound breccia bodies.

Two types of pyrite were noted: pre-sphalerite, diagenetic pyrite ($\delta^{34}S$ of –16.1‰ and –20.0‰) and syn-sphalerite pyrite that is intergrown with sphalerite ($\delta^{34}S$ of 31.3‰ to 33.7‰, Fig. 3-10). Two textural varieties of sphalerite mineralization (banded and non-banded) were characterized. Banded sphalerite exhibits fine (μm to cm) banding that has grown around a carbonate substrate. Banded sphalerite has $\delta^{34}S$ values from 27.8‰ to 51.0‰, high Cd contents (up to 0.96 wt.%) and dark areas that are likely due to minute inclusions of organic C (Fig. 3-11). The non-banded sphalerite has $\delta^{34}S$ values from 20.2‰ to 39.5‰, high Fe content and no organic inclusions.

Regardless of the textural variety of sphalerite mineralization, results by Peevler *et al*. (2003) showed that the S isotopic composition within a single polished thin section is heterogeneous and can vary by as much as 15‰. The $\delta^{34}S$ values recorded are among the heaviest ever reported for MVT deposits. Their data suggest multiple S sources and sulfide precipitation by fluid mixing. The most probable scenario involves significant S input from a sulfate- and metal-bearing fluid of variable $\delta^{34}S$ composition mixing with a gas cap containing H_2S of relatively homogeneous $\delta^{34}S$ composition. The gas cap provided lesser amounts of S to the system. Mixing of two isotopically different S sources of variable proportions can account for the microscale variation in $\delta^{34}S$ observed.

Diagenetic Studies and Sedimentary Sulfides: Compared to conventional bulk analysis, *in situ* microanalytical studies using secondary ion microprobes (SHRIMP and CAMECA) of zoned or fine-grained sulfides in sedimentary environments show the largest stable isotope variation known in natural minerals. Some of these data remain unpublished because most current models for S isotope fractionation cannot adequately explain the

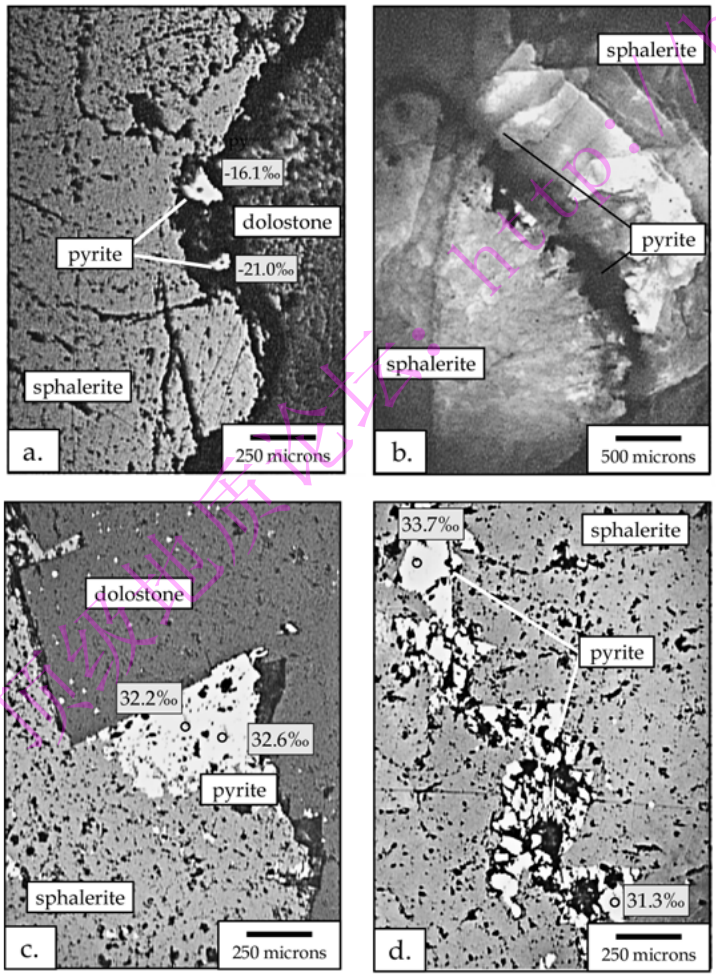


*FIG. 3-10. Photomicrographs of pyrite textures, Mascot-Jefferson City District Zn district, East Tennessee.
a) Reflected light image of diagenetic pyrite, with very light $\delta^{34}S$ values, occurring in host dolostone (sample jp7, New Market mine);
b) Reflected light image of a sphalerite rosette with fine-grained ore stage pyrite occurring within an organic-rich (bitumen) zone (Sample 3590, Coy mine);
c) Reflected light image (sample 3278, Jefferson City mine) of pyrite in contact with sphalerite;
d) Reflected light image of the pyrite in (c).
Open circles represent spots of SIMS analysis with corresponding $\delta^{34}S$ values (‰ CDT) noted to the side (from Peevler *et al*. 2003).
Color available at http://www.mineralogicalassociation.ca/index.php?p=160

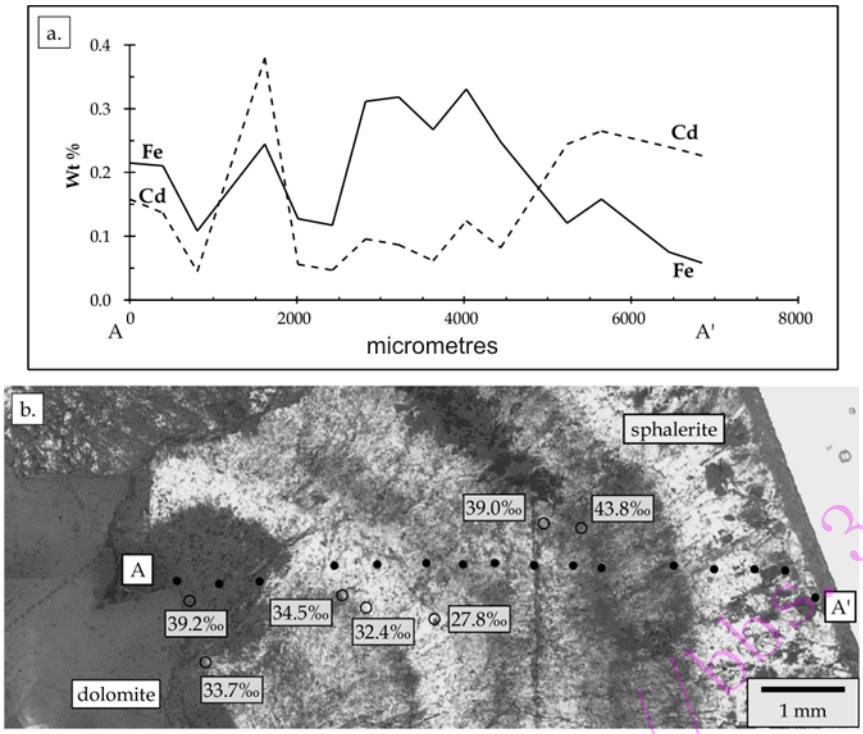


*FIG. 3-11. Sphalerite rosette (sample sds1 from Young Mine) with compositional and isotopic data.
(a) Graph of electron microprobe data for Fe, and Cd;
(b) Photomicrograph of rosette under plane-polarized light. The line A to A' represents the electron microprobe traverse and corresponds to the graph above. The open circles represent spots where ion microprobe data were obtained with $\delta^{34}S$ (‰ CDT) values noted to the side (from Peevler *et al.* 2003).
Color available at http://www.mineralogicalassociation.ca/index.php?p=160

extreme S isotope fractionation (very high or low S isotope ratios) documented by *in situ* microanalysis. For example, in search of the origin of the Creede base metal-Ag vein deposits in Colorado, McKibben *et al.* (1994) studied diagenetic sulfides in the Oligocene moat lake sediments of the Creede Caldera. Conventional bulk analysis and SHRIMP analysis of diagenetic pyrite gave very similar values from about –30 to +40‰. However, conventional bulk analysis of vein pyrite gave values between –4 and +18‰, where as SHRIMP data for the same vein pyrite ranged from –23 to +111‰. These pyrite samples typically show multiple growth zones with framboidal centers with $\delta^{34}S$ values of about –17‰ and progressively enriched rims (up to +111‰). McKibben *et al.* (1994) concluded that these extreme values imply closed system behavior where sulfate reduction during vein formation was characterized by multiple stages of precipitation and involved much larger fractionation than during diagenetic pyrite formation.

Riciputi *et al.* (unpublished data) using a Cameca 4f secondary ion mass spectrometer measured very large ranges in $\delta^{34}S$ values (>100‰) for pyrite from sandstone of the Brent Group in the North Sea. Pyrite occurs in both reservoir sandstone and shale and has a variety of textures including fine-grained framboids (<10 μm) as well as large concretions (>1 mm). Euhedral pyrite occurs as cements along faults, stringers, and disseminated matrix pyrite infilling pore space. The largest range in $\delta^{34}S$ values occurs along the large faults. $\delta^{34}S$ values of pyrite adjacent to the faults are generally low (–10 to –35‰), whereas pyrite cements away from the fault have higher $\delta^{34}S$ values of up to +35‰. Small matrix pyrite has values from –5 to +80‰. Large pyrite grains in shale units are isotopically zoned, where $\delta^{34}S$ values from core to rim range from 0 to +30‰. Although the origin of the exceedingly high $\delta^{34}S$ values (> +60‰) is uncertain, McKibben & Riciputi (1998) showed preliminary results (Fig. 3-12) that suggest the isotopic composition and the trace element content of pyrite may be related.

Mesogenetic and early formed pyrite from the Cretaceous sandstone of the Scapa Field in the western North Sea display similar broad ranges in high $\delta^{34}S$ values (–10 to +55‰ for mesogenetic pyrite and –56 to +10‰ for early pyrite). Paragenesis and geochemical constraints suggest that the pyrite formed from Fe-rich fluids during rapid Paleocene diagenesis (McKibben & Riciputi. 1998). Large grains of pyrite show complex isotopic zonation patterns (Fig. 3-13) where some grains show lower $\delta^{34}S$ values towards the rim and others

版权所有 http://bbs.3soon.com

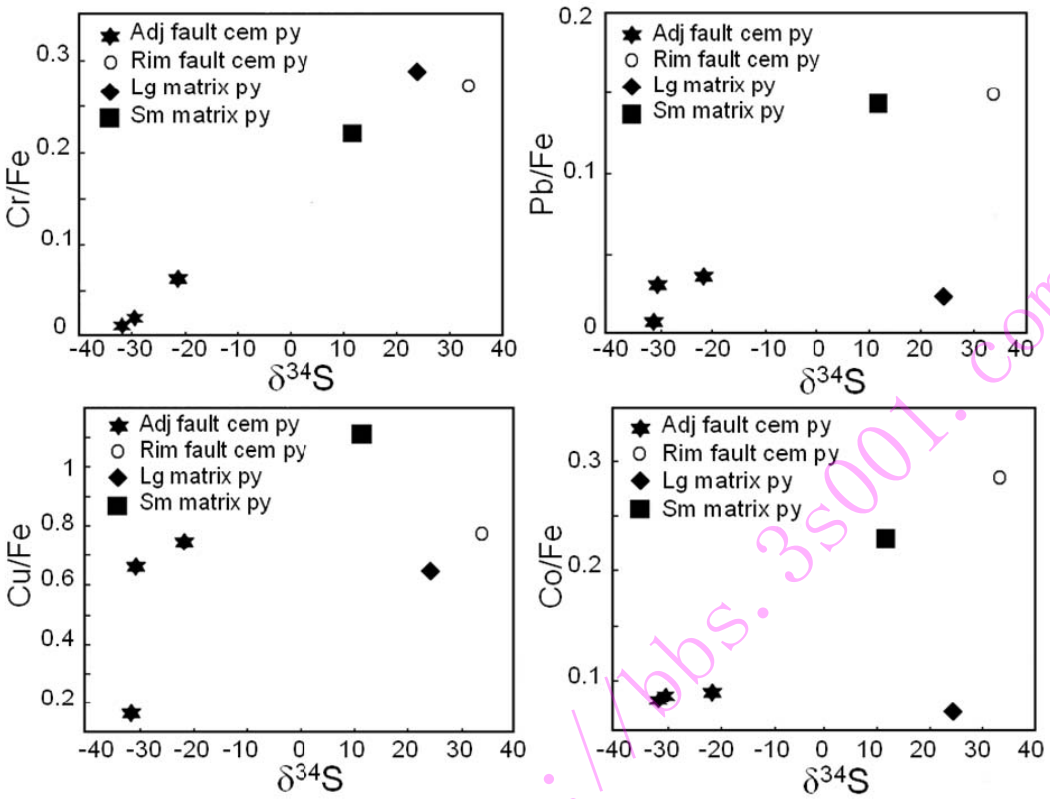


FIG. 3-12. Trace element ratios and S isotopic composition of pyrite from the North Sea. Note that the $\delta^{34}S$ values seem to correlate with the trace element composition of the pyrite. The trace element ratios are uncalibrated raw values obtained by SIMS (from McKibben & Riciputi 1998).

have the opposite patterns. These complex and conflicting patterns argue against simple Rayleigh fractionation processes of bacterial sulfate reduction in a closed system, which would lead to progressive enrichment in the ^{34}S in the sulfide that formed. McKibben & Riciputi (1998) argued that there was likely more than one source of S during the formation of these sulfides.

The SIMS was also used to investigate S isotopic ratios of pyrite from the Cerro Negro drill site located in New Mexico, where long-term survival of subsurface bacteria has been investigated. Pyrite in the sandstone typically consists of small framboids made up of individual sub-micrometre sized particles. Such pyrite also displays a broad range in $\delta^{34}S$ values (–22 to +70‰), similar to values in pyrite from the North Sea, and the isotopic composition does somewhat correlate with pyrite texture. For example, small, pore-filling pyrite, generally have lower $\delta^{34}S$ values (–20 to 0‰), whereas coarser pyrite has $\delta^{34}S$ values from 0 to +50‰. However, once again isotopic values from core to rim in larger pyrite grains are complex and suggest that S isotope systematics in diagenetic systems are complicated and are not only governed by bacterial sulfate reduction (McKibben & Riciputi 1998).

Current microbial reduction models (Rudnicki *et al*. 2001, Wortman *et al*. 2001, Brunner & Bernasconi 2005) cannot account for the extreme S isotope fractionation that produces the very high and low $\delta^{34}S$ values or the mass balance problem (*e.g.*, the lack of sulfides with very low $\delta^{34}S$ values) observed in many of the studies described above, likely because current models of S isotope fractionation relied mainly on bulk isotope measurement, which produce less isotopic variability because bulk analyses generally homogenize extreme isotopic values. However, the similar and extreme values reported for sedimentary systems such as Creede, Cerro Negro, and the North Sea suggest that existence of sulfides with very high and low $\delta^{34}S$ values may be relatively common in these environments and that new models are required to explain these extreme values.

http://bbs.3s001.com/

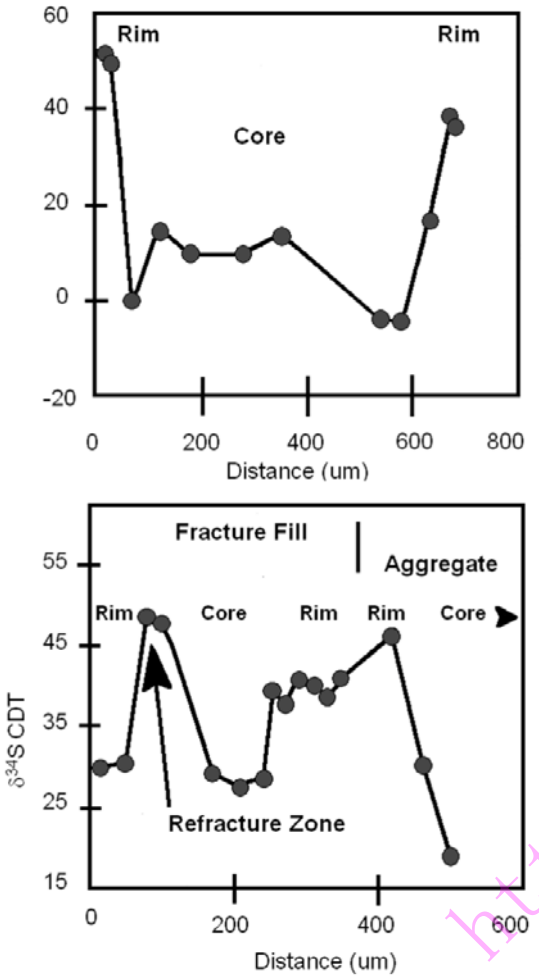


FIG. 3-13. $\delta^{34}S$ values *vs*. distance (core to rim transects) for pyrite grains from the Scapa oil field, North Sea (from McKibben & Riciputi 1998).

CONCLUSIONS

Light stable isotopic analysis of geological materials by secondary ion mass spectrometer has steadily improved over the last two or more decades and therefore has been applied to a wide variety of areas in the geosciences. Microscale SIMS analyses provide textural context for studies that enrich our understanding of natural phenomena. However, to obtain high precision and accurate light stable isotopic data the following is required:

1. In addition to atomic ions, sputtering creates a wide variety of molecular secondary ions (*e.g.*, hydrides, oxides) that may interfere with the desired atomic ion. These isobaric interferences need to be eliminated or separated using either energy filtering or mass resolution.
2. Isotope ratios measured by SIMS undergo mass-dependent fractionation during sputtering, extraction, transmission, and detection. This phenomenon is known as instrumental mass fractionation (IMF). The ionization efficiencies for different elements vary widely and depend on the chemical composition of the material. These matrix effects can also significantly affect the measured stable isotope ratio. The combined effect of IMF and matrix effect is known as mass bias and can be several 100s of ‰, but can vary by 10s of ‰ for the same element depending on the chemical composition of the mineral analyzed. Therefore, having a suite of standards that cover a range of chemical compositions (*i.e.*, are similar in composition to the unknown samples) is critical to obtain high precision and accurate stable isotope analysis of minerals.
3. Charge build-up on the sample surface can reduce the production of secondary ions, change the effective energy of the secondary ions, or cause uneven charge dissipation, which all can lead to variations in the measured isotope ratio across a sample. Therefore, most geological materials need to be coated with a conductive layer (*e.g.*, Au), and if a positive primary beam (*e.g.*, Cs^+, O_2^+) is used on non-conductive samples, an electron flood gun is required to balance the positive charge build-up on the sample surface.

ACKNOWLEDGMENTS

The author would like to thank Professors Alfredo Camacho, Andrey Bekker, Frank Hawthorne and Kurt Kyser, and Drs. Rong Liu and Lee Riciputi for their for helpful conversations. The author would also like to thank Carolyn English for her help in drafting some of the figures in this chapter. The SIMS facility at the University of Manitoba is partially supported by NSERC, Canadian Foundation for Innovation, and the Canada Research Chair program. This chapter greatly benefitted from the insightful and careful review by Dr. Penny King.

REFERENCES

ANDERS, E. & ZINNER, E. (1993): Interstellar grains in primitive meteorites: Diamond, silicon, carbide, and graphite. *Meteoritics* **28**, 490-514.

矿物岩石论坛：http://bbs.3501.com/

BENNINGHOVEN A., RÜDENAUER F. G. & WERNER H. W. (1987): Secondary ion mass spectrometry: Basic concepts, instrumental aspects, applications and trends. *Chemical Analysis Monograph* **86**, Wiley & Sons, NY, 1216 p

BOLES, J.R. (1987): Six million year diagenetic history, North Coles Levee, San Joaquin Basin, California. *AAPG Memoirs* **37**, 217-224.

BOLES, J.R. (1998): Carbonate Cementation in Tertiary sandstones, San Joaquin Basin, California. *In* Special Publication of the International Association of Sedimentologists (J. A. Morad, *ed*.) **26**, 261-283.

BOLES, J.R. & RAMSEYER, K. (1987): Diagenetic carbonate in Miocene sandstone reservoir, San Joaquin basin, California. *AAPG Bull.* **71**, 1475-1487.

BRUNNER B. & BERNASCONI S.M. (2005): A revised isotope fractionation model for dissimilatory sulfate reduction in sulfate reducing bacteria. *Geochim. Cosmochim. Acta* **69**, 4759-4771.

COATH, C.D. & LONG, J.V.P. (1995): A high-brightness duoplasmatron ion source for microprobe secondary-ion mass spectrometry. *Review of Scientific Instruments* **66**, 1018-1023.

COLEMAN, M.L., CURTIS, C.D. & IRWIN, H. (1986): Burial rate: Key to source and reservoir potential. *World Oil*, 83-92.

CRAFT, B.C. & HAWKINS, M. (1991): Applied Petroleum Reservoir Engineering (2nd ed.) revised by R.E. Terry, Prentice Hall, Englewood Cliffs, NJ, 431 p.

CRAIG, H. (1957): Isotopic standards from carbon and oxygen and correction factors from mass spectrometric analysis of carbon dioxide. *Geochim. Cosmochim. Acta* **12**, 133-149.

DELOULE E., FRANCE-LANORD C. & ALBARÈDE F. (1991): D/H analysis of minerals by ion probe. *In* Stable Isotope Geochemistry: A tribute to Samuel Epstein. (H.P. Taylor Jr., J. R. O'Neil & I.R. Kaplan, *eds*.). *The Geochemical Society, Spec. Publ.* **3**, 53-62.

EILER, J.M., GRAHAM, C. & VALLEY, J.W. (1997a): SIMS analysis of oxygen isotopes: matrix effects in complex minerals and glasses. *Chem. Geol.* **138**, 221-244.

EILER, J.M., VALLEY, J.W. & GRAHAM, C.M. (1997b): Standardization of SIMS analysis of O and C isotope ratios in carbonates from ALH84001. 28th LPSC.

ELDRIDGE C. S., COMPSTON W., WILLIAMS I. S., WALSHE J. L. & BOTH R. A. (1987): *In situ* microanalysis for 34S/32S ratios using the ion microprobe SHRIMP. *Int. J. Mass Spectrom. Ion Proc*. **76**, 65-83.

ENGLAND J. G., ZINDLER A., REISBERG L. C., SALTERS V., MARCANTONIO F., BOURDON B., BRUECKNER H., TURNER P. J., WEAVER S. & READ P. (1992): The Lamont-Doherty Geological Observatory Isolab 54 isotope ratio mass spectrometer. *Int. J. Mass Spectrom. Ion Proc*. **121**, 201-240.

ESAT T. M. (1984): A 61 cm radius multi-detector mass spectrometer at the Australian National University. *Nucl. Instrum. Meth. Phys. Res*. **B5**, 545-553.

FAYEK M., HARRISON T. M., GROVE M., MCKEEGAN K. D., COATH C. D. & BOLES J. R. (2001): *In situ* isotopic evidence for protracted and complex carbonate cementation in a petroleum reservoir, North Coles Leveem, San Joaquin Basin, California, U.S.A. *J. Sedim. Res*. **71**(3), 444-458.

GILETTI, B.J. & SHIMIZU, B. (1989): Use of the ion microprobe to measure natural abundances of oxygen isotopes in minerals. New Frontiers in Stable Isotope Research, (W.C. Shanks & R.E. Criss, *eds*.). *USGS Bull.* **1890**, 129-136.

HAGEMANN, R., NEIF, G. & ROTH, E. (1970): Absolute isotope scale for deuterium analysis of natural waters-absolute d/h ratio for SMOW. *Tellus* **22**, 712-715.

HARBOTTLE, G. & WEIGAND, P. C. (1992): Turquoise in pre-Columbian America. *Scientific American* **266**(2), 78-85.

HARMON R. S. & HINTON R. W. (1992): Frontiers in isotope geosciences, part II. *Chem. Geol*. **102**, 169-199.

HARTE B. & OTTER M. L. (1992): Carbon isotope measurements in diamonds. *Chem. Geol*. **101**, 177-183.

HARTE B., FITZSIMONS I. C. W., HARRIS J. W. & OTTER M. L. (1999): Carbon isotope ratios and

下载地址论坛：http://bbs.3s001.com/

nitrogen abundances in relation to cathodoluminescence characteristics for some diamonds from the Kaapvaal Province, S. Africa. *Mineral. Magazine* **63**(6), 829-856.

HAURI, E., WANG, J., DIXON, J.E., KING, P.L., MANDEVILLE, C. & NEWMAN, S. (2002): SIMS analysis of volatiles in silicate glasses 1. Calibration, matrix effects and comparison with FTIR. *Chem. Geol*. **183**, 99-114.

HAURI, E., SHAW, A.M., WANG, J., DIXON, J.E., KING, P.L. & MANDEVILLE, C. (2006): Matrix effects in hydrogen isotope analysis of silicate glasses by SIMS. *Chem. Geol.* **235**, 352-365.

HAYES, J.B. (1979): Sandstone diagenesis-the whole truth. (P.A Scholle & P.R. Schluger, *eds*.). *Aspects of diagenesis, Soc. Econ. Geol., Paleo, Min., Spec. Pub*. **26**, 127-139.

HEALD, M.T. & LARESE, R.E. (1973): The significance of the solution of feldspar in porosity development. *J. Sed. Pet*. **43**, 458-460.

HERVIG R. L. (1992): Oxygen isotope analysis using extreme energy filtering. *Chem. Geol., Isot. Geosci. Sect.* **101**, 185-186.

HERVIG, R.L., WILLIAMS, P., THOMAS, R.M., SCHAUER, S.N. & STEELE, I.M. (1992): Microanalysis of oxygen isotopes in insulators by secondary ion mass spectrometry. *Int. J. Mass Spectrom Ion Process.* **20**, 45-63.

HINTON R.W. (1995): Ion microprobe analysis in geology. *In* Microbe techniques in Earth sciences. (P. J. Potts, J. F. W Bowles, S. J. B. Reed & M. R. Cave, *eds*.). *Chapman & Hall*, *London*, 235-289.

HULL, S.K., FAYEK, M., MATHIEN, F.J., SHELLEY, P., DURAND, K.R. (2008): A new approach to sourcing turquoise using hydrogen and copper isotopes. *J. Archeal. Sci.* **35**, 1355-1369.

IRELAND T.R. (1986): *Isotope systematics of refractory inclusions from carbonaceous chondrites*. PhD Thesis, The Australian National University (unpublished).

IRELAND T.R. (1995): Ion microprobe mass spectrometry: Techniques and applications in cosmochemistry, geochemistry, and geochronology. *In* Advances in analytical geochemistry. (M. Hyman & M. Rowe, *eds*.) *JAI Press* **2**, 1-118.

IRELAND T. R. (2004): SIMS measurement of stable isotopes. *In* Handbook of Stable Isotope Analytical Techniques, Chapter 30, 652-691. (P. de Groot, *ed*.) Elsevier, Amsterdam, the Netherlands.

JAMTVEIT, B. & HERVIG, R.L. (1994): Constraints on the transport and kinetics in hydrothermal systems from zoned garnet crystals. *Nature* **263**, 505-508.

JENSEN, M.L. & NAKAI, N. (1962): Sulfur isotope meteorite standards; results and recommendations. *In* Biogeochemistry of Sulfur Isotopes. (M. L. Jensen, *ed*.) NSF symp.

KAUFMAN, A.J. & XIAO, S. (2003): High CO_2 levels in the Proterozoic atmosphere estimated from analyses of individual microfossils. *Nature* **425**, 279-282.

KINGSLEY, R.H., SCHILLING, J.G., DIXON, J.E., SWART, P., POREDA, R. & SIMONS, K. (2002): D/H ratios in basalt glasses from the Salas y Gomez mantle plume interaction with the East Pacific Rise: water from old D-rich recycled crust or primordial water from the lower mantle? *Geochem. Geophys. Geosyst.* **3,** (2001GC000199).

KOGA, K., HAURI, E.H., HIRSHMANN, M. & BELL., D.R. (2003): Hydrogen concentration analysis using SIMS and FTIR: comparison and calibration for nominally anhydrous minerals. *Geochem. Geophys. Geosyst.* **4,** (2002GC000378).

LARRAS-REGARD E. & MONY M.-C. (1997): Improvements in biomedical imaging by SIMS (IMS 3F, 4F, and nanoSIMS). *In* SIMS XI. (G. Gillen, R. Lareau, J. Bennett & F. Stevie, *eds*.). 119-122.

LESHIN, L.A., MCKEEGAN, K.D., CARPENTER, P.K. & HARVEY, R.P. (1998): Oxygen isotopic constraints on the genesis of carbonates from martian meteorite ALH84001. *Geochim. Cosmochim*. **62**, 1, 3-13.

LIEBL H. (1983): *Ion gun systems for submicron SIMS*. *In* SIMS. (J. Okano, R. Shimizu & H. W. Werner, *eds*.). Springer **IV**, 114-118.

LIU, D.Y., NUTMAN, A.P., COMPSTON, W., WU, J.S. & SHEN, Q.H. (1992): Remnants of 3800 Ma crust in the Chinese part of the Sino-Korean craton. *Geology* **20**, 339-342.

LORIN, J.C., SLODZIAN, R., DENNEBOUY, R. & CHAINTREAU, M., (1990): SIMS measuerment of oxygen isotopes-ratios in meteorites and primitive solar matter. *In* SIMS VII (A. Benninghoven, C.A. Evans, K.D. McKeegan, H.A. Storms & H.W. Werner, *eds*.). John Wiley, Chichester, 377-380.

LORINCIK, J., HERVIG, R., FRANZREB, K., SLODZIAN G. & WILLIAMS, P. (2006): Isotope ratio measurement with a multi-collector detector on the Cameca IMS nf. *Appl. Surf. Sci*. **252**, 7301-7303.

LUETH, V.W. (1998): Two diverse origins of turquoise at the Orogrande Mining District, Otero County, New Mexico. *New Mexico Geology* **20**, 64-65.

LYON, I.C., SAXTON, J.M. & TURNER, G. (1994): Isotopic fractionation in secondary ionization mass spectrometry. *Rapid comun. mass spectro.* **8**, 837- 843.

MACFARLANE A.W. & SHIMIZU N. (1991): SIMS measurement of δ34S in sulfide minerals from adjacent vein and stratabound ores. *Geochim. Cosmochim. Acta.* **55**, 525-541.

MAHON, K.I., HARRISON, T.M. & GROVE, M. (1998): The thermal and cementation histories of a sandstone petroleum reservoir, Elk Hills, California. Part 2: *In situ* oxygen and carbon isotopic results. *Chem. Geol.* **152**, 257-271.

MATHEZ, E.A., FOGEL, R.A., HUTCHEON, I.D., MARSHINTSEV, V.K. (1995): Carbon isotopic composition and origin of SiC from kimberlites of Yakutia, Russia. *Geochim. Cosmochim*. **59**, 781-791.

MCINTYRE, N.S., FICHTER, D., METSON, J.B., ROBINSON, W.H. & CHAUVIN, W. (1985): Suppression of molecular ions in SIMS spectra of metals and semiconductors. *Surf. Inter. Anal*. **7**, 69-73.

MCKEEGAN, K.D. (1987): Oxygen isotopes in refractory stratospheric dust particles: proof of extraterrestrial origin. *Science* **237**, 1468-1471.

MCKEEGAN K.D., LESHIN L. A., RUSSELL S. S. & MACPHERSON G. J. (1998): Oxygen isotopic abundances in calcium-aluminum-rich inclusions from ordinary chondrites: Implications for nebular heterogeneity. *Science* **280**, 414-418.

MCKIBBEN M.A. & RICIPUTI, L.R. (1998): Sulfur isotopes by ion microprobe. *In* Applications of microanalytical techniques to understanding mineralizing processes. Reviews in Economic Geology (M.C. McKibben, W.C. Shanks, W.I Ridley, *eds*.). *Pubco*. **7**, 121-139.

MCKIBBEN M.A. & SHANKS W.C. (1998): Applications of microanalytical techniques to understanding mineralizing processes. Reviews in economic geology. (C.M. Lesher, *ed*). *Pubco*. **7**, 263 p.

MCKIBBEN, M.A., RYE, R.O., ELDRIDGE, C.S. & BETHKE, P.M. (1994): Sulfur isotope geochemistry of the Creede Formation and implications for hydrothermal vein mineralization. GSA abstracts **26**, no. 7, A-339.

MOJZSIS S. J., ARRHENIUS G. A., MCKEEGAN K. D., HARRISON T. M., NUTMAN A. P. & FRIEND R. L. (1996): Evidence of life on Earth before 3,800 million years ago. *Nature* **384**, 55-59.

NEAL, C.R., DAVIDSON, J.P. & MCKEEGAN, K.D. (1995): Geochemical analysis of small samples: Micro-analytical techniques for the nineties and beyond. *Rev. Geophysics*, 25-32.

NUTMAN, A.P. & COLLERSON, K.D. (1991): Very early Archean crustal accretion complexes preserved in the North Atlantic craton. *Geology* **19**, 791-794.

PATERSON, B.A., RICIPUTI, L.R. & MCSWEEN, H.Y. (1997): A comparison of sulfur isotope ratio measurement using two ion microprobe techniques and application to analysis of troilite in ordinary chondrites. *Geochim. Cosmochim*. **61**, 601-609.

PEEVLER, J., FAYEK, M., MISRA, K. & RICIPUTI, L. (2003): Sulfur isotope microanalysis of sphalerite by SIMS: constraints on the genesis of mississippi valley-type mineralization from the Mascot-Jefferson City District, East Tennessee. *J. Geochem. Explor.* **80**, 277-296.

PIMMINGER M., GRASSERBAUER M., SCHROLL E. & CERNY I. (1984): Microanalysis in galena by secondary ion mass spectrometry for determination of sulfur isotopes. *Anal. Chem*. **56**, 407-411.

REED, S.J.B. (1989): Ion microprobe analysis-a review of geological applications. *Miner. Mag.* **53**, 3-24.

http://jbs.sgpj.com/

REED, S.J.B. (1990): Recent developments in geochemical microanalysis. *Chem. Geol.* **83**, 1-9.

RICIPUTI L.R. (1996): A comparison of extreme energy filtering and high mass resolution techniques for measurement of 34S/32S ratios by ion microprobe. *Rapid Commun. Mass Spectrom.* **10**, 282-286.

RICIPUTI, L.R. & PATERSON, B.A. (1994): High spatial resolution measurement of O isotope ratios in silicates and carbonates by ion microprobe. *Am. Mineral* **79**, 1227-1230.

RICIPUTI L. R. & GREENWOOD J. P. (1998): Analysis of sulfur and carbon isotope ratios in mixed matrices by secondary ion mass spectrometry: Implications for mass bias corrections. *Int. J. Mass Spec.* **178**, 65-71.

RICIPUTI, L.R., PATERSON, B.A. & RIPPERDAN, R.L. (1998): Measurement of light stable isotope ratios by SIMS: Matrix effects for oxygen, carbon, and sulfur isotopes in minerals. *Int. J. Mass Spec.* **178**, 81-112.

RUDNICKI, M.D., ELDERFIELD, H. & SPIRO, B. (2001): Fractionation of sulfur isotopes during bacterial sulfate reduction in deep ocean sediments at elevated temperatures. *Geochim. Cosmochim.* **65**, 777-789.

SANGÉLY, L., CHAUSSIDON, M., MICHELS, R. & HUAULT, V. (2005): Microanalysis of carbon isotope composition in organic matter by secondary ion mass spectrometry. *Chem. Geol.* **223**, 179-195.

SANGÉLY, L., CHAUSSIDON, M., MICHELS, R., BROUAND, M., CUNEY, M., HUAULT, V. & LANDAIS, P. (2007): Micrometer scale carbon isotopic study of bitumen associated with Athabasca uranium deposits: constraints on the genetic relationship with petroleum source-rock and the abiogenic origin hypothesis. *Earth Planet. Sci. Let.* **258**, 378-396.

SAXTON J. M., LYON I. C., CHATZITHEODORIDIS E., PERERA I. K., VAN LIERDE P., FREEDMAN P. & TURNER G. (1996): The Manchester Isolab 54 ion microprobe. *Int. J. Mass Spectrom. Ion Proc.* **154**, 99-131.

SAXTON, J.M., LYON, I.C. & TURNER, G. (1998): Correlated chemical and isotopic zoning in carbonates in the Martian meteorite ALH84001. *Earth Planet. Sci. Lett.* **160**, 811-822.

SHARP, Z.D. (2005): *Principles of Stable Isotope Geochemistry*. Prentice Hall, 334 p.

SHARP, J.M., JR., GALLOWAY, W.E., LAND, L.S., MCBRIDE, E.F., BLANCHARD, P.E., BODNER, D.P., DUTTON, S.P., FARR, M.R., GOLD, P.B., JACKSON, T.J., LUNDEGARD, P.D., MACPHERSON, G.L. & MILLIKEN, K.L. (1988): Diagenetic processes in north western Gulf of Mexico sediments. (G.V. Chilligarian & K.H. Wolf, *eds*.). *Diagenesis, II. Developments in Sedimentology* **43**, 43-113.

SHIMIZU, N. & HART, S.R. (1982): Applications of the ion microprobe to geochemistry and cosmochemistry. *Annu. Rev. Earth Planet. Sci.* **10**, 483-526.

SHIVELY, J. M. & BARTON, L. L. (1991): *Variations in Autotrophic Life*. Academic New York, 1–346.

SHROEER, J.M., RHODIN, T.N. & BRADLEY, R.C. (1973): A quantum-mechanical model for the ionization and excitation of atoms during sputtering. *Surface Sci*. **34**, 571-580.

SIGMUND, P. (1969): Theory of sputtering, I. Sputtering yield of amorphous and polycrystalline targets. *Phy. Rev.* **184**, 383-416.

SLODZIAN, G., LORIN, J.C. & HAVETTE, A. (1980): Isotopic effect on the ionization probabilities in secondary ion emission. *J. Phys*. **41**, L555-L558.

SLODZIAN, G., CHAINTEAU, M.P. & DENNEBOUY, R.C. (1987): SIMS: Self-regulated potential at insulating surfaces in presence of strong electrostatic field: CAMECA News, May 1987.

VALLEY, J.W. & GRAHAM, C.M. (1991): Ion microprobe analysis of oxygen isotope ratios in granulite facies magnetites: diffusive exchange as a guide to cooling history. *Contrib. Miner. Petrol.* **109**, 38-52.

VALLEY, J.W. & GRAHAM, C.M. (1996): Ion microprobe analysis of oxygen isotope ratios in quartz from sky granite: healed micro-cracks, fluid flow, and hydrothermal exchange. *Contrib. Miner. Petrol.* **124**, 225-234.

VALLEY, J.W. & KITA, N.T. (2009): *In situ* oxygen isotope geochemistry by ion microprobe. *In* Secondary Ion Mass Spectrometry in the Earth and Planetary Sciences: Gleaning the Big Picture

http://pbs.3s001.com

from a Small Spot (M. Fayek, *ed.*). *Mineral. Assoc. Can*. **41**, 19-63.

VALLEY, J.W., EILER, J.M., GRAHAM, C.M., GIBSON, E.K. JR., ROMANEK, C.S. & STOLPER, E.M. (1997): Low temperature carbonate concretions in Martian meteorite ALH84001: Evidence from stable isotopes and mineralogy. *Science* **275**, 1633-1638.

VALLEY, J.W., GRAHAM, C.M., HARTE, B., EILER, J.M. & KINNY, P.D. (1998): Ion microprobe analysis of oxygen, carbon, and hydrogen isotope ratios. *In* Applications of Microanalytical Techniques to understanding Mineralizing Processes (M.A. McKibben & W.C. Shanks, *eds*.). *Soc. Econ. Geol. Rev.* **7**, 73-98.

WEATHERS, D.L., SPICKLEMIRE, S.J., TOMBRELLO, T.A., HUTCHEON, I.D. & GNASER, H. (1993): Isotopic fractionation in the sputtering of ^{92}Mo-^{100}Mo targets. *Nucl. Instrum. Methods.* **B73**, 135-150.

WILLIAMS, P. (1979): The sputtering process and sputtered ion emission. *Surface Sci.* **90**, 588-643.

WOOD, J.R. & BOLES, J.R. (1991): Evidence for episodic cementation and diagenesis recording of seismic pumping events, North Coles Levee, California, U.S.A. *Appl. Geochem.* **6**, 509-521.

WORTMAN U.G., BERNASCONI S.M. & BÖTTCHER M.E. (2001): Hypersulfidic deep biosphere indicates extreme sulfur isotope fractionation during single-step microbial sulfate reduction. *Geology* **29,** 647-650.

YU, M.L. & LANG, N. (1986): Mechanisms of atomic ion emission during sputtering. *Nuclear Instrum. Methods* **B14**, 403-413.

YURIMOTO, H. NAGASAWA, H., MORI, Y. & MATSUBAYA, O. (1994): Micro-distribution of oxygen isotopes in a refractory inclusion from the Allende meteorite. *EPSL* **128**, 47-53.

ZINNER E. (1989): Isotopic measurements with the ion microprobe. *In* New frontiers in stable isotopic research: Laser probes, ion probes, and small-sample analysis. (W.C. Shanks III & R.E. Criss, *eds*.) *U.S. Geol. Surv. Bull*. **1890**, 145-162.

ZINNER E. & CROZAZ G. (1986): A method for the quantitative measurement of rare earth elements in the ion microprobe. *Int. J. Mass Spectrom. Ion Proc*. **69,** 17-38.

ZINNER E., TANG M. & ANDERS E. (1987): Large isotopic anomalies of Si, C, N and noble gases in interstellar silicon carbide from the Murray meteorite. *Nature* **330**, 730-732.

APPENDIX A

Although each lab has its own routine, which is generally linked to the type of SIMS instrument (*e.g.*, small radius *vs*. large radius, SHRIMP *vs*. CAMECA), there are a series of universal steps that are prerequisite to SIMS analysis:

1. ***Sample characterization:*** the optical image on the SIMS is usually a reflected light image and the sample is usually coated with a conductive coating (*e.g.*, C or Au). Therefore, areas or minerals of interest are often difficult to locate using the SIMS optical image. Good sample characterization (*e.g.*, back-scattered electron, CL, and transmitted light images at different scales, knowing the major element chemistry of the minerals of interest) is essential to obtaining accurate and precise SIMS data.
2. ***Special sample preparation:*** some samples, particularly for H isotope analysis, require careful sample preparation and should be placed in the sample in airlock under vacuum overnight prior to the analytical session to achieve the best possible vacuum during analysis.
3. ***The primary beam*** generally needs to be tuned on a daily basis, as well as optimizing the secondary ion counts, and tuning the electron gun. Once the secondary column is tuned for a particular application, only minor adjustments are required to achieve the best possible secondary ion signal.
4. ***Proper standards:*** based on the major element chemistry of the minerals of interest, several standards (2-5) may be required to bracket the compositional range of the samples. In a typical analytical session, analyses of unknowns are interspersed with standards to monitor mass bias and drift.
5. ***Data processing:*** once the data are obtained (ratios measured by SIMS), off-line data processing is generally required to correct for drift, mass bias, and obtain the corrected values (*e.g.*, $\delta^{13}C_{PDB}$).

http://gbss.gscn.com.cn/

CHAPTER 4: Li, B AND Cl ISOTOPE DETERMINATION BY SIMS

Graham D. Layne
Department of Earth Sciences
Memorial University of Newfoundland
INCO Innovation Centre, Room 1047
St. John's, NL Canada, A1C 5S7
gdlayne@mun.ca

INTRODUCTION

Li, B and Cl isotopes have become increasingly recognized as useful in many geochemical applications; including cosmochemistry, basalt petrogenesis, paleoclimatology, and diagenetic studies. In contrast to $\delta^{18}O$ determinations, they involve the use of trace element analytes (often <100 ppm) for the determination of $\delta^{7}Li$, $\delta^{11}B$ and $\delta^{37}Cl$. This adds the following complications:

- Some sample suites (*e.g.*, volcanic glasses, solid solutions, mixed mineral assemblages) are variable in their major element concentrations, requiring attention to the possibility of substantial matrix effects on Instrumental Mass Fractionation (IMF). Recent studies have underlined the importance of this consideration for many applications in igneous geochemistry. Conversely, carbonate biomineralization benefits from rather consistent major element matrix ($CaCO_3$), and may be far less susceptible to significant IMF effects.
- The analyte element itself may be extremely variable in concentration within sample suites of glasses, melt inclusions or minerals. Therefore, care must be taken to maintain detector linearity. This is especially important if available reference materials have substantially different magnitudes of concentration of the analyte element compared to the samples.
- Surface contamination effects from sample preparation can be a major contributor to secondary ion signal if appropriate simple precautions are not taken.

Therefore – despite the natural inclination to focus on the settings of the actual mass spectrometer component of SIMS instruments – the most important practical considerations, as for many light stable isotope analysis by SIMS, are:

- *Calibration of IMF effects directly related to the production of analyte secondary ions by sample sputtering.* These are essentially related to variations of IMF due to sample matrix, and require one or more reference materials that are adequately matched to the range of sample compositions to be analyzed.

  Further, IMF can vary for individual analyses if care is not taken to stabilize the effective sample potential during analysis. Charge compensation is generally effectively maintained by a 300–500 Å gold coating for work involving O^- primary ion bombardment. However, care must be taken to monitor and stabilize drift in sample potential when very large (>~40 nA) primary beam currents are used in focused spots. $\delta^{37}Cl$ determinations in most materials will also generally require active charge compensation by electron-gun flooding.
- *Calibration of the accuracy and stability of the ion detectors over a wide dynamic range.* Detector performance actually forms an arithmetic component of the overall IMF correction. The measurements discussed in this chapter are most readily performed with pulse-counting electron multipliers (EMs). The essential requirements are, therefore, accurate definition of deadtime for EMs, and drift/aging correction and inter-calibration if multiple collectors are used. Fortunately, none of these three isotope pairs have a particularly extreme dynamic range, the natural abundance ratios of $^{7}Li/^{6}Li$, $^{11}B/^{10}B$ and $^{35}Cl/^{37}Cl$ being approximately 12.3, 4.3 and 3.1, respectively, compared to 489 for $^{16}O/^{18}O$. This makes them amenable to magnetic peak switching and detection by EM, or by dual EMs in a multicollector array. Many applications do, however, involve substantial count rates, so EM deadtime correction remains important at a per mil level.
- *Exotic Li, B and Cl.* These elements are commonly present as contaminants at sample surfaces, as a consequence of laboratory preparation. However, an intrinsic advantage of SIMS is the ability to combine pre-sputtering of

Mineralogical Association of Canada Short Course 41, Toronto, May 2009, p. 89-108

the sample surface with an appropriately restricted field of view (Field Aperture) in the mass spectrometer. This may be used to great advantage in reducing signal from surface contamination to an insubstantial level – in fact, often well below the comparable "blank" levels that limit some other mass spectrometric approaches to these determinations.

If these considerations can be properly addressed, SIMS can give access to accurate and precise δ^7Li, δ^{11}B and δ^{37}Cl determinations in a wide variety of natural materials, and at a spatial resolution generally inaccessible by any other existing technique. Many applications also require these ratios to be determined at accuracies of better than ±1‰. This provides additional challenges in materials where the analyte element is at the ppm level and requires careful optimization of instrument transmission and sensitivity to provide the best possible precision in isotope ratio determinations.

All errors cited within this paper are 1σ, unless otherwise noted. Li, B and Cl *concentrations* are abbreviated throughout the text as [Li], [B] and [Cl], respectively.

Li ISOTOPES

Li isotope compositions are expressed in per mil notation as δ^7Li relative to the L-SVEC Li_2CO_3 standard (^{7}Li/^{6}Li = 12.173; Coplen *et al.* 2002). Some authors have chosen to use the alternative notation δ^6Li (*e.g.*, Decitre *et al.* 2002).

Instrumental Approach

Published studies summarized here (Tables 4-1 and 4-2) have all involved sputtering with a primary beam of O^-, and extraction of Li^+ secondary ions from the sample. Ushikubo *et al.* (2008) used 10–15 μm spots at 0.5–3.0 nA, to facilitate the analysis of complexly zoned zircon crystals. Most studies have opted to use primary beam currents of 10–60 nA, providing concomitantly larger Li^+ signals, from sputtered craters of 20–30 μm diameter.

No energy filtering has been used for δ^7Li determinations (sample offset voltage of 0 eV), and the Energy Slit has been maintained at widths >40 eV. However, in the bulk of these studies, Mass Resolving Power (MRP) has been maintained at values >1100, to ensure effective separation of $^6LiH^+$ from $^7Li^+$. The single exception to this was Bell *et al.* (2009), who asserted that the $^6LiH^+$ signal in their samples of olivine was insignificant at a sub-per mil level, and consequently they maintained an MRP of only 600. This lower MRP would result in an estimated signal increase of ~10–20% in small format (IMS 3f/4f/5f/6f/7f) instruments. However, it is not relevant to the operation of large format instruments (*e.g.*, IMS 1270/1280) where the minimum MRP (*i.e.*, base MRP at maximum transmission) is greater than 2000.

Most workers noted a spot pre-sputter of 2–5 minutes, to ensure removal of surface contamination before beginning data collection.

Precision and Reproducibility

Most published studies with small format (IMS f-series) instruments have managed to achieve individual spot precisions for δ^7Li better than ±1‰ for analytical times of 20 minutes or less per spot. Overall reproducibility has generally been cited as better than ±1‰, in a wide variety of glass and mineral samples.

Vigier *et al.* (2007) and Kasemann *et al.* (2005) used large format instruments in monocollection mode to achieve individual spot precisions of ±0.4 ‰ (calcite standard; 2 ppm [Li]) and ±0.2 ‰ (synthetic basalt glass; 37 ppm [Li]), respectively. Kobayashi *et al.* (2004) used an IMS 1270 in multicollector mode to maintain a precision of ±0.6 ‰ in synthetic basalt glass with only 0.83 ppm [Li]. Ushikubo *et al.* (2008) achieved individual spot precisions of better than ± 1.5–2 ‰ in zoned zircon samples (1–100 ppm [Li]). The best overall reproducibility reported to date was ±0.5 ‰ in synthetic basalt glass using an IMS 1270 in monocollection mode (Kasemann *et al.* 2005; Table 4-1).

Precision of δ^7Li determinations by SIMS benefits from the intrinsically high ion yield of Li^+ under O^- sputtering. Implied sensitivities for IMS 1270/1280 instruments (with no sample offset voltage applied) are 2000 cps/ppm/nA for basaltic glass (Kobayashi *et al.* 2004), 2345 cps/ppm/nA for zircon and 1125 cps/ppm/nA for NIST 612 (Ushikubo *et al.* 2008). No data was provided in published studies to allow direct comparison to f-series instruments. However, given the modest MRP applied for these determinations, the intrinsic transmission advantage over f-series instruments may only be 10–25%, if optimal Entrance Slit and Exit Slit settings are used to maintain MRP at 1100. Based on measurements in NIST 610 of the same low initial energy secondary ions typically measured in the Table 4-1 studies, the ion yield of Li^+ is approximately 15 times higher than that for B^+ under O^- bombardment (Hinton 1990).

In order to maximize transmission for any given setup, it seems advisable to deploy i) the largest available Contrast Aperture, ii) as wide an Energy Slit setting as practical (minimum ±25 eV) and, iii) the widest Entrance Slit and Exit Slit settings possible while still achieving 1100 MRP (or less for samples with a very high $^{7}Li^{+}/^{6}LiH^{+}$).

Some other procedures may also improve signal and reproducibility. Periodic re-centering of the Energy Slit bandpass (by scanning and adjusting the sample offset) will help ensure that any drift due to sample charging during analysis is compensated (*e.g.*, Bell *et al.* 2009). With focused O^{-} primary beams of 25 nA or greater, effective sample offset in Au-coated samples can still drift off by tens of eV during lengthy analyses. Bell *et al.* (2009) also noted that, although $^{7}Li^{+}/^{6}Li^{+}$ stabilized during the pre-sputtering period, intensity of Li^{+} relative to Si^{+} continued to rise gradually during the first 50 cycles of analysis. Consequently they used only subsequent cycles for [Li] determination.

$^{7}Li^{+}$ and $^{6}Li^{+}$ ($\Delta M/M = 1.166$) lie just within the nominal maximum dispersion of the IMS 1270/1280 multicollector array. Multicollection is one obvious approach to improve precision, and this application has been shown practical by Kobayashi *et al.* (2004) and Ushikubo *et al.* (2008). However, there is additional time overhead in the periodic intercalibration of the detector pair used. For example, Ushikubo *et al.* (2008) noted that, even with maximum count rates maintained below 100,000 cps, aging of the miniature EM detectors of the multicollection array produced a drift of up to 4 ‰ in the calculated IMF over a 10 hour analytical session. This required periodic replicate measurement of a reference material to bracket IMF corrections.

[Li] Determination

Li concentration ([Li]) is an obviously useful datum to acquire in tandem with $\delta^{7}Li$, and easily amenable to SIMS analysis. However, most authors have chosen to determine [Li] in an entirely separate instrument session from $\delta^{7}Li$. This is usually accomplished by measuring $^{7}Li^{+}/^{28}Si^{+}$ or $^{7}Li^{+}/^{30}Si^{+}$ in samples, and one or more similar reference materials, with or without an energy filter applied (Table 4-2).

In many applications, [Li] could be determined more quickly, and in the same sample volume as $\delta^{7}Li$, with little marginal effect on time or precision. For monocollection applications this would simply involve adding a cyclical peak on $^{28}Si^{++}$ or $^{30}Si^{++}$, to minimize the magnitude of magnet field switching relative to $^{6}Li^{+}$ and $^{7}Li^{+}$. In multicollection, a supplementary peak switch to a middle collector may be programmed at the end of each spot determination.

A few authors (*e.g.*, Ushikubo *et al.* 2008, Kasemann *et al.* 2005) have chosen simply to estimate [Li] from measurement of $^{6}Li^{+}$ and $^{7}Li^{+}$ only for $\delta^{7}Li$, by directly comparing the raw signal intensity ($I\ ^{7}Li^{+}$) in the samples to that in a standard material, with some allowance for drift in primary beam current. This technique allows an estimate of [Li] to better than perhaps 25%, but allows no means of accurately assessing matrix effects or intra-session drift in primary beam current.

Standards and Matrix Effects

Instrumental Mass Fractionation (IMF) of $^{7}Li^{+}$ versus $^{6}Li^{+}$ is large and often positive. Vigier *et al.* (2007) noted IMF of about +23‰ for silicate glass matrices, but about –14‰ for calcite matrices. Decitre *et al.* (2002) observed stable IMF of +34 to +39‰ over individual sessions on mafic minerals. Chaussidon & Robert (1998) reported IMF of about +40‰ in silicate glass, as opposed to –42‰ for $^{11}B^{+}$ *versus* $^{10}B^{+}$ under similar conditions. The *positive* IMF routinely observed for $\delta^{7}Li$ (and for $\delta^{37}Cl$, in some matrices) is unusual, but awaits a quantitative explanation in the literature.

Most applications of SIMS for $\delta^{7}Li$ determination will require stabilizing and calibrating IMF at a better than ±1‰ level. In this regard, the two major issues are i) calibration of matrix dependency of IMF and, ii) the characterization of highly homogeneous reference materials.

Matrix dependence of IMF. Decitre *et al.* (2002) studied the relative matrix dependencies of [Li] and $\delta^{7}Li$ determinations in natural basaltic glass, and also in a suite of mafic minerals of interest to them in a study of Li isotope behavior during serpentinization of oceanic peridotite. Although subsequently cited as proof that distinguishable matrix effects are *absent* in these materials, this study actually demonstrated that matrix effects existed, though limited to levels of 10–15% for [Li] and ~1‰ for $\delta^{7}Li$, if a fused basalt powder (BHVO) was used as a standard for the analysis of certain mafic minerals (olivine [BZ29; fo_{89}], ortho-pyroxene, clinopyroxene, amphibole). They also demonstrated that reproducibility on individual homogeneous materials, such as a natural basalt glass (Nazca), is better than about ±1‰ for $\delta^{7}Li$.

TABLE 4-1. INSTRUMENTAL CONDITIONS FOR δ^7Li DETERMINATIONS (TABLE CONTINUES ON NEXT PAGE).

Study	Instru-ment	Samples	Primary Beam Current (paV); φ	MRP*	HVO(EW)	Time; cycles; peaks
Bell et al (2009)	IMS 3f/6f	Olivine	15–30nA; 30–50µm	~600	0eV (±20eV)	; 50–200 cyc; $^6Li^+$(10s); $^7Li^+$(1s)
Ushikubo et al (2008)	IMS 1280 multicoll	Zircon	0.5–3.0nA (13kV); 10–15µm	2200	0eV (±20eV)	400 s; ; $^6Li^+$ (L2), $^7Li^+$ (H2)
Vigier et al (2007)	IMS 1270 monocoll	Foraminifera	~60nA(13kV); 20–30µm	~3000	0eV (>120eV)	~20 min; 40–60cyc; 5.5Da( ); $^6Li^+$(12s); $^7Li^+$(10s)
Kasemann et al (2005)	IMS 1270 monocoll	Ref Mat (glass)	10nA(12kV); 25µm	2400	0eV (±15eV)	100 cyc; $^6Li^+$(5s); $^7Li^+$(2s)
Kasemann et al (2005)	IMS 4f	Ref Mat (glass)	20nA(10kV); 25µm	1200	0eV (±26eV)	120 cyc; $^6Li^+$(5s); $^7Li^+$(2s)
Kobayashi et al (2004)	IMS 1270 multicoll	Olivine-hosted melt incl.	15nA; 20µm	~2000	0eV (±25eV)	550 s; ; $^6Li^+$ (L2); $^7Li^+$ (H2)
Decitre et al (2002)	IMS 3f	Ref Mat (glass & mafic mineral)	10–20nA(10kV); ~20µm	1100	0eV (>120eV)	;120 cyc; $^6Li^+$(6s); $^7Li^+$(3s)
Chaussidon & Robert (1998)	IMS 3f	Semarkona Meteorite chondrules	(10kV); ~25µm	~1600	0eV (>120eV)	150–200 cyc; $^6Li^+$(8s); $^7Li^+$(4s); $^{10}B^+$(8s); $^{11}B^+$(4s)

Unless otherwise noted IMS 3f/4f/5f instruments were operated with a secondary ion extraction voltage (sample potential) of 4.5 kV, and IMS 6f/1270/1280 instruments with 10 kV. Primary ions were O^-. All detection by EM in pulse counting mode.*A nominal MRP of 1010 (10% definition) is the minimum required to effectively eliminate isobaric interference of $^6LiH^+$ on $^7Li^+$.

In fact, matrix effects cannot be assumed insubstantial for *all* sample compositions. Bell *et al.* (2009) recently demonstrated a pronounced matrix effect on IMF for Fe–Mg solid solution in olivine using an IMS 6f. For δ^7Li determinations they observed that IMF varied by 1.3‰ per mole % forsterite (fo_{XX}) in samples ranging between fo_{75} and fo_{95} (Fig. 4-1), a >25‰ difference in the IMF correction required for this range of common naturally occurring olivine compositions. This effect may well become more extreme, and likely non-linear, for lower fo values (Fig. 4-2) – but additional data will be needed to quantify the effects below fo_{75}. It may also depend on instrument type and/or specific settings (such secondary ion extraction voltage) to various degrees below fo_{80}. The observations of Bell *et al.* (2009) are broadly similar to the effect of forsterite content on δ^{18}O determinations documented by Eiler *et al.* (1997).

Bell *et al.* (2009) concurred with Decitre *et al.* (2002) in terms of similar limited matrix effects for [Li] determination between high-fo olivine (KBH-1; fo 90.5) and the basaltic glass reference materials examined by Kasemann *et al.* (2005; see below). However, [Li] calibration between these same reference materials and high-silica glasses (NIST 610 and UTR-2 pantellerite) diverged by as much as 20%.

Especially for δ^7Li determinations, Bell *et al.* (2009) emphasized that the consideration of matrix effects is especially important where "inter-mineral isotopic equilibrium is being assessed, or where quantitative interpretations of isotope profiles in compositionally zoned minerals are desired."

http://bbs.3s001.com/

TABLE 4-1 (CONTD). INSTRUMENTAL CONDITIONS FOR δ^7LI DETERMINATIONS.

Reference Material	Precision (1σ)	Reproducibility (1σ)	Sensitivity ($^7Li^+$)	Other Parameters
Olivine KBH-1 (1.2ppm [Li])	±0.7 – 1.0‰ (KBH-1; 100 cyc)			Spot presputter 3–5 min; Energy offset recentered every 20 cyc
Xinjiang Zircon (6.4 ppm [Li])	±1.0 – 1.9‰ (Zircon samples)	±1.5 ‰ (Xinjiang zircon); ±1.0 ‰ (NIST 612)	1690 cps/ppm [Li] (1.5nA; NIST 612); 4690 cps/ppm [Li] (2.0 nA; Xinjiang Zircon)	Sputter area collim 70% by FA. Spot presputter 300s. [Li] by direct comparison of I^7Li^+ to Ref Mat
CAL-HTP synth calcite (2 ppm[Li])	±0.4‰ (CAL-HTP); ±0.65‰ (Foraminifera)	±1.0 ‰ (Foraminifera)		Spot presputter 2 min
GSD-1G synth basalt glass	±0.2‰ (GSD-1G; 37 ppm[Li])	±0.5‰ (GSD-1G)		
GSD-1G synth basalt glass	±0.4‰ (GSD-1G; 37ppm[Li]); < ±1.0‰ (glass samples)	±0.6‰ (GSD-1G)		[Li] by direct comparison of I^7Li^+ to Ref Mat
Lin Regr synth basaltic andesite glasses (5)	±0.6‰ (synth glass; 0.83 ppm [Li])	±1.0 ‰ (Ref Mat glasses); Accuracy of IMF correction ±0.4 – 0.6‰	~30K cps/ppm [Li] (15.0 nA; basaltic andesite glass)	Spot presputter 5 min
Fused BHVO basalt glass (5ppm [Li])		±1.0 ‰ (Fused BHVO, 5ppm [Li]); ±0.85 ‰ (CPx samples)		Bfield rescanned- recentred every 10cyc
Synth glass doped w LSVEC	±4.0‰ (chondrules; 0.5–3.7 ppm [Li])	±3.4 ‰ ("peridotite" Ref Mat)		Tandem w δ^{11}B; general conds. of Chaussidon et al (1997)

TABLE 4-2. INSTRUMENTAL CONDITIONS FOR [LI] DETERMINATIONS

Study	Instru-ment	Samples	Primary Beam Current (paV); φ	MRP	HVO (EW)	Time; cycles; peaks	REF MAT	Precision (1σ)	Other
Bell *et al.* (2009)	IMS 3f/6f	Olivine	15–30nA; 30–50µm	~600	–75eV (±20eV)	; ; $^7Li^+$;$^{30}Si^+$	Olivine KBH-1 (1.2ppm [Li]); BCR-2G (9 ppm [Li])		
Bell *et al.* (2009)	IMS 3f/6f	Olivine	15–30nA; 30–50µm	~600	0eV (±20eV)	; ; $^7Li^+$;$^{28}Si^+$	Olivine KBH-1 (1.2ppm [Li]); BCR-2G (9 ppm [Li])		
Kasemann *et al.* (2005)	IMS 4f	Ref Mat	20nA (15kV); ;25µm	1200	0eV (±26eV)	;120 cyc; $^6Li^+$(5s); $^7Li^+$(2s)	NIST 610	±3%	[Li] by direct comparison of I^7Li^+ to Ref Mat
Decitre *et al.* (2002)	IMS 3f	Ref Mat	10–20nA (10kV); 25µm	500	–80eV (±10eV)	;30cyc; $^7Li^+$(4s); $^{30}Si^+$(4s)	Regr of mineral Ref Mats (1.5–1200ppm[Li])	±5% (ref mats > 5ppm [Li]) ±15% (ref mats <1ppm [Li])	Uncert in Regr of Ref Mats 10–15%

质谱地质论坛: http://bbs.3s001.com/

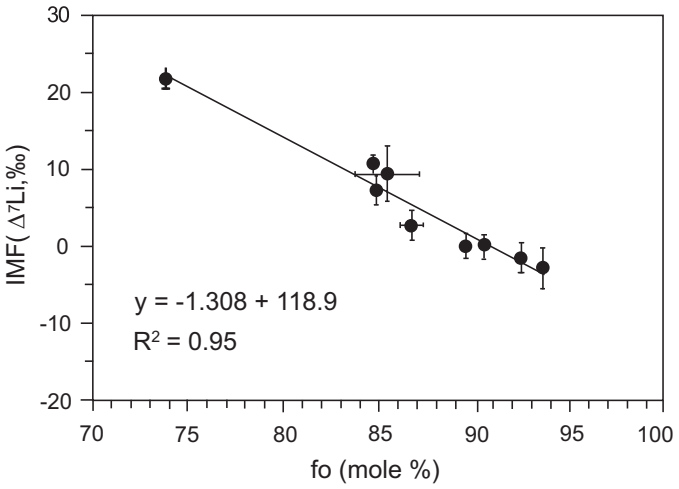


FIG. 4-1. IMF as a function of mole% forsterite (fo) for Mg-rich olivine (fo>74; IMS 6f). The y-axis is IMF calculated as the difference between the average δ^7Li measured by SIMS on a collection of grains (n=5 to 15) and that determined by either TIMS or MC–ICP–MS after dissolution and chromatographic purification of a bulk olivine separate. All SIMS analyses referenced to KBH1 olivine ($fo_{90.5}$) for correction of IMF. Errors bars shown for both solution and SIMS analyses represent ±2σ of the population of these measurements. After Bell *et al.* (2009).

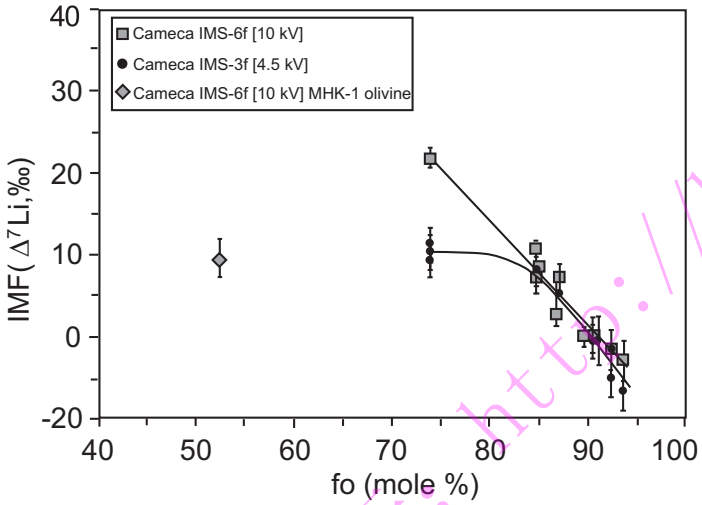


FIG. 4-2. IMF as a function of mol.% forsterite (fo) in olivine, including Fe-rich olivine, with additional data (from IMS 3f) for the same samples in Figure 4-1. All SIMS analyses referenced to KBH1 olivine ($fo_{90.5}$) for correction of IMF. Note the implied departure from linearity for i) Fe-rich olivine MHK-1 (fo_{52}) for IMS 6f determinations and, ii) an olivine (PMD99-149) with fo < about 85 for IMS 3f determinations. After Bell *et al.* (2009).

Homogeneity of reference materials. The intrinsic homogeneity of available reference materials may be a limiting factor in SIMS determinations of light stable isotope ratios. The inherently high diffusion rate of Li through many materials may in fact increase the difficulty in synthesizing or locating materials homogeneous in [Li] and δ^7Li.

Kobayashi *et al.* (2004) used the approach of synthesizing five basaltic andesite composition glasses from natural starting material (8.05 ppm [Li]; 31.2 ppm [B]), and progressively increasing [Li] and [B] via doping with ^{6}Li- and ^{10}B-enriched spikes (CMNM-IRM-15: 1.020 ppm [Li]; NIST 952: 1.482 ppm [B]). These glasses were designed to be similar in major element composition to the olivine-hosted melt inclusions of interest in their study, minimizing the uncertainties due to matrix effects. δ^7Li and δ^{11}B were first determined by TIMS, and the glasses were then used to produce regression lines for the calibration of IMF (Fig. 4-3). In this manner, the uncertainty in the absolute value of IMF correction was reduced to ±0.4–0.6‰.

Kasemann provided a thorough test and comparison of available glass reference materials, including high-silica synthetic glasses (NIST 610, 612, 614), USGS basaltic glasses (BHVO-2G, BCR-2G, and BIR-1G), and a newer series of basaltic glasses from USGS – GSA-1G, GSC-1G, GSD-1G, and GSE-1G (Jochum *et al.* 2005; Wolf & Wilson 2007).

Their [Li] determinations by SIMS for the older USGS "B-series" glasses implies substantial loss of Li from the starting component powder reference materials (eponymous natural basalt powders). However, SIMS profiles of both [Li] and δ^7Li imply that all of the glasses assessed are themselves reasonably homogeneous (with the exception of localized δ^7Li inhomogeneities observed

矿物地质学报: http://bbs.3s001.com/

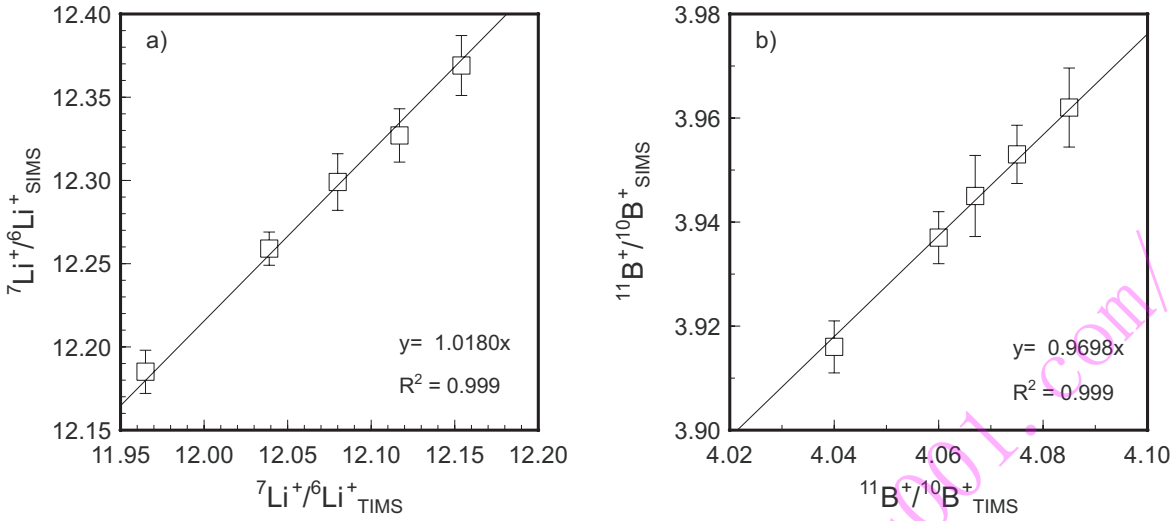


FIG. 4-3. Typical regression lines for a) Lithium isotopes and, b) Boron isotopes in synthetic basaltic andesite glass standards used to calibrate IMF for the SIMS analyses of Kobayashi *et al.* (2004). Error bars represent 2σ (n=4) reproducibility for the replicate SIMS spots on each synthetic glass standard (for these relatively homogeneous glasses, they thus overestimate the error of the quantities used for the linear regression by a factor of approximately $\sqrt{n}$). Data from Kobayashi *et al.* (2004). Note the large positive IMF for $^{7}Li^{+}/^{6}Li^{+}$ (~+18‰) evidenced by the slope of the regression plotted in a).

in parts of GSC-1G). When referenced to NIST 610, [Li] results for the synthetic USGS basalt glasses are (generally) within the broad ranges currently certified by USGS (with the exception of the GSA-1G glass). However a matrix effect of less than 10–15% between NIST 610 and the basaltic glasses would not have been statistically detectable within the current uncertainties of the accepted [Li] for these glasses, again implying the desirability of using separate standards for accurate studies of rhyolite and other high-silica materials.

SIMS results for GSA-1G imply that up to 40% of the Li in this nominally <1 ppm [Li] material is processing blank from the production of a fused powder. Another useful finding of this study is the extreme δ^{7}Li zonation observed in the outer 600 μm of a BIR-1G pellet (up to 60‰ > bulk δ^{7}Li), which was attributed to mixing/contamination during glass synthesis and implies that caution must be exercised in the avoidance of rim areas of this and other synthetic glasses.

For both B-series and GS-series USGS glasses, SIMS analyses referenced to GSD-1G agree within 2‰ with MC–ICP–MS (and TIMS) determinations of δ^{7}Li (Fig. 4-4). Kasemann *et al.* (2005) propose USGS glasses GSD-1G (δ^{7}Li 31.1 ±0.8‰) and BCR-2G (δ^{7}Li 4.1 ±0.5‰) as the most suitable SIMS standards for δ^{7}Li in basaltic glasses. However, they also caution that SIMS δ^{7}Li determinations appear to have a significant matrix-induced bias in IMF (they observed +9‰) in high silica materials relative to these basaltic materials

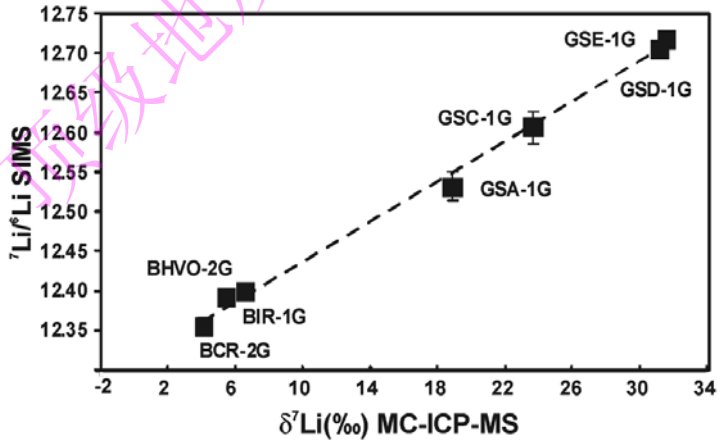


FIG. 4-4. Li isotope ratios measured by SIMS *versus* the δ^{7}Li obtained by MC–ICP–MS for USGS reference glasses. The SIMS error bars are 2*σ*. The y-intercept of this line implies an IMF for δ^{7}Li of > +10‰. If these SIMS determinations are corrected for IMF by simple comparison with GSD-1G (δ^{7}Li 31.1 ±0.8‰) values for all glasses shown lie within 2‰ of MC–ICP–MS and TIMS determinations. After Kasemann *et al.* (2005).

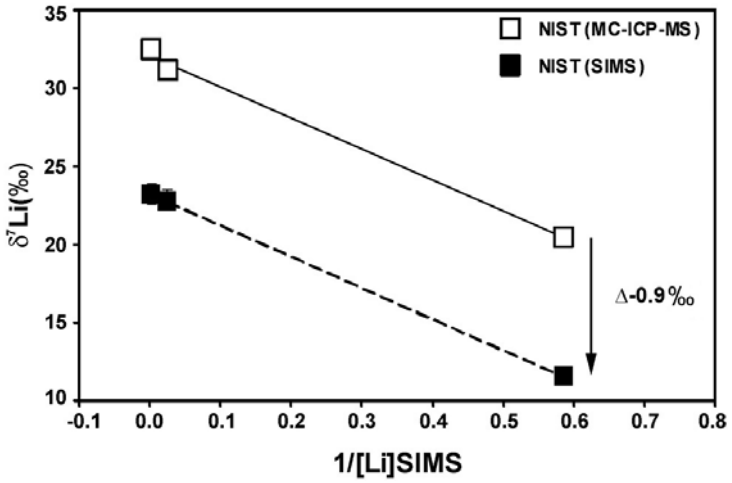


FIG. 4-5. δ^7Li vs 1/[Li] for the synthetic NIST glasses (610, 612, 614), as determined by SIMS using the basaltic glass GSD-1G as a reference for calibrating IMF. The nominal δ^7Li determined for NIST glasses in this manner shows a systematic –0.9‰ offset, implying a consistent matrix effect of this magnitude between basaltic and high-silica glasses. After Kasemann *et al.* (2005).

(Fig. 4-5). IMS 4f and IMS 1270 gave good agreement, and similar reproducibility (Table 4-1) for δ^7Li determinations with better internal precision for individual spots with the IMS 1270.

Applications

Studies by Kobayashi *et al.* (2004) and Gurenko & Schmincke (2002) used SIMS to determine δ^7Li and δ^{11}B in olivine- and pyroxene-hosted melt inclusions for the study of basalt paragenesis at Hawaii and the Iblean Plateau (Sicily), respectively. These are reviewed and summarized in Layne (2006).

The heavy δ^7Li signatures produced by near-surface processes provide a potential tracer of crustal material recycled to the mantle by subduction (Elliot *et al.* 2004). Several other recent studies have utilized SIMS as a tool for mineral analysis to begin defining the δ^7Li of various reservoirs that play an important part in the subduction factory.

Decitre *et al.* (2002) studied the behavior of [Li] and δ^7Li during the serpentinization of oceanic peridotite, using samples collected from the southwest Indian Ridge (SWIR). Through *in situ* analysis of serpentine and relict mafic mineral phases by SIMS, they deduced that, as a consequence of the relatively low [Li] of seawater, serpentinizing hydrothermal fluids derive their Li predominantly from adjacent oceanic basalt. The Li recycled by subduction of this serpentinite, therefore, comprises almost exclusively Li derived from oceanic crust, rather than isotopically heavier Li from seawater. The extremely variable [Li] and δ^7Li in the SWIR serpentinite (0.6–8.2 ppm [Li]; +2.9 to +14‰ δ^7Li) is a consequence of the long-term evolution of the hydrothermal fluids during alteration and exchange, and changing patterns of fluid flow that result in superposition of multiple serpentine generations.

Wagner & Deloule (2007) used SIMS determinations of [Li] and δ^7Li in olivine, clinopyroxene, orthopyroxene and amphibole (following the procedure of Decitre *et al.* 2002; Tables 4-1 & 4-2) in their study of the complex behavior of Li during mantle metasomatism by a hydrated silicate melt, as recorded in spinel lherzolite xenoliths from the French Massif Central.

All petrogenetic studies using δ^7Li are potentially affected by the extremely fast diffusion of Li observed in silicate glasses and minerals. Richter *et al.* (2003) used SIMS in their experimental assessment of Li diffusion and diffusive isotope fractionation between basalt and rhyolite at 1350°C (Fig. 4-6). This provided the first experimental demonstration of large diffusive fractionation effects on δ^7Li (~40‰) at high temperature.

Parkinson *et al.* (2007) (using the procedures of Kasemann *et al.* 2005; Tables 4-1 & 4-2) measured [Li] and δ^7Li in high resolution profiles across clinopyroxene and olivine phenocrysts in primitive arc lavas of the New Georgia Group (Solomon Islands). They observed gradients of up to 25‰ in δ^7Li between rims and interior zones of individual grains, attributed to high T Li diffusion, and modeled as reflecting crystal residence times of 13–148 days. This implies that δ^7Li fractionation might be used as a geospeedometer on timescales of days to hundreds of days, but that this same process will quickly destroy the parent magma δ^7Li signature in, for example, porphyritic lavas or mantle melts. This latter observation obviously has important implications for the use of δ^7Li as a tracer

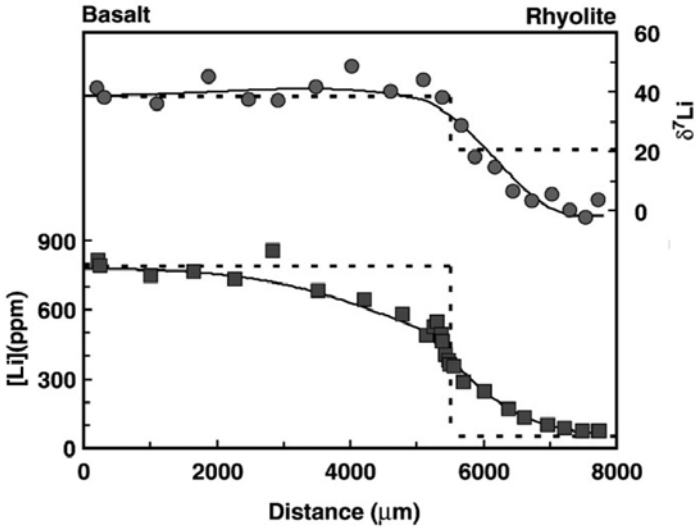


FIG. 4-6. δ^7Li and [Li] measured by SIMS on materials from sample RB-5 (Richter *et al.* 2003), a diffusion couple experiment comprising a Li-doped basalt (left side) and a rhyolite (right side). Annealed for 6 minutes at 1350°C in a piston cylinder apparatus (P = 1.2GPa). Closed circles are individual SIMS determinations of δ^7Li. Closed squares are individual SIMS determinations of [Li]. Dashed lines indicate the original distributions of [Li] and δ^7Li in the starting materials. The solid curve through [Li] data is a model fit using different diffusion coefficients for lithium in the silica-rich rhyolite (72 wt.% SiO_2) and in the silica-poor basalt (50 wt.% SiO_2). The solid curve through δ^7Li data is a fit using $D_{7Li}/D_{6Li} = (m_{6Li}/m_{7Li})^{\beta}$, with $\beta = 0.215$. After Richter *et al.* (2009).

for the study of subduction recycling. Jeffcoate *et al.* (2007) also concluded, based on their SIMS profiles of olivine and pyroxenes from both Hawaiian basalts and mantle xenoliths, that the diffusion-induced fractionation of δ^7Li had potential as a high-resolution geospeedometer, but that diffusion effects must be taken into account when inferring the δ^7Li of a primary magma from analyses of volcanic phenocrysts. The SIMS study by Bell *et al.* (2009) of δ^7Li in olivine phenocrysts from Ko'olau (Hawaii) basalt showed isotopic variability greater than that expected from high T equilibrium fractionation of Li, providing additional evidence that δ^7Li is easily disturbed in young basalt by diffusive fractionation.

Vigier *et al.* (2007) have recently demonstrated the potential of SIMS for the determination of δ^7Li in individual foraminifers. Results on modern *Globigerinoides* and *Globorotalia* species suggest that they preserve seawater δ^7Li (within analytical uncertainty) making them a potentially useful record of seawater δ^7Li over time. These particular species have relatively thick test walls, enabling them to be analyzed with spot diameters as large as 30 μm (Table 4-1). Bice *et al.* (2005) have recently documented the utility of SIMS for Mg/Ca determinations in more delicate species of foraminifera, and it appears that the approach of Vigier *et al.* (2007) could be extended to these as well, if sufficient signal could be derived for Li^+ at a spatial resolution of 10μm or better.

Ushikubo *et al.* (2008) presented a novel application of [Li] and δ^7Li determinations by IMS 1280 to Hadean zircon from Jack Hills, with implications for extensive weathering of the Earth's earliest crust.

B ISOTOPES

B isotope compositions are expressed in per mil notation as δ^{11}B relative to the NIST 951 boric acid standard ($^{11}B/^{10}B$= 4.0436; Coplen *et al.* 2002).

Instrumental Approach

As for δ^7Li, all published studies (including those examples summarized here in Tables 4-3 & 4-4) have involved sputtering with a primary beam of O^-, and extraction of positive (B^+) secondary ions from the sample. This is sensible, given the expected superior yields of Li^+ and B^+ in this mode compared to, for example, Cs^+ sputtering with extraction of Li^- or B^-.

Many studies have closely adapted the settings originally published by Chaussidon *et al.* (1997) – no energy filtering (sample offset voltage of 0 eV; wide energy slit (>120 eV)), MRP maintained at values >1400 to ensure separation of $^{10}BH^+$ from $^{11}B^+$, and sufficient cyclical counting of $^{10}B^+$ and $^{11}B^+$ to develop useful precision on δ^{11}B. MRP >1400 is also sufficient to separate $^9BeH^+$ from $^{10}B^+$ in glasses with significant Be/B. Chaussidon *et al.* (1997) used extremely large primary beam currents (as high as 100 nA) and concomitantly large spot diameters (up to 100 μm) in order to increase precision in samples with ultra low [B] (0.1–1.0 ppm [B] in meteoritic chondrules). Terrestrial materials with tens of ppm [B] are generally amenable to analysis using more modest primary beam currents and spot diameters on IMS f-series

TABLE 4-3. INSTRUMENTAL CONDITIONS FOR $\delta^{11}B$ DETERMINATIONS

Study	Instru-ment	Samples	Primary Beam Current (paV); φ	MRP*	HVO(EW)	Time; cycles; peaks	Reference Material	Precision (1σ)	Reproducibility (1σ)	Sensitivity ($^{11}B^+$)	Other Para-meters
Kobayashi *et al.* (2004)	IMS 1270 multi-coll	Olivine-hosted melt inclusions	20nA; 30μm	~2000	0eV (±25eV)	550 s; ; $^{10}B^+$(L1); $^{11}B^+$(H1)	Lin regr synth basaltic andesite glasses (5)	±0.5‰ (synth glass; 23 ppm [B])	±1.0‰ (synth ref glass); Accuracy of IMF ±0.3 – 0.8‰	~10^3cps/ppm[B] (20nA)	Spot pre-sputter 5 min
Rollion-Bard *et al.* (2003)	IMS 1270 mono-coll	Coral aragonite	; 30–50 μm	2000			Aragonite ($\delta^{11}B$ +23±1 ‰)	±0.6‰	±0.9 ‰ (Aragonite ref mat)	~4•10^4 cps (nA and [B] not provided)	
Straub & Layne (2002)	IMS 1270 mono-coll (rect mode)	Tephra and melt inclusions	8nA; 12μm	>2000	0eV (–15,+75 eV)	25–50 min; 80–160 cyc 9.33Da (1s); $^{10}B^+$(6s); $^{11}B^+$(4s); $^{30}Si^{++}$(2s)	GB-4	±0.3-0.5‰ (glasses; ≥10ppm [B])	±0.3 - 0.6‰ (IZB90 glass; 49 ppm [B]); ±0.7‰ (glass ≥10ppm[B])	>10^3cps/ppm[B] (8nA)	FA adj for 15-20 μm FOV; Pre-sputtered 5 min with 15 μm^2 R
Schmitt *et al.* (2002)	IMS6f**/ IMS3f	Quartz-hosted melt inclusions	20nA; 25μm	1800	0eV (±25eV)	15–50 min; 30–150 cyc; $^{10}B^+$(12s); $^{11}B^+$(6s)	NIST 610	±1 ‰ (glasses; 40-70 ppm[B])	±1.7 ‰ (NIST610); ±2 ‰ (melt inclusions)	>65 cps/ppm[B] (20nA)	Spot pre-sputter 10 min
Chaussidon *et al.* (1997)	IMS 3f	Meteoritic chond-rules; Basalt glass	≤100nA (10kV); 30–100 μm	1800	0eV (>120eV)	≤ 90 min; 220 cyc; $^{10}B^+$(15s); $^{11}B^+$(8s)	GB-4	±5 ‰ (chondrules); ±1 ‰ (glasses >0.5 ppm[B])	±5 ‰ (chondrules; 0.1-1.0 ppm [B]); ±1.5 ‰ (glasses >0.5 ppm[B])		Optim-ized for samples 100 ppb–1 ppm[B]

Unless otherwise noted IMS 3f/4f/5f instruments were operated with a secondary ion extraction voltage (sample potential) of 4.5 kV, and IMS 6f/1270/1280 instruments with 10 kV. Primary ions were O^-. All detection by EM in pulse counting mode.*A nominal MRP of 1416 (10% definition) is the minimum required to effectively eliminate isobaric interference of $^9BeH^+$ on $^{10}B^+$; MRP of 961 for $^{10}BH^+$ on $^{11}B^+$. ** IMS6f operated with 7kV sample potential.

原创地质论坛: http://bbs.3s001.com/

TABLE 4-4. INSTRUMENTAL CONDITIONS FOR [B] DETERMINATIONS

Study	Instrument	Samples	Primary Beam Current (paV); φ	MRP	HVO (EW)	Time; cycles; peaks	REF MAT	Precision (1σ)	Other
Straub & Layne (2002)	IMS 1270 mono-coll	Tephra and melt inclusions							Simultaneous with $\delta^{11}B$; see Table 4-3
Schmitt *et al.* (2002)	IMS6f/ IMS3f	Quartz-hosted melt inclusions	1nA	~300	75eV (±25eV)		NIST 610/612		
Kobayashi *et al.* (2004); Nakano & Nakamura (2001)	IMS 5f	Olivine-hosted melt inclusions	10nA; 10μm	~300	60eV (±10eV)	~7 min; $^{7}Li^{+}$,$^{11}B^{+}$, $^{30}Si^{+}$	HW11-2 (4.41 ppm [Li]; 1.60 ppm [B])		Spot pre-sputtering 3 mins
Chaussidon *et al.* (1997)	IMS 3f	Meteoritic chondrules; baslat glass	≤100nA (10kV); 30–100 μm	300	60eV (±10eV)		GB-4 synth glass (970 ppm[B]); +Regr of multiple glass stds		Samples 100 ppb – 1 ppm[B]

instruments (*e.g.*, 20 nA, 25 μm; Schmitt *et al.* 2002). As for $\delta^{7}Li$, most workers documented the use of a spot pre-sputter procedure before beginning data collection. Straub & Layne (2002) used a programmed pre-sputter with a slightly rastered beam, to clean the sample surface area of contamination to a distance completely beyond the field of view of the mass spectrometer, as restricted by a small Field Aperture setting. This latter procedure reduces the signal from exotic B at the sample surface to an absolute minimum.

Considerable gains in precision are available using IMS1270/1280 instruments, due to their intrinsically higher transmission at the MRP required for $\delta^{11}B$ determination. As discussed above, IMS1270/1280 instruments retain ~100% transmission in the mass spectrometer at their minimum (2000–2400) working MRP. Schmitt *et al.* (2002) noted a sensitivity of ~3.25 cps/ppm/nA for B in dacitic to rhyodacitic glass melt inclusions using IMS 3f and IMS 6f instruments operated at 1800 MRP (Table 4-3). Kobayashi *et al.* (2004) reported a sensitivity of ~50 cps/ppm/nA in basaltic andesite glasses using the IMS 1270 (Table 4-3).

Straub & Layne (2002), using an IMS 1270 operated with the supplementary rectangular coupling lenses energized, reported a sensitivity of >125 cps/ppm/nA for B in basaltic glass. The rectangular coupling lenses (LC1Y and LC2Y) of the IMS 1270/1280 act to increase the Y:X aspect ratio of the secondary ion image of the Field Aperture to >> 1:1, enhancing transmission of secondary ions through the main Exit Slit of the instrument when in monocollection mode (deChambost *et al.* 1991, 1996). The rectangular lenses are not normally useful in multicollection mode, however, because of the more limited vertical acceptance of the individual optics of the multicollection detectors.

Kobayashi *et al.* (2004) deployed multi-collection EMs on the IMS 1270 to achieve precisions of ±0.5‰ (synthetic glass; 23 ppm [B]) with data acquisition times of <10 min (20 nA, 30 μm spot). Straub & Layne (2002) achieved precisions of ±0.3–0.5‰ (glasses ≥10ppm [B]) in monocollection mode, while simultaneously determining [B], in 25 minutes using an 8 nA 12 μm diameter spot. The best reproducibility reported to date was ±0.7‰ (sample glasses ≥10 ppm [B]) by Straub & Layne (2002).

The conditions summarized above are closely comparable to those required for $\delta^{7}Li$, suggesting that in some applications these quantities could be acquired simultaneously.

http://bbs.3s001.com/

[B] Determination

As for δ^7Li and [Li], most authors have chosen to determine [B] in an entirely separate instrument session from δ^{11}B (Table 4-4). This is usually accomplished by measuring $^{11}B^+/^{28}Si^+$ or $^{11}B^+/^{30}Si^+$ in samples, and in one or more similar reference materials, using an energy bandpass with an upper edge of +50 eV and Entrance and Exit Slits wide open (MRP ~300). This modest level of energy filtering is apparently sufficient to effectively eliminate contributions from $^{10}BH^+$ (or $^{29}SiH^+$) at the level of error required in these applications.

However, as for [Li], [B] can be determined more quickly, and in the same sample volume as δ^{11}B, with little marginal effect on time or precision. For monocollection applications, an additional cyclical peak switch to $^{28}Si^{++}$ or $^{30}Si^{++}$ for ~2 s (Straub & Layne 2002; Table 4-4), requires a minimal change in magnet field switching relative to $^{11}B^+$ and $^{11}B^+$, and adds little additional time. In multicollection applications, it is quite practical to program a cyclical or terminal magnet switch to one of these same masses as part of the δ^{11}B determination.

Standards and Matrix Effects

Matrix dependence of IMF. Chaussidon *et al.* (1997) demonstrated a relatively small dependence of B^+ ionization efficiency on matrix effects over a wide range of natural and synthetic glass compositions including natural basalt, pantellerite, and synthetic glasses that approximated high-silica rhyolite. Their analytical settings produced a single universal working line for determinations of [B] in this spectrum of compositions (Fig. 4-7), with an implied accuracy of better than ±10% for [B]. They also demonstrated that the IMF for $^{11}B^+/^{10}B^+$ was extremely consistent (–48.4 ±1.6‰ for their specific analytical conditions) over a very wide range of matrix compositions (silicate glasses, marine salts and even boric acid).

Although the matrix dependency of IMF for δ^{11}B determinations therefore seems considerably less than that observed for δ^7Li, it still comprises a potential contribution of > ±1‰ to overall uncertainty if reference materials are not closely matched to samples. However, for the case of natural glasses, Rosner *et al.* (2008) confirmed that the difference in IMF between basaltic and rhyolitic compositions (JB-2G, StHs6/80-G, B6) was < ±1‰, when measured with IMS3f and IMS 6f instruments using conditions essentially similar to those of Chaussidon *et al.* (1997). They did, however, caution that NIST 610 and NIST 612 synthetic glasses routinely gave an IMF 3.4‰ lower than that for the natural material standards and, on that basis, were potentially unsuitable as reference materials for δ^{11}B determinations.

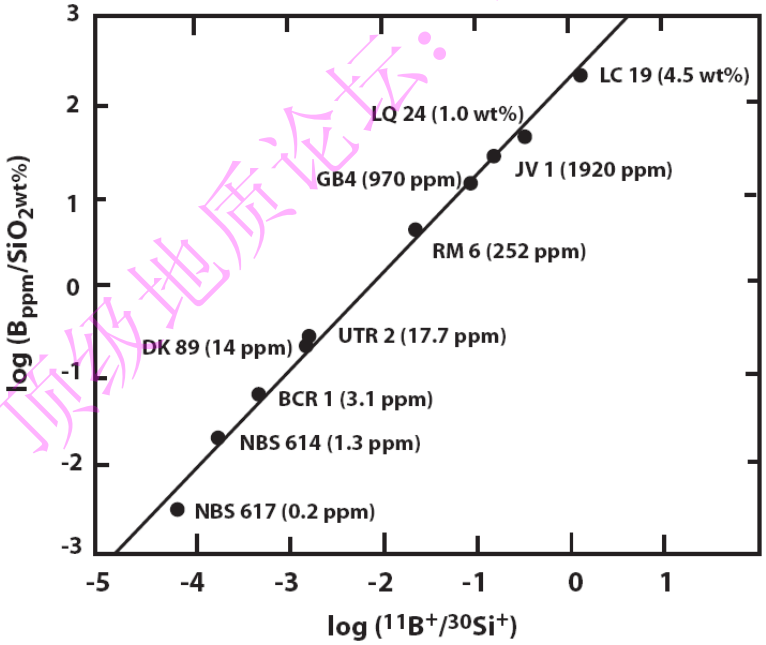


FIG. 4-7. Calibration line for B concentration measurements – $[B]/SiO_2$ *versus* $^{11}B^+/^{30}Si^+$ (data from Chaussidon & Libourel, 1993). The linear fit obtained for standards of diverse composition shows that the background for B is low (<0.05 µg g^{-1}) and that matrix effects on ionization yield of B^+ are negligible at a level of <10%. As presented here, on logarithmic axes, the estimated precision of these analyses is smaller than the plotted symbols. (after Chaussidon *et al.* 1997).

质谱地质论坛：http://blog.sina.com.cn/

Homogeneity of reference materials. In Chaussidon *et al.* (1997) and many subsequent studies, IMF was corrected for by comparison with intraday measurements of the synthetic glass standard GB4. However, this material is only homogeneous to approximately ±1.5‰ in $\delta^{11}B$ (Straub & Layne 2002, Chaussidon & Jambon 1994). In the Straub & Layne (2002) study overall reproducibility for $\delta^{11}B$ was demonstrated to be better than ±0.3–0.6‰ on individual shards of dacite glass sample IZB90 (65 wt.% SiO_2; 48–51 ppm [B]). Reproducibility better than ±0.7 ‰ was routinely possible, even for glass with 10 ppm [B]. The homogeneity of GB-4 thus became a limiting factor in the quality of analyses.

In subsequent work at WHOI, GB-4 was replaced by B6, natural obsidian from Lipari Island (75.3 wt.% SiO_2, 204 ppm [B]; Gonfiantini *et al.* 2003). Based on replicate IMS 1270 analyses at WHOI (summarized in Gonfiantini *et al.* 2003), B6 appears homogeneous to better than ±0.2‰ for $\delta^{11}B$. The WHOI replicates also yielded a value of –3.3 ± 0.1‰ for $\delta^{11}B$ as referenced to GB-4. This overlaps with the compiled value of –3.3 ± 1.8‰ from the multi-technique interlaboratory comparison of Gonfiantini *et al.* (2003).

In light of the findings of Rosner *et al.* (2008), NIST 610/612 are best supplanted by highly homogeneous natural standards such as B6 for studies of high-silica glasses. Published $\delta^{11}B$ values by TIMS and MC–ICP–MS, and assessments of microscale homogeneity, are also becoming available for other widely distributed reference materials of both rhyolitic and basaltic compositions (see Kasemann *et al.* 2001, Rosner & Meixner 2004).

Applications

A number of recent applications specifically involving $\delta^{11}B$ determinations in melt inclusions by SIMS have been reviewed and summarized by Layne (2006). These include: i) studies by Gurenko & Chaussidon (1997), Gurenko & Schmincke (2002) and Kobayashi *et al.* (2004) of olivine-hosted melt inclusions as applied to the study of parent melt sources at Iceland, Sicily and Hawaii, respectively, ii) the study by Schmitt *et al.* (2002) of quartz-hosted melt inclusions as a guide to the crustal source of Andean calc-alkaline volcanic rocks and, iii) the Straub & Layne (2002) study of B recycling during subduction at the Izu arc front, using [B] and $\delta^{11}B$ determinations in both tephra matrix glasses and plagioclase-hosted melt inclusions. It is notable that SIMS is effectively the only technique that allows determination of $\delta^{11}B$ in individual melt inclusions. LeRoux *et al.* (2004) have demonstrated excellent capability for the accurate determination of $\delta^{11}B$ in basalt glass shards with LA–ICP–MS. However, the sample volume consumed for a precise $\delta^{11}B$ analysis by LA–ICP–MS is 10^5 higher than for SIMS, rendering analysis of individual melt inclusions impossible.

Schmitt & Simon (2004) studied volcanic material from the high-silica Bishop Tuff (Long Valley) comparing SIMS-determined $\delta^{11}B$ in water-rich quartz-hosted melt inclusions to that from P–TIMS analysis of degassed pumice glass. They demonstrated that degassed pumice effectively preserves the $\delta^{11}B$ signature of the pre-eruptive melt implying that shallow or syn-eruptive degassing of rhyolitic magmas does not fractionate B isotopes.

Rose-Koga & Sigmarrson (2008) combined SIMS determinations of [B] and $\delta^{11}B$ in Holocene tephra from Iceland with Th and O isotope data to define a model involving mixing between i) high $\delta^{18}O$, high $^{230}Th/^{232}Th$ mantle-derived basalt ($\delta^{11}B$ < –5‰) and ii) rhyolite derived from shallower crustal melting of hydrothermally altered basalt. The high $\delta^{11}B$ values of some rift-related rhyolite in Iceland (>+6‰) are best explained by this hydrothermal alteration having involved a predominantly meteoric fluid that derived up to 10% of its B from seawater.

Other recent contributions in the general field of igneous geochemistry include those by Clift *et al.* (2001), Clift *et al.* (2003) and Rose *et al.* (2001) using SIMS determinations in melt inclusions and tephra in the study of the Tonga-Kermadec arc, Izu/NE Japan arcs and Cascadia subduction systems, respectively.

Other workers have extended the application of SIMS to the study of $\delta^{11}B$ in a wide variety of natural materials. Rollion-Bard *et al.* (2003) determined $\delta^{11}B$, $\delta^{13}C$ and $\delta^{18}O$ in the modern tropical coral *Porites lutea*, using an IMS 1270 instrument (Table 4-3). $\delta^{11}B$ values ranged from +19 to +31‰, and were interpreted by these authors to indicate that pH at the sites of skeletal aragonite formation varied between 7.1 and 9.0. They linked the "vital effect" bias observed in paleoclimatic reconstructions of sea surface temperature based on coral $\delta^{18}O$ to these pH variations and suggested that measuring $\delta^{18}O$ only in the lowest $\delta^{11}B$ zones of the skeleton would significantly improve the quality of such data.

Tourmaline is a relatively common accessory mineral in crustal rocks, and contains B as a major

constituent element. As such, it can provide a robust and convenient record, readily accessible by SIMS, of $\delta^{11}B$ in a wide variety of environments. Further, the high [B] of tourmaline makes high precision determinations readily amenable to analysis via small format SIMS instruments.

Xavier *et al.* (2008) discovered high $\delta^{11}B$ (+14 to +26.5‰) in gangue tourmaline, supporting their model of a marine evaporite-derived source for the high salinity ore-forming fluids associated with the Igarapé Bahia and Salobo Fe oxide Cu–Au (IOCG) deposits of the Carajás Mineral Province (Brazil). This study relied on the procedures previously detailed by Krienitz *et al.* (2008) for their study of tourmaline from an orogenic Au deposit (Hira Buddini) in the late Archean of southern India.

SIMS analysis of $\delta^{11}B$ has also recently been applied to the study of tourmalines for provenance studies in high pressure metasedimentary rocks (Marschall *et al.* 2008), and as a record of subduction-zone devolatilization and B cycling in metasedimentary rocks from Catalina (California) and Lago di Cignana (Italy) (Bebout & Nakamura 2003). An earlier study by Chaussidon & Appel (1997) used analyses of accessory tourmaline from 3.8 Ga Isua supracrustal rocks to infer a $\delta^{11}B$ value of +27 ±11‰ for early Archean seawater.

Williams *et al.* (2001a, b) have demonstrated the practicality and utility of $\delta^{11}B$ determinations in clay and other minerals by SIMS in the study of burial diagenesis and related processes in sedimentary reservoirs. For example, pumice fragments (25 to 575 ppm [B]) within the sedimentary rocks of the Cold Lake oil reservoir (Alberta) are the major source of B in the coexisting formation waters (Williams *et al.* 2001a). Williams *et al.* (2001a) used $\delta^{11}B$ analysis of these fragments by SIMS to study the exchange of B between pumice and "produced water" from commercial steam injection processing of the reservoir. The large magnitude of B isotope fractionation between minerals and fluid over the range of temperatures encountered (96–190°C in the Cold Lake study) makes $\delta^{11}B$ a useful geothermometer for monitoring fluid mixing and cross-contamination in hydrothermally stimulated oil reservoirs.

Cl ISOTOPES

Cl isotope compositions are expressed in per mil notation as $\delta^{37}Cl$ relative to Standard Mean Ocean Chloride (SMOC), which has a defined value of $^{37}Cl/^{35}Cl = 0.31963$ (Coplen *et al.* 2002).

Instrumental Approach

Chlorine has an excellent yield of Cl^- secondary ions under sputtering by Cs^+ primary beams. This means that many minerals and glasses are readily amenable to $\delta^{37}Cl$ determination by SIMS at [Cl] levels as low as 10 ppm.

Due to its role as a ligand in hydrothermal fluids, and potential as a tracer of the recycling of crustal material in the subduction factory, there is considerable curiosity about the $\delta^{37}Cl$ systematics of glassy lavas and melt inclusions in volcanic phenocrysts from subduction-related volcanism, mid-ocean ridge basalt (MORB) and ocean island basalt (OIB). These types of natural glass commonly contain considerable S, and the S/Cl ratio is thus routinely high enough to produce an isobaric interference of $^{34}SH^-$ on $^{35}Cl^-$ in the secondary ion spectrum that is significant at the per mil level when determining $\delta^{37}Cl$. This must be taken in to account in the application of small format (f-series) instruments, because hydride interferences like SH^- are difficult to eliminate using energy filtering, and the alternative of using very high MRP will substantially reduce transmission of the Cl signal.

Layne *et al.* (2004) have published a detailed technique for determining $\delta^{37}Cl$ in natural glasses using high MRP with a large format IMS 1270 instrument. Figure 4-8 is a mass spectrum at 35 Da using an IMS 1270 at MRP 5250 (10% definition) in a sample of synthetic basalt glass with an *extreme* enrichment in Cl (2.79 wt.% [Cl]). It displays the major peaks that may be expected in volcanic glasses. These include $^{19}F^{16}O^-$ and $^{16,18}O_2H_x^-$ peaks, which will also be of concern in the $\delta^{37}Cl$ analysis of apatite or hydrous glasses/minerals. However, these more distant isobaric interferences are readily reduced by energy filtering or eliminated by an MRP ≥1400–1450, similar to that required for $\delta^{11}B$ determinations

The closest isobaric interference apparent in Figure 4-8 is, indeed, that of $^{34}SH^-$ on $^{35}Cl^-$. Importantly, the average S/Cl ratios documented for many oceanic basalt samples are 10^3–10^4 times larger than in the synthetic basalt glass of Figure 4-8, and so will produce a $^{34}SH^-$ peak of ~10% to 100% the height of the $^{35}Cl^-$ peak. Total [Cl] of these same basalt samples are also commonly < 500 ppm, and often < 100 ppm. In practice, MRP 5250 provides the best balance of Cl^- transmission and mass resolution, effectively reducing SH^- interferences to << 0.1 ‰ level, even for high S/Cl samples.

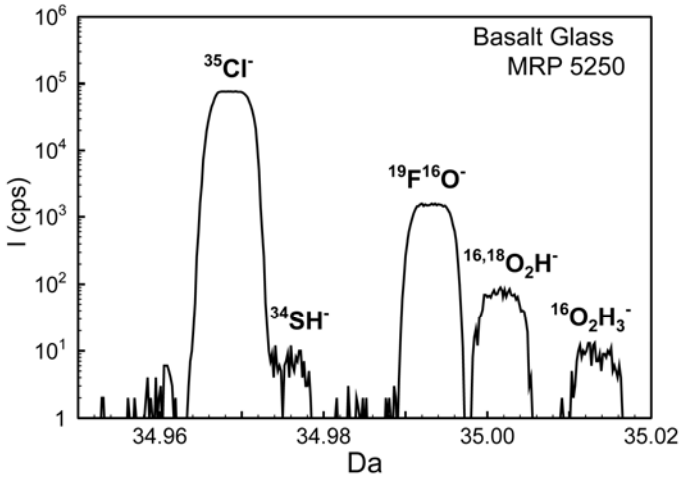


FIG. 4-8. Secondary ion spectrum (EM detection) at nominal mass 35 Da for a very high [Cl] synthetic basalt glass ("Basalt Glass B" of Godon *et al.* 2004; 2.79 wt.% Cl) to illustrate isobaric interferences at MRP 5250 (10% definition) (after Layne *et al.* 2004). Most natural basalt glasses have substantially lower Cl/S ratios, making $^{34}SH^-$ a potentially significant contributor to $^{35}Cl^-$ signals at lower MRP. Da is Daltons (equivalent to the unified atomic mass unit (u)).

In the procedure of Layne *et al.* (2004), simultaneous $\delta^{37}Cl$ and [Cl] determinations are performed by bombarding the sample with a primary ion beam of 150–300 pA of Cs^+ focused into a 10–20 µm diameter spot. The normal incidence electron gun (NEG) of the IMS 1270 (Migeon *et al.* 1990) is used for active charge compensation. Any exotic Cl contaminating the immediate surface of the sample is removed by 1–2 minutes of pre-sputtering with a slightly rastered beam before data accumulation begins. Any surface Cl remaining on the periphery of this pre-sputtered area is excluded by restricting the field of view of the mass spectrometer to the immediate area of sputtering during the subsequent spot analysis. This is accomplished with the continuously variable square Field Aperture (FA) of the IMS 1270, in concert with the center ("150 µm") Transfer Lens, to produce an effective field of view of the sample surface of 25 x 25 µm. The extremely high ionization efficiency of Cl under these conditions, coupled with the high transmission of the IMS 1270 (further enhanced by the use of the supplementary rectangular mode coupling lenses), provides excellent sensitivity, typically >650 cps/ppm Cl/nA_{Cs^+} in high SiO_2 glasses.

Peaks are counted by cyclical magnetic peak switching with pulse mode ion counting using a regular format multi-dynode EM (ETP 133H) as the off-axis "monocollection" detector. The typical counting times and peak sequence are background position (29.67 Da; 1.0 s), $^{30}Si^-$ (2.0 s), $^{35}Cl^-$ (2.0 s) and $^{37}Cl^-$ (4.0 s). Waiting times of 0.5 s are inserted before each peak counting position, and 1.0 s before background, to allow for magnet settling. Sufficient precision is usually achieved by accumulating 60 of these peak cycles, which requires less than 12 minutes. Simultaneous determinations of [Cl] are quantified by comparing $^{35}Cl^-/^{30}Si^-$ (normalized for SiO_2 content) for unknown and standard glasses.

Precision and Reproducibility

Analyses accumulated in 12 minutes, using the monocollection procedure of Layne *et al.* (2004), routinely yield internal precisions better than ±0.45‰. Individual analyses of homogeneous materials have internal precisions (0.30–0.45‰) which closely approach the theoretical limits calculated from Poisson counting statistics (0.25–0.30‰). Overall reproducibility of individual spots is better than ±0.7‰, even for sessions spanning several days, and can be maintained at this level in samples with as little as 250 ppm [Cl].

The multicollector of the IMS1270/IMS1280 will permit simultaneous collection of $^{35}Cl^-$ and $^{37}Cl^-$ signals, with obvious advantages for reducing total analysis time and/or improving precision. However, the increase in overall counting time efficiency will be partially offset by the necessity of much more frequent calibration on standard material. This is required to monitor properly the aging-related drift in relative gain of the two miniature EMs when used at count rates of $>10^3$ cps. Further, the acquisition of a reference mass for [Cl] determination necessitates at least one programmed magnetic peak switch to enable counting on $^{30}Si^-$ (although this can be executed either before or after the multicollection acquisition for $\delta^{37}Cl$). Nonetheless, large format ion microprobes with multicollection arrays further improve the internal precisions and, consequently, the reproducibility of SIMS determinations of $\delta^{37}Cl$. Initial trials with IMS 1270 multicollection have shown that overall reproducibilities should improve

http://www.iso9001.com

to well below ±0.5‰ for natural glasses and melt inclusions.

One practical example of the advantages of multicollection for $\delta^{37}Cl$ is evident in recent data for extremely low-[Cl] MORB, containing as little as 12 ppm [Cl] (Layne *et al.* 2009)). The procedure was the same used by Layne *et al.* (2004), except for the substitution of dual EM detectors for the $^{37}Cl^-/^{35}Cl^-$ measurements ($^{35}Cl^-$ on L2; $^{37}Cl^-$ on H1; IMS 1270). This permitted multiple (n = 12 to 30) replicate analyses of ~6 minutes each (plus pre-sputtering) to be accumulated in pre-programmed arrays from inclusion-free areas of these glasses during a period of 2–3 hours. These replicate data were then integrated to produce $\delta^{37}Cl$ determinations of similar precision to those performed with the monocollection procedure on basalts with ≥250 ppm [Cl]. In this manner, accurate analyses are possible of material with [Cl] well below that practical for $\delta^{37}Cl$ determination by gas-source mass spectrometry (~40 ppm [Cl]).

Standards and Matrix Effects

IMF of $^{37}Cl^-/^{35}Cl^-$ is *highly* matrix dependent for natural volcanic glass ranging from rhyolite to basalt (Godon *et al.* 2004). IMF for high-SiO_2 rhyolite is on the order of +6 to +10‰ depending on instrumental conditions. That for basalt is as much as 8‰ lower. Consequently, in studies of systems where individual samples span a broad range of melt compositions, a series of standards is required. It is also notable that the IMF of $^{37}Cl^-/^{35}Cl^-$ for many SiO_2 rich glasses is *positive*, as also observed for $^7Li^+/^6Li^+$ in silicate matrices.

Godon *et al.* (2004) have demonstrated that IMF is a highly correlated function of SiO_2, Al_2O_3, CaO and FeO, permitting correction of the measured $\delta^{37}Cl$ value to ±0.5‰ over this wide compositional range, using a simple linear fit to these parameters based on a set of synthetic standard materials (Fig. 4-9). For studies on samples of more limited compositional ranges (*e.g.*, basalt) it is sufficient to use a small set of reference glasses of similar major element chemistry to the samples. To minimize any dynamic range-induced variations in detector linearity potentially caused by using the very high-[Cl] synthetic glasses of Godon *et al.* (2004) as reference materials for lower-[Cl] natural basaltic samples, Layne *et al.* (2009) used a set of clean natural basaltic glasses with [Cl] < 450 ppm. A similar strategy would be appropriate in the study of high-silica rhyolite, where standards such as natural rhyolite RMR (+0.29 $\delta^{37}Cl$; 1700 ppm [Cl]; Godon *et al.* 2004) would be a more than adequate match to many samples.

Applications

The instrumental approaches detailed above were applied by Layne *et al.* (2009) to a study of $\delta^{37}Cl$ systematics of basalt from the Lau Basin back-arc spreading system, including the first published analyses of $\delta^{37}Cl$ in melt inclusions. SIMS analyses were able to distinguish the variable effects of mantle source, subduction and shallow

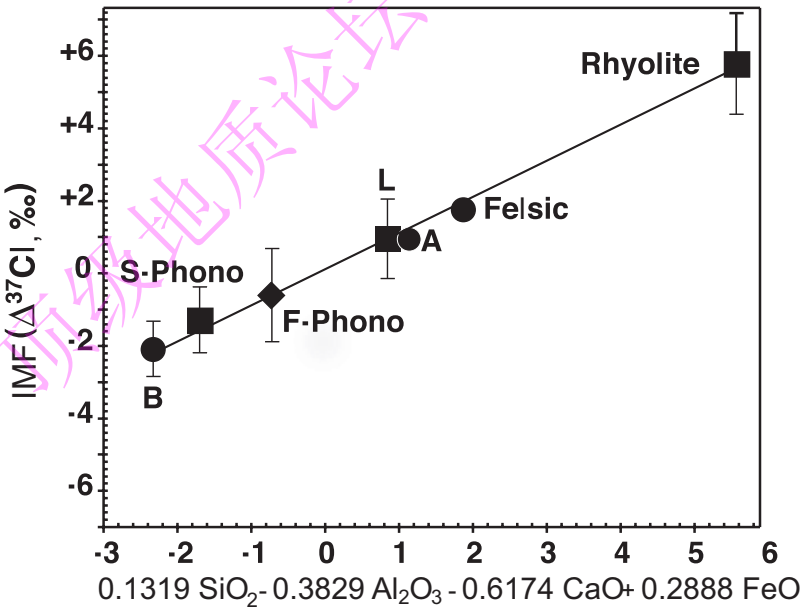


FIG. 4-9. Plot of the instrumental mass fractionation (IMF, in ‰) as a function of major element composition (0.1319 SiO_2 – 0.3829 Al_2O_3 – 0.6174 CaO + 0.2888 FeO) of seven silicate glass standards ranging from basalt to rhyolite (after Godon *et al.* 2004). The error bars are 1σ of replicate analyses of each glass standard (n = 3 to 5). As for Figure 4-3, they thus overestimate the error of the quantities used for the linear regression by a factor of approximately √n.

地质论坛 http://bbs.sinoni.com/

assimilation on $\delta^{37}Cl$ in different parts of the basin. The results were also used to infer a distinctly negative $\delta^{37}Cl$ for the depleted mantle source (≤ -3.0 ‰). Analyses of individual melt inclusions from basalt of the Valu Fa Ridge affirmed the inherent value of these objects in resolving the effects of the small volume variability and episodic behavior inherent in basalt petrogenesis.

Of course, the techniques of Layne *et al.* (2004, 2009) are very much geared to the analysis of volcanic glass and melt inclusions. Additional applications will no doubt emerge in the near future as the capability of SIMS to determine $\delta^{37}Cl$ with a high level of accuracy is more widely recognized. For example, extremely precise determinations (using Faraday cup (FC) detection) appear practical for $\delta^{37}Cl$ in Cl-apatite, or hydrous silicate minerals, which routinely contain >1000 ppm [Cl]. These minerals have the potential to enable studies of $\delta^{37}Cl$ systematics in a wide variety of crustal environments.

Given the apparent sensitivity of IMF to matrix composition, considerable attention will be required to the development of additional reference materials for the analysis of new mineral phases. However, many of these same minerals may prove to have inherently low S/Cl, enabling the use of small format SIMS instruments in a variety of $\delta^{37}Cl$ studies.

SUMMARY AND CONCLUSIONS

SIMS determination of $\delta^{7}Li$, $\delta^{11}B$ or $\delta^{37}Cl$ with a per mil level of accuracy requires:

- Use of appropriate, well-characterized, homogeneous reference materials for the calibration of IMF.
- Careful optimization of instrument transmission and sensitivity to provide the best possible precision in isotope ratio determinations.
- Attention to detector dead time stability for EM detectors, and to the calibration of EM gain drift in the case of multicollection approaches.
- Elimination of surface contamination effects by pre-sputtering and the judicious use of field apertures to limit field of view of the mass spectrometer

However, SIMS enables $\delta^{7}Li$, $\delta^{11}B$ or $\delta^{37}Cl$ determination *in situ*, in nanogram aliquots of solid material. It is, for example, essentially the only available means of determining light stable isotope ratios in individual melt inclusions, or in fine scale biomineralization such as foraminifera.

In many cases, high quality $\delta^{7}Li$, $\delta^{11}B$ or $\delta^{37}Cl$ determinations are possible using small format SIMS instruments. Large format (IMS1270/1280) instruments have distinct benefits in terms of maintaining higher transmission at MRPs above ~600. This can be essential for $\delta^{37}Cl$ determinations in materials with high S/Cl ratios, and beneficial in measuring $\delta^{7}Li$ or $\delta^{11}B$ precisely, especially for materials with sub-ppm [Li] or [B].

Many improvements and adaptations of the published techniques described above already appear feasible. For example, multicollection using FCs will likely become the preferred approach for $\delta^{11}B$ or $\delta^{37}Cl$ in high concentration minerals such as tourmaline and apatite. Some studies may benefit from the simultaneous determination of [Li], $\delta^{7}Li$, [B] and $\delta^{11}B$ or [S], $\delta^{34}S$, [Cl] and $\delta^{37}Cl$. However, for studies of natural glasses, these are most likely only practical in monocollection arrangements due to the difficulty in matching the dynamic ranges of the respective element pairs to the limitations of miniaturized EMs.

Given the growing interest and utility of these three isotopic systems in many areas of geochemical research, it seems likely that the notable recent growth in application of SIMS to their analysis will continue.

ACKNOWLEDGEMENTS

My heartfelt thanks to the many authors who have, in recent years, gone to considerable effort to develop procedures and reference materials for quantitative SIMS determinations of light stable isotope ratios and whose detailed published descriptions I have drawn on substantially in the text and tables of this chapter. Also, to my longtime Research Engineer, Peter Landry, whose ingenuity made so much of my own work possible while at Woods Hole Oceanographic Institution. Martin Whitehouse (NORDSIMS) has provided invaluable advice, support and instrument access for almost a decade, most recently, facilitating major improvements in our technique for $\delta^{37}Cl$ determinations. Timm John (PGP-Oslo), with the gracious assistance of Jaime Barnes (UNM), made an invaluable contribution to the development of improved glass reference materials for $\delta^{37}Cl$. Finally, I would like to express my appreciation to my many colleagues throughout the geoscience community, who continue to formulate new and exciting challenges for microanalytical geochemists.

版权所有 http://bbs.sinoss.com/

REFERENCES

BEBOUT, G.E. & NAKAMURA, E. (2003): Record in metamorphic tourmalines of subduction-zone devolatilization and boron cycling. *Geology*. **31**, 407–410.

BELL, D.R., HERVIG, R.L., BUSECK, P.R. & AULBACH, S. (2009): Lithium isotope analysis of olivine by SIMS: Calibration of a matrix effect and application to magmatic phenocrysts. *Chem. Geol.* **258**, 5–16.

BICE, K., LAYNE, G.D. & DAHL, K. (2005): Application of secondary ion mass spectrometry to the determination of Mg/Ca in rare, delicate or altered planktonic foraminifera: Examples from the Holocene, Paleogene and Cretaceous. *Geochem. Geophys. Geosyst.* 6, Q12P07, doi: 10.1029 /2005GC000974.

CHAUSSIDON, M. & APPEL, P.W.U. (1997): Boron isotopic composition of tourmalines from the 3.8-Ga-old Isua supracrustals, West Greenland: implications on the $\delta^{11}B$ value of early Archean seawater. *Chem. Geol.* **136,** 171-180.

CHAUSSIDON, M. & JAMBON, A. (1994): Boron content and isotopic composition of oceanic basalts: geochemical and cosmochemical implications. *Earth Planet. Sci. Lett.* **121**, 277-291.

CHAUSSIDON, M. & LIBOUREL, G. (1993): Boron partitioning in the upper mantle: an experimental and ion probe study. *Geochim. Cosmochim. Acta*. **57**, 5053-5062.

CHAUSSIDON, M. & ROBERT, F. (1998): $^{7}Li/^{6}Li$ and $^{11}B/^{10}B$ variations in chondrules from the Semarkona unequilibrated chondrite. *Earth Planet. Sci. Lett.* **164**, 577–589.

CHAUSSIDON, M., ROBERT, F., MANGIN, D., HANON, P. & ROSE, E.F. (1997): Analytical procedures for the measurement of boron isotope compositions by ion microprobe in meteorites and mantle rocks. *Geostandards Newsletter.* **21**(1), 7-17.

CLIFT, P.D., ROSE, E.F., SHIMIZU, N., LAYNE, G.D., DRAUT, A.E. & REGELOUS, M. (2001): Tracing the evolving flux from the subducting plate in the Tonga-Kermadec arc system using boron in volcanic glass. *Geochim. Cosmochim. Acta.* **65**(19), 3347–3364.

CLIFT, P.D., LAYNE, G.D., NAJMAN, Y.M.R., KOPF, A., SHIMIZU, N. & HUNT, J. (2003): Temporal evolution of boron flux in the NE Japan and Izu arcs measured by ion microprobe from the forearc tephra record. *J. Petrology.* **44**(7), 1211-1236.

COPLEN, T.B., HOPPLE, J.A., BÖHLKE, J.K., PEISER, H.S., RIEDER, S.E., KROUSE, H.R., ROSMAN, K.J.R., DING, T., VOCKE, R.D., JR., REVESZ, K.M., LAMBERTY, A., TAYLOR, P., & DE BIEVRE, P. (2002): Compilation of minimum and maximum isotope ratios of selected elements in naturally occurring terrestrial materials and reagents, USGS Water Resources Investigations Report 01-4222.

DE CHAMBOST, E., HILLION, F., RASSER, B. & MIGEON, H.N. (1991): The Cameca IMS1270: A description of the secondary ion optical system: In: Benninghoven **A**., J**a**nssen K. T. F., Tumpner J., Werner H. W., eds., **S**IMS VIII Proceedings. Wiley, New York. 207–210.

DE CHAMBOST, E., SCHUHMACHER, M., LOVESTAM, G. & CLAESSON, S. (1996): Achieving high transmission with the Cameca IMS1270, In: Benninghoven A, Hagenhoff B, Werner HW (eds) Secondary ion mass spectrometry, SIMS X. Wiley, Chichester. 1003– 1006.

DECITRE, S., DELOULE, E., REISBERG, L., JAMES, R., AGRINIER, P. & MEVEL, C. (2002): Behavior of Li and its isotopes during serpentinization of oceanic peridotites. *Geochem. Geophys. Geosyst.* **3 (1),** doi 10.1029/2001GC000178.

EILER, J.M., GRAHAM, C. & VALLEY, J.W. (1997): SIMS analysis of oxygen isotopes: Matrix effects in complex minerals and glasses. *Chem. Geol.* **138**, 221-244.

ELLIOTT, T., JEFFCOATE, A. & BOUMAN, C. (2004): The terrestrial Li isotope cycle: light-weight constraints on mantle convection. *Earth Planet. Sci. Lett.* **220**, 231-245.

GODON, A., WEBSTER, J.D., LAYNE, G.D., JENDRZEJEWSKI, N. & PINEAU, F. (2004): Secondary Ion Mass Spectrometry for the determination of $\delta^{37}Cl$. Part II. Intercalibration of SIMS and IRMS for aluminosilicate glasses. *Chem. Geol.* **207**(3-4), 291-303.

GONFIANTINI, R., TONARINI, S., GRÖNING, M., ADORNI-BRACCESI, A., AL-AMMAR, A.S., ASTNER, M., BÄCHLER, S., BARNES, R.M., BASSETT, R.L., COCHERIE, A., DEYHLE, A., DINI, A., FERRARA, G., GAILLARDET, J., GRIMM, J., GUERROT, C., KRÄHENBÜHL, U., LAYNE, G.D., LEMARCHAND, D., MEIXNER, A., NORTHINGTON, D.J., PENNISI, M., REITZNEROVÁ, E., RODUSHKIN, I., SUGIURA, N., SURBERG, R., TONN, S., WIEDENBECK, M., WUNDERLI, S., XIAO, Y. & ZACK, T. (2003): Intercomparison of boron

http://mc.csu.edu.cn/

isotope and concentration measurements, Part II: Evaluation of results. *Geostandards Newsletter: J. Geostandards and Geoanalysis.* **27**(1), 41-57.

GURENKO, A.A. & CHAUSSIDON, M. (1997): Boron concentrations and isotopic compositions in the Icelandic mantle: evidence from glass inclusions in olivine. *Chem. Geol.* **135**, 21-35.

GURENKO, A.A. & SCHMINCKE, H-U. (2002): Orthopyroxene-bearing tholeiites of the Iblean Plateau (Sicily): Constraints on magma origin and evolution from glass inclusions in olivine and orthopyroxene. *Chem. Geol.* **183**, 305-331.

HINTON, R.W. (1990): Ion microprobe trace-element analysis of silicates: Measurement of multi-element glasses. *Chem. Geol.* **83,** 11-25.

JEFFCOATE, A.B., ELLIOT, T., KASEMANN, S.A., IONOV, D., COOPER, K. & BROOKER, R. (2007): Li isotope fractionation in peridotites and mafic melts. *Geochim. Cosmochim. Acta*.**71**, 202–218.

JOCHUM, K.P., WILLBOLD, M., RACZEK, I., STOLL, B. & HERWIG, K. (2005): Chemical characterisation of the USGS reference glasses GSA-1G, GSC-1G, GSD-1G, GSE-1G, BCR-2G, BHVO-2G and BIR-1G Using EPMA, ID-TIMS, ID-ICP-MS and LA-ICP-MS**,** *Geostandards and Geoanalytical Research*, **29**(3), 285 – 302.

KASEMANN, S., MEIXNER, A., ROCHOLL, A., VENNEMANN, T., ROSNER, M., SCHMITT, A. K. & WIEDENBECK, M. (2001): Boron and oxygen isotope composition of certified reference materials NIST SRM 610/612 and reference materials JB-2 and JR-2. *Geostandards Newsletter, Journal of Geostandards and Geoanalysis.* **25**, 405–416.

KASEMANN, S.A., JEFFCOATE, A.B. & ELLIOT, T. (2005): Lithium isotope composition of basalt glass reference material. *Analytical Chemistry.* **77**, 5251-5257.

KOBAYASHI, K., TANAKA, R., MORIGUTI, T., SHIMIZU, K. & NAKAMURA, E. (2004): Lithium, boron, and lead isotope systematics of glass inclusions in olivines from Hawaiian lavas: evidence for recycled components in the Hawaiian plume. *Chem. Geol.* **212**, 143–161.

KRIENITZ, M.S., TRUMBULL, R.B., HELLMANN, A., KOLB, J., MEYER, F.M. AND WIEDENBECK, M. (2008): Hydrothermal gold mineralization at the Hira Buddini Gold Mine, India: Constraints on fluid evolution and fluid sources from boron isotopic compositions of tourmaline: *Mineralium Deposita*. **43**, 421–434.

LAYNE, G.D. (2006): Application of secondary ion mass spectrometry to the determination of traditional and non-traditional light stable isotopes in melt inclusions, *in* Melt Inclusions in Plutonic Rocks (J.D. Webster, *ed.*), *Min. Assoc. Can. Short Course*. **36**, 27-50.

LAYNE, G.D., KENT, A.J.R. & BACH, W. (2009): Chlorine isotope systematics of a back-arc spreading system: The Lau Basin. *Geology*, **37(5)**, 427-430.

LAYNE, G.D., GODON, A., WEBSTER, J.D. & BACH, W. (2004): Secondary Ion Mass Spectrometry for the determination of δ^{37}Cl. Part I. Ion microprobe analysis of glasses and fluids. *Chem. Geol.* **207**(3-4), 277-289.

LEROUX, P.J., SHIREY, S.B., BENTON, L., HAURI, E.H. & MOCK, T.D. (2004): *In situ*, multiple-multiplier, laser ablation ICP-MS measurement of boron isotopic composition (δ^{11}B) at the nanogram level. *Chem. Geol.* **203**, 123-138.

MARSCHALL, H.R., ALTHERR, R., KALT, A. & LUDWIG, T. (2008): Detrital, metamorphic and metasomatic tourmaline in high pressure metasediments from Syros (Greece): intra-grain boron isotope patterns determined by secondary-ion mass spectrometry. *Contrib. Mineral. Petrol.* **155,** 703–717.

MIGEON, H.N., SCHUHMACHER, M. & SLODZIAN, G. (1990): Analysis of insulating specimens with the Cameca IMS 4f. *Surface Interface Analysis.* **16**, 9-13.

NAKANO, T. & NAKAMURA, E. (2001): Boron isotope geochemistry of metasedimentary rocks and tourmalines in a subduction zone metamorphic suite. *Phys. Earth Planet. Inter.* **127**, 233– 252.

PARKINSON, I.J., HAMMOND, S.J., JAMES, R.H. & ROGERS, N.W. (2007): High-temperature lithium isotope fractionation: Insights from lithium isotope diffusion in magmatic systems. *Earth Planet. Sci. Lett.*, **257**, 609–621.

RICHTER, F.M., DAVIS, A.M., DEPAOLO, D.J. & WATSON, E.B. (2003): Isotope fractionation by chemical diffusion between molten basalt and rhyolite. *Geochim. Cosmochim. Acta*. **67**, 3905–3923.

RICHTER, F.M., DAUPHAS, N. & TENG, F.-Z. (2009): Non-traditional fractionation of non-traditional isotopes: Evaporation, chemical diffusion and Soret diffusion. *Chem. Geol.* **258**, 92–103.

ROLLION-BARD, C., CHAUSSIDON, M. & FRANCE-LANORD, C. (2003): pH control on oxygen isotopic composition of symbiotic corals. *Earth and Planetary Science Letters.* **215,** 275-288.

ROSE, E.F., SHIMIZU, N., LAYNE, G.D. & GROVE, T.L. (2001): Melt production beneath Mt. Shasta from boron data in pristine melt inclusions. *Science*. **293**, 281-283.

ROSE-KOGA, E.F. & SIGMARSSON. O. (2008): B–O–Th isotope systematics in Icelandic tephra. *Chem. Geol.* **255**, 454–462.

ROSNER, M. & MEIXNER, A. (2004): Boron isotopic composition and concentration of ten geological reference materials. *J. Geostandards and Geoanalysis*. **28**, 431-441.

ROSNER, M., WIEDENBECK, M. & LUDWIG, T. (2008): Composition-induced variations in SIMS instrumental mass fractionation during boron isotope ratio measurements of silicate glasses. *J. Geostandards and Geoanalysis*. **32**, 27-38.

SCHMITT, A.K. & SIMON, J.I. (2004): Boron isotopic variations in hydrous rhyolitic melts: a case study from Long Valley, California. *Contrib. Mineral. Petrol.* **146**, 590–605.

SCHMITT, A.K., KASEMANN, S., MEIXNER, A. & RHEDE, D. (2002): Boron in central Andean ignimbrites: Implications for crustal boron cycles in an active continental margin. *Chem. Geol.* **183**, 333-347.

STRAUB, S.M. & LAYNE, G.D. (2002): The systematics of boron isotopes in Izu arc front volcanic rocks. *Earth Planet. Sci. Lett.* **198**(1-2), 25-39.

USHIKUBO, T., KITA, N.T., CAVOSIE, A.J., WILDE, S.A., RUDNICK, R.L. & VALLEY, J.W. (2008): Lithium in Jack Hills zircons: Evidence for extensive weathering of Earth's earliest crust. *Earth Planet. Sci. Lett.* **272**, 666–676.

VIGIER, N., ROLLION-BARD, C., SPEZZAFERRI, S. & BRUNET, F. (2007): *In situ* measurements of Li isotopes in foraminifera. *Geochem. Geophys. Geosyst.* **8**, Q01003, doi:10.1029/2006GC001432.

WAGNER, C. & DELOULE, E. (2007): Behaviour of Li and its isotopes during metasomatism of French Massif Central lherzolites. *Geochim. Cosmochim. Acta.* **71**, 4279–4296.

WILLIAMS, L.B., HERVIG, R.L., HOLLOWAY, J.R. & HUTCHEON, I. (2001a): Boron isotope geochemistry during diagenesis. Part I. Experimental determination off fractionation during illitization of smectite. *Geochim. Cosmochim. Acta.* **65**(11) 1769–1782.

WILLIAMS, L.B., WIESER, M.E., FENNELL, J., HUTCHEON, I. & HERVIG, R.L. (2001b): Application of boron isotopes to the understanding of fluid-rock interactions in a hydrothermally stimulated oil reservoir in the Alberta Basin, Canada. *Geofluids*. **1**, 229-240.

WOLF, R.E. & WILSON, S.A. (2007): USGS Reference Materials Program: U.S. Geological Survey Fact Sheet 2007-3056, 4 p.

XAVIER, R.P., WIEDENBECK, M., TRUMBULL, R.B., DREHER, A.M., MONTEIRO, L.V.S., RHEDE, D., DE ARAÚJO, C.*E.G.* & TORRESI, I. (2008): Tourmaline B-isotopes fingerprint marine evaporites as the source of high-salinity ore fluids in iron oxide copper-gold deposits, Carajás Mineral Province (Brazil). *Geology*. **36,** 743–746.

顶级地质论坛 http://bbs.geo.com/

CHAPTER 5: QUATERNARY GEOCHRONOLOGY BY SIMS

Axel K. Schmitt
Department of Earth and Space Sciences
University of California, Los Angeles
Los Angeles, CA USA, 90095
axel@oro.ess.ucla.edu

INTRODUCTION

The timing of geologic events throughout the Quaternary period covering the past 2.6 Ma is of utmost importance for assessing the current state of the Earth, and to predict future changes. Quaternary geochronology represents a cornerstone in studying the geologic records of climate and landscape changes, biota evolution, and human origins. Quaternary geochronology covers an extremely wide range with regard to scope and methods (*e.g.*, Noller *et al.* 2000) which even warranted the recent inauguration of a dedicated journal by the same name (Gruen 2006). Secondary ionization mass spectrometry (SIMS) has only recently become a player in this field, and earlier reviews of methods in Quaternary geochronology omitted SIMS (*e.g.*, Noller *et al.* 2000). The high sensitivity and micrometre-scale spatial resolution of SIMS, however, is in the course of enhancing conventional uranium decay series (U-series) Quaternary geochronology in much the same way as it revolutionized U–Pb and ^{232}Th–^{208}Pb geochronology (*e.g.*, Ireland & Williams 2003).

Because of the extremely low abundances of short lived intermediate U-series isotopes, complex mass spectra, and the low radiogenic yield of Pb in Quaternary minerals, U-series and U–Pb Quaternary geochronology by SIMS is the domain of high transmission, high sensitivity ion microprobes such as the CAMECA ims 1270 and 1280, SHRIMP, and SHRIMP–RG instruments. Many laboratories operating large radius magnetic sector SIMS instruments have published on various aspects of Quaternary geochronology (here citing the first relevant publication of each lab; ANU: Baldwin & Ireland 1995; UCLA: Reid *et al.* 1997; Curtin: Brown & Fletcher 1999; Stanford-USGS: Dalrymple *et al.* 1999; Woods Hole: Layne & Sims 2000; Hiroshima: Sano *et al.* 2002), but it may not be coincidental that the two labs historically engaged in this field (UCLA and Stanford-USGS) are located in volcanically and seismically active regions where interest in the most recent geologic past is high. Research applying SIMS has thus significantly contributed to elucidating important issues such as volcanic unrest, geothermal reservoirs, paleoclimate reconstruction, and land surface changes.

Over the past decade, SIMS Quaternary geochronology publications have steadily increased in number, and it is timely to review SIMS-specific techniques and applications with the aim of (1) providing a theoretical background of U-series dating by SIMS; (2) guiding through the analytical steps involved; and (3) showcasing case studies with emphasis on those where the SIMS approach significantly improved the understanding of the timing of geologic processes compared to conventional methods. Different aspects of U-series dating have been comprehensively reviewed elsewhere (*e.g.*, Ivanovich & Harmon 1992, Bourdon *et al.* 2003, Condomines *et al.* 2003, Ludwig 2003, Cooper & Reid 2008), and novices are also referred to introductory chapters in textbooks on radiogenic isotope geochemistry. The treatment of SIMS U–Pb and Th–Pb geochronology (*e.g.*, Ireland & Williams 2003) is limited here to issues pertaining to SIMS dating of young samples (*e.g.*, alternative common Pb corrections, disequilibrium corrections). Chemical dating methods are beyond the scope of this review, and the interested reader is referred to literature on enhanced obsidian hydration dating by SIMS (*e.g.*, Anovitz *et al.* 2008 and references therein).

THEORY OF U-SERIES DATING

Principles and assumptions

Uranium decays to stable Pb via two separate decay chains, one initiating with parental ^{238}U (half-life [$t_{½}$] = 4.468 Ga) decaying to its stable daughter ^{206}Pb, and the second with the respective parent and stable daughter pair ^{235}U ($t_{½}$ = 0.7038 Ga) and ^{207}Pb (Fig. 5-1). The ^{238}U and ^{235}U chains involve eight and seven α-decays, respectively (Fig. 5-1). In both decay chains, the half-lives of intermediate daughter isotopes are significantly shorter than those of the

Mineralogical Association of Canada Short Course 41, Toronto, May 2009, p. 109-131

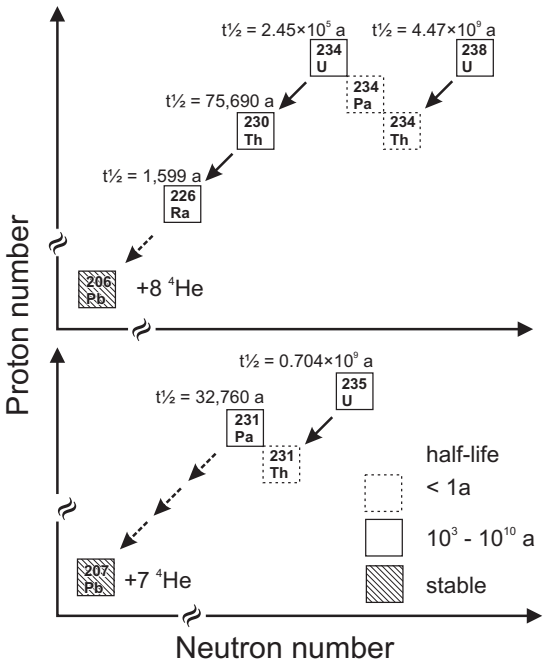


FIG. 5-1. Abbreviated U-decay series with half-lives ($t_{½}$) as compiled in Bourdon *et al.* (2003).

parent isotopes (Fig. 5-1). Bateman (1910) demonstrated that such a decay chain will over time mature to a condition where the activity ratio (number of decays per unit time or N × λ, with N = number of atoms and λ = decay constant) between shorter lived intermediate daughters (indices 2 to n) and longer lived parent (index 1) will become unity. This state is known as "*secular equilibrium*", which for a general decay chain with n members is expressed by the relation:

$$N_1\lambda_1 = N_2\lambda_2 = N_3\lambda_3 = \ldots = N_n\lambda_n \qquad (1)$$

Note that activities are conventionally expressed by round parentheses around the elemental symbol. Disequilibrium between parent and daughter isotopes in the U decay chain permits the time elapsed to be measured between an event that generated radioactive disequilibrium at t = 0 and some later time t, whereby the activity ratio of the short lived daughter (index 2) relates to the activity of the long lived parent (index 1) and time as:

$$N_2\lambda_2 = N_1\lambda_1\left(\frac{\lambda_2}{\lambda_2-\lambda_1}\right)\left(1-e^{-(\lambda_2-\lambda_1)t}\right)+N_2^0\lambda_2 e^{-\lambda_2 t} \qquad (2)$$

N^0 is the number of atoms initially present (at t = 0). Equation (2) can be solved for t under the fundamental assumption that all changes in isotopic abundances result from radioactive decay and ingrowth only (closed system). If $\lambda_2 >> \lambda_2$, equation (2) simplifies to:

$$N_2\lambda_2 = N_1\lambda_1\left(1-e^{-\lambda_2 t}\right)+N_2^0\lambda_2 e^{-\lambda_2 t} \qquad (3)$$

In certain cases, such as for ^{230}Th in hydrogenic minerals (*e.g.*, calcite, opal), absence of initial daughter isotope can be reasonably assumed so that equation (3) can be further simplified to:

$$N_2\lambda_2 = N_1\lambda_1\left(1-e^{-\lambda_2 t}\right) \qquad (4)$$

Disequilibrium can be generated instantaneously relative to the half-lives of the U-series isotopes involved, or over protracted time periods. Chemical fractionation between U-series parents and daughters occurs due to differential mineral–melt or mineral–fluid partitioning, in particular if ionic charge differences exacerbate fractionation. U and Th are both tetravalent under reducing conditions, but only U can achieve higher oxidation states (U^{5+}, U^{6+}), which can lead to strong fractionation between U and Th under oxidizing conditions. Other processes that are capable of generating disequilibrium involve isotopic fractionation through preferential leaching or recoil affecting ^{234}U. Recoil results in complete loss of ^{234}U or dislocation to a radiation-damaged site from which it is readily mobilized. The latter is prevalent only at low temperatures because of rapid annealing of lattice damage at high temperatures associated with igneous processes.

Once a parent–daughter system approaches secular equilibrium, no information on the amount of time passed can be obtained (Fig. 5-2). In this case, either U-series pairs with longer $t_{½}$, or accumulation of the stable daughter isotopes (^{206}Pb and ^{207}Pb), need to be used to determine the age. For completeness, it should be pointed out that ^{232}Th decay to stable ^{208}Pb (+6 ^{4}He) lacks long lived (>1 ka) intermediate daughters in the ^{232}Th decay chain, and is thus not further considered here.

Initial disequilibrium in U-series decay chains will also either accelerate or delay the accumulation of stable daughter isotopes relative to equilibrium conditions. These effects are negligible for very short lived intermediate isotopes, but in the case of ^{230}Th, disequilibrium can result in significant excesses or deficits in ^{206}Pb that require corrections in order to determine U–Pb ages accurately (Fig. 5-3, Schaerer 1984). For ^{206}Pb/^{238}U, the measured excess/deficit relative to

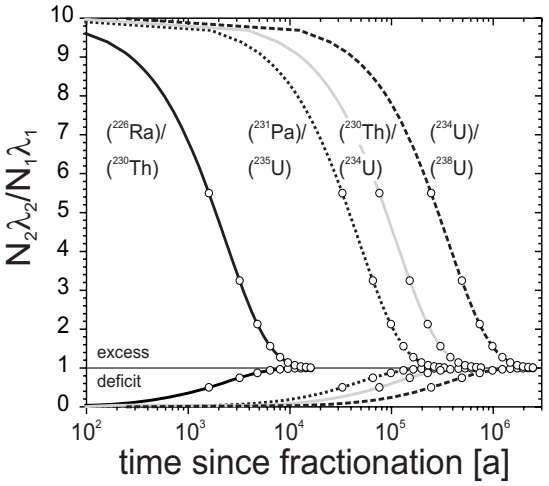


FIG. 5-2. Changes in daughter–parent activity ratios following a fractionation event at t = 0 for different U-series parent–daughter systems. Initial activity ratios were pegged randomly at initial ratios of 10 and 0.2. Open circles along curves are plotted in one-half-life steps.

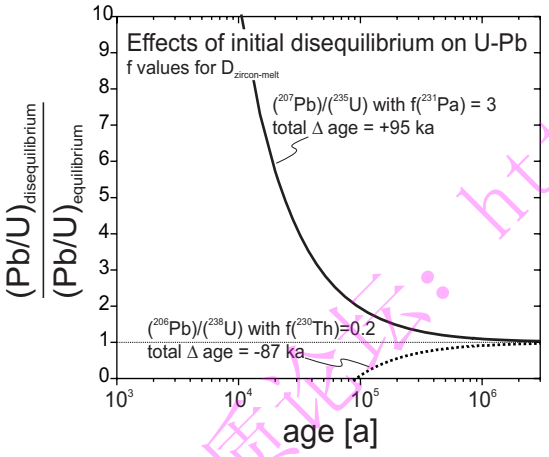


FIG. 5-3. Ratio between disequilibrium-affected Pb/U (Pb/U diseq) and equilibrium Pb/U (Pb/U eq) plotted against age. Excess or deficit in the Pb daughters resulting from disequilibrium is a constant, but the relative contribution diminishes with age because of radioactive ingrowth. The example curves demonstrate the relative amount of over- and underestimation of true U–Pb zircon ages resulting from initial disequilibrium in ^{230}Th and ^{231}Pa for realistic partition coefficient ratios (calculated according to equations 5 and 6; $f = D_{Th}/D_U = 0.2$ from Bindeman *et al.* 2006; $f = D_{Pa}/D_U = 3.4$; see below). Note that plotted curves assume melt equilibrium.

the equilibrium ratio at time t equals:

$$\frac{\left(^{206}Pb/_{238}U\right)_{disequilibrium}}{\left(^{206}Pb/_{238}U\right)_{equilibrium}} = \frac{\frac{\lambda_{238}}{\lambda_{230}}(f-1)}{\left(e^{\lambda_{238}t}-1\right)}+1 \qquad (5)$$

with f defined as the ratio between mineral (xtal)–melt partitioning coefficients D for Th and U:

$$f = \frac{D_{Th}^{xtal-melt}}{D_U^{xtal-melt}} \qquad (6)$$

Equivalent relations can be defined for the ^{235}U decay system with ^{207}Pb substituting for ^{206}Pb, and Pa (λ_{231}) for Th (λ_{230}) in equations (5) and (6), respectively. Not only accumulation of stable Pb is affected by initial disequilibrium, but also production of ^{4}He will be accelerated or delayed by U-series disequilibrium, and corrections are required if young crystals are to be dated accurately (Farley *et al.* 2002). For completeness, fission track dating is briefly mentioned here as another technique that is based on the radioactivity of U. Here, spontaneous fission of ^{238}U (at a fission probability of ~5 × 10^{-7} per decay, Dumitru 2000) occurs independently of disequilibrium in the subsequent intermediate daughters.

The validity of the closed system assumption is largely uncontested for zircon U-series dating because U-series elements are immobile in zircon even at magmatic temperatures (*e.g.*, Cherniak & Watson 2003). For other accessory minerals, actinide diffusion is largely experimentally unconstrained, but geologic case studies indicate closure at high temperatures, for example in the case of allanite (Vazquez & Reid 2004). In contrast to U and Th, He diffuses quickly in zircon, and will accumulate only following eruptive quenching (Reiners *et al.* 2004). Excess He is thus essentially unknown in volcanic zircon which offers great potential for reliable (U–Th)/He dating of volcanic eruptions. For U-series dating of low temperature materials such as calcite or opal, the closed system assumption is frequently verified by solving for initial (^{234}U)/(^{238}U) and comparing the initial ratio to that of a reservoir value (*e.g.*, modern sea water); deviation from the expected ratio is interpreted as open system behavior such as diagenetic alteration (Edwards *et al.* 2003).

质谱地质论坛：http://bbs.gs001.com/

Detection limits and datable materials

Secular equilibrium and detection limits. Secular equilibrium imposes an upper limit for U-series chronology. In the case of complete initial absence of a short lived intermediate daughter, radioactive ingrowth of the daughter over approximately five half-lives leads to daughter–parent activity ratios ~3% below unity, *i.e.*, within typical SIMS analytical uncertainties and thus indistinguishable from secular equilibrium (Fig. 5-2). In the case of strong initial daughter excesses, achieving the same relative deviation from equilibrium requires longer time periods: for an initial daughter/parent activity ratio of 10, the daughter/parent activity will be ~3% above the secular equilibrium ratio after ~8 half-lives (Fig. 5-2). Strong enrichments of U-series intermediate daughters, however, are rare, because D values for actinides mostly differ by a factor of <10 (Blundy & Wood 2003)

SIMS U-series dating is generally performed near analytical detection limits due to the very low abundances of short lived U-series intermediate daughter atoms in sample or standard materials. As a guide for assessing the practicality of SIMS analysis of uraniferous materials for U-series dating, expected count rates for ^{226}Ra, ^{230}Th, ^{231}Pa, and ^{234}U positive ion species are calculated in Fig. 5-4. Useful ion yields (ions detected/atoms sputtered) for species of interest (^{230}ThO$^+$, ^{231}PaO$^+$, and ^{234}UO$^+$; note: O is used here as shorthand for the abundant isotope ^{16}O) are from the literature or estimated from chemically similar species. For ^{230}ThO$^+$, ^{231}PaO$^+$, ^{234}UO$^+$, and ^{226}Ra$^+$ (^{138}Ba$^+$ as a proxy for ^{226}Ra$^+$; Hervig *et al.* 2006) useful ion yields are approximately 1%. Assuming a sputter rate of 0.05 μm^3/nA/sec (typical for zircon) and a total counting time of 1 hour, the detection limits are ~0.5 ppm for ^{234}U, ~2 ppm for ^{230}Th, and ~70 ppm for ^{231}Pa and ^{226}Rd (Fig. 5-4). Higher sputter rates (*e.g.*, for opal) result in lower detection limits, whereas elevated backgrounds increase detection limits, whereby the detection limit scales with the square root of the background intensity. Interferences such as ^{238}U^{12}C$^+$ on ^{234}UO$^+$ may require analysis of ^{234}U$^+$ instead of ^{234}UO$^+$, which is less abundant than ^{234}UO$^+$ by a factor of ~2 (Paces *et al.* 2004). Note that these calculations assume secular equilibrium, and while U-series isotopes of interest can be enriched in some minerals, analysis of equilibrium reference materials is required for calibrating or monitoring instrumental fractionation.

Based on these considerations, the principal targets for SIMS U-series analysis are the long lived

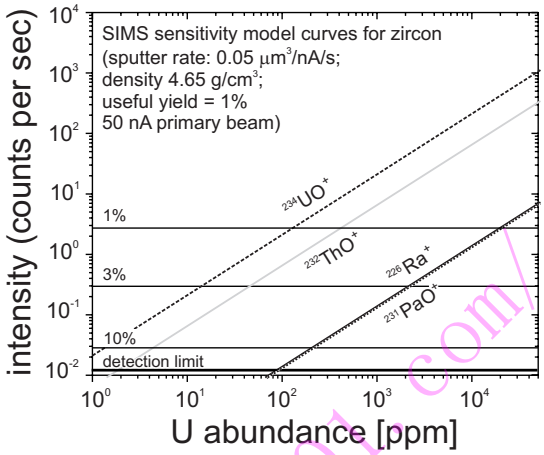


FIG. 5-4. SIMS U-series analysis detection limits as a function of U abundance. Calculations assume equilibrium, a zircon density of 4.65 g/cm^3, and a sputter rate of 0.05 μm/sec/nA, typical for zircon bombardment with a 50 nA ^{16}O$^-$ beam. Thin horizontal lines are drawn for relative uncertainties of 1, 3, and 10 % based on counting statistics for a 60 min analysis. The detection limit (thick solid line) is calculated for the average background at mass/charge 246.3 = 0.04 cps, as measured in 40 sequential analyses of Puy de Dome and AS-3 zircon grains, using the approximation for the detection limit D.L.(at 99% confidence) = 2.3 × (2 c_{bck})$^{0.5}$ (c_{bkc} = total background counts).

($t½ > 10^4$ a) intermediate daughter isotopes in minerals enriched in actinide elements, with abundances exceeding few 10s to 100s of ppm U. In the subsequent paragraphs, occurrences and U-series element-partitioning behavior of some uraniferous minerals are summarized, and their potential for U-series geochronology is discussed.

Zircon Zircon ($ZrSiO_4$) is an accessory mineral common in evolved silicic and carbonatitic rocks. It crystallizes both from melts and hydrothermal fluids (Watson & Harrison 1983, Hoskin & Schaltegger 2003). Nominally, zircon incorporates U with a mineral–melt partitioning coefficient D_U of ~100 (Blundy & Wood 2003), but U and Th abundances frequently vary significantly, even within individual zircon crystals (Fig. 5-5). Because of this variability, it is difficult to provide a range of typical U abundances in zircon, but U abundances between 10 and 1000 ppm are common, whereby high U zircon with of up to several wt.% UO_2 exists in some rhyolitic rocks (*e.g.*, Buff Peak zircon with ~3 wt.% UO_2; Schmitt 2007). Trace element variations in zircon also control its cathodoluminescence (CL) activity, and CL images are frequently

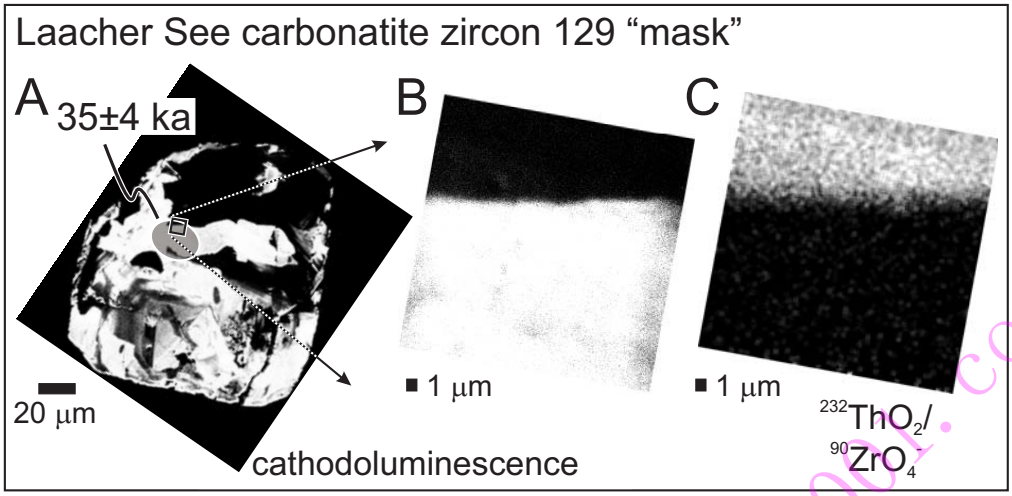


FIG. 5-5. Cathodoluminescence images of Laacher See carbonatite zircon 129 "mask" (A, B) compared to $^{232}ThO_2^-/^{90}ZrO_4^-$ ion intensity map generated in multi-collection mode under bombardment with a ~1 μm diameter Cs^+ primary beam (C). Bright area in C is higher in Th by about ~20-fold compared to dark area.

used to target actinide-rich domains in zircon following the empirical rule that CL-dark regions are higher in U and Th (Fig. 5-5). Despite the apparent complexity of zircon CL patterns, these may or may not reflect significant differences in crystallization age. Average D_{Th}/D_U is approximately 0.2 for a wide variety of magmatic rock types (Bindeman *et al.* 2006), but two to three-fold variations in Th/U exist in igneous zircon even within single crystals (Lowenstern *et al.* 2000).

Zircon is extremely resistant to hydrothermal alteration or weathering. Moreover, U and Th diffusion occurs over vanishingly small length scales so that zircon U-series ages can be reliably interpreted as crystallization ages (Cherniak & Watson 2001, Cherniak & Watson 2003). Intricate age zonation at a few micrometres spatial resolution has been documented through depth profiling of zircon (Reid 2008, Fig. 5-6). Bulk analysis of age-zoned zircon such as the grain depicted in Figure 5-6 would produce mixed ages with little geologic significance. Even at the lateral dimensions of the ion microprobe primary beam of few 10's of μm, averaging different age domains is possible. SIMS depth profiling which greatly enhances spatial resolution relative to the lateral dimensions of the analysis crater is thus an important tool to extract reliable crystallization ages from zoned crystals (Reid 2008).

Allanite Allanite is an epidote-group mineral which incorporates significant amounts of Th and U into its structure and which occurs in silicic igneous rocks and regional metamorphic rocks. Its general mineral formula is $[A_2M_3Si_3O_{12}(OH)]$, where the A sites contain Ca, Sr, or REE, and the M sites octahedrally coordinated cations such as Al, Fe, Mn, or Mg (Gieré & Sorensen 2004). Allanite U-series dating of young volcanic rocks harnesses the preferential incorporation of Th into its structure relative to U (D_{Th}/D_U ~50), and the high abundances of Th (typically 1–2 wt.% ThO_2, Catlos *et al.* 2000, Vazquez & Reid 2004) that facilitates analysis of ^{230}Th. What fuels interest in allanite U-series dating most, however, are systematic compositional variations that provide a record of magmatic differentiation. For example, changes in La/Nd or Mn/Mg due to cation substitution in A and M sites, respectively, can be related to compositional

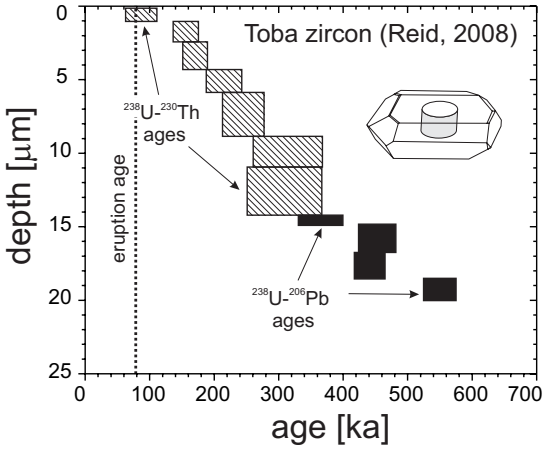


FIG. 5-6. Depth profiling of Toba zircon showing concordance between ^{238}U–^{230}Th and ^{238}U–^{206}Pb ages (Reid 2008).

variations in the host melt over time (Vazquez & Reid 2004). Vazquez & Reid (2004) estimated Th diffusion in allanite to occur over length scales of a few micrometres at most for crystal storage under magmatic temperatures (~800ºC) and durations of hundreds of thousands of years so that post-crystallization re-equilibration in allanite is largely negligible for Th isotopes.

Opal In contrast to minerals mentioned above, opal (amorphous, hydrated silica $SiO_2.nH_2O$) is a low temperature, hydrogenic mineral. It is used as a geochronometer in paleohydrology (*e.g.*, for the Yucca Mountain nuclear repository site, Paces *et al.* 2004) and environmental studies (*e.g.*, pedogenic opal, Maher *et al.* 2007). Common opal typically has much higher U abundances (>1000 ppm, Amelin & Back 2006) than precious opal, and U abundances correlate with ultraviolet (UV) fluorescence. U and Th are characteristically extremely fractionated with Th/U ratios between ~10^{-3} and 10^{-4}, and $^{204}Pb/^{238}U$ ratios are also low (10^{-5}–10^{-7}, Amelin & Back 2006). Precious opal, by contrast, tends to display lower U abundances, higher Th/U ratios of ~ 1, and elevated common Pb abundances so that it is of limited use for geochronology (Amelin & Back 2006).

Other accessory magmatic minerals No SIMS U-series data for accessory minerals in igneous rocks other than zircon and allanite have been published to the author's knowledge. There exist, however, many potentially datable accessory minerals, both in mafic and silicic rocks. Based on their propensity for enriching actinide elements, such minerals include baddeleyite (ZrO_2), zirconolite ($CaZrTi_2O_7$), chevkinite-perrierite ($A_4BC_2D_2Si_4O_{22}$, where A = [La,Ce,Ca,Sr,Th], B = Fe^{2+}, C = [Fe^{2+},Fe^{3+},Ti,Al,Zr,Nb] and D = Ti, MacDonald & Belkin 2002), and pyrochlore ($A_2B_2X_6Y\ nH_2O$, where A = [Na, Ca, Mn, Fe^{2+}, Sr, Sb, Cs, Ba, REE, Pb, Bi, Th, U], B = [Nb, Ta, Ti, Al, Fe^{3+}, Zr, Sn, W], X = [O, OH], and Y = [O, OH, F], Lumpkin & Ewing 1995), which are characteristic accessory minerals in mafic, alkaline, or carbonatitic rocks, that commonly lack other datable minerals. In addition, apatite ($Ca_5[PO_4]_3$[OH, F, Cl]), titanite ($CaTiSiO_5$), and monazite ([Th, REE][PO_3,SiO_4]) are potentially amenable for U-series dating, and they are common accessory minerals in silicic rocks. Apatite and titanite, however, tend to display only comparatively modest enrichments in U and Th, which limits analytical precision.

Bulk sample ^{238}U–^{230}Th analysis by SIMS
Although not the main focus of this review, bulk U-series dating by SIMS is briefly mentioned here. Several studies have harnessed the high sensitivity of SIMS for actinides (typically exceeding that of TIMS and ICP–MS techniques by at least one order of magnitude, Goldstein & Stirling 2003) for Quaternary geochronology. In these studies, rocks, minerals or corals were digested in bulk, and ion-exchange column separation techniques were used to enrich U and Th. Layne & Sims (2000) evaporated purified Th-enriched solutions on carbon planchets and analyzed the dried residue using a CAMECA ims 1270. Bischoff *et al.* (2005) loaded pre-concentrated U and Th on single ion-exchange beads (~100 µm diameter), which were subsequently charred and mounted in epoxy for analysis using SHRIMP–RG. Both studies applied oxygen primary beams, and analyzed positive secondary ions as atomic species. Analytical uncertainties were generally found to be similar or better than those of conventional techniques (Layne & Sims 2000, Bischoff *et al.* 2005).

Applicable methods and time ranges

U–Pb Among the individual parent-daughter systems in U-series geochronology, U–Pb dating stands out as it can be applied over the entire geologic time scale. Because extensive reviews of SIMS U–Pb dating are available (*e.g.*, Ireland & Williams 2003), only the lower bounds of applicability of SIMS U–Pb dating are discussed here. Multiple case studies have demonstrated that concordant SIMS ^{238}U–^{206}Pb and ^{238}U–^{230}Th zircon ages can be obtained (Vazquez *et al.* 2007, Reid 2008, Fig. 5-6), and thus the lower age limit for U–Pb dating can be empirically constrained as the age at which ^{238}U–^{230}Th dates become more precise than ^{238}U–^{206}Pb dates, typically for ages <200–300 ka. For Quaternary samples, SIMS U–Pb dating focuses on ^{238}U–^{206}Pb because of the low abundance of ^{235}U (present day $^{238}U/^{235}U = 137.88$) and concomitantly low radiogenic ^{207}Pb. Moreover, SIMS analytical uncertainties for U–Pb of 1–2% (relative) largely prevent a meaningful check for concordance between young ^{235}U–^{207}Pb and ^{238}U–^{206}Pb ages as a criterion for Pb-loss, but metamictization and Pb mobility can be ruled out for most Quaternary zircon with typical U abundances (Cherniak & Watson 2001). It is, however, advantageous to use ^{207}Pb as a proxy for common Pb (Baldwin & Ireland 1995, Schmitt *et al.* 2003a), instead of ^{204}Pb. This is because $^{207}Pb/^{206}Pb$ throughout the Cenozoic is

http://bbe.sbc.com/

essentially invariant (*e.g.*, Getty & DePaolo 1995). Conventionally ^{204}Pb-corrected ages for Quaternary zircon analyses are less precise due to a combination of high uncertainties of ^{204}Pb measurements and low radiogenic yields, and can lead to an overcorrection in U–Pb ages, likely due to unidentified interferences on the ^{204}Pb peak (Schmitt *et al.* 2003a, Fig. 5-7). Because ^{207}Pb intensities are about ~15 times higher than ^{204}Pb, there will be less uncertainty in the common Pb correction. Using a ^{207}Pb-based common Pb correction, ^{206}Pb/^{238}U ages for Quaternary reference zircon are in good agreement with TIMS results (Schmitt *et al.* 2003a). Another approach is to use ^{208}Pb as a proxy for common Pb (Compston *et al.* 1984), which is advantageous for low Th (and thus low radiogenic ^{208}Pb) minerals such as opal (Nemchin *et al.* 2006).

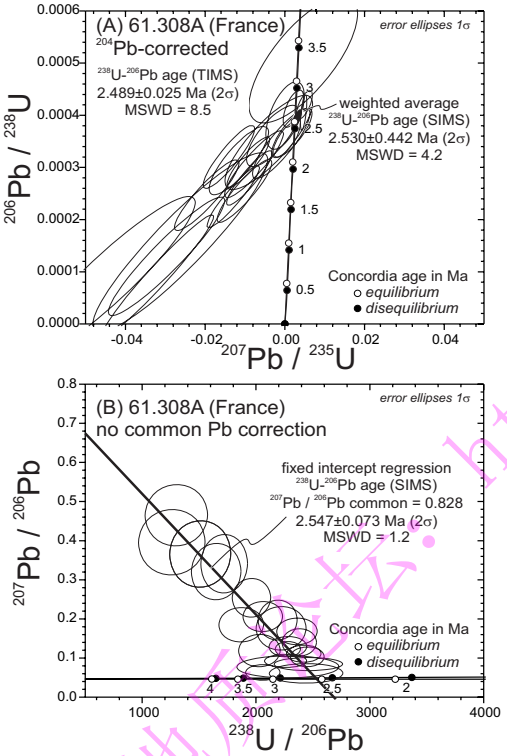


FIG. 5-7. (**A**) Conventionally ^{204}Pb-corrected ^{238}U–^{206}Pb age for Quaternary zircon standard 61.308A (France). Overcorrection due to uncorrected interferences or backgrounds in ^{204}Pb leads to future ^{235}U–^{207}Pb ages for analyses with low radiogenic Pb. (**B**) The same data uncorrected for common Pb. Note that the spread in the uncorrected data reflects deliberate changes in the analytical parameters (narrowing the field aperture, concomitant with increasing primary beam intensity) that led to variable contributions of surface-derived common Pb. Average TIMS age from Wiedenbeck *et al.* (1995), SIMS data published in Schmitt *et al.* (2003a).

In addition to non-conventional common Pb correction schemes, initial disequilibrium corrections are a specific requirement for Quaternary zircon U–Pb dating. The effects of disequilibrium on U–Pb (or Th–Pb) ages depend on the partitioning ratio between long lived parent and intermediate daughter, and scales with the half-life of the daughter isotope (see equations 5 and 6). Zircon commonly discriminates against ^{230}Th relative to ^{238}U, because of different zircon–melt partition coefficients. This causes a deficit in ^{206}Pb that for f = 0.2 (equation 6) amounts to approximately –87 ka (assuming melt equilibrium, Fig. 5-3). Zircon Th/U can be directly analyzed, whereas melt Th/U is inferred from compositions of whole rocks, matrix glass (Reid & Coath 2000), or melt inclusions (Schmitt *et al.* 2003a). Initial ^{231}Pa-excess results in unsupported ^{207}Pb, leading to a +95 ka age excess (assuming melt equilibrium, Fig. 5-3). Such excesses were detected in some high precision TIMS studies of Quaternary and Tertiary zircon (*e.g.*, Schmitz *et al.* 2001, Crowley *et al.* 2007). Other accessory minerals such as allanite or monazite will exhibit excess ^{206}Pb due to preferential partitioning of Th relative to U, but by the same token, these minerals will preferentially be dated by ^{232}Th–^{208}Pb, instead of U–Pb methods. This has the advantage that corrections of disequilibrium are obsolete due to the absence of long lived intermediate daughters in the ^{232}Th decay chain.

^{238}U–^{234}U ^{234}U ($t_{½}$ = 245,250 a) is the longest lived intermediate U-series isotope. Magmatic processes such as melting and crystallization do not fractionate ^{234}U and ^{238}U, and fresh igneous rocks and minerals are typically in secular equilibrium (Edwards *et al.* 2003). Natural waters, by contrast, generally display (^{234}U)/(^{238}U) ratios >1, whereas soil (^{234}U)/(^{238}U) ratios are sub-unity (Edwards *et al.* 2003). Aqueous precipitates such as carbonates and opal inherit elevated (^{234}U)/(^{238}U) from their precipitating waters. Combined SIMS ^{238}U–^{234}U–^{230}Th and ^{238}U–^{234}U–^{206}Pb opal dating is feasible over time ranges of ~50 ka to ~1 Ma (Paces *et al.* 2004, Nemchin *et al.* 2006).

^{238}U–^{230}Th The second longest U-series half-life is that of ^{230}Th ($t_{½}$ = 75,690 a), which results in a maximum age for ^{238}U–^{230}Th dating of ~350 ka. ^{238}U–^{230}Th dating of accessory minerals has been

applied to volcanic rocks with eruption ages as young as 650 a (Reid *et al.* 1997), and Holocene zircon ^{238}U–^{230}Th ages have been obtained (Schmitt & Vazquez 2006, Bacon *et al.* 2007, Fig. 5-8).

In contrast to hydrogenic minerals such as calcite and opal, accessory minerals incorporate some degree of initial ^{230}Th, so that the second term in equation (3) plays a significant role. An isochron method is thus applied, in which the age is determined based on the slope defined by coeval samples in a $(^{230}Th)/(^{232}Th)$ *vs.* $(^{238}U)/(^{232}Th)$ diagram. The age is derived using equation (3), whereby daughter 2 = ^{230}Th, parent 1 = ^{238}U, and both sides of equation (3) are divided by the ^{232}Th activity:

$$\frac{N_{230}\lambda_{230}}{N_{232}\lambda_{232}} = \frac{N_{238}\lambda_{238}}{N_{232}\lambda_{232}}\left(1-e^{-\lambda_{230}t}\right)+\frac{N^0_{230}\lambda_{230}}{N_{232}\lambda_{232}}e^{-\lambda_{230}t} \quad (7)$$

This equation is restated in (8) with activities expressed by parentheses:

$$\frac{\left(^{230}Th\right)}{\left(^{232}Th\right)} = \frac{\left(^{238}U\right)}{\left(^{232}Th\right)}\left(1-e^{-\lambda_{230}t}\right)+\frac{\left(^{230}Th\right)^0}{\left(^{232}Th\right)}e^{-\lambda_{230}t} \quad (8)$$

This equation represents that of a straight line in a $(^{230}Th)/(^{232}Th)$ *vs.* $(^{238}U)/(^{232}Th)$ isochron diagram, whereby age is calculated from slope m by:

$$t = -\frac{\ln(1-m)}{\lambda_{230}} \quad (9)$$

Two approaches are frequently used to determine an age: (1) two-point model isochrons using mineral–melt pairs whereby melt U-series compositions need to be analyzed by bulk techniques due to low U-series isotope abundance in whole rocks or glasses (*e.g.*, Reid *et al.* 1997), and (2) internal isochrons for multiple spots on single crystals or multicrystal analyses (*e.g.*, Lowenstern *et al.* 2000). Figure 5-9 presents an example of both isochron approaches: both yielding ages overlapping within uncertainty, with the zircon–melt pair yielding a more precise result compared to zircon data alone. Mineral–melt two point isochron ages are, strictly speaking, model ages because the composition of the melt and mineral crystallized may not be the same as the melt composition inferred from analysis of whole rocks or glass. Fortunately, disequilibrium due to accessory mineral fractionation is much larger than that imparted on melts by magmatic processes such as melting and fractional crystallization of major phases so that uncertainties with regard to melt composition in many cases

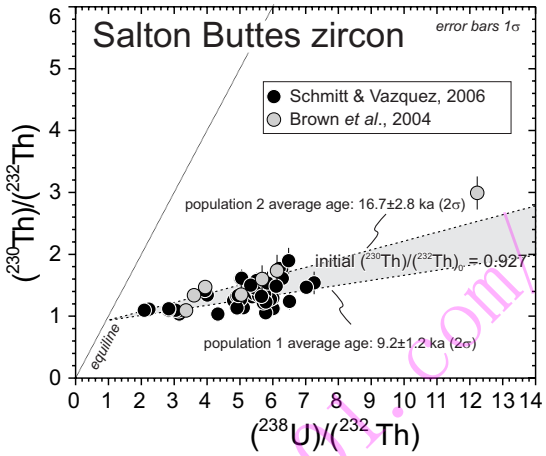


FIG. 5-8. $(^{230}Th)/(^{232}Th)$ vs. $(^{238}U)/(^{232}Th)$ isochron diagram with wedge-shaped "sphenochron" (Chen *et al.* 1996) defined by Salton Buttes zircon. Zircon populations 1 and 2 were determined using the mixing algorithm by Sambridge & Compston (1994) for model ages defined by initial $(^{230}Th)/(^{232}Th)$ = 0.972 (from linear regression of all data). The results for population 1 demonstrate the potential of SIMS for dating Holocene crystals. Also note the close overlap between data from Brown *et al.* (2004) obtained on SHRIMP-RG and Schmitt & Vazquez (2006) data using a CAMECA ims 1270.

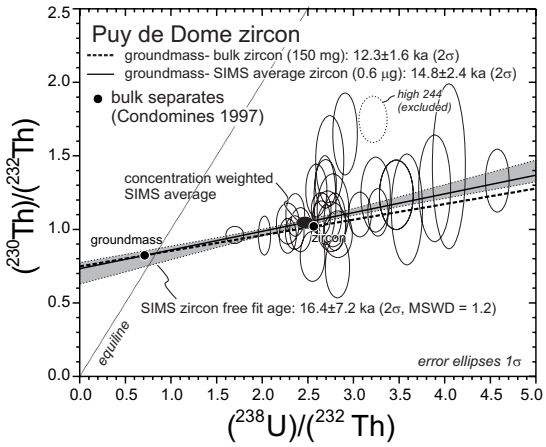


FIG. 5-9. Isochron diagram for Puy de Dome zircon in comparison with bulk TIMS/α-spectrometry results (Condomines 1997). SIMS analysis of 30 zircon grains acquired in fully automated mode over ~24 hours using the UCLA CAMECA ims 1270. Interspersed AS-3 zircon analyses yielded an weighted average $(^{230}Th)/(^{238}U)$ = 1.010±0.028 (2σ, MSWD = 0.5, n = 10). One analysis of a small zircon grain with beam overlap on epoxy and concomitant elevated intensities on masses 244 and 246 is excluded from average.

http://www.geokniga.org

weigh little on the overall uncertainty of the two point isochron age (see paragraph on *Error assessment*). Internal isochrons require that the time scale of crystallization is short relative to the decay rate of ^{230}Th. Prolonged crystallization, however, is a hallmark of many magmatic systems so that zircon in some cases will not form well defined isochrons but rather fall into a wedge-shaped field (also termed "sphenochron", Chen *et al.* 1996, Fig. 5-8) for which lower and upper age bounds can be determined applying mixing algorithms such as by Sambridge & Compston (1994).

^{235}U–^{231}Pa ^{231}Pa is the third longest lived U-series isotope, and the longest lived intermediate isotope in the ^{235}U decay chain ($t_{½}$ = 32,760 ka). While theoretically applicable to an age range of ~150 ka, and therefore complimentary to ^{230}Th–^{238}U dating, its abundance at equilibrium is ~70 times lower than ^{230}Th (Fig. 5-4). Consequently, SIMS ^{231}Pa analysis has been primarily conducted with the goal of constraining Pa partitioning in zircon to provide an empirical basis for correcting high precision U–Pb ages (*e.g.*, Schmitz & Bowring 2001, Crowley *et al.* 2007) rather than to employ it as a new chronometer. Experimental constraints on partitioning of ^{231}Pa are lacking, but lattice strain partitioning models suggest strong compatibility of pentavalent Pa in zircon (Blundy & Wood 2003). If valid, initial ^{231}Pa excesses could indeed lead to significant unsupported ^{207}Pb, a possibility that has been raised frequently in the U–Pb TIMS literature (*e.g.*, Anczkievicz *et al.* 2001). Schmitt (2007), however, detected only minor excesses in (^{231}Pa)/(^{235}U) in zircon from Holocene Salton Buttes rhyolite. An initial activity ratio of ~2 measured in Salton Buttes zircon demonstrates that Pa is indeed more compatible in zircon compared to U, but ^{231}Pa disequilibrium will cause only small excesses in ^{207}Pb (Schmitt 2007). Additional analyses of (^{231}Pa)/(^{235}U) in zircon crystals from the China Hat rhyolite support these earlier findings, as demonstrated by the (^{231}Pa)/(^{235}U) *vs.* (^{230}Th)/(^{238}U) model concordia for initial zircon (^{231}Pa)/(^{235}U)$_0$ = 2 and (^{230}Th)/(^{238}U)$_0$ = 0.2 (Fig. 5-10). The zircon ages are concordant with the eruption age (57 ±8 ka, 2σ, Heumann 1999) and the zircon (^{230}Th)/(^{232}Th) *vs.* (^{238}U)/(^{232}Th) isochron age of 66 ±9 ka (2σ, MSWD = 0.57), both overlapping within uncertainties (Fig. 5-10). For China Hat rhyolite initial (^{231}Pa)/(^{235}U)$_0$ = 0.6 (Heumann 2004), this results in a model D_{Pa}/D_U (D = zircon–melt partition coefficient ratio of 3.4 ±0.4. This is equivalent to the values proposed by Schmitt (2007) for Salton Buttes zircon.

Other short lived chronometers Of the short lived U-series isotopes, only ^{226}Ra ($t_{½}$ = 1599 a) is briefly considered here. *In situ* SIMS analysis of ^{226}Ra is hampered by its extremely low abundance (see Fig. 5-4), especially as Ra is predictably incompatible in most minerals (using Ba as a proxy, Blundy & Wood 2003). Even in minerals where ^{226}Ra is compatible (*e.g.*, K-feldspar: Blundy & Wood 2003, leucite: Fabbrizio *et al.* 2008), enrichment is at best ~10-fold relative to the melt. Low abundances of parent and daughter nuclei limit the capability of *in situ* SIMS ^{230}Th–^{226}Ra dating. There is, however, potential for SIMS ^{226}Ra analysis of doped experimental samples.

METHODS

Sample Preparation

The main advantage of SIMS U-series analysis is its capability to measure spatially resolved isotopic compositions. Sample preparation techniques for bulk digestion methods followed by SIMS analysis of chemically separated and/or enriched U-series isotopes are described in Layne & Sims (2000) and Bischoff *et al.* (2005). Samples for spatially resolved analysis are prepared by embedding crystals either in epoxy resin, or alternatively in a soft metal (*e.g.*, indium In). It is also possible to perform *in situ* analysis using

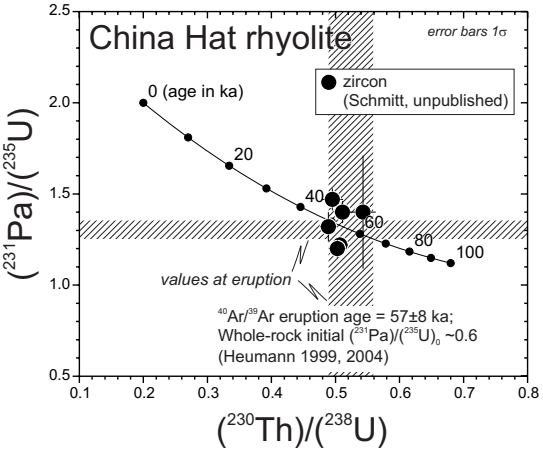


FIG. 5-10. (^{231}Pa)/(^{235}U) vs. (^{230}Th)/(^{238}U) isochron diagram for ~57 ka zircon from China Hat rhyolite showing concordance of both decay systems for model initial (^{231}Pa)/(^{235}U)$_0$ = 2 and (^{230}Th)/(^{238}U)$_0$ = 0.2. Gray bars indicate Ar–Ar eruption age and uncertainty bands (Heumann 1999).

petrographic thin sections or polished blocks. Samples are required to be solid and flat, and must not outgas under ultrahigh vacuum. Sample holder dimensions of commercial instruments are typically ~2.54 cm in diameter, but the useful area is restricted to the inner ~2 cm bull's eye because steering of primary and secondary beams is compromised when targeting areas near the edges of the sample holder. Standard petrographic grinding and polishing techniques are employed, but for euhedral crystals such as zircon, it is also possible to press grains into In metal so that crystal faces are flush with the mount surface, without any further grinding or polishing (Fig. 5-11). Sample processing is followed by several cleaning steps in order to remove surface contaminants (*e.g.*, dilute HCl for zircon). Prior to analysis, samples are plated with a thin (several tens of nm) Au layer to generate a conducting sample surface.

SIMS Analytical Conditions

Primary beam SIMS U-series analysis is typically conducted with a mass-filtered primary beam of $^{16}O_2^-$ or $^{16}O^-$ ions generated in a duoplasmatron source. Oxygen primary beams employed have currents mostly between ~10 and 60 nA, and are focused into ~15–40 µm diameter spots (*e.g.*, Schmitt *et al.* 2006, Schmitt 2007, Maher *et al.* 2007). With primary beam impact energies of 22.5 kV and oblique incidence, zircon sputter rates are

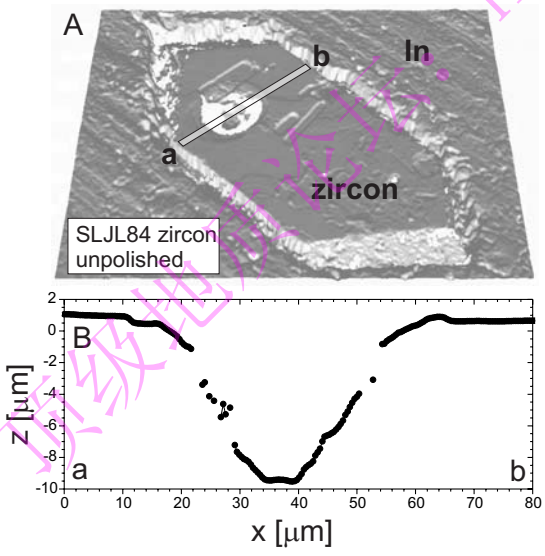


FIG. 5-11. **A,** Indium (In)-mounted zircon in MicroXAM optical interferometry surface map. Entire grains were pressed into In metal, washed with 1N HCl and Au-coated. **B**, Depth transect through analysis crater after 30 min bombardment with a 60 nA $^{16}O^-$ beam (B).

~0.05 µm^3/nA/sec (or 0.2 pg/nA/sec, Schmitt 2007), whereas those for opal are reported to be approximately four to five times higher (*e.g.*, Maher *et al.* 2007). For a typical U–Th analysis duration of ~20 min, the depth of the analysis crater will thus be a few µm, about one order of magnitude smaller than the lateral resolution of the primary beam spot.

Secondary ion species For the analysis of silicate minerals, the abundance of oxide molecular ion species (*e.g.*, ThO^+, PaO^+, and UO^+) is about two to ten times that of the corresponding atomic species at the peak of the energy distribution (typically 10 keV with an energy band-pass of 50 eV). By contrast, Pb isotopes are analyzed as atomic species (Pb^+). Mass tables for ^{230}Th–^{238}U SIMS analysis of zircon, allanite, or opal thus contain as a minimum the following species: $^{230}ThO^+$, $^{232}ThO^+$, and $^{238}UO^+$. For U–Pb, the key masses of interest are: $^{204}Pb^+$, $^{206}Pb^+$, $^{207}Pb^+$, $^{208}Pb^+$, $^{232}Th^+$ (or $^{232}ThO^+$), $^{238}U^+$, and $^{238}UO^+$. In addition, reference species that relate to stoichiometric components in the target mineral are typically included ($^{28}Si_4O_7^+$ for opal, $^{90}Zr_2O_4^+$, and/or $^{90}Zr^{92}ZrO_4^+$ for zircon). These can be used as a normalizing species to calculate relative sensitivity factors (RSFs) from standards with known concentrations to determine U and Th concentrations in the unknown materials. In addition, these species also serve as reference peaks for magnet-centering for neighboring low intensity U-series peaks. Finally, one or more background mass stations are included which are characteristically 0.04 amu (Maher *et al.* 2007) to 0.3 amu (Schmitt *et al.* 2006) to the high mass side of $^{230}ThO^+$ and $^{231}PaO^+$ to correct for tailing of the adjacent $^{232}ThO^+$ peak. For zircon and other accessory minerals with high Th abundances, it is highly advisable also to include a background with mass/charge = 244.03 ($^{232}Th^{12}C^+$) because of a possible isobaric interference on 246.03 ($^{232}Th_2{}^{12}CO^{2+}$). For opal dating, $^{234}U^+$ and/or $^{234}UO^+$ are included in the mass table (Paces *et al.* 2004, Maher *et al.* 2007).

Interferences Most mass interferences for U-series and Pb-isotope analysis require a mass-resolving power ($\Delta m/m$) of ~4000–5000 (Compston *et al.* 1994). For zircon, interferences result from molecular isobars involving oxides of Si, Zr, heavy rare earth elements and/or Hf (Fig. 5-11). In addition to matrix elements, isobars need to be considered that involve elements present in the conductive coating (*e.g.*, $^{197}AuO_3H^+$) or embedding

material (*e.g.*, $^{232}Th_2{}^{12}CO^{2+}$). The latter interference is particular detrimental to $^{230}ThO^+$ analysis, as it is irresolvable at Δm/m <40,000. All sources of C (*e.g.*, beam overlap with epoxy, Fig. 5-12) or residual C coating from electron beam imaging thus need to be carefully avoided (Schmitt *et al.* 2006). Due to low abundances of Th in opal, this interference is likely to be uncritical, but for $^{234}UO^+$ analysis, epoxy overlap can cause an interference on mass 250 from production of $^{238}U^{12}C^+$ (Paces *et al.* 2004). By contrast, $(^{234}U)/(^{238}U)$ activities for opal calculated from atomic species are not adversely affected from beam overlap onto epoxy (Paces *et al.* 2004).

Detection Secondary ion intensities for minor isotopes of U, Th, and Pb are measured using electron multipliers that are shielded from scattered charged particles by deflecting the secondary ion beam using electrostatic analyzers. For the CAMECA ims 1270, this results in abundance sensitivities for $^{232}Th^{16}O^+$ at mass 247 of ~250 ppb (Schmitt 2007). Most studies used peak-switching into a single EM detector, but there is potential for multicollection because it reduces analysis time while maintaining comparable precision to single EM analysis. For high U zircon or high Th minerals such as allanite, secondary ion intensities of major isotopes $^{238}UO^+$ and/or $^{232}ThO^+$ may require Faraday cup analyses. If multiple detectors

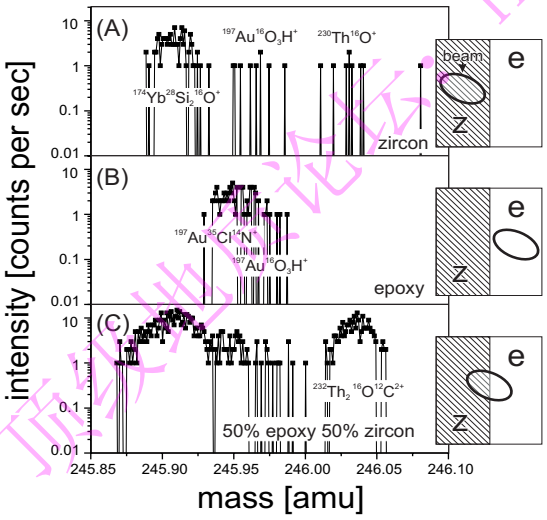


FIG. 5-12. High mass-resolution scans of zircon, epoxy, and zircon-epoxy overlap around mass/charge 246. Elevated counts on mass/charge = 246.03 for the zircon-epoxy overlap scan are likely due to a doubly charged Th–O–C interference irresolvable from $^{230}ThO^+$ (after Schmitt *et al.* 2006).

are used, correction for differential yields are applied, *e.g.*, by normalizing to an invariant isotopic ratio such as $^{235}U/^{238}U$. If this is attempted via measurement of $^{235}U^{16}O^+/^{238}U^{16}O^+$, interferences such as $^{238}U^{12}CH^+$ must be absent. EM deadtime corrections are of second order importance due to relative low count rates achieved in U-series isotope analysis.

Data Analysis

Data reduction and representation Isotopic fractionation of heavy masses is insignificant in SIMS, and activity ratios such as $(^{230}Th)/(^{232}Th)$ or $(^{234}U)/(^{238}U)$ can be calculated directly from measured intensities after subtraction of backgrounds, and possibly correcting for secondary intensity drift. Inter-element activity ratios require relative sensitivity corrections which are strongly dependent on analytical conditions (*e.g.*, primary beam species, sample charging, energy window analyzed) and composition of the matrix. Consequently, appropriate RSFs need to be determined on compositionally well matched standard materials (see below) for each individual analysis session, preferentially on the same mounts as the unknown materials. RSF calibration for SIMS U–Pb zircon dating that is based on empirical correlations between UO^+/U^+ or $UO_2{}^+/U^+$ and U–Pb are described in detail elsewhere (*e.g.*, Compston *et al.* 1984, Stern & Amelin 2003). U–Th fractionation in SIMS is generally much smaller (RSF ~0.9–1.1) compared to U–Pb (zircon RSF ~0.2), and is also largely insensitive to any variations in the production of atomic *vs*. molecular oxide species. Two approaches of determining the U–Th RSF are used: first, in cases where radiogenic (*) $^{208}Pb^*/^{206}Pb^*$ can be precisely determined (*e.g.*, for Precambrian zircon such as AS-3, Paces & Miller 1993), true $^{232}Th/^{238}U$ can be calculated from measured $^{208}Pb^*/^{206}Pb^*$ and the standard's known age. The RSF is then determined from the ratio of measured Th and U species (*e.g.*, $^{232}ThO^+/^{238}UO^+$) to true $^{232}Th/^{238}U$ (Reid *et al.* 1997). The advantage of this method is that it is independent of assumptions for U-series equilibrium in the standard, and the only requirement is that standards are concordant with regard to U–Pb and Th–Pb ages.

A second approach is used when $^{208}Pb^*/^{206}Pb^*$ cannot be precisely determined (*e.g.*, due to high common Pb of the reference mineral). In this case, RSF is calculated from a measured parent–daughter ratio (*e.g.*, $^{230}ThO^+/^{238}UO^+$) of a secular equilibrium

standard material, multiplying it with the respective decay constants (*e.g.*, Paces *et al.* 2004, Vazquez & Reid 2004). Schmitt (2007) similarly determined U–Pa RSF by analyzing Miocene Buff Peak high U zircon. By independently calibrating U–Th RSF on AS-3 zircon (see above), it was demonstrated that Buff Peak zircon is in secular equilibrium with regard to (^{230}Th)/(^{238}U), and thus equilibrium of the shorter lived ^{231}Pa daughter could be reasonably assumed (Schmitt 2007).

Quaternary U–Pb data are frequently displayed in the ^{207}Pb/^{206}Pb *vs.* ^{238}U/^{206}Pb diagram (Tera & Wasserburg 1972), an approach pioneered for SIMS data by Baldwin & Ireland (1995). Baldwin & Ireland (1995) regressed data uncorrected for common Pb in the ^{207}Pb/^{206}Pb *vs.* ^{238}U/^{206}Pb concordia diagram based on a well defined mixing array between radiogenic and common Pb as the y-axis intercept (see also Fig. 5-7). An additional advantage of the ^{207}Pb/^{206}Pb vs. ^{238}U/^{206}Pb concordia diagram is that errors between measured ^{207}Pb/^{206}P and ^{238}U/^{206}Pb are essentially uncorrelated. It is important to realize that the location of concordia will be shifted as a consequence of U-series disequilibrium (Fig. 5-7). Accessory mineral ^{238}U–^{230}Th results are commonly displayed in the (^{230}Th)/(^{232}Th) vs. (^{238}U)/(^{232}Th) diagram (Figs. 5-8, 5-9, 5-13), or as model ages derived from the two point isochron slope defined by crystal and melt compositions in an age probability diagram (Lowenstern *et al.* 2000, Fig. 5-13). (^{234}U)/(^{238}U) *vs.* (^{230}Th)/(^{238}U) activity diagrams are in use for displaying opal results (Fig. 5-14, Paces *et al.* 2004, Maher *et al.* 2007).

Standards Ireland & Williams (2003) have summarized the characteristics of the main zircon U–Pb standards in use. Comparatively little work has been done on Quaternary reference zircon, but for Quaternary zircon standards 61.308A and 61.308B, bulk TIMS results (Wiedenbeck *et al.* 1995) agree well with spatially selective analysis by SIMS (Schmitt *et al.* 2003a, Fig. 5-7) and laser ablation–inductively coupled plasma–mass spectrometry (LA–ICP–MS, Cocherie *et al.* 2009). Because RSFs are matrix-dependent, standards and unknowns should be carefully matched by composition. For U–Pb zircon dating, matrix effects have been described for high U zircon (Williams & Hergt 2000), but they are negligible for U–Th fractionation for zircon with UO_2 of up to 4 wt.% (Schmitt 2007).

U–Pb zircon standards are also analyzed to check for the accuracy of the ^{208}Pb*/^{206}Pb* *vs.* ^{232}Th/^{238}U RSF calibration. SIMS analysis of AS-3 standard zircon (1099 Ma, Paces & Miller 1993) and as 91,500 zircon (1065 Ma, Wiedenbeck *et al.* 1995) yielded unity (^{230}Th)/(^{238}U) ratios within uncertainty (*e.g.*, Reid *et al.* 1997, Schmitt *et al.* 2006, see also caption to Fig. 5-9). For Th–U RSF calibration on allanite, Vazquez & Reid (2004) analyzed equilibrium allanite from the ~760 ka Bishop Tuff and the 500 ka Middle Toba Tuff.

Only a few direct comparisons exist between U-series ages of "young" zircon determined by different techniques (TIMS and SIMS). In particular for cases where zircon crystallized over significant age ranges, differences in sampling scale of bulk methods (mg-sized samples for bulk analysis,

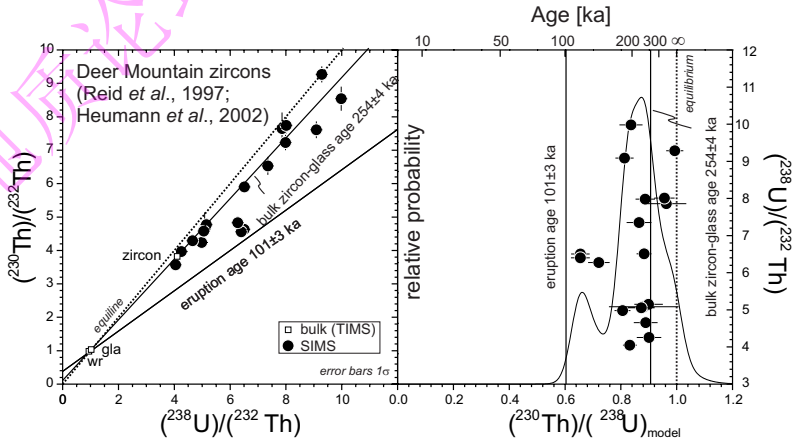


FIG. 5-13. Comparison between SIMS and TIMS zircon results for Deer Mountain rhyolite (Reid *et al.* 1997, Heumann *et al.* 2002). SIMS ages show range which is inconsistent with fitting an isochron (A). Zircon–whole rock model ages are shown in (B) with a probability density curve which indicates protracted, and episodic zircon crystallization between near-eruption and equilibrium ages (Reid *et al.* 1997).

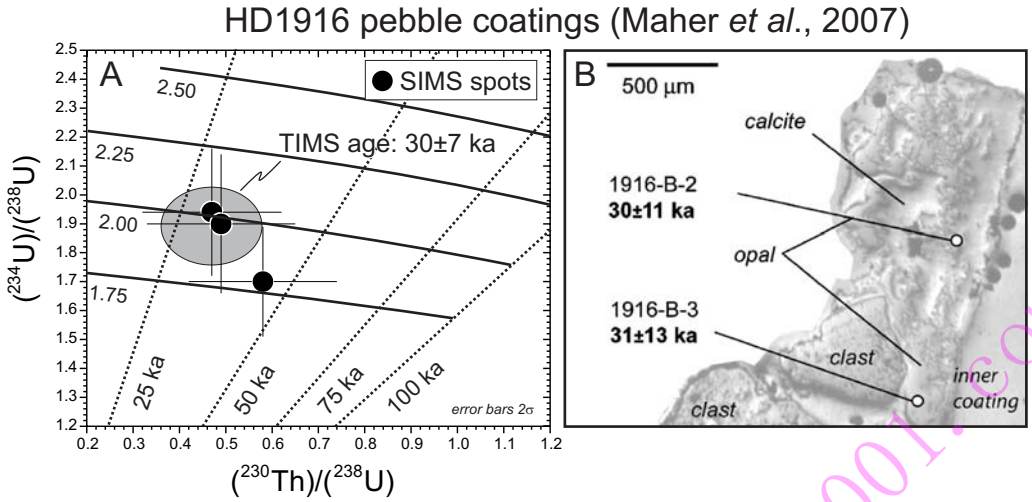


FIG. 5-14. **A** Comparison between SIMS spot and TIMS U-series ages for opaline pebble coatings of terraces deposited in arid to semi-arid environments of the western USA (Fortymile Wash, Nevada, sample HD1916, Maher *et al.* 2007). While both methods yield ages in excellent agreement, the spatial selectivity of SIMS avoids detrital contamination as the pebble coatings are mixtures of opaline silica, calcite and large detrital fragments (**B**).

cumulative ~100s of ng for SIMS, Fig. 5-9) and the bias of SIMS analyses in polished grain mounts towards grain interiors can account for discordant bulk TIMS and U-concentration weighted average SIMS ages (Charlier *et al.* 2005). For zircon with relative simple crystallization history from Puy de Dome (France), bulk TIMS/α-spectrometry results (12.7 ±1.6 ka 2σ error, Condomines 1997) agree with the U-concentration weighted average SIMS age (14.8 ±2.4 ka 2σ error, Fig. 5-9).

For opal U-series dating, M21277 Virgin Valley uraniferous opal is commonly used as a standard. It is ~2.2 Ma old (^{207}Pb/^{235}Pb age) and has U abundances between ~600 and 1100 ppm (Amelin & Back 2006). It is also shown to be in secular equilibrium with regards to (^{230}Th)/(^{238}U) and (^{234}U)/(^{238}U) (Nemchin *et al.* 2006). Although opal is structurally and compositionally more variable than zircon (*e.g.*, Amelin & Back 2006), matrix-dependent bias in Th–U fractionation is not documented (*e.g.*, Paces *et al.* 2004).

Error assessment Sources of random analytical error in SIMS include counting errors, RSF uncertainties, primary beam instabilities, surface roughness, or changes in surface conductivity with depth. In addition, potential sources of systematic bias are matrix effects, drift in detector gain, and detector non-linearity. These sources of uncertainty can be monitored through analysis of suitable secondary standards that are prepared and mounted together with the unknown samples. Significant depth-dependent Th–U fractionation is absent, both for zircon and opal, whereas significant fractionation of U–Pb with increasing crater depth occurs during sputtering of opal (*e.g.*, Nemchin *et al.* 2006). For older crystals, RSF uncertainties (1–2 %, Ireland & Williams 2003) typically dominate, whereas for Quaternary crystals counting errors are prevalent due to low signals. However, if signal intensities are strong (*e.g.*, for chemically separated and enriched bulk samples), SIMS uncertainties <0.5 % are achieved for ^{230}Th/^{232}Th ratios (Layne & Sims 2000).

Zircon ages are generally calculated by linear regression in isochron diagrams such as ^{207}Pb/^{206}Pb *vs.* ^{238}U/^{206}Pb or (^{230}Th)/(^{232}Th) vs. (^{238}U)/(^{232}Th), where ages are determined from the concordia intercept and slope, respectively. The analytical precision of SIMS is such that in many cases, crystal age heterogeneities can be detected which would otherwise be averaged in bulk analysis. This, however, can result in poor linear regression fits. Instead of an isochron age for a grain population, individual model ages can be calculated. In cases where model ages show significant spread, the resulting age spectra can be deconvolved into multiple age components by using mixing algorithms that are based on minimization of error residuals for discrete age populations with Gaussian error distribution (Sambridge & Compston 1994, Fig. 5-8).

For ^{238}U–^{230}Th dating, two point isochrons through melt and crystal compositions can yield

model ages (Fig. 5-13). The caveat in this method is that whole rock or glass ^{238}U–^{230}Th compositions may be inappropriate if these compositions have been modified since the time of zircon crystallization. This could occur via fractional crystallization (in particular of accessory minerals), assimilation, magma mixing, or assimilation. In such a case, zircon–whole rock or zircon–glass isochron ages could be biased. Heumann *et al.* (2002) argued that allanite fractionation subsequent to zircon crystallization could lead to systematically older zircon model ages (Fig. 5-15). These effects are, however, generally small compared to uncertainties in the zircon analysis, at least within reasonable bounds for variability of melt compositions.

Comparison with other in situ techniques Only a few studies have explored the potential of *in situ* U-series analyses using multicollector–laser ablation–inductively coupled plasma–mass spectrometry (MC–LA–ICP–MS). Stirling *et al.* (2000) used a Plasma 54 multiple collector ICP–MS instrument and demonstrated that ablation using a mixed He–Ar carrier gas significantly reduced U–Th fractionation. Their limitations were relatively large sample sizes (~10 µg) at 150 µm spatial resolution, and U-concentration requirements of >100 ppm (Stirling *et al.* 2000). Bernal *et al.* (2005) and Eggins *et al.* (2005) utilized a Neptune Finnigan MAT equipped with a 193 nm excimer laser and ablation in a He atmosphere. Their glass analyses consumed ~0.5 µg in about 30 s (Bernal *et al.* 2005). Potter *et al.* (2005) focused on analysis of low-U carbonates using a Nu Plasma MC–ICP–MS coupled to a 193 nm excimer laser, for which a typical analysis consumes ~70 µg of carbonate.

Aside from Stirling *et al.* (2000), no other LA–ICP–MS study has reported ^{238}U–^{230}Th compositions for materials with significant amounts of ^{232}Th such as zircon. Overall, the main advantages of SIMS compared to MC–LA–ICP–MS are higher useful yields for U-series species (typically one order of magnitude, Goldstein & Stirling 2003), smaller sample requirements (about 10 times less for materials with >100 ppm U, Bernal *et al.* 2005), and lower abundance sensitivities (by ~3-fold, Eggins *et al.* 2005) which provide a cleaner mass spectrum for the minor ^{230}Th isotope. Longer analysis times are a drawback of SIMS compared to MC–LA–ICP–MS.

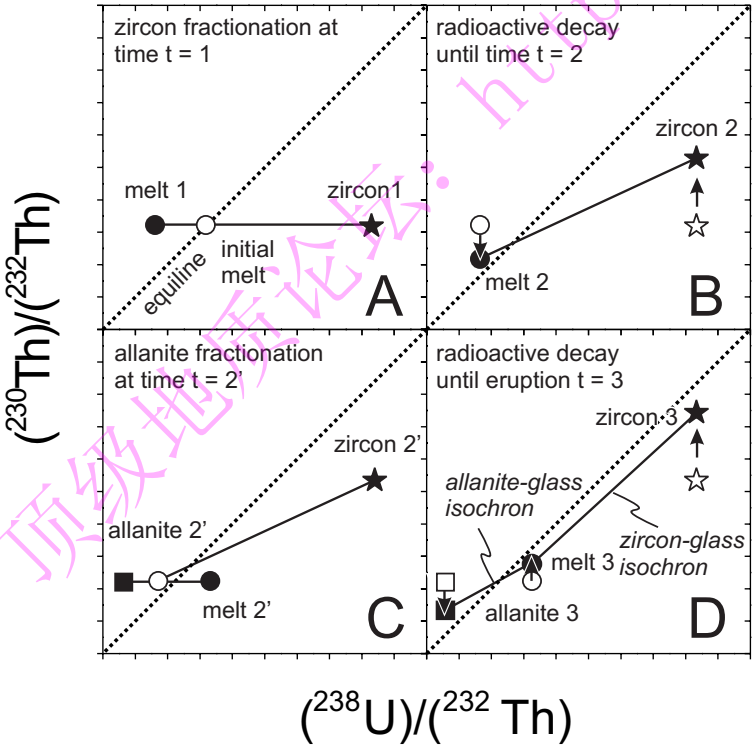


FIG. 5-15. Schematic (^{230}Th)/(^{238}U) evolution for two-stage fractionation involving: (1) melt (circle) and accessory zircon (star), followed by (2) melt–allanite (rectangle) fractionation. **A**, melt in U-series equilibrium crystallizes zircon at t = 1, resulting in a decrease of melt U/Th and disequilibrium in zircon and melt; **B,** subsequent aging until t = 2 moves melt and zircon position towards the equiline; **C,** the onset of allanite fractionation at t = 2' increases the U/Th of the melt; **D**, if the sample was analyzed just after the eruption at t = 3, disparate isochron ages would be obtained for allanite–glass and zircon–glass. Only the allanite–glass isochron would record the time of allanite fractionation at t = 2'; the isochron age for zircon–glass would not correspond to the age of zircon crystallization (after Heumann *et al.* 2002).

顶级地质论坛: http://bbs.5oor.com/

SELECTED APPLICATIONS

Time scales of magmatic processes

Large volume silicic systems High spatial resolution dating of single zircon crystals opened a fresh perspective on the longstanding problem of how long magmas reside in the crust prior to eruption. Among volcanoes studied, Long Valley caldera has long been recognized as an outstanding type example of an intracontinental magma system that is capable of erupting large volumes of silicic magma in a single caldera-forming event (eruption age ~760 ka, see references in Reid 2008). Long Valley also encompasses end members in the style of crustal volcanism, ranging from small volume pre-caldera and post-caldera rhyolite domes (many <1 km^3 in volume) to a cataclysmic explosive event that erupted the voluminous (600 km^3) Bishop Tuff. Early studies, which used whole rock and mineral Rb–Sr isochrons and Ar–Ar and Rb–Sr ages from melt inclusion-bearing quartz crystals, inferred long (0.3–1.1 Ma) pre-eruptive magma residence times (*e.g.*, Davies *et al.* 1994, Van den Bogaard & Schirnick 1995, Christensen & Halliday 1996). Reid & Coath (2000) and Simon & Reid (2005) analyzed zircon from Bishop Tuff and demonstrated that on average it formed ~90 ka prior to eruption, with little to no evidence that crystals were carried over from residual magma or plutons pertaining to the pre-caldera episode of rhyolitic volcanism. Short magma residence times of zircon were later corroborated by bulk TIMS analysis of Bishop Tuff zircon by Crowley *et al.* (2007) who determined even younger average crystallization ages, overlapping within uncertainty with the eruption age. The discrepancy between the bulk zircon average ^{238}U–^{206}Pb age (768 ±2 ka, MSWD = 4.4, n = 19, Crowley *et al.* 2007) and a more protracted period of zircon crystallization with an average of ~850 ka, but ages as young as 753 ±22 ka (n = 71, Simon & Reid 2005), underlines that high spatial resolution crystal ages can reveal complexities in zircon crystallization that are averaged out by bulk techniques. This conclusion is supported by differences in bulk ^{238}U–^{230}Th zircon and average SIMS ^{238}U–^{230}Th zircon ages from Taupo (New Zealand) presented by Charlier *et al.* (2005).

For small volume post-caldera rhyolite NW of Long Valley, Reid *et al.* (1997) documented significant (100s of ka) pre-eruptive zircon crystallization ages. One of these dome lavas, Deer Mountain (Ar–Ar eruption age 101 ±8 ka), yielded zircon model ages that range from as young as ~120 ka with a dominant peak at ~230 ka (Fig. 5-13). Heumann *et al.* (2002) presented bulk TIMS data for whole rocks, glass, sanidine, biotite, amphibole, and zircon. While they found that their zircon–whole rock or zircon–glass isochron age was indistinguishable from the SIMS results by Reid *et al.* (1997), they also noticed that major minerals and glass data did not fall on an isochron. Their interpretation was that the melt composition had been changed due to allanite fractionation (see above, Fig. 5-15), although allanite has not been directly dated, and was only inferred as inclusions in major mineral separates (Heumann *et al.* 2002). Regardless of the possibility of some bias in zircon model ages, SIMS analyses unequivocally reveal protracted zircon crystallization in Deer Mountain rhyolite that otherwise would have gone undetected by bulk analysis techniques.

Basalt-dominated systems To a first order, zircon is an indicator mineral for differentiated melts (Watson & Harrison 1983). Zircon U-series ages thus provide important constraints on the time-scales of magma differentiation. Several case studies have now harnessed the advantages of *in situ* SIMS to avoid natural or laboratory contaminants for rocks that are intrinsically zircon-poor, and to obtain ages from limited amounts of rock sample such as xenoliths that would potentially yield too few crystals for bulk U-series analysis.

In a study of plutonic xenoliths from Hawaiian volcanoes, Vazquez *et al.* (2007) determined ^{238}U–^{230}Th and ^{238}U–^{206}Pb zircon ages that revealed episodes of differentiated magmatism for the eruptive stratigraphy lack any record. Mafic to intermediate zircon-bearing xenoliths have been investigated from Mount Veniaminof (Aleutian Arc), a volcano surficially dominated by eruption of basalt and basaltic andesite (Bacon *et al.* 2007). Zircon in miarolitic cavities in diorite xenoliths from Mount Veniaminof are as young as ~5±10 ka and suggest coeval presence of evolved melts capable of explosive eruptions at shallow level and periodic effusive or weakly explosive leakage of fresh basaltic magma recharged from underneath (Bacon *et al.* 2007). Zircon magma chronology has also been applied to mafic monogenetic volcanoes such as the 12.9 ka Laacher See (East Eifel volcanic field/Germany, Schmitt 2006). The ~5 km^3 Laacher See eruption tapped a stratified magma body that ranged in composition from early erupted phonolite to late erupted basanite. U-series bulk analysis of glass and mineral separates from Laacher See pumice and xenoliths yielded glass and mineral

isochrons between ~13 ka (eruption age) and ~30 ka (Bourdon *et al.* 1994). Schmitt (2006) studied zircon from the earliest erupted and most differentiated Laacher See phonolite and documented that (1) most zircon crystals are xenocrystic contaminants in secular equilibrium with Paleozoic to Precambrian U–Pb ages, and (2) a minor population of young (~17 ka) zircon crystals was derived from an isotopically different syenitic magma and scavenged by the phonolite during or shortly before the eruption. These results were interpreted to support rapid (<10 ka) formation of the Laacher See magma chamber, and also to revise protracted basanite–phonolite differentiation time-scales of ~100 ka (Bourdon *et al.* 1994) that were based on closed system ^{230}Th-decay despite oxygen isotopic evidence for crustal contamination (Schmitt 2006). New evidence from carbonatitic ejecta (Fig. 5-5) shows that carbonatitic intrusions solidified beneath Laacher See by up to ~20 ka prior to eruption, with no evidence for these shallow magmatic events in the eruptive record of the East Eifel volcanic field.

Active geothermal reservoirs U-series dating plays an important role of constraining ages of volcanic or plutonic rocks in magma-driven geothermal reservoirs. Zircon in particular has outstanding chemical and physical stability so that it can yield reliable crystallization ages under conditions of elevated temperatures and intense fluid flow prevailing in active geothermal systems. One of the early case studies was on the Geysers geothermal field (California). Over 400 U–Pb zircon ages from a composite granitic pluton underlying the geothermal reservoir revealed piece-meal emplacement of a sizeable (~300 km^3) shallow pluton that intruded between 1.6-1.2 Ma, in part approximately 1 Ma older as previously thought based on Ar–Ar feldspar dating (Schmitt *et al.* 2003b).

Geothermal wells in the Salton Sea (Imperial County, California) geothermal field penetrated highly altered rhyolitic volcanic rocks at 2–3 km depth and ambient temperatures between ~200–300ºC that yielded U–Pb zircon ages of ~400 ka (Schmitt & Hulen 2008). These ages constrain subsidence and sedimentation in the central part of the geothermal field at average rates of 4 mm/a (Schmitt & Hulen 2008). Oxygen isotopic analysis of dated zircon by SIMS revealed that Salton Sea rhyolite and granophyre intrusive rocks have low δ^{18}O values between ~3–5‰, suggesting an origin by re-melting of hydrothermally altered basalt (Schmitt & Vazquez 2006, Schmitt & Hulen 2008).

Wilson *et al.* (2008) used zircon U–Pb age spectra to correlate eruptive units in the subsurface of the Mangakino geothermal field (New Zealand). Comparison between zircon age spectra from surface volcanic rocks with those of hydrothermally altered volcanic rocks from drillholes is a novel tool to determine the host rocks stratigraphy of the geothermal reservoir (Wilson *et al.* 2008).

Tephrochronology Accessory mineral U-series chronology has been successfully applied in Quaternary tephrochronology. For the ~600 ka Rockland tephra, an important stratigraphic marker in western North America, Lanphere *et al.* (2004) determined near-concordant Ar–Ar plagioclase and U–Pb zircon ion microprobe ages. In many other cases, however, zircon ^{238}U–^{206}Pb or ^{238}U–^{230}Th crystallization ages significantly predate the eruption ages, on average by ~90 ka (Simon *et al.* 2008).

(U–Th)/He zircon dating is a potentially useful chronometer that records the time of eruptive quenching, in particular for volcanic rocks that lack datable high-K phases such as sanidine, or where excess ^{40}Ar causes problems (Farley *et al.* 2002). The accuracy of (U–Th)/He ages for young zircon critically depends on the corrections for initial disequilibrium: in the case of zircon, deficits in ^{230}Th can lead to significant underestimation of the eruption age if the crystals were in disequilibrium at the time of eruption (Farley *et al.* 2002). Under-estimation of the eruption age occurs because six out of eight ^{4}He nuclei in the ^{238}U decay chain are produced subsequent to the decay of ^{230}Th. By measuring the crystallization age, the disequilibrium at the time of eruption can be directly constrained in order to correct (U–Th)/He ages. The first study to apply combined ^{238}U–^{230}Th and (U–Th)/He zircon tephrochronology was on La Vírgen tephra, a ~1 km^3 deposit which erupted from Tres Vírgenes volcano (Baja California, Schmitt *et al.* 2006). Combined ^{238}U–^{230}Th and (U–Th)/He zircon dating results average 36 ±3 ka. This is significantly older than published ^{14}C charcoal ages from a distal tephra deposit of ~6.5 ka. The (U–Th)/He zircon age is, however, stratigraphically consistent with a cosmogenic ^{3}He age for a basalt lava flow that overlies La Vírgen tephra. It is suspected that previously dated charcoal is associated with a reworked deposit and thus not reliable for determining the eruption age of La Vírgen tephra (Schmitt *et al.* 2006).

Environmental studies

Climate change Hydrogenic minerals that precipitate in rock fractures or cavities from percolating fluids have the potential of recording the duration, source, temperature, and amount of past fluid flow regimes. Pluvial climate conditions result in increased soil moisture, infiltration, and percolation flux that is recorded by pedogenic minerals. SIMS U-series and U–Pb dating places constraints on growth rates of opal in Miocene tuff deposits in western USA at the Yucca Mountain (Nevada) prospective nuclear repository site (Paces *et al.* 2004, Nemchin *et al.* 2006). Opal from Yucca Mountain is finely laminated at the micrometre scale, and earlier bulk dissolution TIMS analyses of individual, 0.1–1 mm thick opal hemispheres were limited by the inability to distinguish between a continuous deposition model, or the alternative scenario of episodic precipitation followed by prolonged intervals of non-deposition (Neymark *et al.* 2000, Paces *et al.* 2004). U-series dating by SIMS yielded a microstratigraphically consistent age progression that implied comparatively slow average deposition rates of ~0.68 ±0.22 μm/ka over the past ~1 Ma (Paces *et al.* 2004). These results were further corroborated by sequential microdigestion of opal followed by TIMS U-series dating and results from ^{238}U–^{234}U–^{206}Pb SIMS analysis. ^{238}U–^{234}U–^{206}Pb SIMS geochronology extended the datable range for Yucca Mountain opal beyond 1 Ma, while at the same time taking advantage of the higher precision of ^{238}U–^{234}U–^{206}Pb dating compared to ^{238}U–^{230}Th dating of near-equilibrium opal (Nemchin *et al.* 2006). The ^{238}U–^{206}Pb ages, once corrected for the effects of (^{234}U)/(^{238}U) disequilibrium, yielded growth rates of ~0.99 ±0.08 μm/ka that agree with the previously determined growth rates from SIMS U-series dating of the same opal hemisphere. In contrast, Late Miocene–Pliocene opal coatings show more rapid growth rates (1 and 5 μm/ka), based on TIMS ^{207}Pb/^{235}U ages (Paces *et al.* 2004). These results indicate that opal precipitation was quasi-continuous at least during the Late Pleistocene, and that growth rates may have varied throughout Late Miocene to recent times, potentially as a result of climate-driven changes in groundwater percolation.

Landscape evolution The environmental and structural history of land surfaces commonly produces a record in authigenic minerals that formed under near-surface conditions in soils or as pebble coatings in alluvium (Maher *et al.* 2007). In arid and semiarid environments, growth of these authigenic minerals can be slow and episodic, and their composition strongly depends on water flux and compositions (Maher *et al.* 2007). Moreover, reworking may lead to multiple growth episodes interrupted by protracted periods of non-growth during erosion and transport (Maher *et al.* 2007). Fine scale (10–100 μm) layering commonly exists in authigenic minerals, and despite advances in microsampling techniques (*e.g.*, by microdrilling or microdigestion methods) for TIMS analysis, the possibility of averaging over growth layers widely disparate in age remains a serious concern during bulk sampling. In contrast, SIMS *in situ* analysis is capable of targeting individual layers at lateral spatial resolution of ~20–30 μm (Fig. 5-14, Maher *et al.* 2007). By using shortwave UV fluorescence, Maher *et al.* (2007) were also able to target U-rich layers of opaline silica intergrown with bands of U-poor calcite. Maher *et al.* (2007) applied this technique to well characterized silica-rich pebble coatings from pedogenic carbonate horizons and opaline silica from spring deposits from western USA, and determined SIMS ages in concordance with previous TIMS results, albeit much faster and requiring less laborious sample preparation. Another advantage of SIMS, besides its *in situ* analysis capability and comparatively rapid analysis, is that the near non-destructive nature of SIMS allows samples to be preserved for further geochronological, geochemical or mineralogical characterization (Maher *et al.* 2007).

FUTURE DEVELOPMENTS

The strength of SIMS in Quaternary geochronology lies in its capability of performing isotopic analysis at high spatial selectivity, coupled with high sensitivity and minimal sample consumption. U-series ultra-trace element analysis at ppb to ppt levels is hampered by detection limitations that result from the small number of U-series atoms present in the analyte volume. The ability to sample ~ng amounts of material in SIMS spot analyses compared to μg–mg amounts consumed by other techniques (TIMS, ICP MS) has its trade-off in low secondary ion signals and concomitant large counting errors. Moreover, SIMS analysis of U-series isotopes in mineral matrices without prior chemical separation imposes requirements of monitoring inter-elemental fractionation by using suitable standards. RSF calibrations for U–Pb are typically reproducible to within ~1–2%, independent of the SIMS instrumentation used.

It remains unresolved how much of this is due to heterogeneity of the reference materials used to monitor elemental fractionation at the sampling scale of the SIMS crater (Ireland & Williams 2003). For Quaternary applications, however, in-run errors resulting from low count rates for short lived U-series isotopes or radiogenic Pb generally outweigh uncertainties resulting from RSF calibrations.

Multi-collection increases the duty cycle for secondary ion detection because it reduces the waiting time resulting from magnetic field switching and stabilization, and enhances precision due to minimizing the effects of secondary beam variations during analysis. Initial experiments using the UCLA CAMECA ims 1270 in dual EM collection mode yielded ^{238}U–^{230}Th data for equilibrium standards that are equivalent in accuracy and precision to the results from single EM collection, while reducing the analysis duration by ~30%. Increasing sputter rates while maintaining high lateral spatial resolution could also enhance SIMS analytical precision for U-series ages, for example by employing bright ion sources. Alternative primary beam species such as O_2^+ have been proposed which produce higher sputtering yields, with the caveat that these analyses require careful charge compensation via electron bombardment (Hervig *et al.* 2006).

Harnessing the unrivalled sub-µm spatial resolution of SIMS in depth profiling analysis for U-series and U–Pb geochronology is another avenue of great promise (*e.g.*, Fig. 5-6). It has been empirically determined that positive secondary ion intensities remain nearly constant for depths smaller than the lateral diameter of the crater (Hervig *et al.* 2006). Fortunately, U–Th fractionation is negligible even for sputter crater depths approaching crater diameters, both for opal and zircon. U–Pb fractionation, by contrast, changes significantly with depth and requires an appropriate correction scheme, or frequent regrinding and repolishing of the sample to re-level the bottom of the crater with the surface, if a continuous depth profile is desired.

Sample requirements for SIMS are minimal which results in negligible losses of material so that other types of analysis can be performed on the same crystals or nearby domains in the same materials. This includes analysis of trace elements or stable isotopes for further sample characterization. For Quaternary magmachronology, the recent calibration of the Ti-in-zircon thermometer (Ferry & Watson 2007) allows a combination of age and temperature information to reconstruct the history of magmas. On the other hand, trace element partitioning in accessory minerals remains poorly understood, in particular for the critical elements U and Th. Experimental calibration of trace element partitioning over the entire pressure, temperature, and compositional (including oxygen fugacity) parameter space applicable to magmas is thus required in order to fully utilize the potential of combined geochronology and trace element analysis of accessory minerals. This also holds for the calibration of saturation and diffusion properties of many accessory minerals other than zircon.

A recent study by Maher *et al.* (2007) has showcased the potential for SIMS to date authigenic minerals reliably from a variety of environments. While it remains to be fully explored how widespread U-rich authigenic minerals are outside the arid and semi-arid landscapes of western USA, the value *in situ* SIMS geochronology for environmental studies is indubitable. As is the case for magmachronologic applications, there is further potential of mating SIMS geochronology with high spatial resolution analysis of other geochemical tracers such as stable isotopes and trace elements.

ACKNOWLEDGEMENTS

AKS thanks the extended UCLA ion microprobe group for support and many fruitful discussions over the past years, including Kari Cooper, Marty Grove, T. Mark Harrison, George Jarzebinski, Kevin D. McKeegan, Oscar Lovera, Mary Reid, Justin Simon, Jorge Vazquez, and Haibo Zou. Insightful comments by Jorge Vazquez, Bill Davis, and Mostafa Fayek considerably improved this review. The ion microprobe facility at UCLA is partly supported by a grant from the Instrumentation and Facilities Program, Division of Earth Sciences, National Science Foundation.

REFERENCES

AMELIN, Y. & BACK, M. (2006): Opal as a U/Pb geochronometer; search for a standard. *Chem. Geol.* **232**, 67-86.

ANCZKIEWICZ, R., OBERLI, F., BURG, J.-P., VILLA, I.M., GUENTHER, D. & MEIER, M. (2001): Timing of normal faulting along the Indus Suture in Pakistan Himalaya and a case of major 231Pa/235U initial disequilibrium in zircon. *Earth & Planet. Sci. Lett.* **191**, 101-114.

ANOVITZ, L.M., COLE, D.R. & FAYEK, M. (2008): Mechanisms of rhyolitic glass hydration below the glass transition. *Am. Mineral.* **93**, 1166-1178.

BACON, C.R., SISSON, T.W. & MAZDAB, F.K. (2007): Young cumulate complex beneath Veniaminof Caldera, Aleutian Arc, dated by zircon in erupted plutonic blocks. *Geology* **35**, 491-494.

BALDWIN, S.L. & IRELAND, T.R. (1995): A tale of two eras; Pliocene–Pleistocene unroofing of Cenozoic and late Archean zircons from active metamorphic core complexes, Solomon Sea, Papua New Guinea. *Geology* **23**, 1023-1026.

BATEMAN, H. (1910): The solution of a system of differential equations occurring in the theory of radio-active transformations. *Proc. Cambridge Philosoph. Soc.* **15**, 423-427.

BERNAL, J.P., EGGINS, S.M. & MCCULLOCH, M.T. (2005): Accurate *in situ* U-238–U-234–Th-232–Th-230 analysis of silicate glasses and iron oxides by laser–ablation MC–ICP–MS. *J. Analyt. Atomic Spectrom.* **20**, 1240-1249.

BINDEMAN, I.N., SCHMITT, A.K. & VALLEY, J.W. (2006): U/Pb zircon geochronology of silicic tuffs from the Timber Mountain/Oasis Valley caldera complex, Nevada; rapid generation of large volume magmas by shallow-level remelting. *Contrib. Mineral. Petrol.* **152**, 649-665.

BISCHOFF, J.L., WOODEN, J., MURPHY, F. & WILLIAMS, R.W. (2005): U/Th dating by SHRIMP RG ion-microprobe mass spectrometry using single ion-exchange beads. *Geochim. Cosmochim. Acta* **69**, 1841-1846.

BLUNDY, J. & WOOD, B. (2003): Mineral–melt partitioning of uranium, thorium and their daughters. *In* Uranium-series geochemistry, Reviews in Mineralogy and Geochemistry 52 (B. Bourdon, G.M. Henderson, C.C. Lundstrom, and S.P. Turner, eds.). The Mineralogical Society of America, Washington (59-123).

BOURDON, B., ZINDLER, A. & WOERNER, G. (1994): Evolution of the Laacher See magma chamber; evidence from SIMS and TIMS measurements of U–Th disequilibria in minerals and glasses. *Earth Planet. Sci. Lett.* **126**, 75-90.

BOURDON, B., TURNER, S.P., HENDERSON, G.M. & LUNDSTROM, C.C. (2003): Introduction to U-series geochemistry. *In* Uranium-series geochemistry, Reviews in Mineralogy and Geochemistry 52 (B. Bourdon, G.M. Henderson, C.C. Lundstrom, and S.P. Turner, eds.). The Mineralogical Society of America, Washington (1-21).

BROWN, K.L., CARTER, C.A., FOHEY, N.K., WOODEN, J.L., YI, K. & BARTH, A.P. (2004): A study of the origin of rhyolite at mid-ocean ridges; geochronology and petrology of trachydacite and rhyolite from Salton Sea, California, and Torfajokull, Iceland, *Abstr. Programs – Geol. Soc. Am.* **36**, 79.

BROWN, S.J.A. & FLETCHER, I.R. (1999): SHRIMP U–Pb dating of the preeruption growth history of zircons from the 340 ka Whakamaru Ignimbrite, New Zealand; evidence for >250 k.y. magma residence times. *Geology* **27**, 1035-1038.

CATLOS, E.J., SORENSEN, S.S. & HARRISON, T.M. (2000): Th–Pb ion-microprobe dating of allanite. *Am. Mineral.* **85**, 633-648.

CHARLIER, B.L.A., WILSON, C.J.N., LOWENSTERN, J.B., BLAKE, S., VAN CALSTEREN, P.W. & DAVIDSON, J.P. (2005): Magma generation at a large, hyperactive silicic volcano (Taupo, New Zealand) revealed by U–Th and U–Pb systematics in zircons. *J. Petrol.* **46**, 3-32.

CHEN, Y., SMITH, P.E., EVENSEN, N.M., YORK, D. & LAJOIE, K.R. (1996): The edge of time; dating young volcanic ash layers with the ^{40}Ar-^{39}Ar laser probe. *Science* **274**, 1176-1178.

CHERNIAK, D.J. & WATSON, E.B. (2001): Pb diffusion in zircon. *Chem. Geol.* **172**, 5-24.

CHERNIAK, D.J. & WATSON, E.B. (2003): Diffusion in zircon. *In* Zircon, Reviews in Mineralogy and Geochemistry 53 (J.M. Hanchar, and P.W.O. Hoskin, eds.). The Mineralogical Society of America, Washington (113-143).

CHRISTENSEN, J.N. & HALLIDAY, A.N. (1996): Rb–Sr ages and Nd isotopic compositions of melt inclusions from the Bishop Tuff and the generation of silicic magma. *Earth Planet. Sci. Lett.* **144**, 547-561.

COCHERIE, A., FANNING, M.C., JEZEQUELA, P. & ROBERT, M. (2009): LA–MC–ICPMS and SHRIMP U–Pb dating of complex zircons from Quaternary tephras from the French Massif Central: Magma residence time and geochemical implications. *Geochim. Cosmochim. Acta* **73**, 1095-1108.

COMPSTON, W., WILLIAMS, I.S. & MEYER, C.E. (1984): U–Pb geochronology of zircons from lunar breccia 73217 using a sensitive high mass-resolution ion microprobe. *J. Geophys. Res.* **89, Suppl.** (B), 525-534.

http://rules.geoscienceworld.org/

CONDOMINES, M. (1997): Dating Recent volcanic rocks through ^{230}Th–^{238}U disequilibrium in accessory minerals; example of the Puy de Dome (French Massif Central). *Geology* **25**, 375-378.

CONDOMINES, M., GAUTHIER, P.-J. & SIGMARSSON, O. (2003): Timescales of magma chamber processes and dating of young volcanic rocks. *In* Uranium-series geochemistry, Reviews in Mineralogy and Geochemistry 52 (B. Bourdon, G.M. Henderson, C.C. Lundstrom, and S.P. Turner, eds.). The Mineralogical Society of America, Washington (125-174).

COOPER, K.M. & REID, M.R. (2008): Uranium-series Crystal Ages. *In* Minerals, Inclusions and Volcanic Processes, Reviews in Mineralogy and Geochemistry 69 (K.D. Putirka, and F.J. Tepley III, eds.). The Mineralogical Society of America, Washington (479-544).

CROWLEY, J.L., SCHOENE, B. & BOWRING, S.A. (2007): U–Pb dating of zircon in the Bishop Tuff at the millennial scale. *Geology* **35**, 1123-1126.

DALRYMPLE, G.B., GROVE, M., LOVERA, O.M., HARRISON, T.M., HULEN, J.B. & LANPHERE, M.A. (1999): Age and thermal history of the Geysers Plutonic Complex (Felsite Unit), Geysers Geothermal Field, California. *Earth Planet. Sci. Lett.* **173**, 285-298.

DAVIES, G.R., HALLIDAY, A.N., MAHOOD, G.A. & HALL, C.M. (1994): Isotopic constraints on the production rates, crystallisation histories and residence times of pre-caldera silicic magmas, Long Valley, California. *Earth Planet. Sci. Lett.* **125**, 17-37.

DUMITRU, T.A. (2000): Fission-track geochronology. *In* Quaternary Geochronology: Methods and Applications, AGU Reference Shelf 4 (J.S. Noller, J.M. Sowers, W.R. Lewis, eds.). American Geophysical Union, Washington (131-155).

EDWARDS, R.L., GALLUP, C.D. & CHENG, H. (2003): Uranium-series dating of marine and lacustrine carbonates. *In* Uranium-series geochemistry, Reviews in Mineralogy and Geochemistry 52 (B. Bourdon, G.M. Henderson, C.C. Lundstrom, and S.P. Turner, eds.). The Mineralogical Society of America, Washington (363-405).

EGGINS, S.M., GRUEN, R., MCCULLOCH, M.T., PIKE, A.W.G., CHAPPELL, J., KINSLEY, L., MORTIMER, G., SHELLEY, M., MURRAY-WALLACE, C.V., SPOETL, C. & TAYLOR, L. (2005): *In situ* U-series dating by laser-ablation multi-collector ICPMS; new prospects for Quaternary geochronology. *Quat. Sci. Rev.* **24**, 2523-2538.

FABBRIZIO, A., SCHMIDT, M.W., GUNTHER, D. & EIKENBERG, J. (2008): Experimental determination of radium partitioning between leucite and phonolite melt and ^{226}Ra-disequilibrium crystallization ages of leucite. *Chem. Geol.* **255**, 377-387.

FARLEY, K.A., KOHN, B.P. & PILLANS, B. (2002): The effects of secular disequilibrium on (U–Th)/He systematics and dating of Quaternary volcanic zircon and apatite. *Earth Planet. Sci. Lett.* **201**, 117-125.

FERRY, J.M. & WATSON, E.B. (2007): New thermodynamic models and revised calibrations for the Ti-in-zircon and Zr-in-rutile thermometers. *Contrib. Mineral. Petrol.* **154**, 429-437.

GETTY, S.R. & DEPAOLO, D.J. (1995): Quaternary Geochronology Using the U-Th-Pb Method. *Geochim. Cosmochim. Acta* **59**, 3267-3272.

GIERÉ, R. & SORENSEN, S.S. (2004): Allanite and Other REE-Rich Epidote-Group Minerals. *In* Epidotes, Reviews in Mineralogy and Geochemistry 56 (A. Liebscher and G. Franz, eds.).The Mineralogical Society of America, Washington (431-493).

GOLDSTEIN, S.J. & STIRLING, C.H. (2003): Techniques for measuring uranium-series nuclides; 1992-2002. *In* Uranium-series geochemistry, Reviews in Mineralogy and Geochemistry 52 (B. Bourdon, G.M. Henderson, C.C. Lundstrom, and S.P. Turner, eds.). The Mineralogical Society of America, Washington (23-57).

GRUEN, R. (2006): Editorial. *Quaternary Geochronology* **1**, 1.

HERVIG, R.L., MAZDAB, F.K., WILLIAMS, P., GUAN, Y.B., HUSS, G.R. & LESHIN, L.A. (2006): Useful ion yields for CAMECA IMS 3f and 6f SIMS: Limits on quantitative analysis. *Chem. Geol.* **227**, 83-99.

HEUMANN, A (1999) *Timescales of Processes within Silicic Magma Chambers*. PhD Thesis, Vrije Universiteit, Amsterdam (1-200).

HEUMANN, A (2004) Timescales of evolved magma generation at Blackfoot Lava Field, SE Idaho, USA. IAVCEI General Assembly Pucón – Chile, *Conference Abstracts*.

HEUMANN, A., DAVIES, G.R. & ELLIOTT, T. (2002): Crystallization history of rhyolites at Long Valley, California, inferred from combined U-series and Rb-Sr isotope systematics. *Geochim. Cosmochim. Acta* **66**, 1821-1837.

HOSKIN, P.W.O. & SCHALTEGGER, U. (2003): The composition of zircon and igneous and metamorphic petrogenesis. *In* Zircon, Reviews in Mineralogy & Geochemistry 53 (J.M. Hanchar, and P.W.O. Hoskin, eds.). The Mineralogical Society of America, Washington (27-62).

IRELAND, T.R. & WILLIAMS, I.S. (2003): Considerations in zircon geochronology by SIMS. *In* Zircon, Reviews in Mineralogy & Geochemistry 53 (J.M. Hanchar, and P.W.O. Hoskin, eds.). The Mineralogical Society of America, Washington (215-241).

IVANOVICH, M. & HARMON, R. S. (eds.) (1992): *Uranium-series disequilibrium: Applications to Earth, Marine, and Environmental Sciences.* Clarendon Press, Oxford (1-910).

LANPHERE, M.A., CHAMPION, D.E., CLYNNE, M.A., LOWENSTERN, J.B., SARNA-WOJCICKI, A.M. & WOODEN, J.L. (2004): Age of the Rockland Tephra, Western USA. *Quat. Res.* **62**, 94-104.

LAYNE, G.D. & SIMS, K.W. (2000): Secondary ion mass spectrometry for the measurement of Th-232/Th-230 in volcanic rocks. *Internat. J. Mass Spectrom.* **203**, 187-198.

LOWENSTERN, J.B., PERSING, H.M., WOODEN, J.L., LANPHERE, M.A., DONNELLY-NOLAN, J.M. & GROVE, T.L. (2000): U–Th dating of single zircons from young granitoid xenoliths; new tools for understanding volcanic processes. *Earth Planet. Sci. Lett.* **183**, 291-302.

LUDWIG, K.R. (2003): Mathematical-statistical treatment of data and errors for ^{230}Th/U geochronology. *In* Uranium-series geochemistry, Reviews in Mineralogy and Geochemistry 52 (B. Bourdon, G.M. Henderson, C.C. Lundstrom, and S.P. Turner, eds.). The Mineralogical Society of America, Washington (631-656).

LUMPKIN, G.R. & EWING, R.C. (1995): Geochemical alteration of pyrochlore group minerals; pyrochlore subgroup. *Am. Mineral.* **80**, 732-743.

MACDONALD, R. & BELKIN, H.E. (2002): Compositional variation in minerals of the chevkinite group. *Mineral. Mag.* **66**, 1075-1098.

MAHER, K., WOODEN, J.L., PACES, J.B. & MILLER, D.M. (2007): ^{230}Th–U dating of surficial deposits using the ion microprobe (SHRIMP–RG): A microstratigraphic perspective. *Quat. Internat.* **166**, 15-28.

NEMCHIN, A.A., NEYMARK, L.A. & SIMONS, S.L. (2006): U/Pb SHRIMP dating of uraniferous opals. *Chem. Geol.* **227**, 113-132.

NEYMARK, L.A., AMELIN, Y.V. & PACES, J.B. (2000): ^{206}Pb–^{230}Th–^{234}U–^{234}U and ^{207}Pb–^{235}U geochronology of Quaternary opal, Yucca Mountain, Nevada. *Geochim. Cosmochim. Acta* **64**, 2913-2928.

NOLLER, J.S., SOWERS, J.M., COLMAN, S.M. & PIERCE, K.L. (2000): Introduction to Quaternary geochronology. *In* Quaternary Geochronology: Methods and Applications, AGU Reference Shelf 4 (J.S. Noller, J.M. Sowers, W.R. Lewis, eds.). American Geophysical Union, Washington (1-10).

PACES, J.B. & MILLER, J.D., JR. (1993): Precise U–Pb ages of Duluth Complex and related mafic intrusions, northeastern Minnesota; geochronological insights to physical, petrogenetic, paleomagnetic, and tectonomagnetic processes associated with the 1.1 Ga Midcontinent Rift System. *J. Geophys. Res., B, Solid Earth and Planets* **98**, 13,997-14,013.

PACES, J.B., NEYMARK, L.A., WOODEN, J.L. & PERSING, H.M. (2004): Improved spatial resolution for U-series dating of opal at Yucca Mountain, Nevada, USA, using ion-microprobe and microdigestion methods. *Geochim. Cosmochim. Acta* **68**, 1591-1606.

POTTER, E.K., STIRLING, C.H., WIECHERT, U.H., HALLIDAY, A.N. & SPOTL, C. (2005): Uranium-series dating of corals *in situ* using laser-ablation MC–ICPMS. *Internat. J. Mass Spectrom.* **240**, 27-35.

REID, M.R. (2008): How long does it take to supersize an eruption? *Elements* **4**, 23-28.

REID, M.R. & COATH, C.D. (2000): *In situ* U–Pb ages of zircons from the Bishop Tuff; no evidence for long crystal residence times. *Geology* **28**, 443-446.

REID, M.R., COATH, C.D., HARRISON, T.M. & MCKEEGAN, K.D. (1997): Prolonged residence times for the youngest rhyolites associated with Long Valley Caldera; ^{230}Th–^{238}U ion microprobe dating of young zircons. *Earth Planet. Sci. Lett.* **150**, 27-39.

http://bbs.3s001.com/

REINERS, P.W., SPELL, T.L., NICOLESCU, S. & ZANETTI, K.A. (2004): Zircon (U–Th)/He thermochronometry; He diffusion and comparisons with $^{40}Ar/^{39}Ar$ dating. *Geochim. Cosmochim. Acta* **68**, 1857-1887.

SAMBRIDGE, M.S. & COMPSTON, W. (1994): Mixture modeling of multi-component data sets with application to ion-probe zircon ages. *Earth Planet. Sci. Lett.* **128**, 373-390.

SANO, Y., TSUTSUMI, Y., TERADA, K. & KANEOKA, I. (2002): Ion microprobe U–Pb dating of Quaternary zircon; implication for magma cooling and residence time. *J. Volcan. Geotherm. Res.* **117**, 285-296.

SCHAERER, U. (1984): The effect of initial ^{230}Th disequilibrium on young U–Pb ages; the Makalu case, Himalaya. *Earth Planet. Sci. Lett.* **67**, 191-204.

SCHMITT, A.K. (2006): Laacher See revisited: high spatial resolution zircon dating indicates rapid formation of a zoned magma chamber. *Geology* **34**, 597-600.

SCHMITT, A.K. (2007): Ion microprobe analysis of $^{231}Pa/^{235}U$ and an appraisal of protactinium partitioning in igneous zircon. *Am. Mineral.* **92**, 691-694.

SCHMITT, A.K. & HULEN, J.B. (2008): Buried rhyolites within the active, high-temperature Salton Sea geothermal system. *J. Volcan. Geotherm. Res.* **178**, 708-718.

SCHMITT, A.K. & VAZQUEZ, J.A. (2006): Alteration and remelting of nascent oceanic crust during continental rupture; evidence from zircon geochemistry of rhyolites and xenoliths from the Salton Trough, California. *Earth Planet. Sci. Lett.* **252**, 260-274.

SCHMITT, A.K., GROVE, M., HARRISON, T.M., LOVERA, O., HULEN, J. & WALTERS, M. (2003a): The Geysers - Cobb Mountain Magma System, California (Part 1): U–Pb zircon ages of volcanic rocks, conditions of zircon crystallization and magma residence times. *Geochim. Cosmochim. Acta* **67**, 3423-3442.

SCHMITT, A.K., GROVE, M., HARRISON, T.M., LOVERA, O., HULEN, J. & WALTERS, M. (2003b): The Geysers-Cobb Mountain Magma System, California (Part 2): Timescales of pluton emplacement and implications for its thermal history. *Geochim. Cosmochim. Acta* **67**, 3443-3458.

SCHMITT, A.K., STOCKLI, D.F. & HAUSBACK, B.P. (2006): Eruption and magma crystallization ages of Las Tres Virgenes (Baja California) constrained by combined $^{230}Th/^{238}U$ and (U–Th)/He dating of zircon. *J. Volcan. Geotherm. Res.* **158**, 281-295.

SCHMITZ, M.D. & BOWRING, S.A. (2001): U–Pb zircon and titanite systematics of the Fish Canyon Tuff; an assessment of high-precision U–Pb geochronology and its application to young volcanic rocks. *Geochim. Cosmochim. Acta* **65**, 2571-2587.

SIMON, J.I. & REID, M.R. (2005): The pace of rhyolite differentiation and storage in an "archetypical" silicic magma system, Long Valley, California. *Earth Planet. Sci. Lett.* **235**, 123-140.

SIMON, J.I., RENNE, P.R. & MUNDIL, R. (2008): Implications of pre-eruptive magmatic histories of zircons for U–Pb geochronology of silicic extrusions. *Earth Planet. Sci. Lett.* **266**, 182-194.

STERN, R.A. & AMELIN, Y. (2003): Assessment of errors in SIMS zircon U–Pb geochronology using a natural zircon standard and NIST SRM 610 glass. *Chem. Geol.* **197**, 111-142.

STIRLING, C.H., LEE, D.C., CHRISTENSEN, J.N. & HALLIDAY, A.N. (2000): High-precision *in situ* $^{238}U–^{234}U–^{230}Th$ isotopic analysis using laser ablation multiple-collector ICPMS. *Geochim. Cosmochim. Acta* **64**, 3737-3750.

TERA, F. & WASSERBURG, G.J. (1972): U–Th–Pb systematics in lunar highland samples from the Luna 20 and Apollo 16 missions. *Earth Planet. Sci. Lett.* **17**, 36-51.

VAN DEN BOGAARD, P. & SCHIRNICK, C. (1995): $^{40}Ar/^{39}Ar$ laser probe ages of Bishop Tuff quartz phenocrysts substantiate long-lived silicic magma chamber at Long Valley, United States. *Geology* **23**, 759-762.

VAZQUEZ, J.A. & REID, M.R. (2004): Probing the Accumulation History of the Voluminous Toba Magma. *Science* **305**, 991-994.

VAZQUEZ, J.A., SHAMBERGER, P.J. & HAMMER, J.E. (2007): Plutonic xenoliths reveal the timing of magma evolution at Hualalai and Mauna Kea, Hawaii. *Geology* **35**, 695-698.

WATSON, E.B. & HARRISON, T.M. (1983): Zircon saturation revisited; temperature and composition effects in a variety of crustal magma types. *Earth Planet. Sci. Lett.* **64**, 295-304.

WIEDENBECK, M., ALLE, P., CORFU, F., GRIFFIN, W.L., MEIER, M., OBERLI, F., VONQUADT, A., RODDICK, J.C. & SPEIGEL, W. (1995): 3 Natural Zircon Standards for U–Th–Pb, Lu–Hf, Trace-Element and Ree Analyses. *Geostand. Newslett.* **19**, 1-23.

WILLIAMS, I.S. & HERGT, J.M. (2000): U–Pb dating of Tasmanian dolerites; a cautionary tale of SHRIMP analysis of high-U zircon. *In* Beyond 2000: New Frontiers in Isotope Geoscience (J.D. Woodhead, J.M. Hergt, and W.P. Noble Lorne, eds.). University of Melbourne, Melbourne (185-188).

WILSON, C.J.N., CHARLIER, B.L.A., FAGAN, C.J., SPINKS, K.D., GRAVLEY, D.M., SIMMONS, S.F. & BROWNE, P.R.L. (2008): U–Pb dating of zircon in hydrothermally altered rocks as a correlation tool: Application to the Mangakino geothermal field, New Zealand. *J. Volc. Geotherm. Res.* **176**, 191-198.

顶级地质论坛：http://bbs.3s001.com/

顶级地质论坛：http://bbs.3s001.com/

CHAPTER 6: IMPROVING DEPTH PROFILE MEASUREMENTS OF NATURAL MATERIALS: LESSONS LEARNED FROM ELECTRONIC MATERIALS DEPTH-PROFILING

Jerry L. Hunter, Jr.
Nanoscale Characterization and Fabrication Laboratory
Institute for Critical Science and Applied Technology
Virginia Polytechnic Institute and State University
Blacksburg, VA 24061 U.S.A.
hunterje@vt.edu

INTRODUCTION

Given that the secondary ion mass spectrometry (SIMS) signal is derived from the removal of material from a sample surface, it is always a depth-profiling technique. SIMS is commonly used in the geosciences to measure trace element concentrations (MacRae & Russell 1987, Reed 1984), with the most typical being the measurement of the rare earth elements (REEs) and zircon geochronology (Ireland & Williams 2003). Additionally, since SIMS is a mass spectrometry technique, it is commonly used to acquire high precision stable isotopic ratios (King *et al.* 2008, Zhang *et al.* 1996), which are applicable to geologists in paleoenvironmental reconstruction and understanding potential microbial roles in mineral deposition (Papineau & Mojzsis 2006, Kohn *et al.* 1998). All of these applications assume an in-depth homogeneity of the specimens being measured.

SIMS depth-profiling has been applied to geologic materials such as volcanic phenocrysts (Genareau *et al*. 2007), rare earth diffusion kinetics in garnet (Tirone *et al*. 2004), and diffusion kinetics of samarium and neodymium in garnet (Ganguly *et al*. 1998) among others. A developing area for the application of SIMS depth-profiling is for archaeological and cultural heritage materials, such as depth-profiling of the deterioration of glass objects (Spoto 2000, Dowsett & Adriaens 2004) and the corrosion of metallic objects (Palitsin *et al*. 2006). These materials range from metallic to oxide and the depth ranges of interest commonly vary from 10 nm to tens of μm. Depth-profiling of these materials will result in many of the same profile errors observed for the synthetic materials used by the electronic materials community.

Since SIMS gives in-depth distributions with ppm to ppb detection limits it is the primary technique used by the electronic materials community for depth-profiling of intentionally introduced dopants. In response to the needs of the electronic materials industry, significant improvements in the methods used to measure in-depth distributions with SIMS have been made by SIMS users over the past 30 years. Many of the natural materials investigated with SIMS have the same attributes as the synthetic materials investigated by the electronic materials community and therefore will suffer from the same depth-profile limitations. As an example when comparing diffusion profiles in natural materials, initial surface roughness can have a significant impact on the resultant profile and in some cases steps must be taken to minimize the effect of the roughness. In cases where very near surface (<100 nm) information is needed the energy of the primary SIMS beam can be of major importance. If information is desired at an interface between a metallic and a crystalline material then advanced methods of sample preparation may be required. SIMS researchers that deal with electronic materials have developed solutions to all of these problems along with many others that can be applied to natural materials. The primary goal of this paper is to illustrate the obstacles one should be aware of when depth-profiling, and then to show methods to minimize or eliminate these artifacts yielding the best possible depth profiles.

Many parameters are important for acquisition of the best possible depth profile. This paper will systematically review these different parameters starting with simple techniques that can be performed using the standard hardware configuration of most commercial SIMS instruments, and then moving on to more advanced techniques that require special sample preparation or upgrades to the standard hardware configurations.

For depth-profiling, the most important figure of merit is the depth resolution of the measurement. The parameter most commonly used to measure depth resolution is the decay length (λ) (Wilson *et al*. 1989). This parameter is defined as the depth over which it takes the signal to decrease

Mineralogical Association of Canada Short Course 41, Toronto, May 2009, p. 132-148

by 1/e (see Fig. 6-1 for example calculation). Various factors affect the depth resolution achievable, including: 1) primary ion beam conditions such as mass, species, energy and angle of incidence; 2) initial and sputter-induced surface topography; 3) instrumental parameters such as primary beam focus and analyzed area; 4) chemical effects such as radiation-enhanced diffusion and segregation that cause migration of the species of interest either toward the surface or toward the bulk of the material; and 5) the material one is analyzing. The most common type of material for measurement of depth resolution for depth-profiling applications in semiconductors is a "delta-doped" structure (Wittmaack *et al*. 2000). Delta-doped structures are typically manufactured using molecular beam epitaxy (Ohring 2002). Molecular beam epitaxy involves growing atomically thin spikes of an element different from the substrate material sandwiched between thicker layers of the substrate material. For instance a boron delta-doped structure would have 2–3 atomic layers of B sandwiched between layers of Si. Since ideally, these spikes are only several atomic layers thick the decay length measured on them is due entirely to the SIMS experimental conditions allowing a direct measurement of the effect of the primary beam on the observed SIMS depth resolution.

INSTRUMENTATION

The most common type of SIMS instrument used for geological applications is the magnetic sector. This is primarily due to the higher transmission (giving lower detection limits) and the ability to achieve high mass resolution (up to 20,000 m/Δm) *vs.* the quadrupole mass filter commonly used for depth-profiling applications in the semiconductor industry. Typically, a quadrupole offers transmission approximately 100x lower *vs.* a magnetic sector and only offers mass resolution of ~250 m/Δm. Of the commercially available magnetic sector SIMS instruments, the most common is the Cameca IMS 3f-7f variety (Lepareur 1980). In addition to the Cameca 3f-7f series instruments, there are also the large sector field instruments including Cameca IMS-1260, 1270, and 1280 (De Chambost *et al*. 1991) and the SHRIMP (Clement & Compston 1990), commonly used for geochronology and cosmochemistry applications. For this discussion, we will focus on the Cameca IMS 3f-7f variety since these are the most common instruments used for depth-profile measurements. However, the discussion can also be applied to the large radius instruments since they hold much in common with their smaller siblings.

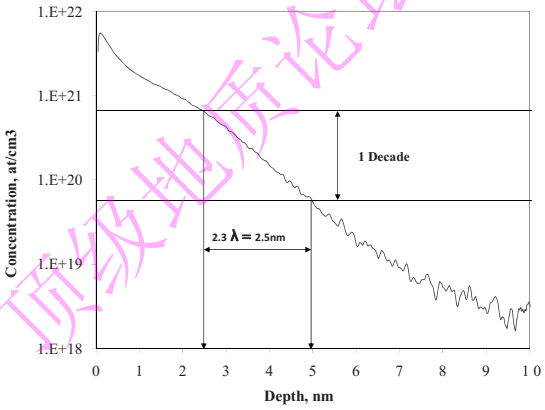


FIG. 6-1. Decay length calculation for depth profiles. Decay length for the above example is 5.0 nm – 2.5 nm = 2.5 nm per decade or 2.5 nm/2.3 = 1.09 nm per factor of e.

On the Cameca-type instruments, the extraction voltage on the sample and the primary ion voltage are independently variable. The primary ion voltage can be varied between 0 and 20 kV and the secondary extraction voltage is variable from 0 to 10 kV (for Cameca 6f and 7f series instruments). The primary beam energy and angle is defined by the combination of the primary and secondary ion voltages. Figure 6-2 shows a representation of the

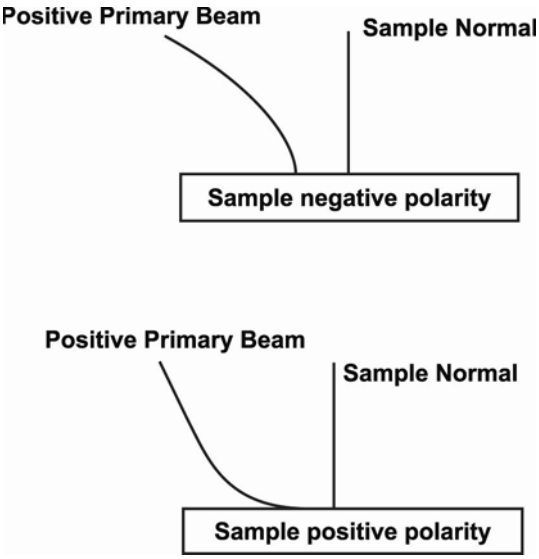


FIG. 6-2. Retarding/accelerating field effect for Cameca IMS 3f-7f SIMS instruments. The bias on the sample results in a change in the energy and the trajectory of the incoming primary ion beam.

质发地质论坛 http://bbs.3sdz.com/

sample region of the Cameca IMS-type instrument. When the primary ion polarity and secondary ion polarity are the same (*i.e.*, positive primary ion with positive secondary ion detection), the primary ion beam experiences a retarding field effect, slowing the primary beam and changing its trajectory. For instance, if the primary ion voltage is +10 kV and the sample voltage is +5 kV, the net impact energy of the primary beam is +5 kV ((+10 $kV_{primary}$) – (+5 $kV_{secondary}$)) and the trajectory of the primary beam becomes more oblique. Likewise, if the primary ion polarity and secondary ion polarity are opposite, the primary beam experiences an accelerating field effect and its trajectory is changed to a more normal angle of incidence. Angle of incidence for the Cameca IMS 3f-7f SIMS instruments can be calculated using the formula given by Meuris *et al*. (1989). The most common conditions used for geological analysis are O^- with positive secondary ion detection and Cs^+ with negative secondary ion detection. Both of these conditions lead to an acceleration effect and an angle of incidence closer to surface normal. As we will show later, these conditions can lead to a loss in depth resolution.

DISCUSSION

Crater edge effects

Since the SIMS signal is derived from sputtering material from the sample surface, in-depth information is always collected. However, for most quantitative geological applications (*e.g.*, trace element and stable isotope analysis), the depth information is discarded. There are fundamental differences in the SIMS instrumental set-up for a "depthless" measurement *vs*. an in-depth measurement. The depthless measurement is typically performed with the goal of achieving the best possible detection limit, requiring that all available secondary ion signal(s) are collected. This is accomplished by gathering signal over the entire sputtered region and assuming that there is no in-depth variation of the ion signal. This method of instrument set-up is not ideal for the measurement

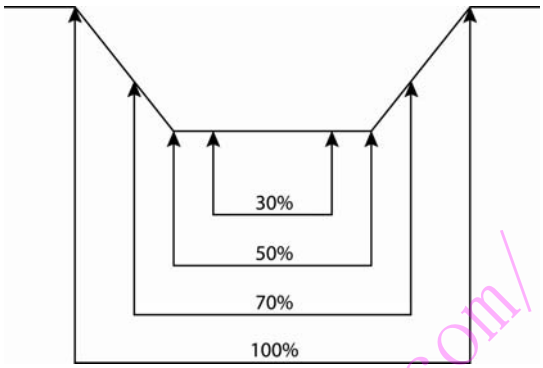


FIG. 6-3. Definition of analyzed area for secondary ion mass spectrometry. For this example, analyzed areas >50% will result in secondary ion signal resulting from a range of depths leading to high background levels on the observed depth profiles.

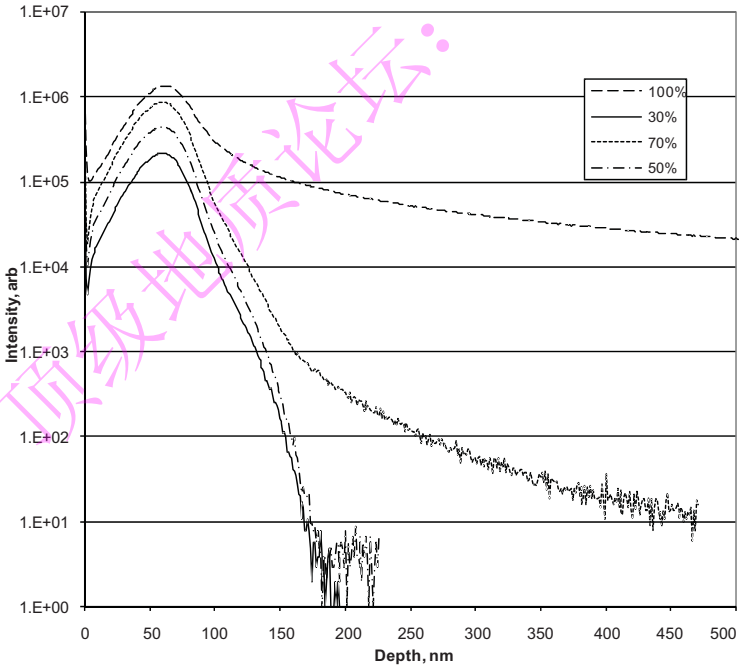


FIG. 6-4. The effect of analyzed area as a function of primary beam raster. Increasing percentage of analyzed area results in a high background level for conditions where the analyzed area is not completely contained within the sputtered crater bottom.

顶级地质论坛: http://bbs.geoc.com/

of specimens that are heterogeneous in the 3rd dimension. To assure that signal comes only from the depth of interest, it is necessary to exclude signal from the sloped edges of the sputtered crater from contributing to the ion signal from the crater bottom. This is normally accomplished by application of an electronic or optical gate that excludes ion signal from the edge of the SIMS crater (Fig. 6-3). Figure 6-4 shows a series of depth profiles measured with an increasingly large percentage of the sputtered area collected, where 100% means signal is acquired from the entire sputtered region. The true depth distribution on this particular sample is given by the 30% analyzed area curve and maintains its shape up to ~50%. Acquiring the signal from >50% of the sputtered area results in an increasing "crater edge" effect which is so severe at 100% that the signal appears to remain high indefinitely. Also note that as signal is acquired from a larger percentage of the sputtered area, the total ion signal increases leading to better ultimate detection limits for depthless measurements. The percentage of the sputtered area that can be collected without crater edge effects depends on instrument tuning, with maintaining a tightly focused primary ion beam being of primary concern. Prior to any depth-profiling, sufficient crater edge rejection should be applied to avoid crater edge effects.

PRIMARY BEAM EFFECTS

Collision cascade

As the SIMS primary beam impacts the sample, surface atoms are displaced from their positions by collisions with each other, which can displace atoms to either shallower or deeper depths than their original position (Fig. 6-5). This process is commonly referred to as the collision cascade (Wilson *et al.* 1989) and is the primary limitation to depth resolution caused by the interaction of the primary beam with the sample surface. The depth of the collision cascade can be controlled by varying the mass, energy and angle of the primary bombardment species. Extensive research has been performed to find the optimal conditions for profiling of ultra-shallow dopant species (Loesing *et al*. 2000, Wittmaack *et al*. 1998, Harrington *et al*. 1998). The most significant outcome of this research has been the development of low energy primary ion columns that can deliver significant primary current at a few hundred eV energies (Dowsett *et al*. 1996). Instruments for analysis of geological materials are rarely equipped for low

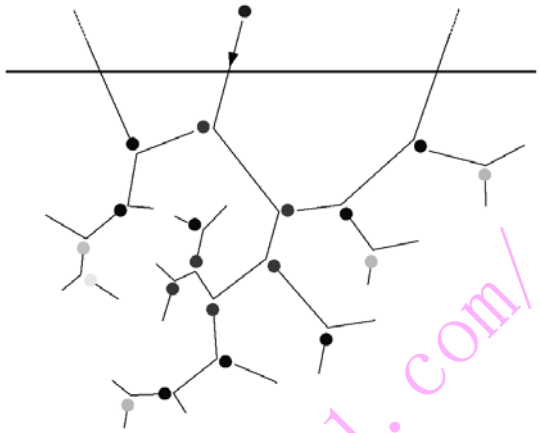


FIG. 6-5. Collision cascade. The incoming SIMS primary ion beam causes a cascade of collisions where surface atoms are displaced from their original location. This displacement leads both to sputtering and mixing of the sample atoms. In the above example primary, secondary, tertiary and quaternary collisions are shown. The mixing causes a loss in depth resolution due to the inability to determine the original position of the mixed atoms. The loss in depth resolution is proportional to the depth of the collision cascade.

energy primary analysis. Therefore, in this paper we concentrate on primary ion conditions that are readily achievable using a standard Cameca instrument configuration.

Energy

As the primary ion energy increases, the primary ion beam penetrates deeper into the sample surface causing a thicker collision cascade region. The thicker collision cascade will result in poorer depth resolution due to the mixing of the sample atoms to greater depths. Figure 6-6 shows TRIM (Ziegler *et al*. 2008) simulations for oxygen bombardment under increasing primary ion energies. These simulations show that the increasing primary ion energy causes a larger collision cascade volume that will result in lower depth resolution. Figure 6-7 illustrates the effect of primary ion energy on the observed depth resolution. For this experiment, a boron delta-doped sample was profiled under various primary ion beam energy conditions. Figure 6-7 shows that as the energy of the primary ion beam is increased, there is a marked loss of depth resolution. Analyses were performed using an O_2^+ primary ion beam with positive secondary ion detection at net impact energies of 3 kV, 5 kV and 10 kV. Additionally, a common condition for analysis of geological samples (23 kV O^-) has been used to illustrate the

http://bbs.3501.com/

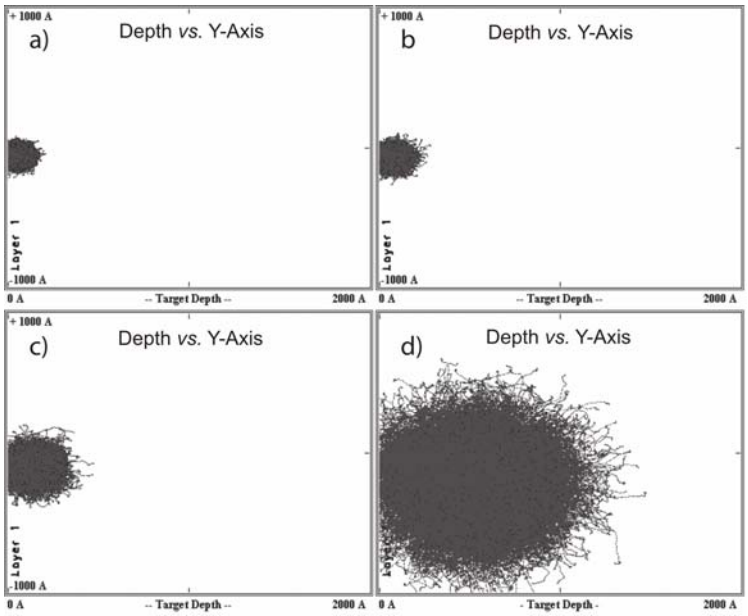


FIG. 6-6. TRIM simulations of oxygen bombardment in silicon: a) 3kV O_2^+; b) 5kV O_2^+; c) 10kV O_2^+; d)23kV O^-. Note the increased damage depth as primary ion energy increases. The increased damage depth leads to poorer depth resolution on the resultant depth profiles.

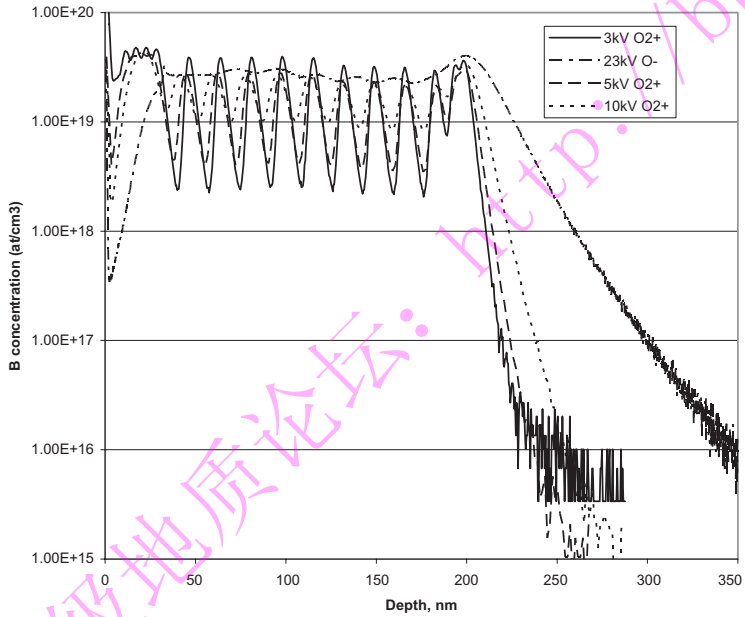


FIG. 6-7. SIMS depth profile of a boron delta-doped structure. Increased energy of the primary ion beam leads to a lowering of the depth resolution with resultant loss in definition of the spikes. Note that for the highest energy (23kV O^-), there is a near-complete loss of resolution between the adjacent delta structures.

effect of using a very high energy primary beam on the observed depth resolution, which results in near-complete loss of the structure and depth resolution on the delta-doped specimen. Note that only for 3 kV bombardment energy is it possible to observe these delta structures. Using a standard configuration Cameca 6f-7f, it is possible to achieve impact energies down to ~500 eV (Schuhmacher *et al*. 2000), although primary beam focus and current are significantly lower than at more typical energies of >5 kV, which will lead to longer analysis times.

The most common instrument set up for analysis of positive secondary ions on geological materials with the Cameca type instruments is bombardment using O^- primary ions and detection of positive secondary ions. These conditions are primarily used due to the difficulties of achieving proper charge neutralization when using O_2^+ bombardment on bulk insulating materials. However, this set-up leads to high primary ion

高级地质论坛：http://bbs.3s001.com/

impact energies (see discussion above). Pivovarov *et al*. 2004) have developed a method that allows the analysis of bulk insulators using O_2^+ (or Cs^+) with positive secondary ion detection using a non-coincident electron beam for charge neutralization. There are several major advantages to this method including higher primary current leading to higher sputter rates, more reliable operation of the duoplasmatron source and the ability to achieve significantly lower primary beam energy giving increased depth resolution. One thing to keep in mind when trying this method is that standard epoxy or indium mounts coated with ~10 nm of Au will melt under the electron beam unless the electron beam current is kept at a minimum value. It is possible to overcome this limitation at high electron currents, by using special sample mounting or extra thick coating combined with masking off the area of interest.

One needs to pay special attention to primary beam energy when attempting to measure contamination in the near surface region (<100 nm). For O bombardment in matrices that do not have a significant (>30%) O concentration, there can be a large variation in the O concentration in the near-surface depending on the primary ion energy. This concentration variation is due to the implantation depth of the O and will not stabilize until the O concentration reaches a steady state condition. Ion yields and sputter rate will vary over this pre-equilibrium region due to the changing concentration of the O content in the specimen. This phenomenon is referred to as the "surface transient" (Wittmaack 1975) and this transient region increases with increasing energy of the primary ion beam (Fig. 6-8). The surface transient can be minimized by directing a jet of O_2 (O flooding) to the sample surface (Wittmaack 1975) which has the effect of stabilizing the near-surface O concentration at shallower depths than ion bombardment alone. Additionally, there is an added benefit of increasing the positive secondary ion yield for many species (Smith *et al*. 1995) which will lead to lower detection limits. The best scenario for reduction of the surface transient for oxygen primary ion bombardment with positive ion detection is medium–low (1–3 kV) bombardment combined with O flooding.

CsM^+

Another method that has been used extensively for improvement in depth resolution is the molecular cesium method (Gao 1988). This method uses Cs^+ primary ion bombardment while monitoring the secondary molecular species $(M)+Cs^+$. This method offers significant advantages, including: 1) reduction of the matrix effect for some materials (Gao *et al*. 1995); 2) lowering of the primary beam impact energy due to the retarding field effect offered by monitoring positive secondary ions with positive primary ion bombardment (see above). The major limitation of this method is the loss in secondary ion intensity vs. monitoring the negative ion (typically 10–1000X less intense). Figure 6-9 shows an example of the reduced matrix effect for profiling an Au layer on Si. Analysis using "standard" protocols (Cs^+ bombardment with Au^- detection or O_2^+

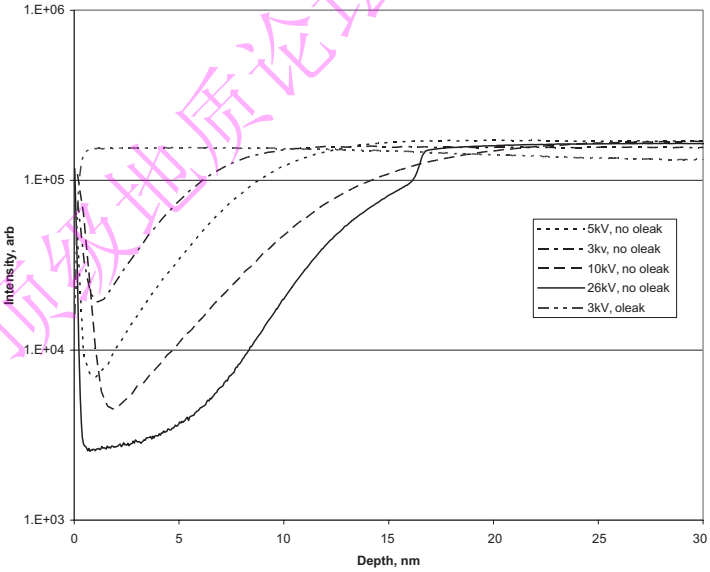


FIG. 6-8. SIMS surface transients. Increasing the primary ion energy results in greater penetration of the primary ion beam into the sample surface. The increased penetration depth results in an increased pre-equilibration where the ion yield and sputter rate of the material may still be changing. Use of low energy bombardment and oxygen leak will result in the shallowest pre-equilibrium depth.

顶级地质论坛 http://bbs.3s001.com/

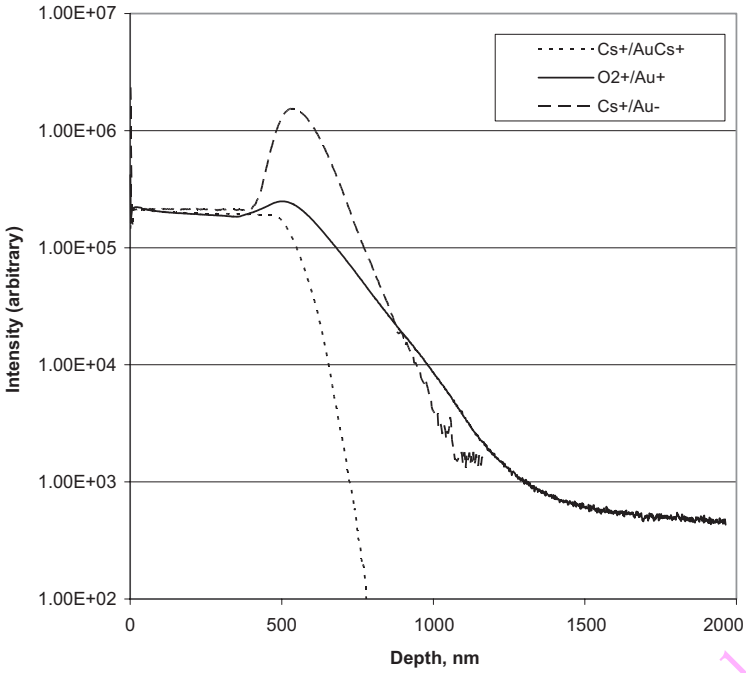


FIG. 6-9. Depth profile of an Au layer with various primary ion beam conditions. Profiling with a Cs^+ primary ion beam coupled with detection of the $AuCs^+$ secondary ion results in the highest depth resolution and the least matrix effect.

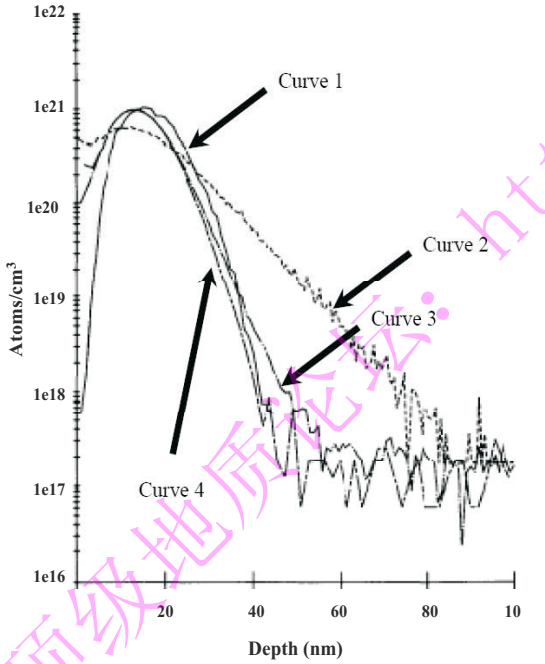


FIG. 6-10. As depth profiles using a Cs^+ primary ion beam: TRIM Simulation (curve 1); 8.9 keV Cs^+ primary beam (curve 2); 1.1 keV Cs^+ primary beam, $AsCs^+$ detected, oxygen flood used (curve 3); 1.1 keV Cs^+ primary beam, $AsCs^+$ detection, no oxygen flood (curve 4) (used by permission of J. Hunter, from Hunter *et al.*, 1990).

bombardment with Au^+ detection) lead to a significant peak at the Au/Si interface due to the SIMS matrix effect. However, Cs^+ bombardment with $AuCs^+$ detection shows no increase of the signal at the Au/Si interface giving a realistic representation of the actual sample (i.e. no increase in the Au concentration at the interface).

Figure 6-10 (Hunter *et al*. 1990) shows depth profiles for shallow arsenic implants acquired using several primary ion conditions including the detection of $AsCs^+$. Monitoring of $AsCs^+$ gives significantly improved depth resolution vs. monitoring of As^-, primarily due to the lower energy of the primary ion beam (1.1 kV vs. 8.9kV). The MCs^+ method can be a powerful technique for minimization of matrix effects and for lowering the primary ion energy to improve depth resolution and, when combined with the capability to profile bulk insulating materials given by the method outlined above (Pivovarov *et al*. 2004), can be applied to a host of natural materials.

Effect of primary ion angle

By combining control of the primary ion energy and the secondary extraction voltage, it is possible to vary the impact angle on the Cameca-type SIMS instruments. As the primary beam angle is less normal to the sample surface, the collision cascade depth also decreases. However, this phenomenon has significantly less effect on the

顶级地质论坛: http://bbs.3560.com/

observed depth resolution than the effect of the primary ion energy, and for most geological applications is of minimal use.

Mass–cluster beams

The mass of the primary ion beam also can have a significant effect on the observed depth resolution. At the same impact energy, heavier masses will penetrate less deeply than lighter masses, leading to a smaller collision cascade depth and higher depth resolution. Additionally, using polyatomic primary ion beams will lead to lower impact energies per atom *vs*. a monoatomic primary species. For example, 10 kV O_2^+ *vs*. 10 kV O^+ gives 5 kV per O atom for the molecular species *vs.* 10 kV for the atomic. The use of polyatomic primary sources has allowed SIMS users to achieve very low primary impact energies (Kim *et al*. 2007, Mahoney *et al*. 2004) and therefore improve depth resolution. For example, Tomita *et al*. (2006) compared the depth resolution achievable using 10 kV O_2^+ and the depth resolution using 10 kV $(Ir_4(CO)_7)^+$ on the boron delta structure described above (Fig. 6-11). At 10 kV, the polyatomic $(Ir_4(CO)_7)^+$ gives 170 eV O, 2 kV Ir and 120 eV C *vs*. 5 kV O for the O_2^+ primary beam. This lower beam energy gives significantly better depth resolution ($\lambda = 1.6$ nm for $(Ir_4(CO)_7)^+$ vs. $\lambda = 4.2$ nm for O_2^+). The main issue with many of the polyatomic beams is that the ion sources used to generate them are not as reliable as O_2 or Cs sources leading to instrument up-time issues.

TOPOGRAPHY

Initial surface topography can have a significant effect on SIMS depth resolution, both through a loss of depth resolution when measuring through interfaces or by causing a rapid onset of induced topography that increases with depth. If the surface is either initially rough or forms roughness during the sputtering process, the roughness will continue to worsen with increasing sputter depth because the topography prevents sputtering of all areas equally due to it shadowing the primary beam. The initial surface topography can be minimized by polishing the sample surface to a fine finish (Corcoran *et al*. 1994). As an example, Figure 6-12 shows an atomic force microscopy image of the surface of a GaN laser structure where the surface has an initial surface roughness of ~100 nm. Figure 6-13 shows the same specimen after polishing to remove the surface roughness with the resultant surface roughness of ~3 nm. The depth profiles for

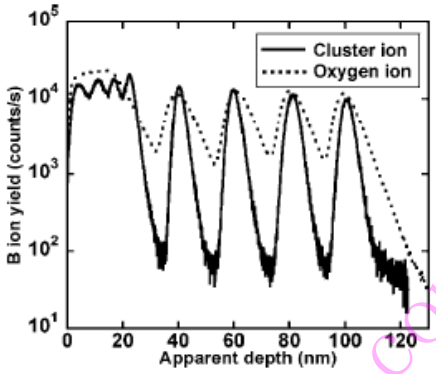


FIG. 6-11. SIMS depth profile of boron delta layers using O_2^+ and $(Ir_4(CO)_7)^+$ with ion energy of 10 keV at 60° using oxygen leak (Tomita *et al.* 2006). There is marked improvement using the cluster ion $(Ir_4(CO)_7)^+$ bombardment, due to the lower primary ion energy (used by permission of Applied Physics Letters, from Tomita, *et al.* 2006).

this specimen before (Fig. 6-14) and after polishing (Fig. 6-15) show dramatically improved depth resolution after removal of the initial surface roughness. The decay length of both Mg and In are dramatically improved after polishing and it is possible to see the delta structures on the In signal. This method only works if the primary interest is in a buried feature, since material on the surface will be removed by the polishing process and therefore the near surface information will be lost.

Surface topography can also have an effect on the external reproducibility of isotopic ratio measurements. Table 6-1 shows data for an $^{18}O/^{16}O$ isotopic ratio taken from a Late Mississippian blastoid (an extinct stalked echinoderm) fossil (Dexter & Schiffbauer 2008a, Dexter & Schiffbauer 2008b) sample. The two specimens for this study were different plates prepared from the same blastoid; however, sample one was polished with an RMS roughness (as measured by surface profilometry) of 500 nm whereas sample 2 had an RMS roughness of 60 nm. Table 6-1 shows a ~3x

TABLE 6-1. ISOTOPIC PRECISION ON BLASTOID SAMPLES AS A FUNCTION OF INITIAL SAMPLE SURFACE ROUGHNESS

Sample ID	R_a, nm	External precision, permil
Blastoid sample 1	500 nm	8.9
Blastoid sample 2	60 nm	2.9

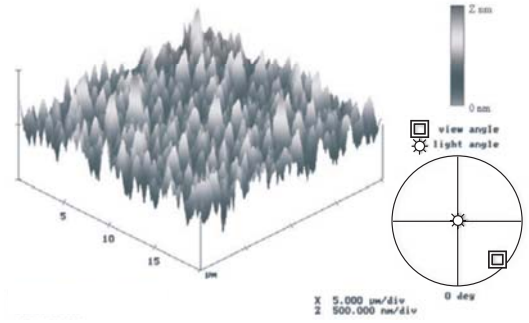


FIG. 6-12. Atomic force microscopy image of initial surface roughness of GaN sample. Average roughness for the initial surface is ~100 nm (used by permission of L. Wang, Evans Analytical Group, Sunnyvale, CA).

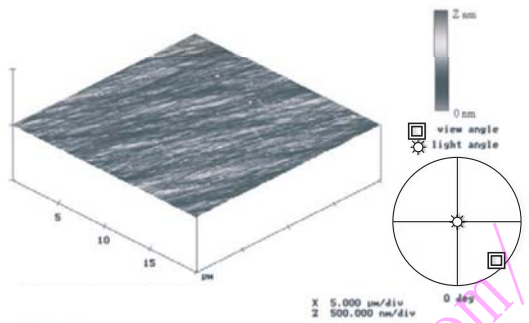


FIG. 6-13. Atomic force microscopy image of GaN sample after polishing to remove surface roughness. Average roughness after polishing is <3 nm (used by permission of L. Wang, Evans Analytical Group, Sunnyvale, CA).

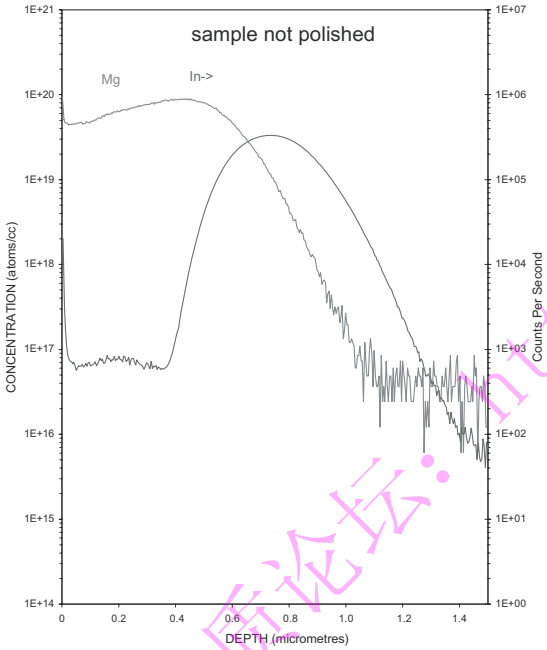


FIG. 6-14. SIMS depth profile of unpolished GaN sample. Surface roughenss results in poor depth resolution causing a complete loss of the in-depth structure of the specimen (used by permission of L. Wang, Evans Analytical Group, Sunnyvale, CA).

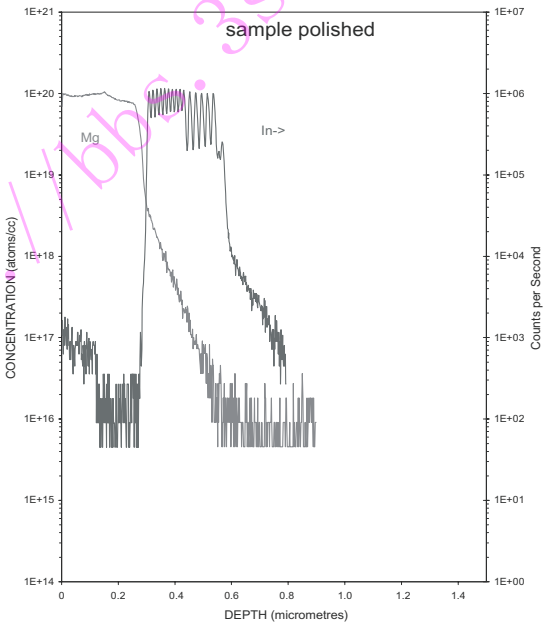


FIG. 6-15. SIMS depth profile of polished GaN sample. Removal of surface roughenss gives a dramatic improvement in the observed depth resolution. Note that the indium delta structures are only visible after removal of the surface roughness (used by permission of L. Wang, Evans Analytical Group, Sunnyvale, CA).

improvement in the observed external reproducibility for the sample with lower roughness.

Various materials have shown that under the sputter beam they will form topography (Stevie *et al*. 1988). This is especially true with polycrystalline materials. For example, Figure 6-16 shows sputter-induced topography in the form of surface waves in silicon. A method to minimize the effect of either initial or induced surface topography is the sample preparation technique known as "backside" profiling (Gu *et al*. 2004). In backside profiling, the sample of interest is mounted (typically using an epoxy adhesive) to a mounting material, and then the sample is thinned by polishing or chemical stripping to <200 nm of the interface (Fig. 6-17). SIMS analysis is then performed from the crystalline material into the polycrystalline material, avoiding the roughening of

顶级地质论坛: http://bbs.3s001.com/

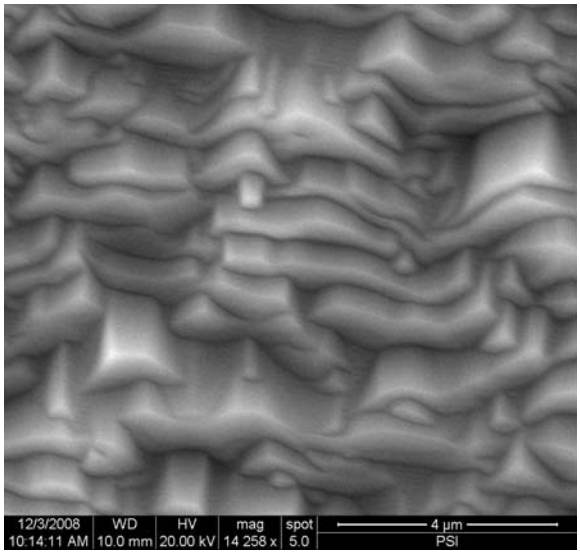


FIG. 6-16. Environmental SEM micrograph of sputter induced topography on Si due to O_2^+ primary ion bombardment. The morphology is typical for oxygen beam induced topography formation in Si.

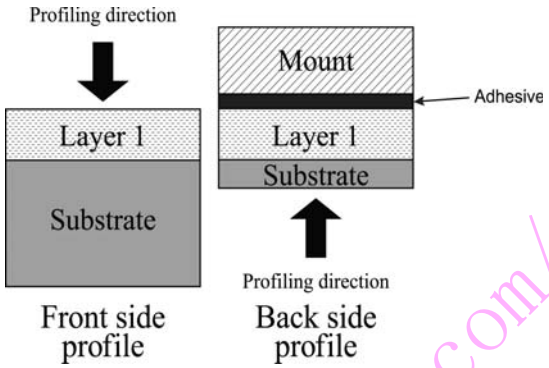


FIG. 6-17. Schematic diagram for back side depth profiling technique. Specimen is fixed to a mounting material and substrate is thinned to <300 nm and depth profile is performed from the substrate material to the top layer avoiding initial or induced topography in the top layer.

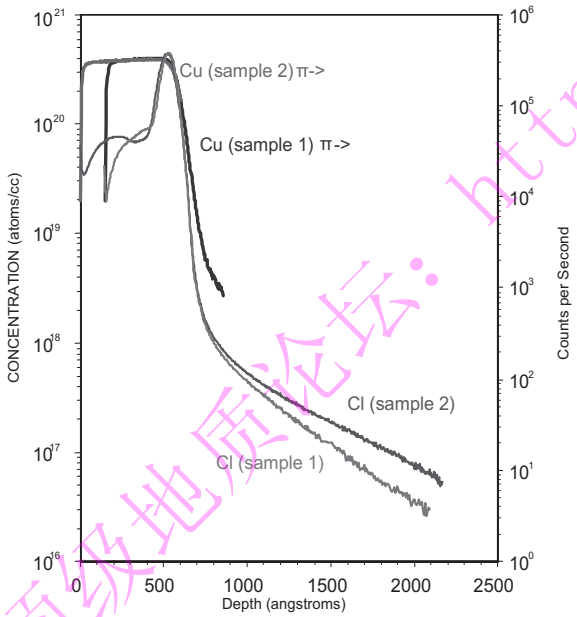


FIG. 6-18. Frontside SIMS depth profile of Cu sample. Profiling from the front side results in sputter topography formation. The sputter topography makes it difficult to ascertain if chlorine has diffused from the copper layer into the underlying silicon (used by permission of L. Wang, Evans Analytical Group, Sunnyvale, CA).

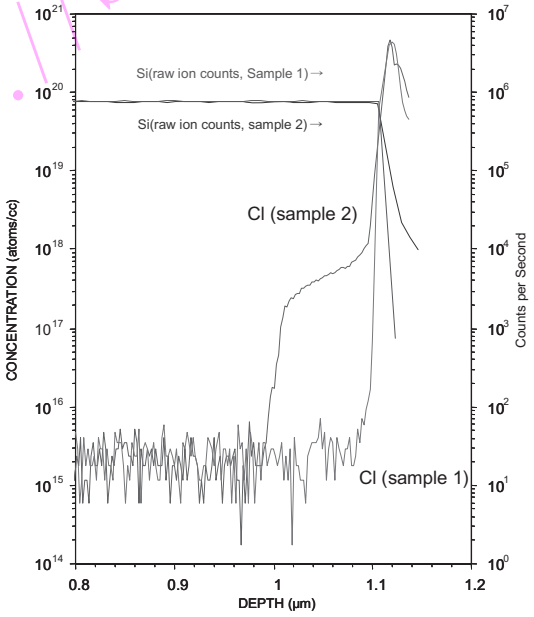


FIG. 6-19. Backside SIMS depth profile of Cu sample. Profiling from the back side avoids sputter topography formation resulting in improved depth resolution at the interface. The backside profile clearly shows that chlorine has diffused from the copper layer into the underlying silicon (used by permission of L. Wang, Evans Analytical Group, Sunnyvale, CA).

顶级地质论坛: http://bbs.3s001.com/

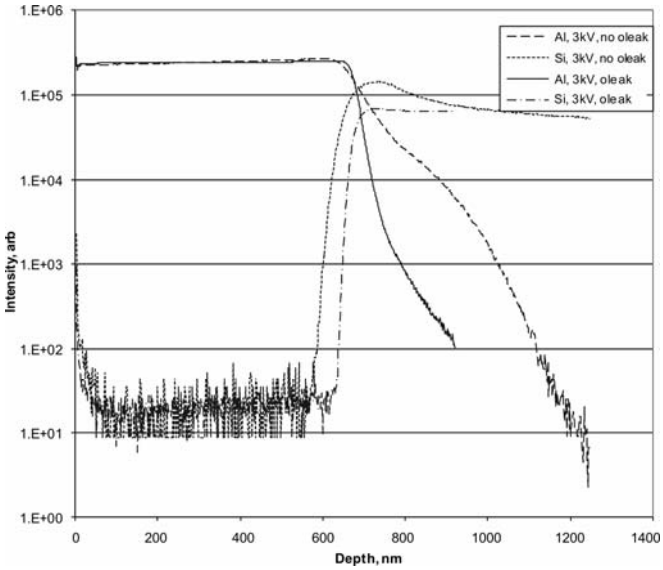


FIG. 6-20. SIMS depth profiles of an Al layer on silicon. A 6x decrease in sputter induced roughness is observed if oxygen leak is used in combination with low energy ion bombardment *vs*. low energy ion bombardment alone.

the polycrystalline layer. This method has proven especially useful when profiling through a polycrystalline or metallic layer into an amorphous or crystalline layer where the concern is with the diffusion of a contaminant from the top layer into the underlying material. Figure 6-18 (Evans Analytical Group) shows an example of backside profiling of a Cu film looking at Cl contamination. The front side (Cu into Si) profiles (Fig. 6-19) show Cl extends from the Cu film into the underlying Si layer with roughly the same concentration. However, when the profiles are performed from backside (Si into the Cu layer), it is quite clear that specimen 2 shows significant penetration of the Cl into the Si while specimen 1 does not.

A method that can sometimes reduce surface topography formation is the use of a directed jet of oxygen to the sputter area (o-leak) (Mahoney *et al*. 2004). Figure 6-20 shows data acquired on 660 nm Al on Si film using 3 kV oxygen bombardment both with and without o-leak There is significant improvement in the Al depth resolution due to oxygen flooding. Table 6-2 shows profilometry measurements of the average roughness on the bottom of the sputter crater that indicate a >6x reduction in the sputter topography when using oxygen flooding *vs*. no oxygen flooding. This method is most useful on metallic surfaces that readily oxidize (*e.g.*, Cu, Al, Ti, *etc*.) and does not work on materials that do not readily oxidize (*e.g.* Au, Pt, *etc*.).

As previously mentioned, once topography forms, it tends to worsen with depth. Additionally, oblique angles of incidence will exacerbate topography formation. With this in mind it is sometimes better to use a primary bombardment angle that is more normal to the sample surface to minimize topography formation. Figure 6-21 shows data on the same Al film used above, profiling with 10kV O_2^+ at 38° *vs*. 3kV O_2^+ at 55°. Significantly improved depth resolution is observed with multiple angles simultaneously preventing the formation of topography. Figure 6-22 (Cirlin *et al*. 1991) illustrates the effect of sample rotation on the observed depth resolution of Al superlattices. Without sample rotation, sputter-induced topography causes a total loss of depth resolution at ~200 nm (curve A) where the individual superlattices can no longer be observed. However, when the sample is rotated under the sputter beam, no loss in depth resolution is observed (curve B). Curve C shows that sputter-induced topography can sample under the high voltage extraction conditions used for this instrument.

TABLE 6-2. AVERAGE ROUGHNESS OF AL FILMS AFTER SPUTTERING.

Conditions	Average roughness, nm
Initial surface	1.0
3kV O_2^+, no o-leak	50.0
3kV O_2^+, o-leak	7.5
10kV O_2^+, no o-leak	3.0

http://www.3s001.com/

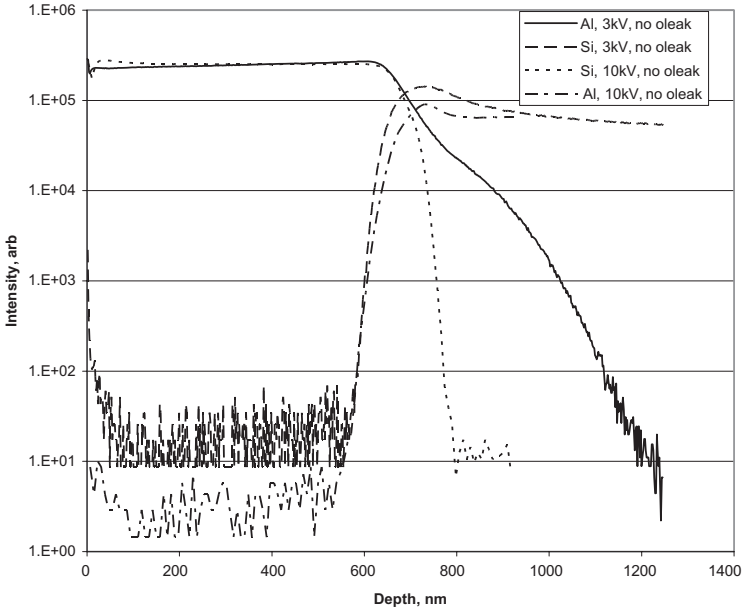


FIG. 6-21. SIMS depth profiles of an Al layer on Si. A 15x decrease in sputter induced roughness is observed if 38° O_2^+ bombardment is used vs. 55° bombardment. The improvement is due to the increased depth onset of sputter-induced topography for more normal incidence ion bombardment.

In many cases, initial or induced surface topography will be the primary limitation to the observed depth resolution for depth profiles or the at the higher beam energy for the more normal be removed by the use of rotation by illustrating that depth resolution returns when the rotation is initiated after surface topography forms. Sample rotation has been applied to Cameca type instruments (Sykes & Chew 1994), however, special care must be taken in the selection of analytical parameters to avoid oscillation in the secondary ion signal caused by rotation of the angle of incidence which results in lower surface roughness (Table 6-2). Unlike the oxygen flooding method, this method is useful for materials that do not readily oxidize.

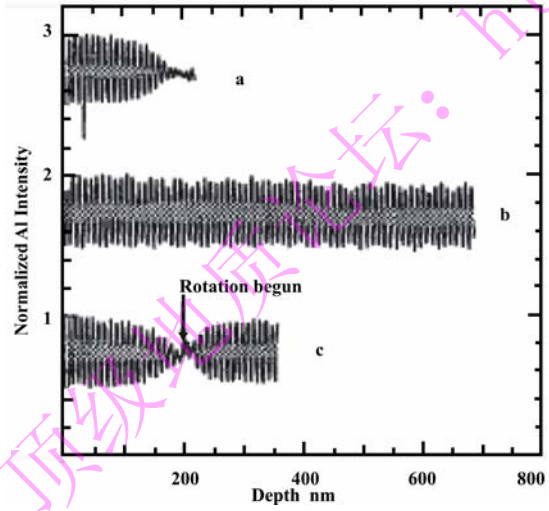


FIG. 6-22. Normalized SIMS depth profiles for an aluminum superlattice (reference) obtained without (a) and with (b) sample rotation. For (c), rotation was begun after sputter to a depth of ~200 nm. The figure illustrates that rotation prevents the formation of sputter induced topography and that sputter rotation can remove topograpy after formation (used by permission of J. Vajo, from Cirlin *et al*., 1991).

An instrumental modification that has been successfully used to minimize or eliminate the sputter-induced topography is rotation of the sample under the sputter beam (Stevie & Moore 1992). Sample rotation has the effect of sputtering from reproducibility for isotopic ratios. For the cases where topography already exists, steps should be taken to minimize the effect of the roughness on the analytical measurement.

CONCLUSIONS

Table 6-3 summarizes the different methods reviewed in this paper for optimizing depth resolution. Optimal instrumental set-up conditions for determination for ppm detection limits and isotopic ratios for geological materials are very different than those required for optimal in-depth distribution analysis. In this paper, we have reviewed the parameters most important to assure accurate depth profiles. Although, most of the materials reviewed here are synthetic, the methods are also applicable to depth-profiling of natural materials. For instance, if one wishes to measure a diffusion profile in the top 100 nm of a garnet material (Tirone *et al*. 2004), it is imperative that the proper primary ion beam conditions are chosen

顶级地质论坛：http://bbs.3s001.com/

TABLE 6-3. SUMMARY OF DEPTH-PROFILE IMPROVEMENT STRATEGIES

Problem	Solution	Special requirements
Crater edge effects	Improve focus of primary ion beam	None, capability exists on most commercial instruments
	Decrease the analyzed/rastered area ratio (smaller analyzed area and larger raster)	None, capability exists on most commercial instruments
Initial Surface roughness	Frontside polishing (Corcoran *et al*. 1994)	Equipment and expertise needed for polish
Sputter Induced topography	Backside polishing (Gu *et al*., 2004)	Equipment and expertise needed for polishing
	Rotational depth profiling (Cirlin *et al*. 1991; Sykes & Chew 1994)	Special sample stage needed (requires instrument modification)
Measurement of near surface (<100nm)	Lower primary beam energy to avoid surface transient	None, capability exists on most commercial instruments
	Use of MCs^+ method to lower primary ion energy (Hunter *et al*. 1990)	None, capability exists on most commercial instruments
Measurement of shallow or thin layers	Lower primary ion energy to minimize collisional cascade mixing	None, capability exists on most commercial instruments
	Use of cluster ion beams for lower primary ion energies (Tomita *et al*. 2006)	Special primary ion source required (requires instrument modification)
	Use of MCs^+ method to lower primary ion energy (Hunter *et al*. 1990)	None, capability exists on most commercial instruments
	Use of O_2^+ bombardment with positive secondary ion detection (Pivovarov *et al*. 2004)	None, capability exits on most commercial instruments with electron gun charge neutralization
Matrix effects	Use of MCs^+ method (Gao *et al*. 1995)	None, capability exists on most commercial instruments

to avoid surface transient effects and minimize the collision cascade volume. When profiling An (anorthite) and Sm in volcanic phenocrysts (Genareau *et al*. 2007) through 7–8 μm of material it is critical to assure that crater edge effects are minimized to avoid missing the interface and that conditions are chosen to avoid sputter-induced topography. For depth-profiling of metallic cultural artifacts (Adriaens *et al*. 2006) one must be aware of the effect of sputter topography on the measurements and methods to minimize the topography. Many of the methods outlined here are straightforward to accomplish on any commercially available SIMS instrument and require little additional instrument set-up time. However, the pay-off can be significant since the best possible depth profiles will be assured.

ACKNOWLEDGEMENTS

The author wishes to thank Evans Analytical Group for the front and backside examples and James Schiffbauer and Troy Dexter of the Virginia Tech Geosciences Department for the blastoid example. Parts of this work were carried out using instruments in the Nanoscale Characterization and Fabrication Laboratory, a Virginia Tech facility operated by the Institute for Critical Technology and Applied Science

http://bbs.3560l.com/

REFERENCES

ADRIAENS, A. & DOWSETT, M.G. (2006): Applications of SIMS to cultural heritage studies. *Appl. Surface Sci.* **252**, 7096-7101.

CIRLIN, E.H., VAJO, J.J., DOTY, R.E. & HASENBERG, T.C. (1991): Ion-induced topography, depth resolution, and ion yield during secondary ion mass spectrometry depth-profiling of a gallium arsenide/aluminum gallium arsenide superlattice: effects of sample rotation. *J. Vacuum Sci. & Tech., A: Vacuum, Surfaces, and Films* **9**, 1395-1401.

CLEMENT, S.W.J. & COMPSTON, W. (1990): SIMS at high sensitivity and high mass resolution. *SIMS 7 (Second. Ion Mass Spectrom.) Proc. Int. Conf.*, 815-819

CORCORAN, S.F., SOZA, D., KINCAID, N. & DANIELSON, D. (1994): Improvement of depth resolution in secondary ion mass spectrometry depth-profiling of silicided poly contacts. *J Vacuum Sci. & Tech., B: Microelectronics & Nanometer Structures* **12**, 230-233.

DE CHAMBOST, E., HILLION, F., RASSER, B., MIGEON, H.N. (1991): The Cameca IMS1270: a description of the secondary ion optical system, *In*: Proc Internat. Secondary Ion Mass Spec. Conference VIII (A. Benninghoven, ed.) 207-210.

DEXTER, T.A. & SCHIFFBAUER, J.D. (2008a): Stable isotope variation between growth lines on the Blastoid *Pentremites*. Geol. Soc. Am. (Southeastern Section), *Abstracts with Programs* **40**, 23.

DEXTER, T.A. & SCHIFFBAUER, J.D. (2008b): Stable isotope variation along the direction of growth in echinoderm plates. *Geol. Soc. Am. Abstracts with Programs* **40**, 391.

DOWSETT, M. & ADRIAENS, A. (2004): The Role of SIMS in Cultural Heritage Studies. *Nucl. Instrum. Methods B* **226**, 38.

DOWSETT, M.G., SMITH, N.S., BRIDGELAND, R., RICHARDS, D., LOVEJOY, A.C. & PEDRICK, P. (1996): *Proceedings SIMS X.* (A. Benninghoven *et al. eds.*) J.Wiley & Sons, 367.

GANGULY, J., TIRONE, M & HERVIG, R.L. (1998): Diffusion kinetics of samarium and neodymium in garnet, and a method for determining cooling rates of rocks. *Science* **281**, 805-807.

GAO, Y. (1988): A new secondary ion mass spectrometry technique for III-V semiconductor compounds using the molecular ions CsM^+. *J. Appl. Phys*. **64**, 3760-3762.

GAO, Y., MARIE, Y., SALDI, F. & MIGEON, H.N. (1995): On the SIMS depth-profiling analysis: reduction of matrix effect. *Internat. J. Mass Spec. & Ion Processes* **143**, 11-18.

GENAREAU, K., HERVIG, R. & CLARKE, A. (2007): Geochemical variations in late-stage growth of volcanic phenocrysts revealed by SIMS depth-profiling. *Am. Mineral.* **92**, 1374-1382.

GU, C., PIVOVAROV, A., GARCIA, R., STEVIE, F., GRIFFIS, D., MORAN, J., KULIG, L. & RICHARDS, J.F. (2004): Secondary ion mass spectrometry backside analysis of barrier layers for copper diffusion. *J. Vacuum Sci. & Tech., B: Microelectronics & Nanometer Structures – Processing, Measurement, and Phenomena* **22**, 350-354.

HARRINGTON, W.L., MAGEE, C.W., PAWLIK, M., DOWNEY, D.F., OSBURN, C.M. & FELCH, S.B. (1998): Techniques and applications of secondary ion mass spectrometry and spreading resistance profiling to measure ultrashallow junction implants down to 0.5 keV B and BF_2. *J Vacuum Sci. & Tech., B: Microelectronics & Nanometer Structures* **16**, 286-291.

HUNTER, J.L., CORCORAN, S.F., GRIFFIS, D.P. & OSBURN, C.M. (1990): Optimization of primary beam conditions for secondary ion mass spectrometry depth-profiling of shallow junctions in silicon using a Cameca IMS-3f. *J Vacuum Sci. & Tech., A: Vacuum, Surfaces, & Films* **8**, 2323-2328.

IRELAND, T.R. & WILLIAMS, I.S. (2003): Considerations in zircon geochronology by SIMS. *In* Zircon (Hanchar, J.M. & Hoskin, P.W.O. *eds*.). *Reviews in Mineralogy & Geochemistry*, Mineral. Soc. Am. 215-241.

KIM, K.J., SIMONS, D. & GILLEN, G. (2007): Quantitative depth-profiling of an alternating Pt/Co multilayer and a Pt-Co alloy multilayer by SIMS using a Buckminsterfullerene (C_{60}) source. *Appl. Surface Sci.* **253**, 6000-6005.

KING, E.M., TRZASKUS, A.P. & VALLEY, J.W. (2008): Oxygen isotope evidence for magmatic variability and multiple alteration events in the Proterozoic St. Francois Mountains, Missouri. *Precamb. Research* **165**, 49-60.

KOHN, M.J., RICIPUTI, L.R., STAKES, D. & ORANGE, D.L. (1998): Sulfur isotope variability in biogenic pyrite: Reflections of heterogeneous bacterial

http://www.35001.com/

colonization? *Am. Mineral.* **83**, 1454-1468.

LEPAREUR, M. (1980): Le micro-analyseur ionique de seconde generation Cameca, modele 3f. *Revue Technique Thomson-CSF* **12**, 225-265.

LOESING, R., GURYANOV, G.M., HUNTER, J.L. & GRIFFIS, D.P. (2000): Secondary ion mass spectrometry depth-profiling of ultrashallow phosphorus in silicon. *J. Vacuum Sci. & Tech., B: Microelectronics & Nanometer Structures* 18, 509-513.

MACRAE, N.D. & RUSSELL, M.R. (1987): Quantitative REE SIMS analyses of komatiite pyroxenes, Munro Township, Ontario, Canada. *Chem. Geol.* **64**, 307-317.

MAHONEY, C.M., ROBERTSON, S. & GILLEN, G. (2004): Dynamic SIMS utilizing SF_5^+ polyatomic primary ion beams for drug delivery applications. *Appl. Surf. Sci.* **231-232**, 174-178.

MEURIS, M., DE BISSCHOP, P., LECLAIR, J.F. & VANDERVORST, W. (1989): Determination of the angle of incidence in a Cameca IMS-4f SIMS instrument. *Surf. & Interface Analysis* **14**, 739-743.

OHRING, M. (2002): *The materials science of thin films*. Academic Press, San Diego.

PALITSIN, V.V., DOWSETT, M.G., GUZMAN DE LA MATA, B., OLOFF, I.W. & GIBBONS, R. (2006): uleSIMS characterization of silver reference surfaces. *Appl. Surf. Sci.* **252**, 7132-7135.

PAPINEAU, D. & MOJZSIS, S.J. (2006): Mass-independent fractionation of sulfur isotopes in sulfides from the pre-3770 Ma Isua Supracrustal Belt, West Greenland. *Geobiology* **4**, 227-238.

PIVOVAROV, A.L., STEVIE, F.A. & GRIFFIS, D.P. (2004): Improved charge neutralization method for depth-profiling of bulk insulators using O_2^+ primary beam on a magnetic sector SIMS instrument. *Appl. Surf. Sci.* **231-232**, 786-790.

REED, S.J.B. (1984): Secondary-ion mass spectrometry/ion probe analysis for rare earths. *Scanning Electron Microscopy* **2**, 529-535.

SCHUHMACHER, M., RASSER, B. & DESSE, F. (2000): New developments for shallow depth-profiling with the Cameca IMS 6f. *J. Vacuum Sci. & Tech., B: Microelectronics and Nanometer Structures* **18**, 529-532.

STEVIE, F.A., KAHORA, P.M., SIMONS, D.S. & CHI, P. (1988): Secondary ion yield changes in silicon and gallium arsenide due to topography changes during oxygen (O2+) or cesium(1+) ion bombardment. *J. Vacuum Sci. & Tech., A: Vacuum, Surfaces, & Films* **6**, 76-80.

SMITH, S.P., WANG, L., ERICKSON, J.W. & CHIA, V.K.F. (1995): SurfaceSIMS, secondary ion mass spectrometry using oxygen flooding: a powerful tool for monitoring surface metal contamination on silicon wafers. *Materials Res. Soc. Symp. Proc.*, **386**,157-162.

SPOTO, G. (2000): Secondary ion mass spectrometry in art and archaeology. *Thermochim. Acta* **365**, 157-166.

STEVIE, F.A. & MOORE, J.L. (1992): Application of sample rotation to secondary ion mass spectrometry depth-profiling of aluminum metalization. *Surface & Interface Analysis* **18**, 147-152.

STEVIE, F.A., KAHORA, P.M., SIMONS, D.S. & CHI, P. (1988): Secondary ion yield changes in silicon and gallium arsenide due to topography changes during oxygen (O^{2+}) or cesium$^{(1+)}$ ion bombardment. *J. Vacuum Sci. & Tech., A: Vacuum, Surfaces, & Films* **6**,76-80.

SYKES, D.E. & CHEW, A. (1994): SIMS depth-profiling with sample rotation in a Cameca IMS 3F. *Surface and Interface Analysis* **21**,231-23.

TIRONE, M., GANGULY, J., DOHMEN, R., LANGENHORST, F., HERVIG, R. & BECKER, H.W. (2004): Rare earth diffusion kinetics in garnet: Experimental studies and applications. *Geochim. Cosmochim. Acta* **69**, 2385-2398.

TOMITA, M., KINNO, T., KOIKE, M., TANAKA, H., TAKENO, S., FUJIWARA, Y., KONDOU, K., TERANISHI, Y., NONAKA, H., FUJIMOTO, T., KUROKAWA, A. & ICHIMURA, S. (2006): Depth resolution improvement in secondary ion mass spectrometry analysis using metal cluster complex ion bombardment. *Appl. Phys. Lett.* **89**, 053123/1-053123/3.

WILSON, R.G., STEVIE, F.A. & MAGEE, C.W. (1989): *Secondary ion mass spectrometry: A practical handbook for depth-profiling and bulk impurity analysis*. Wiley Interscience, New York, 384 p.

WITTMAACK, K. (1975): Preequilibrium variation of the secondary ion yield. *Internat. J. Mass Spec. & Ion Phys.* **17**, 39-50.

WITTMAACK, K., PATEL, S.B. & CORCORAN, S.F. (1998). Identification, simulation and avoidance of artifacts in ultra-shallow depth-profiling by secondary ion mass spectrometry. *AIP Conference Proceedings* **449**, 791-795.

http://www.iscan.com/

WITTMAACK, K., GRIESCHE, J., OSTEN, H.J. & PATEL, S.B. (2000): In search of optimum conditions for the growth of sharp and shallow B-delta markers in Si by molecular beam epitaxy. *J. Vacuum Sci. & Techn., B: Microelectronics and Nanometer Structures – Processing, Measurement & Phenomena* **18**, 524:528.

ZHANG, C., LIU, S., PHELPS, T.J., COLE, D.R., FORTIER, S.M., HORITA, J. & VALLEY, J.W. (1996): Mineralogy and oxygen isotope composition of microbially produced magnetic iron oxides at thermophilic temperatures. *Book of Abstracts, 211th ACS National Meeting*, New Orleans, LA, March 24-28, GEOC-122.

ZIEGLER, J.F., ZIEGLER, M.D. & BIERSACK, J.P. (2008): *The stopping power and range of ions in matter version 2008.4*. Chester, MD, USA.

顶级地质论坛：http://bbs.3s001.com/

Mineralogical Association of Canada

Publication Order Form 2009

You can send your order by mail, fax or e-mail. You can also order online.

A. The Canadian Mineralogist Thematic Issues

ISSN 0008-4476

Title	Qty	Price	Member	Total
TI 46-6 A Tribute to Joseph V. Smith (1928-2007)		$40	$32.00	
TI 46-4 The Mineralogy and Petrology of Carbonatites: A Tribute to John Gittins		$40	$32.00	
TI 45-1 Contaminated Granites		$40	$32.00	
TI 44-3 Rare-Element Geochemistry and Mineral Deposits		$40	$32.00	
TI 43-6 50th Anniversary Symposium Volume		$40	$32.00	
TI 43-5 S: Sulfides, Structures, and Synchrotron Light – A Tribute to Michael E. Fleet		$40	$32.00	
TI 43-1 Truth and Beauty in Metamorphism		$50	$40.00	
TI 42-5 Pacrofi VIII: Fluid Inclusions		$40	$32.00	
TI 42-2 Platinum-group Elements		$40	$32.00	
TI 40-2 The Cabri Issue		$40	$32.00	
TI 39-2 Phase Equilibria in Basaltic Systems		$40	$32.00	
TI 38-2 Tectonometamorphic Studies in the Canadian Shield – Part II		$38	$30.40	
TI 37-2 Mineral Scale Processes in Met. Pet.		$38	$30.40	
TI 36-6 XRD and Electron–Microscopy Investigations of Layer Silicates		$38	$30.40	
TI 36-2 Granitic Pegmatites: Černý–Foord Volume		$38	$30.40	
TI 35-5 Tectonometamorphic Studies in the Canadian Shield – Part I		$38	$30.40	
TI 35-2 Nature and Origin of Primitive Magmas...		$38	$30.40	
TI 34-2 Alkaline Rocks: Petrology and Mineralogy		$38	$30.40	
TI 33-2 Microbeam Techniques in the Earth Sciences		**$20**	**$16**	
TI 30-3 Granitic Pegmatites		**$20**	**$16**	
TI 29-4 Quantitative Methods in Petrology		**$20**	**$16**	
TI 28-3 Advances in the Study of PGE		**$20**	**$16**	
TI 26-3 Seafloor Hydrothermal Mineralization		**$20**	**$16**	

Total A $ _____

B. Special Publications Series

SP-10 Pegmatites		$125	$100	
SP-9 Atlas of Migmatites		$140	$112	
SP-8 Mineral Species First Described from Greenland		$40	$32	
SP-6 Mineral Species Discovered in Canada		$45	$36	
SP-5 The Health Effects of Chrysotile Asbestos	$38		$30.40	
SP-4 New Minerals 1995–1999		**$20**	**$16**	
SP-3 Atlas of Micromorphology of Mineral Alterations and Weathering		**$100**	**$80**	
SP-2 Glossary of Mineral Synonyms		**$40**	**$32**	
SP-1 Encyclopedia of Mineral Names		**$30**	**$24**	
SP-0 A Compilation of IMA Reports		**$10**	**$8**	

Total B $ _____

C. Short-Course Volumes

Title	Qty	Price	Member	Total
SC 40 Laser Ablation ICP-MS in the Earth Sciences		$55	$44.00	
SC 39 Recent and not-so recent developments in uranium deposits and implications for exploration		$50	$40.00	
SC 38 Working with Migmatites		$40	$32.00	
SC 37 Geology of Gem Deposits		$50	$40.00	
SC 36 Melt Inclusions in Plutonic Rocks		$40	$32.00	
SC 35 Exploration for Platinum-Group Element Deposits		$55	$44.00	
SC 34 Mercury: Sources, Measurements, Cycles, and Effects		$40	$32.00	
SC 33 Infrared Spectroscopy		$40	$32.00	
SC 32 Fluid Inclusions		$45	$36.00	
SC 31 Environmental Aspects of Mine Wastes		$50	$40.00	
SC 30 Synchrotron Radiation		$40	$32.00	
SC 28 Fluids and Basin Evolution		$38	$30.40	
SC 27 Ore and Environmental Mineralogy		$38	$30.40	
SC 26 Mineralized Intrusion-related Skarn Systems...		$48	$38.40	
SC 25 Biological-Mineralogical Interactions		$38	$30.40	
SC 24 Undersaturated Alkaline Rocks...,		**$20**	**$16**	
SC 21 Experiments at High Pressure and Applications...		**$20**	**$16**	
SC 20 Low Temperature Thermochronology		**$20**	**$16**	
SC 19 Applications of Radiogenic Isotope Systems...		**$20**	**$16**	
SC 18 Fluids in Tectonically Active Regimes of the Continental Crust		**$20**	**$16**	
SC 16 Image Analysis Applied...		**$15**	**$12**	
SC 15 Burial Diagenesis		**$15**	**$12**	
SC 14 Heat, Metamorphism and Tectonics		**$15**	**$12**	
SC 13 Stable Isotope Geochemistry of Low T Fluids		**$15**	**$12**	
SC 12 Silicate Melts		**$10**	**$8**	
SC 11 Electron Microscopy in the Earth Sciences		**$10**	**$8**	
SC 9 Sediment-Hosted Stratiform Lead-Zinc Deposits		**$10**	**$8**	
SC 5 Neutron Activation Analysis		**$10**	**$8**	
SC 4 Asbestos Determination		**$10**	**$8**	
SC 2 Thermodynamics • Petrology & Ore Deposits		**$10**	**$8**	

Total C $ _____

Total A Thematic Issues

Total B Special Publications Series

Total C Short-Course Volumes

PUBLICATIONS – TOTAL $ _____

Shipping charge (see table below)

GRAND TOTAL $ _____

Complete shipping information at back.

Prices

The prices quoted are in **Canadian dollars for orders shipped within Canada and in US dollars for orders shipped in the USA and overseas**

Courier shipping available with customers account

Customer account number

Name of courier

Order online at: www.mineralogicalassociation.ca

Shipping and Handling Charges

	Canada		USA		Overseas	
	Regular mail	Courier	Surface mail	Airmail or courier	Surface mail	Airmail or courier
1 book	$10	$16	$16	$25	$20	$28
2 books	$13	$20	$18	$30	$40	$50
3-4 books	$16	$24	$24	$40	$50	$80
5 books and more (per book)	$4 per book	$6 per book	$6 per book	$8 per book	$12 per book	$20 per book

矿物地质论坛：http://bbs.3s001.com/

Mineralogical Association of Canada

Membership Application or Renewal Form 2009

In Canada: CAN$ funds Outside Canada: US$ funds

individual MeMbershiP

Ordinary membership

- ❑ Membership plus subscription to Canadian Mineralogist (print and e-access)* $105
- ❑ Membership plus electronic access to Journal $85
- ❑ Membership only $55

Student membership**

- ❑ Membership plus subscription to Canadian Mineralogist (print and e-access)* $55
- ❑ Membership plus electronic access to Journal $25
- ❑ Membership only $15

Retired membership (New applicants must have been ordinary members for 5 years to qualify)

- ❑ Membership plus subscription to Canadian Mineralogist (print and e-access)* $65
- ❑ Membership plus electronic access to Journal $30
- ❑ Membership only $20

Life membership $2000

InStItUtIon AI memberShIp corp./libraries

- ❑ Print version and site-license electronic*** access The Canadian Mineralogist $495
- ❑ Site-license electronic*** access The Canadian Mineralogist $425
- ❑ Sustaining subscription – print version and site-license electronic*** access The Canadian Mineralogist plus one copy of all publications published during the current year $695

*** See online activation instructions at www.mineralogicalassociation.ca/doc/ONLINE_ACTIVATION_INSTRUCTIONS.pdf/

Membership dues 2009 _____

Back dues for year(s) _____ _____
(at current annual rate)

I enclose a donation for the MACstudents travel and research grants program _____

PUBLICATIONS – Grand total _____

TOTAL _____

* Passwords issued in 2008 will be automatically renewed when your renewal is processed. For new subscribers, your customer number will be sent to you upon processing of your application with instructions to activate your online access.

To request online access send an email message to eaccess@mineralogicalassociation.ca

** Student status certified by:

Supervisor's name _____

Institution _____

Signature _____

membership fee includes-:

- ✓ A subscription to *Elements – An International Magazine of Mineralogy, Geochemistry, and Petrology* (replaces MAC Newsletters)
- ✓ A 20% discount on short-course volumes and special publications
- ✓ Special discount on registration fee for annual meeting (Toronto 2009) and 2009 sponsored short course

❑ **New application** ❑ **Renewal membership #** _____

PLEASE COMPLETE INFORMATION

Name (first name – initials – surname) _____

Institution/Company _____

Mailing Address _____

City _____

Prov /State _____ Country _____ Postal code _____

Telephone _____ Fax _____

E-mail _____

Method of Payment **mail or fax to (418) 653-0777**

Canadian funds for Canadian orders, US funds for non-Canadian orders.

❑ Cheque ❑ Money order ❑ Credit card

Cheque payable to: **Mineralogical Association of Canada**
For payment by bank draft, contact the business office.

CREDIT CARD:

I authorize the Mineralogical Association of Canada to charge the TOTAL AMOUNT

DUE _____ to my: ❑ VISA ❑ MasterCard ❑ EuroCard

Number _____/_____/_____/_____

Expiry Date _____/_____ Security code _____

Name _____

Signature _____

Mineralogical Association of Canada
Association minéralogique du Canada

Send order to:
Mineralogical Association of Canada
490, rue de la Couronne
Québec, Québec
CANADA G1K 9A9
Phone: (418) 653-0333 • Fax: (418) 653-0777
E-mail: office@mineralogicalassociation ca

Order online: www.mineralogicalassociation.ca

矿物地质论坛：bbs.3s001.com